Ultralow-Noise Modelocked Lasers

by

Leaf Alden Jiang

Submitted to the Department of Electrical Engineering and Computer Science
in partial fulfillment of the requirements for the degree of

Doctor of Philosophy

at the

MASSACHUSETTS INSTITUTE OF TECHNOLOGY

May 2002

Author .....
Department of Electrical Engineering and Computer Science
May 3, 2002

Certified by .....
Erich P. Ippen
Elihu Thomson Professor of Electrical Engineering
Thesis Supervisor

Accepted by .....
Arthur C. Smith
Chairman, Department Committee on Graduate Students

Ultralow-Noise Modelocked Lasers

by

Leaf Alden Jiang

Submitted to the Department of Electrical Engineering and Computer Science
on May 3, 2002, in partial fulfillment of the
requirements for the degree of
Doctor of Philosophy

Abstract

The measurement, design, and theory of ultralow-noise actively modelocked lasers are presented. We demonstrate quantum-limited noise performance of a hybridly modelocked semiconductor laser with an rms timing jitter of only 47 fs (10 Hz to 10 MHz) and 86 fs (10 Hz to 4.5 GHz). The daunting task of measuring ultralow-noise levels is solved by a combined use of microwave and optical measurement techniques that yield complete characterization of the laser noise from DC to half the laser repetition rate.

Optical cross-correlation techniques are shown to be a useful tool for quantifying fast noise processes, isolating the timing jitter noise component, measuring timing jitter asymmetries, and measuring correlations of pulses in harmonically modelocked lasers. A noise model for harmonically modelocked lasers is presented that illustrates how to correctly interpret the amplitude noise and timing jitter from microwave measurements. Using information about the supermodes, the amplitude and timing noise can be quantified independently, thereby making it possible to measure the noise of harmonically modelocked lasers with multi-gigahertz repetition rates.

Methods to further reduce the noise of a modelocked laser are explored. We demonstrate that photon seeding is effective at reducing the noise of a modelocked semiconductor laser without increasing the pulse width. Experimental demonstrations of a timing jitter eater, consisting of a phase modulator and dispersive fiber, show that the noise power spectral density can be reduced by more than 12 dB. Finally, we demonstrate how to reduce the timing jitter with electronic feedback to the saturable absorber and gain terminals.

An analytical theory for semiconductor lasers that includes carrier dynamics is presented. Ultralow noise performance is achieved by reducing the dispersion of the cavity, reducing the linear losses in the cavity, by operating at high optical powers, and with a tight optical filter. The gain dynamics of the semiconductor laser do not severely degrade the noise performance.

Thesis Supervisor: Erich P. Ippen
Title: Elihu Thomson Professor of Electrical Engineering

Acknowledgments

I would like to thank Dora for her love and support during my entire student life at MIT. Her poppy-seed cake that she made a few weeks back was delicious. I look forward to many more in the future.

Thanks to my family for all their support. I would like to thank my mom for her numerous vitamin supplements and patience. I would like to thank my dad for driving the family up to Boston on many occasions to visit Dora and I, and buying tons of groceries for us. Thanks for all the stuff that they got us, including the 3 years of Microwaves and RF and Microwave Journal that they brought last time. I am also thankful for some of the test equipment my dad lent me – multimeters, oscilloscopes, soldering equipment, function generators – that have been useful for this thesis on many occasions. I would like to thank my brothers for checking up on me. I would like to thank Will for all his fun emails, phone calls, and humor. I'd like to thank Justice (a.k.a. Baber) for his therapeutic punches and showing me how to skateboard and rollerblade. Thanks to Chung, James, and Ching for their kindness and support.

I would like to thank my advisor Prof. Ippen for his advice and insight that made this thesis possible. It was a real pleasure to be his graduate student, and appreciate the freedom he gave me in my thesis work. I would like to thank Paul Juodawlkis for his guidance and support for this thesis. Even though he was busy, he made time to come down to campus and discuss our work. I would also like to thank Prof. Haus for his lively discussions. All three advisors were a great source of good ideas and suggestions.

I would like to thank H. Yokoyama at NEC for providing the semiconductor laser devices. I would like to thank Jesse Searls and Cam McNeilage at Poseidon Scientific Instruments for their interest in our work, loaning us their Shoebox oscillator, and sending Cam to help us with our noise measurements. This thesis would not have been possible without these collaborations.

I would like to thank my lab mates for good discussions, their friendliness, and creating a positive lab environment. I would like to especially acknowledge Matt

Grein for sharing lab space, giving good suggestions, and helping with experiments. Special thanks to Juliet Gopinath for her saturable absorbers, Kazi Abedin for his help with the photon seeding part of this thesis, Dan Ripin for lending equipment, Pete Rakich for his discussions about photon counting and low noise detection, Laura Tiefenbruck and Jason Sickler for adding some life to the lab, my office mates Thomas Schibli and JP Laine, and Farhan Rana for detailed discussions of laser noise.

I also appreciate the work of Cindy, Donna, and Mary, who have kept the office mechanics running smoothly on a daily basis.

I appreciate the support of our sponsors which have made this work possible: Bose Foundation fellowship, National Science Foundation fellowship, Air Force Office of Scientific Research (AFSOR), and Defense Advanced Research Projects Agency Photonics A/D Converter Technology Program (DARPA PACT).

Contents

List of Figures

List of Tables

Chapter 1

Introduction

The generation of low-noise photonic pulse trains is critical to optical sampling and communications applications. Modelocked lasers are excellent pulse sources since they can produce short picosecond or sub-picosecond pulses at gigahertz repetition rates with low timing jitter. Erbium-doped fiber lasers and semiconductor lasers are the lasers of choice for these applications since they operate at the popular telecommunications wavelength of 1.5 μm and are technologically mature. Picosecond pulse widths and multi-gigahertz repetition rates have been demonstrated with fiber and semiconductor lasers by many groups [6, 7, 8, 9], but the timing jitter is usually measured to be greater than half a picosecond.[1]

This thesis reports on the theory, measurement, and design of ultralow-noise modelocked lasers with an emphasis on semiconductor lasers. With careful cavity design, it is shown that sub 100-fs jitter can be obtained. One major achievement in this thesis was the demonstration of quantum-limited noise performance of a semiconductor laser with only 47 fs jitter (10 Hz to 10 MHz).

The theory of actively modelocked laser noise presented in chapter 2 of this thesis is based upon the work of Haus and Mecozzi [10], Moores [11], and Grein [12]. The new additions to the theory are the inclusion of oscillator noise and gain dynamics. This work presents probably the most rigorous testing of a laser noise model against

[1]These groups compute the timing jitter of their lasers by integrating their phase noise measurements from tens to hundreds of Hertz to hundreds of kilohertz or megahertz.

actual experimental results. Phase noise measurements of the semiconductor laser output as a function of modulation depth, saturable absorption, and filter bandwidth are compared with the theory, and the theory is found to be exceptionally accurate at predicting real experimental results. Having a trustworthy theory provides a solid theoretical foundation for understanding how to design low noise lasers. I hope that this work dispels several misconceptions about low-noise laser design. One of the major misconceptions is that one can make the jitter arbitrarily small by extending the cavity length. This is certainly not true and the presented noise theory provides a way to understand this.

In chapter 2 of this thesis, a new model for noise in harmonically modelocked lasers is presented. Harmonically modelocked lasers are lasers that contain multiple pulses in the cavity. Since all fiber lasers, as well as some semiconductor lasers, are harmonically modelocked, this is an extremely important issue. The model shows how to correctly interpret the phase noise measurement into a number for timing jitter. Numbers less than 10 fs (100 Hz to 1 MHz) have been reported [13], but are about 100 times smaller than the actual value!

Chapter 3 is intended to be a comprehensive treatment of modelocked laser jitter measurement. Residual phase noise measurements are shown to be an extremely sensitive measurement technique for phase noise of fundamentally modelocked cavities. It is shown that the nonlinear cavity response of the harmonically modelocked laser makes it difficult to obtain a true residual measurement at all frequency offsets. Here it is explained why many have observed that their "residual" measurements depend on the phase noise of their microwave oscillator. Section 3.2 of this chapter summarizes the work that was done with optical cross-correlations. This optical measurement technique can be used to characterize the pulse-to-pulse timing jitter, reveal the pulse-to-pulse jitter correlations in the modelocked laser, and verify the noise model for harmonically modelocked lasers. In addition, we use it to find the probability density function of the timing jitter and show how it simplifies jitter measurements in recirculating loop experiments.

Chapter 4 focuses on methods to reduce the timing jitter in modelocked lasers.

Reducing the jitter of a laser without increasing the pulse width proves to be a difficult problem. Section 4.1 shows how photon seeding can be used to reduce the timing jitter of a laser without penalty to the pulse width. Section 4.3 shows how phase modulation plus dispersion can be used to reduce the timing jitter of any pulse train. This apparatus is called the "timing jitter eater," and over 12 dB reduction in the phase noise has been demonstrated with just a single phase modulator.

1.1 Jitter Timescales

In simplest terms, jitter refers to the uncertainty, or variability, of waveform timing. Although the definition is straightforward, describing the physical origin of noise in lasers, measuring the noise and understanding the measurements, as well as understanding how timing jitter degrades optical sampling and communication systems is rather complicated.

One important concept is that the timing jitter of modelocked lasers arises from distinctly different physical mechanisms that have different timescales. On long timescales, > 100 μs, length fluctuations and flicker noise of the voltage and current sources dominate. On medium timescales, 100 μs to 100 ns, the jitter is held constant by re-timing from the active modulator. On faster timescales, < 100 ns, spontaneous emission is the dominant noise source. Fig. 1-1 shows how these various noise mechanisms show up in the pulse-to-pulse jitter and the phase noise spectrum. The solid line plots the timing variance between the first pulse and pulse n and resembles the single-sideband phase noise curve. For sampling applications, high-frequency noise must be mitigated since this affects the quality of sampling from pulse-to-pulse. For optical clock applications, reducing low-frequency phase noise is critical.

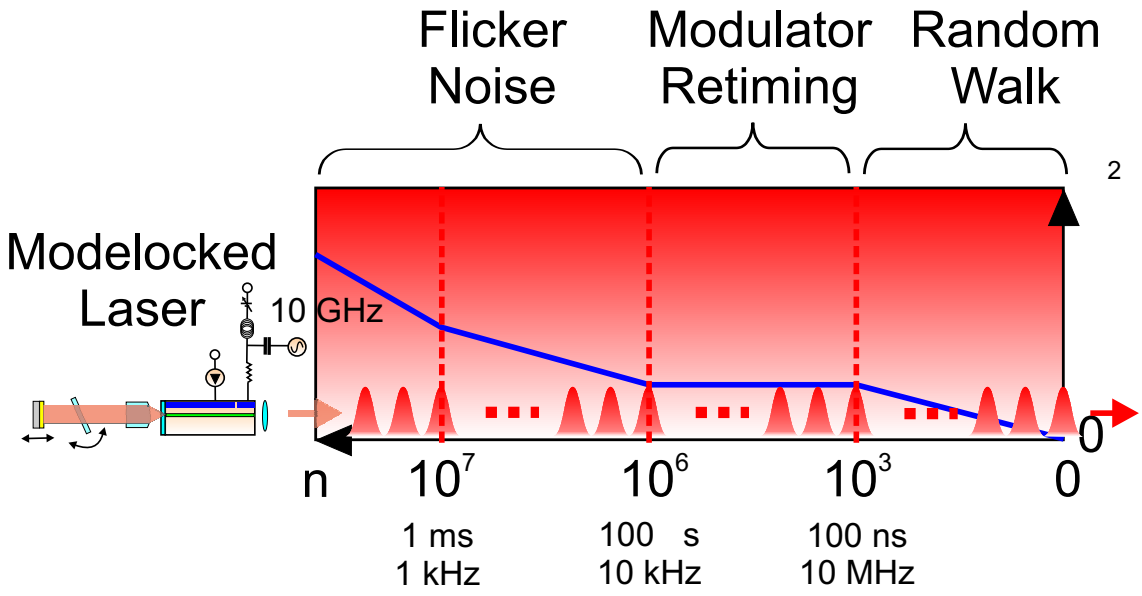

Figure 1-1: Timing jitter mechanisms and timescales.

1.2 Importance of Ultralow-Noise Modelocked Lasers in Optical Communications

In optical time-division multiplexed communications systems [14, 15, 16], high bit rates are achieved by using short pulses and packing them tightly together. Transmission at 160 Gbit/s has been demonstrated with 1.2 ps pulses [17]. This repetition rate corresponds to a bit period of only 6.25 ps, which means that the modelocked laser source must have small timing jitter to yield acceptable bit error rates. Timing jitter should be less than 10% of the bit period to have better than a 10^{-9} bit error rate. This implies that the timing jitter must be better than 625 fs at 160 Gbit/s. Fig. 1-2 shows a plot of the maximum allowed timing jitter as a function of bit rate. As the bit rate increases the pulses must be correspondingly shorter. In the theoretical section of this thesis, we will see that the timing jitter increases dramatically as the pulse width decreases. Therefore, as the bit rate increases, the laser source must not only have lower timing jitter, but it must also be able to do so with shorter pulses.

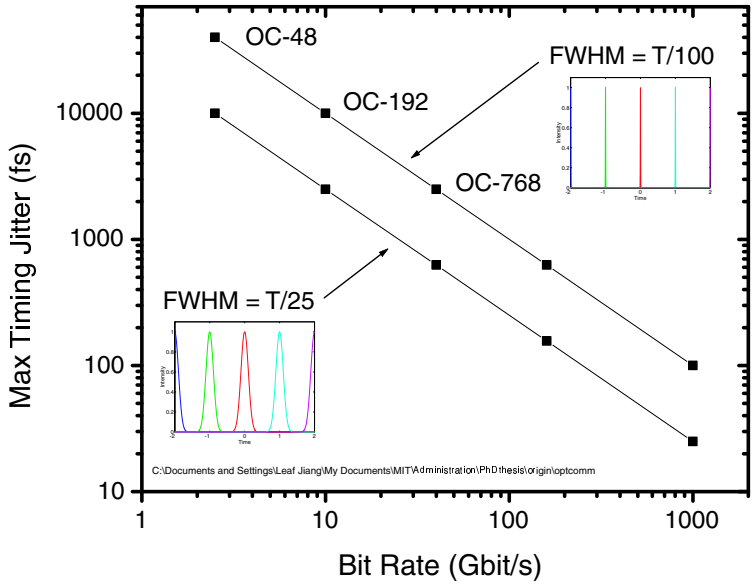

Figure 1-2: Bit rate versus maximum allowed timing jitter.

1.3 Importance of Ultralow-Noise Modelocked Lasers in Optical Sampling

A new generation of optical analog-to-digital converters is being investigated as a possible route to obtain better sampling resolution and rates than what can be achieved electronically [18]. There is an inherent tradeoff between the sampling rate and the bits of resolution for a given amount of jitter in the sampling gate. The maximum allowable jitter in the optical pulse train used to electro-optically sample an electrical waveform is plotted in Fig. 1-3 [18]. The figure shows that less than 20 fs of timing jitter is required for a sampler with 12-bits of quantization at a sampling rate of 10 Gsamples/s. The benefit of improving ADC performance with optical sampling techniques is to improve signal-processing capabilities for pulsed radar, electronic warfare, and cell phone bay stations. Requirements on the optimal sampling pulse width are presented in Appendix D.

The recent interest in developing optical sampling systems also brought attention to the high-frequency jitter of the modelocked laser output. The power spectral

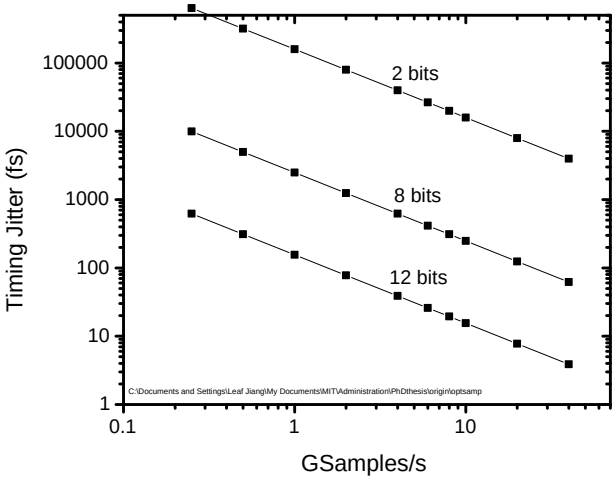

Figure 1-3: The maximum allowable timing jitter is plotted as a function of sampling rate for 2, 8, and 12 bits of resolution. The relationship between pulse width and timing can be derived by considering a sinusoidal signal at frequency ω_M. The most difficult point to sample is at the zero crossing where the slope is the greatest. A pulse that samples at the zero crossing yields no detected power. If that pulse experiences a time displacement of Δt, the detected output would be $\omega_M \, \Delta t$. This quantity must be less than the quantization spacing, $2/2^N$. Remember that according to Nyquist, the sampling rate must be at least $2\pi f_{samp} = 2\omega_M$. Therefore, $\pi f_{samp} \, \Delta t < 2/2^N$.

density of the timing jitter up to the half the repetition rate of the laser causes sampling errors. Since we can express any amplitude or timing change from one pulse to the next as a sum of sinusoids with maximum frequency of $1/2T_M$, where T_M is the repetition rate, the timing variance is found by integrating the power spectral density of the timing jitter from $-\omega_M/2 < \omega < \omega_M/2$, where $\omega_M = 2\pi/T_M$.

1.4 Choice of Modelocked Laser

Out of all possible gain media and laser types, Erbium-doped fiber lasers (EDFLs) and semiconductor lasers are most appropriate for optical sampling and telecommunication applications due to the following reasons

1. Both laser media can operate at a wavelength of 1.5 μm which corresponds

to the low-loss wavelength in silica fiber. In addition, there are many optical components that are commercially available at this wavelength.

2. The gain bandwidth can easily support sub-picosecond pulses.

3. Active modelocking at high repetition rates in excess of 10 GHz of these lasers has been routinely demonstrated.

4. These lasers can be packaged into reasonable sizes. Less than a few cubic centimeters in the case of the semiconductor laser.

5. Low noise operation has been demonstrated with both lasers.

Ti:Sapphire lasers have been shown to have 1 ps (1 Hz to 40 MHz) of integrated timing jitter [19]. This number is a bit surprising since Ti:Sapphire lasers have very low internal loss. These lasers are passively modelocked which means that the repetition rate of the laser changes with fluctuations in the cavity length. The length is often stabilized by adjusting the length with a PZT and locking to a microwave reference frequency. This is equivalent to using a modulator with a very weak modulation depth. Our theory predicts that the timing variance should scale as the inverse of the modulation depth. Hence, the 1 ps of timing jitter could be due to the way in which the repetition rate is stabilized. The introduction of an active electro-optic modulator into the Ti:Sapphire cavity increases the cavity loss. In addition, the gain bandwidth of Ti:Sapphire does not cover 1.5 μm.

The gain-switched semiconductor laser is another optical pulse source that may be considered for optical sampling. Even with optical and electronic feedback schemes [20], the noise of these lasers is typically well above 0.5 ps [21]. Physically, each pulse must arise from spontaneous emission, and the turn-on time is a stochastic process.

Other non-modelocked pulse sources such as those produced by a combination of modulation, amplification, and then dispersion decreasing fiber are not well studied. Optical pulses of 200 fs duration at 10 GHz repetition rate have been demonstrated [22]. Random nonlinear effects such as stimulated Raman backscattering and intensity to phase noise conversion through the Kerr effect may limit the noise performance.

For a long time, it was thought that semiconductor lasers could not obtain low noise operation due to their slightly higher inversion parameter compared to Erbium-doped fiber lasers and to their short nanosecond upper-state lifetime. Through the work of Derickson [23], DePriest [24] and our work [25], it has been shown that semiconductor lasers can indeed be very quiet with under 100 fs of timing jitter, thereby reviving interest in these lasers as optical sampling sources.

1.5 Organization of Thesis

This thesis is organized into three parts. The first part describes the salient features of the noise theory that are necessary for designing ultralow noise modelocked lasers. The second part explains how to accurately measure the noise power spectral density over a large range of frequency offsets. The last part demonstrates several techniques that we have used to reduce the noise of modelocked lasers even further. Many of the detailed theoretical calculations and pulse characterization algorithms can be found in the appendix.

Chapter 2

Modelocked Laser Noise Theory

2.1 Timing Variance and Power Spectral Density

The pulses in an actively modelocked laser cavity are randomly pushed around their equilibrium positions by noise. The resulting variability in the pulse train timing is called timing jitter. When noise nudges a pulse, the amplitude or phase modulator in the laser cavity drives the pulse back to its equilibrium position. Timing restoration of the optical pulses has been found to behave like a mass on a spring with a dashpot [12]. The displacement of the mass is equivalent to delaying or expediting the pulse. The mass is analogous to the pulse energy. A larger mass is less sensitive to small noise perturbations just as a pulse with many signal photons is not greatly perturbed by a few noise photons. The amplitude modulator is analogous to the spring since they both apply restoration forces.[1] Noise applies randomly directed forces on the mass.

There are two major analytical theories for noise in actively modelocked lasers. The soliton noise theory (chapter B, section B.3) describes the noise in soliton lasers in which the pulse intensity has a hyperbolic secant shape [26]. The Hermite-Gaussian noise theory (chapter B, section B.2) describes the noise for lasers in which the pulse intensity is closer to a Gaussian shape. Depending on the magnitude of the saturable

[1] Comparing equation (B.102) for the laser noise with (B.208) for a mass with dashpot and spring, we see that the analogy is $\alpha = 2\gamma_0^{\Re}$ and $\omega_0 = 2\gamma_0^{\Im}$.

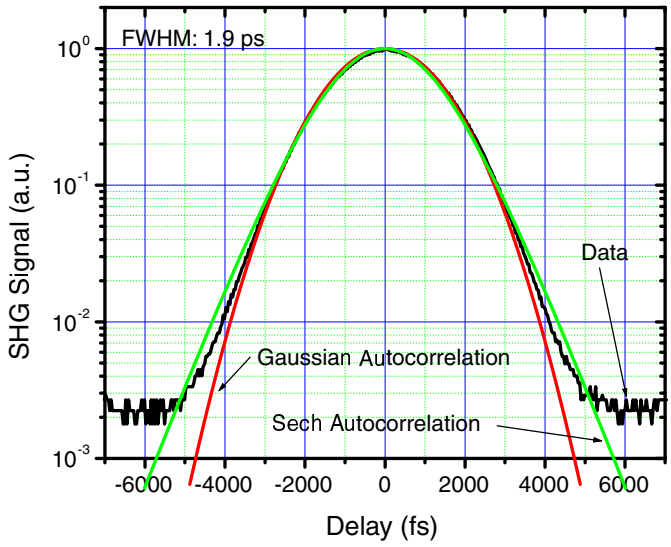

Figure 2-1: Autocorrelation of the temperature-controlled external-cavity modelocked semiconductor laser at 10 GHz. The modulation power to the saturable absorber was 23.8 dBm, the injection current was 35 mA, and the saturable absorber bias was -2.08 V. The pulse shape could be described with either a Gaussian or hyperbolic secant function.

absorber bias, the pulse shape can be anywhere between a hyperbolic secant and a Gaussian. For high saturable absorber biases (-2 V), the pulse shape is hyperbolic secant-like, as shown in Fig. 2-1. For low saturable absorber biases (< -1.6 V), the pulse intensity profile is Gaussian, as shown in Fig. 2-2. The differences between the two noise theories are discussed in chapter B, section B.4 and are found to yield similar expressions for the timing jitter power spectral density.

The power spectral density for timing jitter in an AM actively modelocked laser is derived in chapter B, section B.2, equation (B.108) and found to be equal to

$$|\Delta\tilde{t}(\Omega)|^2 = \tilde{C}(\Omega)\tilde{N}(\Omega) \tag{2.1}$$

where $\tilde{C}(\Omega)$ is the laser cavity response and $\tilde{N}(\Omega)$ is the noise power spectral density. The cavity response is

$$\tilde{C}(\Omega) = \frac{2\tau^2}{w_0}\frac{1}{\Omega^2 + (2\gamma_0^{\Re})^2}, \tag{2.2}$$

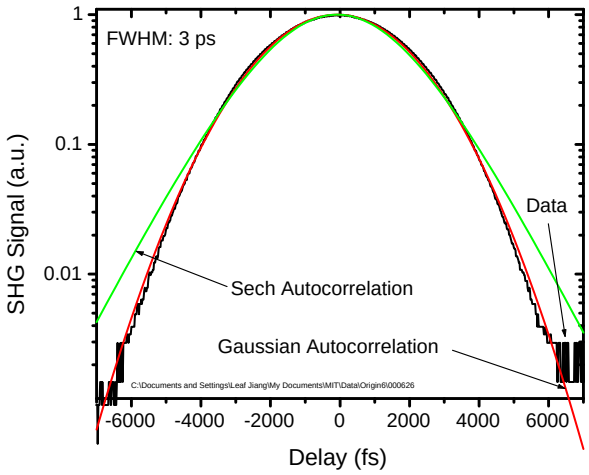

Figure 2-2: Autocorrelation of the non-temperature-controlled external-cavity mode-locked semiconductor laser at 5 GHz. The applied rf power was about 20 dBm, the injection current was 50 mA, and the saturable absorber bias was -1.6 V. The autocorrelation function fits well to a Gaussian function.

where τ is the pulse width, w_0 is the pulse energy,

$$\gamma_0^{\Re} = \frac{M_{AM}\omega_M^2\tau^2}{4T_R} \tag{2.3}$$

is a function of the modulation depth M_{AM}, modulation frequency ω_M, and round-trip time T_R. The cavity response is Lorentzian and hence is analogous to a critically damped mass on a spring and dashpot. The noise is a sum of the spontaneous emission noise, cavity length fluctuations, and microwave oscillator noise. The noise power spectral density is

$$\tilde{N}(\Omega) = \frac{P_{ASE}}{4\pi} + \frac{w_0}{2\tau^2}\left(\frac{1}{v_g T_R}\right)^2 |\Delta\tilde{L}(\Omega)|^2 + \frac{w_0}{8}\left(\frac{M_{AM}\omega_M\tau}{T_R}\right)^2 |\Delta\tilde{\phi}_{osc}(\Omega)|^2, \tag{2.4}$$

where P_{ASE} is the amplified spontaneous emission power, v_g is the group velocity, $|\Delta\tilde{L}(\Omega)|^2$ is the power spectral density of the cavity length fluctuations, and $|\Delta\tilde{\phi}_{osc}(\Omega)|^2$ is the phase noise of the microwave oscillator. More exactly, the numer-

ator $P_{ASE}T_R$ is the spontaneous emission energy that overlaps with the pulse.

Equation (2.1) is integrated over all frequencies to obtain the timing variance[2]

$$\boxed{\sigma_t^2 = \frac{P_{ASE}/2}{w_0}\frac{\tau^2}{2\gamma_0^{\Re}} = \frac{(P_{ASE}T_R)/2}{w_0}\frac{1}{M_{AM}\omega_M^2}} \tag{2.5}$$

In obtaining this expression, the length fluctuations and microwave oscillator noise was ignored. Hence, equation (2.5) yields the fundamental quantum noise of the laser due to spontaneous emission.

The fast gain dynamics in a semiconductor laser due to short nanosecond upper-state lifetimes were examined to see whether they affect the timing jitter. Section B.2.3 in Appendix B shows how to include gain dynamics in the laser noise theory and it is found that the effect on timing jitter is negligible.

2.2 Design Rules for Ultralow-Noise Modelocked Lasers

A summary of the design rules for ultralow noise modelocked lasers can be obtained from equation (2.5) and is as follows

1. Minimize cavity loss. The slope of the P-I curve in saturation, shown in Fig. 2-3, steepens for decreasing cavity loss. Therefore, the ratio of the spontaneous emission power to the signal power decreases resulting in a reduction of the timing jitter according to equation (2.5).

2. Increase output power. Above threshold, Fig. 2-3 shows that the spontaneous emission power clamps at a constant value since the carrier concentration clamps at N_{th} and the spontaneous emission rate is proportional to N^2. The signal power, on the other hand, increases with increasing pump current. Therefore, the signal-to-noise ratio in equation (2.5) improves and the timing jitter decreases.

[2]This is the pulse-to-clock variance.

3. Maximize modulation depth. The timing variance is inversely proportional to M_{AM}.

4. Increase modulation curvature by either increasing the frequency or using an comb generator, such as a resonant tunnelling diode (RTD) or step-recovery diode (SRD). The timing variance is inversely proportional to ω_M^2. Generally, operating at higher microwave frequencies does not introduce significant excess timing jitter since doublers are relatively quiet.

5. Increase saturable loss relative to the linear loss. This will improve the signal energy to noise energy ratio.

6. Minimize dispersion for AM modelocked lasers. This can be seen from equation (B.329). Dispersion gives rise to Gordon-Haus jitter. This can quickly become a problem for short pulses since the timing variance scales as $1/\tau^8$.

7. Reduce classical noise sources: (1) use quiet rf oscillator, (2) remove ground loops, (3) use quiet current and voltage supplies, (4) protect laser from thermal variations and vibrations, (5) use isolator on output port to prevent back reflections into the cavity. Even a 4% reflection can cause the laser output to be chaotic.

Making the cavity longer does not improve the noise performance since the gain-per-pass and noise-per-pass added to each pulse remains the same. This will be explained in more detail in section 2.5.

2.2.1 Semiconductor Lasers vs. Fiber Lasers

It is hard to compare the timing jitter performance of semiconductor modelocked lasers with fiber modelocked lasers since there are no valid residual phase noise measurements of fiber lasers in the literature.[3] If we assume that both lasers have same

[3]To accurately measure the noise of these lasers requires a low noise oscillator (such as Poseidon's shoe box oscillator), and the measurement of all the supermodes up to half the repetition rate. Most measurements in the literature are absolute phase noise measurements of the first supermode.

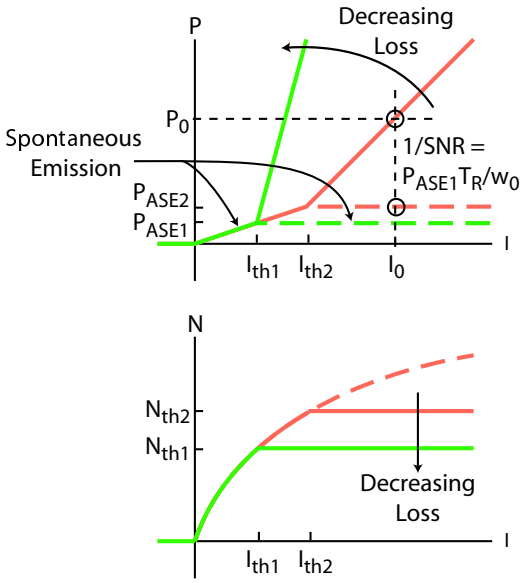

Figure 2-3: The steady-state photon density and carrier density as a function of injection current. Adapted from [1, p.41,43].

modulation depth M and frequency ω_M and the total dispersion in the EDFL is zero, then the rms timing jitter of the EDFL can be about five times better than the MLLD according to equation (2.5). The spontaneous emission energy in the MLLD is about 1-3 times larger than the EDFL since the inversion factor is $n_{sp} = 1 - 3$. In addition, the output power of the EDFL can easily be 10 mW versus the typical 1 mW output of the MLLD. This implies that the EDFL pulse energy is approximately ten times larger than that of the MLLD.

Both lasers will continue to be interesting since there are advantages to both technologies (1) it is difficult to get close to zero dispersion in an EDFL; (2) feedback techniques may be used to dramatically reduce the laser noise level so that the small difference in the laser noise between EDFLs and MLLDs is not important; (3) MLLD can be small, compact, and environmentally more stable; and (4) the low frequency noise of the EDFL is generally cleaner than that of the MLLD.

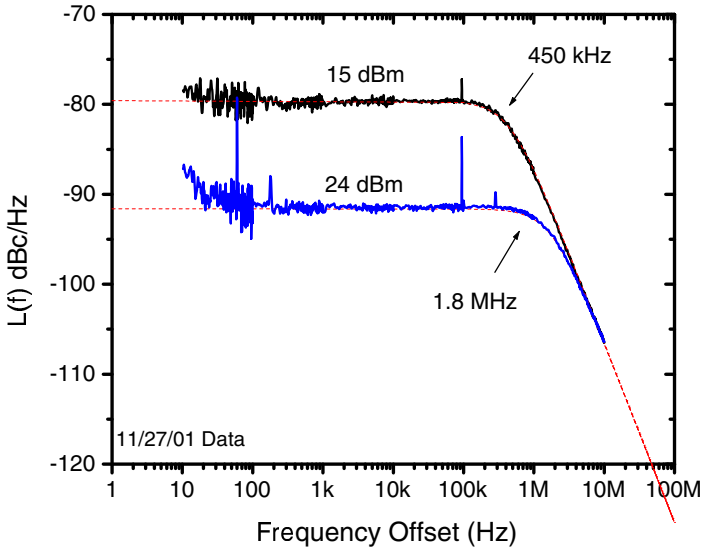

Figure 2-4: Single-sideband phase noise of the temperature controlled external-cavity modelocked semiconductor laser at 10 GHz with a 5-nm optical BPF. The phase noise increases as the microwave driving power to the saturable absorber decreases from 24 dBm to 15 dBm. The dashed lines show the theoretical values.

2.3 Comparison Between Theory and Experiment

The derivation of the power spectral density of the timing jitter, equation (2.1), contains many simplifications that are outlined in appendix B, but is nonetheless amazingly powerful at predicting the actual phase noise of our lasers.

2.3.1 Timing Jitter vs. Modulation Depth

The residual phase noise of the temperature-controlled modelocked semiconductor laser at 10 GHz is shown in Fig. 2-4 for two different modulation strengths. The noisier curve corresponds to an applied rf power of 15 dBm and the lower curve corresponds to an applied rf power of 24 dBm. These two curves fit very well to the theoretically predicted Lorentzian power spectral densities for the spontaneous emission noise. At high offsets, the laser noise rolls off at 20 dB/decade.

The theoretical curves (the dashed lines) in Fig. B-5 fit very closely to the measured values. The values used in constructing the dashed lines were $P_{ASE} = 0.008$ mW,

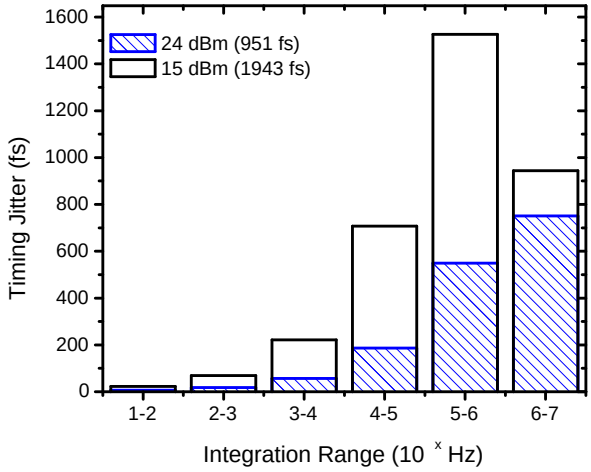

Figure 2-5: Integrated timing jitter of temperature-controlled external-cavity semiconductor laser corresponding to Fig. B-5.

$w_0 = 0.7$ pJ, $\tau = 3.5$ ps, $T_M = 100$ ps, $2\gamma_0^{\Re}(24\text{ dBm}) = 2\pi \times 1.8$ MHz, and $2\gamma_0^{\Re}(15\text{ dBm}) = 2\pi \times 450$ kHz. The re-timing parameter, $\gamma_0^{\Re}$, was chosen to fit the knee of the measured noise data. All the other values were measured.

The modulation depth was increased by a factor of 4 from increasing the applied rf power from 15 to 24 dBm. Equations (2.2) and (2.3) show that if M_{AM} increases by a factor of 4, then the roll-off frequency decreases by a factor of 4 and the phase noise at low offsets decreases by a factor of $M^2 = 16$ or 12 dB. The measured values show excellent agreement with the theoretically predicted trends.

The importance of noise at high-frequency offsets becomes apparent when the timing jitter is plotted as a function of integration range. Fig. 2-5 shows a histogram plot of the integrated timing jitter due to the noise in each decade. The integrated noise values from 10 Hz to 10 MHz are 951 fs (with 24 dBm drive) and 1943 fs (with 15 dBm drive). Most of the noise is due to high-frequency (100 kHz to 10 MHz) fluctuations. For ultralow-noise lasers with large modulation depths, the largest contributions to the integrated timing jitter come from high frequency offsets.

2.3.2 Timing Jitter vs. Saturable Absorption

Neither the soliton nor Hermite-Gaussian noise theory predict how the timing jitter changes with saturable absorption. Nevertheless, the saturable absorption can be tuned by changing the applied reverse bias of the saturable absorber. Fig. A-8 shows that the saturable absorption increases as the reverse bias increases. If the saturable loss increases, then the small-signal noise is attenuated more than the high-peak-intensity pulse. The ratio of the ASE power to the signal power decreases, and hence equation (2.5) shows that the timing jitter must decrease. Increasing the magnitude of the saturable absorber bias also has the effect of shortening the output pulses.

Fig. 2-6 shows the residual phase noise of an actively modelocked semiconductor laser for a reverse bias of -0.95 V and -2.00 V. The applied rf power was kept at 10 dBm for both measurements and the applied rf frequency was 9.5 GHz. The phase noise for the $V_{SA} = -2.00$ V curve is about 12 dB lower than the phase noise for the $V_{SA} = -0.95$ V curve. The theoretical curves for the spontaneous emission noise spectra, shown with dashed lines, fit well to the measurements.[4]

The phase noise at low offsets in Fig. 2-6 shows a $1/f$ characteristic from the flicker noise of the current and voltage sources as well as large electrical pickups at harmonics of 60 Hz. A detailed discussion of these classical noise sources is given in appendix B. The non-temperature controlled semiconductor laser was mounted in an aluminum mount that was securely bolted to the optical table. Ground loops between the saturable absorber ground, current source ground, and the grounded tabletop are probably the cause for the enhanced noise at frequency offsets less than 1 kHz. Our temperature controlled mount was electrically isolated from the optical table, and the resulting phase noise spectrum does not exhibit as much low frequency noise, see Fig. B-5. Therefore careful isolation of the ground loops, not grounding the power supplies to the rf amplifiers, running the voltage supply off of alkaline batteries, by using inner/outer DC blocks on all rf feeds as well as electrically isolating the diode

[4]Theoretical values corresponding to Fig. 2-6: The lower curve corresponds to $I_j = 65$ mA, $V_{SA} = -2$ V, $P_{ASE} = 0.001$ mW, $2\gamma_0^{\Re} = 2\pi \times 450$ kHz, $w_0 = 0.7$ pJ, and $\tau = 1.74$ ps. The upper curve corresponds to $I_j = 65$ mA, $V_{SA} = -0.95$ V, $P_{ASE} = 0.01$ mW, $2\gamma_0^{\Re} = 2\pi \times 350$ kHz, $w_0 = 0.7$ pJ, and $\tau = 1.74$ ps.

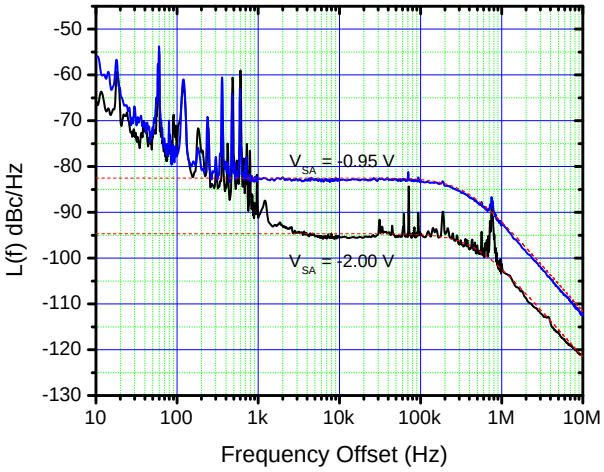

Figure 2-6: Residual phase noise of modelocked semiconductor laser as a function of saturable absorption.

chip from the optical table is critical for good noise performance at low frequency offsets.

2.3.3 Timing Jitter vs. Filter Bandwidth (Pulse Width)

According to the noise theory outlined in appendix B, the rms timing jitter scales either as $1/\tau^2$ for actively modelocked lasers or as $1/\tau^4$ for lasers with dispersive cavities that are dominated by Gordon-Haus jitter. Hence, there is an inherent tradeoff between low noise performance and pulse width.

Fig. 2-7 shows a plot of the timing jitter as a function of pulse width for several lasers. Points C and D are fiber lasers and the other points correspond to semiconductor lasers. Since fiber lasers generally have large dispersion, a dotted line with slope $1/\tau^4$ is drawn through those points that indicates a constant figure of merit. The figure of merit depends on cavity loss and the inversion of the gain. Since semiconductor lasers generally have negligible dispersion[5], a dashed line with slope $1/\tau^2$

[5]The dispersion of our laser was measured at $< -16.8 \pm 1.7$ fs/nm.

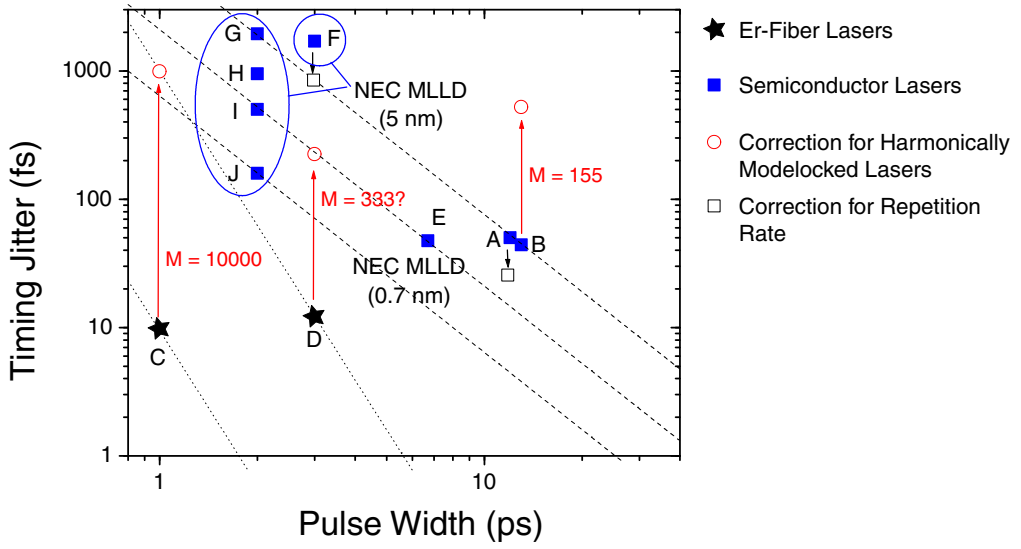

Figure 2-7: Timing jitter plotted as a function of pulse width for several lasers. Dashed lines have a slope of $1/\tau^2$. Dotted lines have a slope of $1/\tau^4$. Reported results for harmonically modelocked lasers are corrected by multiplying the reported number by $\sqrt{M}$ and shown with hollow circles (see section 2.5 for explanation). The hollow squares show how the noise should theoretically improve if the repetition rate increased from 5 to 10 GHz (rms timing jitter is inversely proportional to the modulation frequency). Table 2.1 shows the repetition rate, integration range, and reference for points A to J.

is drawn through those points.

Points B, C, D correspond to harmonically modelocked lasers. The reported values considered only the first supermode. Section 2.5 shows that these numbers need to be multiplied by the square root of their harmonic number (assuming that all pulses in the cavity are uncorrelated). The solid circles indicate the corrected timing jitter for points B, C, and D.

Points E and J corresponds to the best results with 0.7 and 5 nm optical band-pass filters, respectively. The internal cavity loss of the 0.7-nm filter was larger and hence has a lower figure of merit.[6] For reference, their phase noise plots are shown in Fig. 2-8 and 2-9 for the 0.7 and 5 nm filters, respectively.[7]

[6]For $V_{SA} = 0$ V, $I_{th}(0.7 \text{ nm}) = 29.6$ mA, and $I_{th}(5 \text{ nm}) = 22$ mA.

[7]Theoretical values corresponding to Fig. 2-9: The lower curve corresponds to $I_j = 35$ mA,

Point	Repetition Rate	Integration Range	Laser Type	Reference
A	5 GHz	100 Hz to 100 MHz	Semiconductor	[23]
B	10 GHz	10 Hz to 10 MHz	Semiconductor	[27, 28]
C	10 GHz	100 Hz to 1 MHz	Er-Fiber	[13]
D	10 GHz	100 Hz to 30 MHz	Er-Fiber	[29]
E	9 GHz	10 Hz to 10 MHz	Semiconductor	[25]
F	5 GHz	200 kHz to 2.5 GHz	Semiconductor	[26]
G	10 GHz	10 Hz to 10 MHz	Semiconductor	11/27/01 data
H	10 GHz	10 Hz to 10 MHz	Semiconductor	11/27/01 data
I	10 GHz	10 Hz to 10 MHz	Semiconductor	3/15/02 data
J	10 GHz	10 Hz to 10 MHz	Semiconductor	3/15/02 data

Table 2.1: Description of points A to J in Fig. 2-7

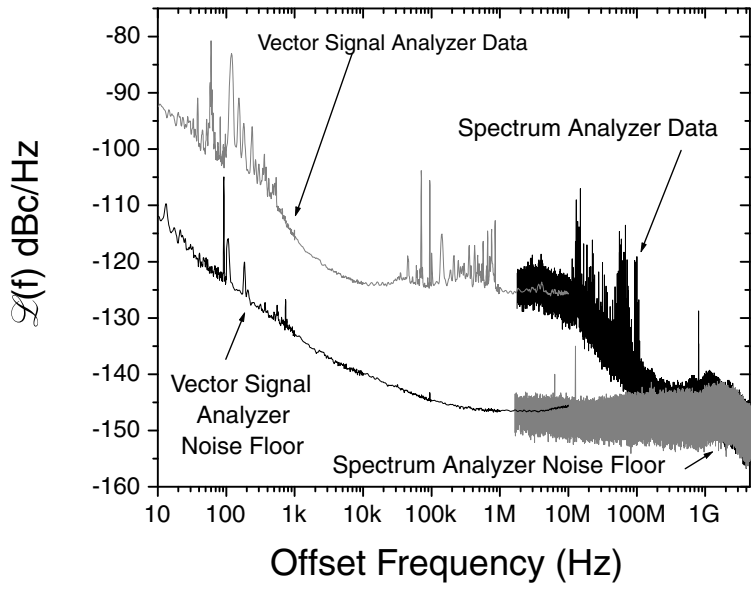

Figure 2-8: Best phase noise results in external-cavity modelocked semiconductor laser with 0.7-nm filter.

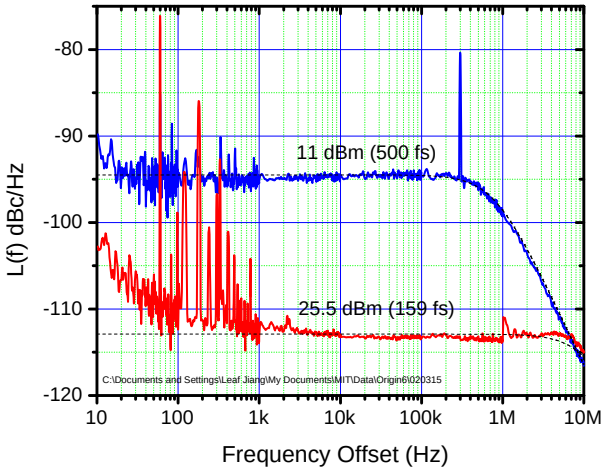

Figure 2-9: Best results for temperature-controlled external cavity modelocked semiconductor laser with 5-nm filter.

2.4 Pulse-to-Pulse Timing Jitter Correlations

The noise theory outlined in appendix B predicts that the timing variance between pulse 1 and pulse N are

$$\langle|\Delta t(T+T_0)-\Delta t(T_0)|^2\rangle = \begin{cases} \sigma_{pp}^2 T, & \text{Passively Modelocked} \\ 2\sigma_{pc}^2\left[1-\exp(-2\gamma_0^{\Re}T)\right], & \text{Actively Modelocked} \end{cases} \tag{2.6}$$

where $T = NT_R$. The variance grows linearly and is unbounded for passively modelocked lasers since there are no restoration forces on the pulses.[8] The variance grows as $1-\exp(-T)$ for actively modelocked lasers. For long delays, the variance is bounded by the active modulation which forces the pulses back into their time slots. The constant $2\gamma_0^{\Re}$ corresponds to the angular frequency at which the phase noise

$V_{SA} = -1.841$ V, $P_{ASE} = 0.009$ mW, $2\gamma_0^{\Re} = 2\pi \times 11$ MHz, $w_0 = 0.7$ pJ, and $\tau = 1.74$ ps. The upper curve corresponds to $I_j = 35$ mA, $V_{SA} = -1.841$ V, $P_{ASE} = 0.0033$ mW, $2\gamma_0^{\Re} = 2\pi \times 800$ kHz, $w_0 = 0.7$ pJ, and $\tau = 1.74$ ps.

[8] There are however weak forces that can bound their position such as electrostriction in fibers and gain saturation [30].

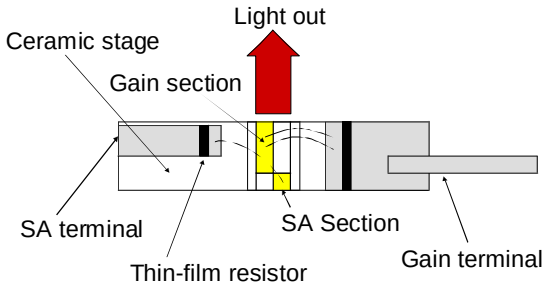

Figure 2-10: A schematic showing the 45 GHz monolithically integrated passively MLLD.

rolls off. If there is significant high frequency noise, then $2\gamma_0^{\Re}$ is large, and not much delay is required to obtain most of the jitter in the cross-correlations. In section 2.5, correlations in harmonically modelocked lasers will be discussed.

The pulse-to-pulse timing jitter was measured for a passively and actively modelocked laser.[9] The passively modelocked laser is shown in Fig. 2-10 and its timing variance in Fig. 2-12. The actively modelocked laser is shown in Fig. 2-11 and its timing variance in Fig. 2-13. Just as the theory predicted, the timing variance of the passively modelocked laser has a linear dependence and the timing variance of the actively modelocked laser has a $1 - \exp(-T)$ dependence.

The pulse position in the passively MLLD is said to undergo a random walk, since the timing variance increases linearly as a function of delay. For the measurements reported here, the pulse-to-pulse kicks of the random walk are 73 fs.

In the actively MLLD, the timing variance is approximately linear for delays of less than 1500 round-trips, which indicates that the pulses do not feel the effect of the modulator and locally undergo a random walk. By fitting a line to the timing variance in Fig. 2-13 over the interval of 0 to 1500 round-trips, we estimate that the pulse-to-pulse kicks are 18 fs.

[9]The MLLDs that we used in our experiments are shown in Fig. 2-10 and Fig. 2-11. The 45 GHz MLLD [31] has a 960 μm gain section driven with an injection current of 38.2 mA and a 60 μm saturable absorber section, which was reverse biased at 0.224 V. The resulting output pulses were 1.3 ps in duration. The hybridly MLLD shown in Fig. 2-11 was driven at 5 GHz (to match fundamental cavity round-trip time) with 19 dBm of RF power, an injection current of 50 mA, and a reverse-biased saturable absorber voltage of 1.55 V. The resulting pulses were 3 ps wide.

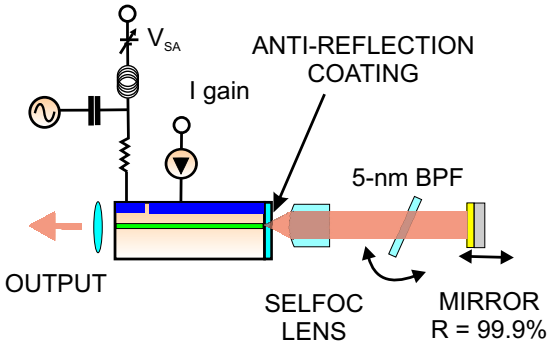

Figure 2-11: A schematic showing the hybridly MLLD with external cavity.

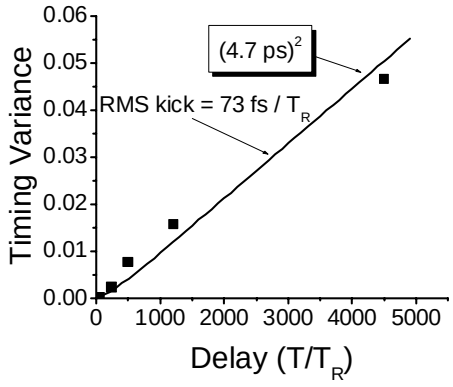

Figure 2-12: Timing variance of the passively MLLD. The pulse-to-pulse timing variance is normalized to T_R^2, $< |\Delta t(T + T_0) - \Delta t(T_0)|^2 > /T_R^2$ and plotted as a function of delay (normalized to the round-trip time T_R). The RMS pulse-to-pulse kicks of the random walk were computed by taking the slope of the total noise, multiplying by T_R^2, and then taking the square root of the result. The 4.7 ps refers to the pulse-to-clock RMS timing jitter after a delay of 4500 round-trips.

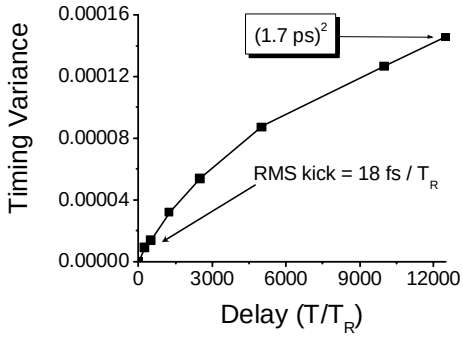

Figure 2-13: Timing variance of the actively MLLD. The squares represent experimental data and the solid lines represent theoretical values.

The pulse-to-pulse timing jitter correlations were measured using a second-harmonic non-colinear optical cross-correlation technique shown in Fig. 2-14. The details of this technique are explained in chapter 3.2. Pulses from the hybridly or passively modelocked laser diode (MLLD) were amplified and split into two different paths with a beam-splitter. One arm was delayed with respect to the other arm using a fiber delay line so that pulse 1 and pulse n would overlap in the nonlinear crystal (a 4 mm POM crystal with type II phase matching). The fine delay stage was used to sweep pulse 1 and pulse n through each other as the second-harmonic signal was detected with a photo-multiplier tube and lock-in detection. For greater delays, or equivalently, for increasing n, the cross-correlation width increases, since timing jitter increases as a function of delay.

2.5 Harmonically Modelocked Lasers

Until recently [32, 33], the noise of harmonically modelocked lasers and how to characterize it has not been well understood. Most of the lowest noise actively modelocked lasers reported to date are harmonically modelocked, but their amplitude noise and timing jitters have been reported incorrectly. This section will show how to correctly measure the noise of a harmonically modelocked laser using residual phase noise measurements and spectrum analyzer measurements. Optical cross-correlation

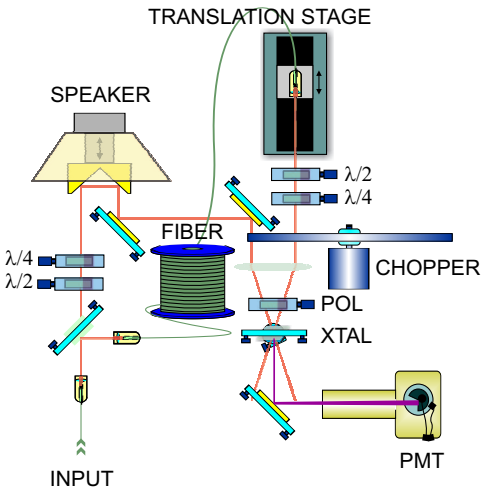

Figure 2-14: Cross-correlator.

measurements are also used to check the results.

Modelocked Erbium-doped fiber lasers [34] and semiconductor ring lasers [27] are typically harmonically modelocked since their cavity round-trip time is longer than the active modelocker's modulation period. Understanding the pattern noise in harmonically modelocked lasers is of particular importance for high-speed optical sampling systems [18].

Models for the noise in gain-switched lasers [35, 21] and fundamentally modelocked lasers [36, 37] are well known, but there is currently no treatment for patterning effects, which are inherent in harmonically modelocked lasers. The noise model for gain-switched lasers and the noise model for fundamentally modelocked lasers cover two extremes: in the case of gain-switched lasers, each pulse independently builds up from ASE and therefore the pulse-to-pulse timing jitter is mainly independent and uncorrelated. In the case of fundamentally modelocked lasers, the same pulse recirculates through the cavity and hence the pulse-to-pulse jitter is highly correlated. In a harmonically modelocked laser, there is a mix of these two effects. Just like a gain-switched laser, all M pulses in the cavity at any time instant are independent of each other since they all arise separately from spontaneous emission. On the other hand, similar to a fundamentally modelocked laser, the pulses recirculate in the laser

cavity and hence the output is correlated, e.g. pulse 1 is correlated with pulse $M+1$, but pulse 1 and 2 are not strongly correlated. The assumption that all M pulses in the cavity are independent is a good approximation as long as the gain dynamics or other scattering and coupling mechanisms do not cause pulse-to-pulse correlations, i.e. the gain recovers between pulses (semiconductor laser) or is not significantly affected by a single pulse (Erbium laser). The case in which neighboring pulses are highly correlated has also been investigated [32]. In this analysis we assume that all M pulses in the cavity are uncorrelated.

The correlated/uncorrelated output of a harmonically modelocked laser leads to an interesting power spectral density shape. There are delta functions spaced at multiples of the modulation frequency and noise energy at multiples of the cavity round-trip frequency.

2.5.1 Model

Following the notation of [37], the intensity of the pulses can be written as sum of equally spaced delta functions

$$I(t) = \sum_{k=0}^{M-1} I_k(t) \tag{2.7}$$

where

$$\begin{aligned} I_k(t) &= \frac{PT_L}{M}\left[1 + N_k(t)\right] \times \\ &\quad \sum_{n=-\infty}^{\infty} \delta\left(t - nT_L - \frac{kT_L}{M} - J_k(t)\right) \end{aligned} \tag{2.8}$$

is a set of pulses separated by T_L and time-shifted by kT_L/M (see Fig. 2-15) with average power P/M (the average power of $I(t)$ is P), and $N_k(t)$ and $J_k(t)$ are the amplitude and jitter fluctuations of the kth pulse in the group of M independent pulses. Since we can express any amplitude changes from pulse $I_k(t)$ to neighboring pulse $I_k(t+T_L)$ as a sum of sinusoids with maximum frequency of $1/2T_L$, $\tilde{N}_k(\omega)$ is bandlimited to $-\omega_L/2 < \omega < \omega_L/2$. For the same reason, the Fourier transform of

$J_k(t)$ is also bandlimited to the same range. Using the identity

$$\sum_{n=-\infty}^{\infty} \delta(t - nT_L - J_k(t)) = \frac{1}{T_L} \sum_{m=-\infty}^{\infty} \exp\left[jm\omega_L(t - J_k(t))\right] \tag{2.9}$$

where $\omega_L = 2\pi/T_L$, and expanding $\exp(jn\omega_L J_k(t))$ to first order, equation (2.8) can be simplified to

$$\begin{aligned} I_k(t) &= \frac{P}{M}\left[1 + N_k(t)\right] \sum_{m=-\infty}^{\infty} \exp\left[jm\omega_L(t - kT_L/M)\right] \times \\ &\quad (1 - jm\omega_L J_k(t)) \end{aligned} \tag{2.10}$$

The Fourier transform of (2.10) is

$$\begin{aligned} \tilde{I}_k(\omega) &= \int_{-\infty}^{\infty} I_k(t) \exp(-j\omega t) dt \\ &= \frac{P}{M} \sum_{n=-\infty}^{\infty} \Big[2\pi\delta(\omega - n\omega_L) - jn\omega_L \tilde{J}_k(\omega - n\omega_L) \\ &\quad + \tilde{N}_k(\omega - n\omega_L)\Big] \exp\left(-j\frac{2\pi nk}{M}\right). \end{aligned} \tag{2.11}$$

where second order perturbation terms, $N_k(t)J_k(t)$, were dropped. The power spectral density of $I(t)$ is

$$\begin{aligned} S_I(\omega) &= \left|\sum_{k=0}^{M-1} \tilde{I}_k(\omega)\right|^2 \\ &= P^2 \sum_{m=-\infty}^{\infty} 2\pi\delta(\omega - m\omega_M) \\ &\quad + \left(\frac{P^2}{M}\right) \sum_{n=-\infty}^{\infty} \Big[n^2\omega_L^2 S_J(\omega - n\omega_L) \\ &\quad + S_N(\omega - n\omega_L)\Big] \end{aligned} \tag{2.12}$$

where $\omega_M = M\omega_L$ is the modulation frequency,

$$S_J(\omega) = |\tilde{J}_1(\omega)|^2 = |\tilde{J}_2(\omega)|^2 = |\tilde{J}_3(\omega)|^2 = \ldots \tag{2.13}$$

is the power spectral density of the timing jitter fluctuations and

$$S_N(\omega) = |\tilde{N}_1(\omega)|^2 = |\tilde{N}_2(\omega)|^2 = |\tilde{N}_3(\omega)|^2 = \ldots \tag{2.14}$$

is the power spectral density of the amplitude fluctuations. Equations (2.13) and (2.14) are valid since each pulse in the cavity experiences the same noise excitations and hence should have the same noise power spectral densities. Equation (2.12) looks very similar to the expression one would obtain for fundamentally modelocked lasers [37, Eq. 3], except there are a few important differences. First, there are delta functions only at multiples of the modulation frequency; the delta functions at multiples of the cavity round-trip frequencies cancel out. It may appear as if the cavity axial modes were delta functions when measured experimentally with an electrical spectrum analyzer, implying that there is a periodic signal of infinite duration, but upon closer inspection, the peaks of cavity axial modes are due to long-time-scale variations. When viewing the cavity axial modes of a harmonically modelocked laser, the resolution bandwidth of the spectrum analyzer is typically tens of kilohertz or larger. Therefore all the low-frequency variations in a ten kilohertz bandwidth are integrated into one bin and hence appear like a delta function on the spectrum analyzer display. Second, there is a factor of $1/M$ multiplying the noise power spectral densities in (2.12). Later, we will see that this means that the integrated single-sided phase noise spectrum from 0 Hz to $1/2T_L$ needs to be multiplied by a factor of $\sqrt{M}$ to obtain the standard deviation of the timing jitter probability density function.

Equation (2.12) shows that the timing jitter component of the power spectral density of $I(t)$ scales as the square of the round-trip frequency harmonic number as well as the square of the modulation-frequency harmonic number. Fig. 2-16 shows the power spectral density of a harmonically modelocked laser. The amplitude power spectral density repeats every multiple of ω_L. The timing jitter power spectral density increases quadratically as a function of harmonic number. This means that $S_I(\omega)$ is highly insensitive to timing jitter fluctuations at low offsets. Therefore, there is no need to measure out to high modulation-frequency harmonics to separate timing

from amplitude fluctuations. One simply can measure the amplitude contribution by recording the noise of the first cavity axial mode at ω_L with a spectrum analyzer. The power density spectrum of the first cavity axial mode at ω_L can be subtracted from the power density spectrum of the first modulation harmonic at ω_M to obtain the timing jitter power density spectrum. Therefore, it is easy to separate timing and amplitude fluctuations in harmonically modelocked lasers. In addition, this measurement scheme has the advantage over previous schemes since it is not always possible to go out to high modulation-harmonics since this is limited by the detection electronics and spectrum analyzer bandwidth which are typically limited to 50 GHz. In addition, by measuring the noise around the axial modes, it may be possible to characterize the intensity noise and timing jitter of extremely high-repetition rate lasers [38].

The RMS intensity and timing fluctuations are given by

$$\sigma_N^2 = \langle N_1^2(t) \rangle = \frac{1}{2\pi} \int_{-\infty}^{\infty} S_N(\omega) d\omega, \tag{2.15}$$

where σ_N is unitless and

$$\sigma_J^2 = \langle J_1^2(t) \rangle = \frac{1}{2\pi} \int_{-\infty}^{\infty} S_J(\omega) d\omega, \tag{2.16}$$

where σ_J has units of time. Notice that the RMS values are not equal to $\sum_{k=0}^{M-1} \langle N_k^2(t) \rangle$ or $\sum_{k=0}^{M-1} \langle J_k^2(t) \rangle$ since the intensity and timing noise of each $I_k(t)$ does not overlap in time, and hence the random variables do not add. The RMS intensity and timing fluctuations are equal to the standard deviation of the probability density function for the intensity and timing displacements.

Measuring laser noise with an RF spectrum analyzer

A spectrum analyzer does not directly measure $S_N(\omega)$ and $S_J(\omega)$, but measures a power density proportional to $S_I(\omega)$, which we relabel as $P(\omega)/B$, where B is the bandwidth resolution. Since it is not straightforward to determine the proportionality constant, which depends on quantum efficiency of the detector and various settings

on the spectrum analyzer, it is easier to normalize the measured spectral density to the carrier power, $P_c = P(\omega_M)$. Therefore, assuming no timing jitter noise,

$$\frac{P(\omega)/B}{P_c} = \frac{PS_N(\omega)/M}{2\pi} \tag{2.17}$$

for $-\omega_L/2 < \omega < \omega_L/2$, or assuming no intensity noise,

$$\frac{P(\omega)/B}{P_c} = \frac{P\omega_M^2 S_J(\omega)/M}{2\pi} \tag{2.18}$$

for $\omega_M - \omega_L/2 < \omega < \omega_M + \omega_L/2$. The RMS intensity fluctuations from 0 Hz to $\omega_L/2$ can be found from the measured RF spectrum according to (substituting (2.17) into (2.15))

$$\sigma_N^2 = M \int_{-\omega_L/2}^{\omega_L/2} \frac{P(\omega)}{BP_c} d\omega. \tag{2.19}$$

It is difficult to make measurements at DC due to flicker noise and low-pass filtering (the Agilent 8565EC rf spectrum analyzer only goes down to 7 kHz). The intensity noise can measured from the noise spectrum centered at ω_L. Since the timing jitter decreases as the square of the cavity harmonic number, n^2, for M large, the first cavity axial mode is almost entirely dominated by intensity noise. Therefore,

$$\sigma_N^2 \approx M \int_{\omega_L-\omega_L/2}^{\omega_L+\omega_L/2} \frac{P(\omega)}{BP_c} d\omega. \tag{2.20}$$

The intensity noise can be separated from the timing jitter noise by measuring the spectral content of the first cavity axial mode.

The RMS timing fluctuation can be determined from measuring the noise skirts around the first modulation harmonic at $\omega = M\omega_L$ and subtracting out the intensity noise computed by (2.20). The RMS timing fluctuation from 0 Hz to $\omega_L/2$ can be found by using (2.18) in (2.16) and is equal to (note that the intensity noise contribution is subtracted out)

$$\sigma_J^2 = M\omega_M^2 \int_{M\omega_L-\omega_L/2}^{M\omega_L+\omega_L/2} \underbrace{\frac{P(\omega) - P(\omega-(M-1)\omega_L)}{BP_c}}_{\equiv S_\phi(\omega)/(2\pi)^2} d\omega \tag{2.21}$$

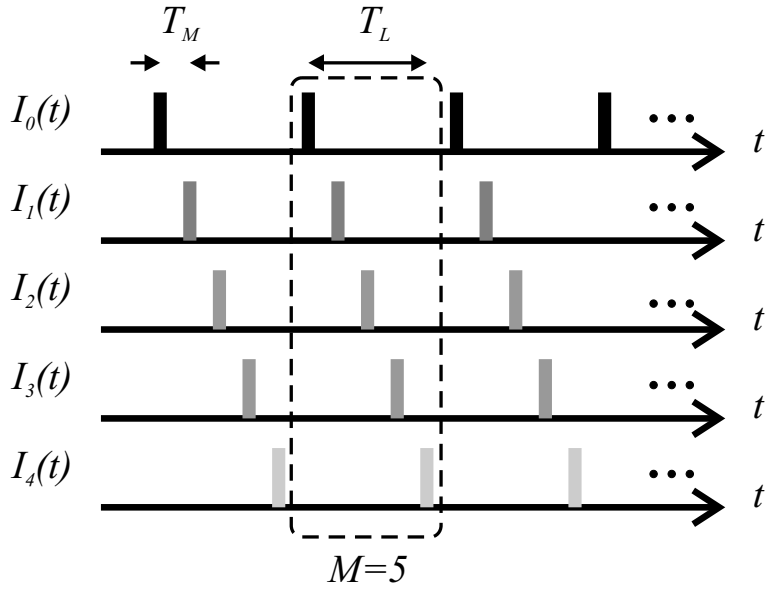

Figure 2-15: The output of a harmonically modelocked laser is a sum of independent pulse patterns.

$$\boxed{\sigma_J^2 = M\left(\frac{T_M}{2\pi}\right)^2 \int_{M\omega_L-\omega_L/2}^{M\omega_L+\omega_L/2} S_\phi(\omega)d\omega}, \tag{2.22}$$

where $T_M = T_L/M$. The factor of M in the equation above is often ignored in the literature for noise measurements of harmonically modelocked lasers.

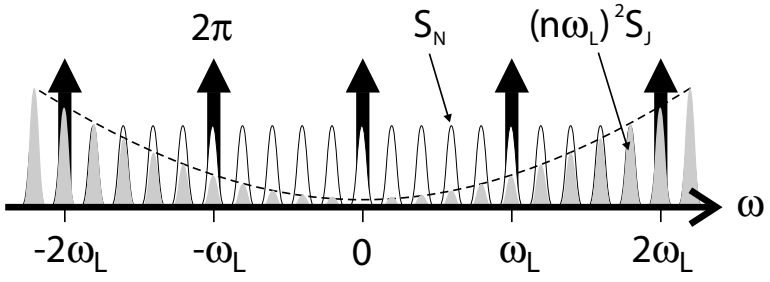

Figure 2-16: The power spectral density of a harmonically modelocked laser.

Measuring laser noise with residual noise technique

The intensity noise and timing jitter of a harmonically modelocked laser can also be measured with a residual phase noise measurement, which are discussed in detail in chapter 3. This technique involves mixing the directly detected signal with the same oscillator used to modelock the laser with the relative delay set so that the measurement is either AM or PM sensitive. For phase noise measurements, the detected power spectral density of the voltage from the IF port of the mixer is the product of the detected signal voltage and the sinusoidally modulated clock:

$$\begin{aligned} S_V(\omega) &= \left|FT\left\{I(t)\times B\sin(\omega_M t)\right\}\right|^2 \\ &= \left|\tilde{I}(\omega) * j\pi B[-\delta(\omega-\omega_M)+\delta(\omega+\omega_M)]\right|^2 \\ &= \frac{B^2\pi^2}{(2\pi)^2}\left|\tilde{I}(\omega-\omega_M)-\tilde{I}(\omega-\omega_M)\right|^2 \\ &= B^2P^2\omega_L^2\sum_{r=-\infty}^{\infty}\left|\sum_{k=-\infty}^{\infty}\tilde{J}_k(\omega-r\omega_L)e^{-\frac{j2\pi rk}{M}}\right|^2 \end{aligned} \tag{2.23}$$

where FT is the Fourier transform operator, $B\sin(\omega_M t)$ is the microwave oscillator, and $\tilde{J}_k$ is the Fourier transform of $J_k(t)$. The mixer conversion efficiency, detector quantum efficiency, loss in the microwave cables, and other proportionality constants can be lumped into the unknown quantity, B. We consider three cases:

- Case I (Single noisy pulse): For the case where all pulses are perfectly timed except for one pulse in the cavity such that $\tilde{J}_0 \neq 0$ and $\tilde{J}_1 = \tilde{J}_2 = \tilde{J}_3 = \ldots = 0$, equation (2.23) simplifies to

$$S_V^I(\omega) = B^2P^2\omega_M^2\sum_{r=-\infty}^{\infty}\frac{S_J(\omega-r\omega_L)}{M^2}. \tag{2.24}$$

- Case II (Uncorrelated pulses): For uncorrelated pulses where $\tilde{J}_m\tilde{J}_n = S_J(\omega)\delta_{mn}$, equation (2.23) simplifies to

$$S_V^{II}(\omega) = B^2P^2\omega_M^2\sum_{r=-\infty}^{\infty}\frac{S_J(\omega-r\omega_L)}{M}. \tag{2.25}$$

- Case III (Correlated pulses): If we assume that the pulses in the cavity are correlated so that $\tilde{J}_0 = \tilde{J}_1 = \tilde{J}_2 = ... = \tilde{J}_{M-1}$, equation (2.23) simplifies to

$$S_V^{III}(\omega) = B^2 P^2 \omega_M^2 \sum_{r=-\infty}^{\infty} S_J(\omega - r\omega_M). \tag{2.26}$$

  Notice that the noise spectrum repeats at frequency intervals of ω_M rather than ω_L.

To convert the voltage spectral density to a phase spectral density requires dividing by a calibration constant κ_ϕ^2. The calibration constant is obtained by changing relative phase between the oscillator and signal (ϕ) and measuring the DC voltage level (V). The output voltage of the IF port of the mixer is

$$\begin{aligned}
V_{DC} &= DC\left\{FT\left\{\left[PT_M \sum_{n=-\infty}^{\infty} \delta(t - nT_M)\right]\right.\right. \\
&\quad \left.\left. \times B\sin(\omega_M t - \phi)\right\}\right\} \\
&= DC\left\{FT\left\{-PT_M B \sum_{n=-\infty}^{\infty} \delta(t - nT_M)\right\}\right\} \\
&= DC\left\{-PT_M B \sin\phi \times \frac{2\pi}{T_M} \sum_{k=-\infty}^{\infty} \delta\left(\omega - \frac{2\pi k}{T_M}\right)\right\} \\
&= -2\pi PB\sin\phi \\
&\approx -2\pi PB\phi
\end{aligned} \tag{2.27}$$

where DC is an operator that takes the DC part of the bracketed expression. The calibration constant is therefore given by

$$\kappa_\phi = \frac{V_{DC}}{\phi} = -2\pi PB, \tag{2.28}$$

and the power spectral density of the phase is

I: Single noisy pulse	$S_\phi^{\mathrm{I}}(\omega) = \frac{S_V^I(\omega)}{\kappa_\phi^2} = \frac{\omega_M^2}{(2\pi)^2} \sum_{n=-\infty}^{\infty} \frac{S_J(\omega - n\omega_L)}{M^2}$,
II: Uncorrelated	$S_\phi^{\mathrm{II}}(\omega) = \frac{S_V^{II}(\omega)}{\kappa_\phi^2} = \frac{\omega_M^2}{(2\pi)^2} \sum_{n=-\infty}^{\infty} \frac{S_J(\omega - n\omega_L)}{M}$,
III: Correlated	$S_\phi^{\mathrm{III}}(\omega) = \frac{S_V^{III}(\omega)}{\kappa_\phi^2} = \frac{\omega_M^2}{(2\pi)^2} \sum_{n=-\infty}^{\infty} S_J(\omega - n\omega_L)$,

for the single noisy pulse, uncorrelated, and correlated cases, respectively. The units of $10\log_{10} S_\phi(2\pi f)$ are in dBc/Hz. Surprisingly, extracting the timing jitter from the phase noise power spectral density is different depending on the correlations of the pulses. The rms timing jitter can be calculated from the residual phase noise measurement by

$$\sigma_J^2 = M^2 \frac{(2\pi)^2}{\omega_M^2} \int_{-\omega_L/2}^{\omega_L/2} S_\phi^{\mathrm{I}}(\omega) \frac{d\omega}{2\pi} \tag{2.29}$$

$$= M \frac{(2\pi)^2}{\omega_M^2} \int_{-\omega_L/2}^{\omega_L/2} S_\phi^{\mathrm{II}}(\omega) \frac{d\omega}{2\pi} \tag{2.30}$$

$$= \frac{(2\pi)^2}{\omega_M^2} \int_{-\omega_L/2}^{\omega_L/2} S_\phi^{\mathrm{III}}(\omega) \frac{d\omega}{2\pi}. \tag{2.31}$$

Note that experimentally, a vector signal analyzer will fold a double-sided spectrum into a single-sided spectrum, so one integrates a residual phase noise measurement from 0 to $\omega_L/2$. Note that in case II, the uncorrelated case, the timing jitter is also equal to

$$\sigma_J^2 = \frac{(2\pi)^2}{\omega_M^2} \int_{-\omega_M/2}^{\omega_M/2} S_\phi^{\mathrm{II}}(\omega) \frac{d\omega}{2\pi} \tag{2.32}$$

and therefore one must integrate the residual phase noise spectrum up to half the repetition rate to obtain the rms timing jitter.

Physically, the residual phase noise measurement contains the sum of the noise energy from the timing jitter of each pulse in the pattern. Therefore, if one wants to obtain the uncertainty of the pulse position relative to clock for an uncorrelated pattern, the residual phase noise measurement must be integrated from 0 to $\omega_L/2$ and multiplied by M. For phase noise measurements, often the single-side band phase noise, $2L(\omega) = S_\phi(\omega)$ for $\omega < \omega_L/2$, is quoted, but only contains $1/M$ of the total noise.

An important result of this analysis is that the timing jitter power spectral density does not scale as the round-trip frequency harmonic number in the residual phase noise measurement as it does in the RF spectrum analyzer measurement.

The relation between the power spectral density of the phase and the power spectral density of the timing jitter is not simple. For a given amount of timing jitter, it

seems strange that the magnitude of the phase noise power spectral density changes depending on the correlation of the pulses. In addition, in case I, it is also strange that there is noise energy at high frequencies, since at first hand, it would seem that the power spectral density of the phase noise should be band-limited to $-\omega_L < \omega < \omega_L$ as well. In fact, the power spectral density of the phase noise is not band-limited (assuming delta function pulses and infinite bandwidth mixer) since the output of the mixer is a periodic train of impulses. Assume that we take the first pulse in the pattern and delay it by a constant amount. Then the mixer output is a periodic train of impulses with period T_L. The Fourier transform of the mixer output is also a sum of delta functions centered at frequency multiples of ω_L. Therefore, the phase noise in case I should not be band-limited to $-\omega_L < \omega < \omega_L$.

Case II can be understood as follows. A single pulse in the pattern generates phase noise with magnitude proportional to S_J/M^2 at frequency multiples of ω_L. If all M uncorrelated pulses in the pattern now have timing jitter, their phase noises at multiples of ω_L add to give a total phase noise proportional to S_J/M at frequency multiples of ω_L. This case corresponds to the timing jitter found in most harmonically modelocked Er-fiber lasers. An interesting consequence of equation (2.30) is that for a given amount of timing jitter, the phase noise becomes increasingly difficult to measure as M is increased. The reason is that the power spectrum of the phase noise is spread over all the supermodes, and so each supermode has very little phase noise. Therefore, residual phase noise measurements of the first supermode are generally contaminated by the phase noise of the oscillator for reasons outlines in Section 3.1.4. Therefore, one should not multiply the phase noise of the first supermode by M to get the timing variance since the first supermode is mainly due to oscillator noise injected through the LO port of the mixer.

Case III is a pulse train in which the timing jitter of each pulse in the cavity is the same. In other words, if pulse 0 moves forward by time τ, so does pulse 2 through $M-1$. For this correlated case, the phase noise is terrible for a given S_J. The physical picture necessary to understand this case is to think of all the pulses in one round-trip as a super-pulse since they all move together. If we were to do a phase noise

measurement using a local oscillator with angular frequency ω_L instead of ω_M, then the phase noise and timing jitter are related by $S_\phi(\omega) = (\omega_L/2\pi)^2 \sum_{r=-\infty}^{\infty} S_J(\omega - r\omega_L)$. Increasing the oscillator frequency to $\omega_M = M\omega_L$ is equivalent to increasing the slope of the local oscillator with frequency ω_L in the previous case by a factor of M, which scales the voltage by M and the power by M^2. The resulting phase noise is then $S_\phi(\omega) = (M\omega_L/2\pi)^2 \sum_{r=-\infty}^{\infty} S_J(\omega - r\omega_L) = (\omega_M/2\pi)^2 \sum_{r=-\infty}^{\infty} S_J(\omega - r\omega_L)$ which is the same as equation 2.31.

A similar analysis can be carried out for the residual amplitude noise by replacing $A\sin(\omega t)$ with $A\cos(\omega t)$. Likewise, the optical intensity variance can be obtained by methods integrating according to methods (1) and (2) above. Again, the many authors just integrate the residual amplitude noise from $-\omega_L/2$ to $\omega_L/2$ but do not multiply the variance by M for case II.

Cavity Length and Timing Jitter

The timing jitter of the harmonically modelocked laser does not improve as the cavity length is increased and the modulation rate is kept the same, i.e. harmonic modelocking does not provide any advantages over fundamental modelocking for noise performance. According to equation (2.2), if the cavity length is increased by a factor of 2, the knee of the phase noise plot, $L(f)$, also moves in by a factor of 2. But since there are two supermodes that must be integrated to obtain the total timing jitter according to equation (2.32), the total noise is the same. The next section will show experimental evidence that the timing jitter does not change as the cavity length is increased.

If we keep the laser fundamentally modelocked, the modulation curvature fixed at ω_M, and increase the cavity length, then the timing jitter will improve. Fig. 2-3 shows that the average output signal power and average spontaneous emission power are constant for a given injection current. A common trick to increase the pulse energy in passively modelocked lasers is to increase the cavity length [39]. Since the average power and pulse width are approximately constant, the peak pulse energy must increase. Equation 2.5 shows that the timing jitter is proportional to the ratio

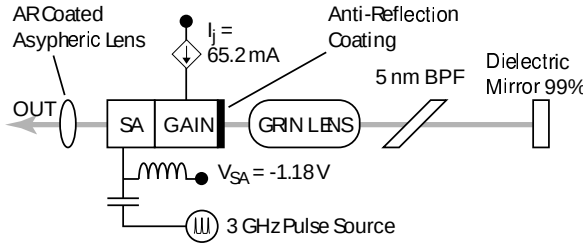

Figure 2-17: Experimental setup for semiconductor laser.

of the spontaneous emission energy to the pulse energy. By increasing the pulse energy with the spontaneous emission energy kept fixed, the timing jitter can improve, but the repetition rate decreases.

2.5.2 Experiments

To experimentally verify our model for noise in harmonically modelocked lasers, we measured the optical cross-correlation and residual phase noise of a semiconductor laser and a fiber laser. We found that the supermodes contain timing jitter noise energy that must be included in the total timing jitter.

The semiconductor laser shown in Fig. 2-17 was actively modelocked at a 3 GHz repetition rate [25]. In these experiments, the cavity length was adjusted while the driving modulation frequency was kept constant at 3 GHz. The cavity length was adjusted to a repetition rate of 3 GHz ($M = 1$) or 600 MHz ($M = 5$). The injection current was 65.2 mA, the saturable absorber reverse bias was -1.18 V, and the rf power driving the saturable absorber was 25 dBm. The rf pulse source that drove the saturable absorber consisted of a step-recovery diode driven by a 3 GHz sinusoid. The resulting microwave pulses were 73 ps long.

The residual phase noise measurement of the semiconductor laser is shown in Fig. 2-18. The knee of the power spectral density moves in by a factor of about 5 as the cavity round-trip length is increased by a factor of 5. In addition, the the power spectral density of the two laser configurations at offset frequencies less than 1 MHz are approximately equal. The 1.5 dB difference is most likely due to differences

in the cavity Q. The threshold current of the fundamentally modelocked laser was 22 mA versus 30 mA for the harmonically modelocked laser, which indicates that the fundamentally modelocked laser suffered less diffraction loss. Looking closely at the 600 MHz supermodes reveals that the first through fourth supermodes have similar shapes and magnitudes, which indicates that the pulses are uncorrelated [32].

Integrating the residual phase noise plot of the fundamentally modelocked laser from 10 Hz to 1 GHz yields an rms timing jitter of 2489 fs. Integrating the residual phase noise plot of the harmonically modelocked laser from 10 Hz to 300 MHz yields 1161 fs of timing jitter. Multiplying this number by $\sqrt{M}$ yields $1161 \times \sqrt{5} = 2597$ fs, which is very close to the total noise of the fundamentally modelocked laser.

Additional proof of the fact that the supermodes contribute to the total integrated timing jitter is given by measurements of the cross-correlation between pulses. The optical auto and cross-correlations of the fundamentally and harmonically modelocked laser pulses are shown in Fig. 2-19 and 2-20, respectively. Unfortunately, the autocorrelation reveals satellite pulses, but nonetheless illustrates the following points. The timing jitter of the fundamentally modelocked laser from pulse 1 to pulse 2 is the same as the timing jitter from pulse 1 to pulse 10. For the harmonically modelocked laser, the timing jitter between pulses in the cavity (pulse 1 to 2, and pulse 1 to 9) are uncorrelated and hence large, while the timing jitter of a pulse relative to itself after two round-trips (pulse 1 to 10) is small.

Optical and rf noise measurements for a $M = 25000$ harmonically modelocked fiber laser again revealed that the timing jitter noise energy in the supermodes is significant [40]. The fiber laser was constructed with a sigma shaped cavity with 500 m of standard single-mode fiber. An amplitude modulator driven at 10 GHz was incorporated inside the cavity and the resulting output pulses were 4.6 ps in duration. A residual phase noise measurement of the first supermode is shown in Fig. 2-21 and the optical auto and cross-correlations are shown in Fig. 2-22. Integrating the first supermode from 10 Hz to 200 kHz in the residual phase noise plot leads to the incorrect rms timing jitter of 7.13 fs (10 Hz at -90 dBc/Hz, 100 Hz at -100 dBc/Hz, 1 kHz at -110 dBc/Hz, 10 kHz at -120 dBc/Hz, 100 kHz at -130 dBc/Hz, and 200 kHz at

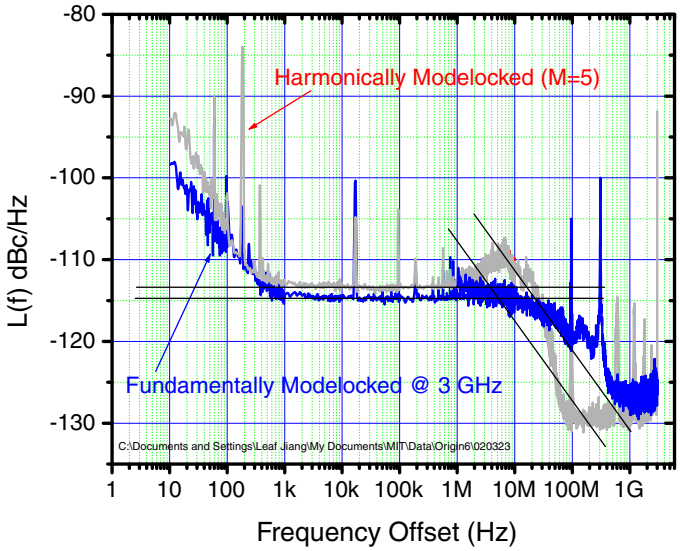

Figure 2-18: Residual phase noise measurement of the semiconductor laser. The thin solid lines show the theoretically predicted noise due to spontaneous emission. The low frequency noise below 1 KHz is dominated by flicker noise of the voltage and current sources. The noise enhancement at 6 MHz in the harmonically modelocked laser also appears at 30 MHz (factor of $M = 5$ larger) in the fundamentally modelocked laser.

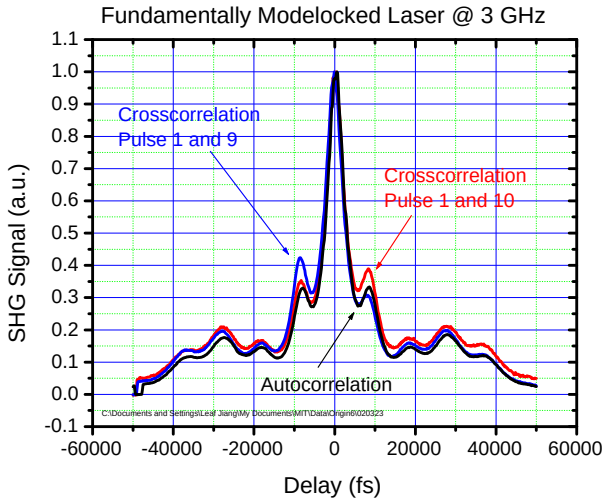

Figure 2-19: Optical auto and cross-correlations of the fundamentally modelocked semiconductor laser. The auto and cross-correlations almost completely overlap.

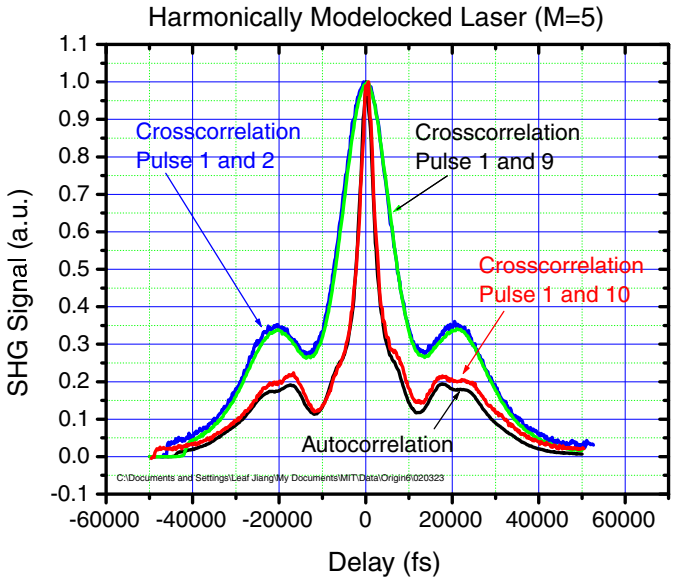

Figure 2-20: Optical auto and cross-correlations of the harmonically modelocked semiconductor laser.

-135 dBc/Hz). The total timing jitter is $7.13 \times \sqrt{25000} = 1128$ fs. The optical cross-correlation in Fig. 2-22 shows that the autocorrelation FWHM is 6462 fs ($\sigma_{AC} = 2744$ fs) and the cross-correlation FWHM is 7092 fs ($\sigma_{XC} = 3012$ fs). Assuming Gaussian pulse shapes, the rms jitter is $\sqrt{\sigma_{XC}^2 - \sigma_{AC}^2} = 1242$ fs. Therefore, the optical cross-correlation measurements verify that the phase noise is approximately 1 ps rather than 7 fs.

Further evidence that the SSB phase-noise measurements are not entirely amplitude noise is given by Juodawlkis et al. in which the timing jitter of a Er-fiber modelocked laser is measured with a novel phase-encoded optical sampling technique [41].

In conclusion, we have developed a model for the noise of harmonically modelocked lasers which clarifies the meaning of the supermodes in the spectrum analyzer and residual phase noise measurements. Measuring the power spectral density of the first supermode in a spectrum analyzer measurement yields intensity fluctuation information, which allows us to separate timing and intensity fluctuations with smaller detection bandwidth (0 Hz to the modulation drive frequency). In addition, we have

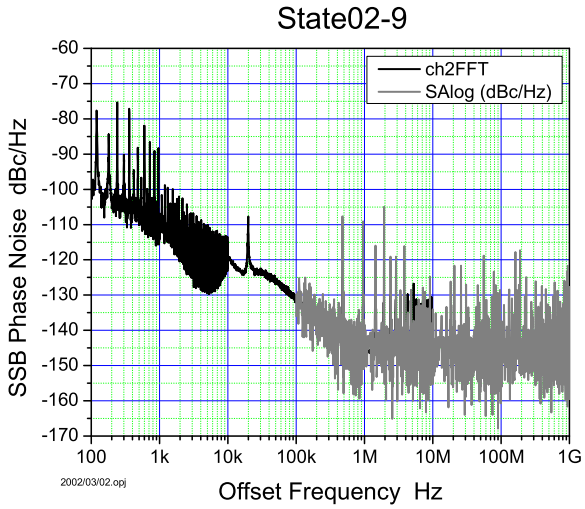

Figure 2-21: Residual phase noise measurement of the fiber laser. Courtesy of Matthew Grein.

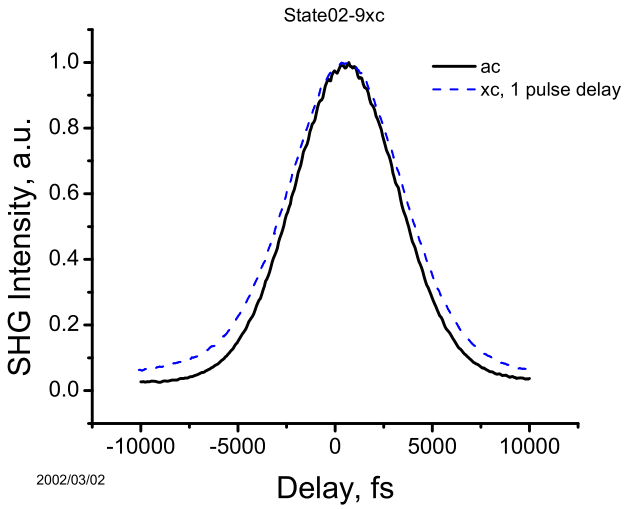

Figure 2-22: Optical auto and cross-correlations of the harmonically modelocked fiber laser. Courtesy of Matthew Grein.

experimentally verified our model with optical and rf noise measurements of mode-locked semiconductor and fiber lasers and have shown that supermode timing jitter exists and that it is not entirely amplitude noise.

Chapter 3

Modelocked Laser Noise Measurements

The measurement of noise is a challenging task since it is orders of magnitude smaller than the signal. The single-sideband phase noise of the laser is can be over ten orders of magnitude smaller than the carrier. Sampling scope measurements of the timing jitter or spectrum analyzer measurements of the timing jitter are not able to resolve 50 fs of timing jitter. The oscillator noise in a state-of-the-art spectrum analyzer (HP8565EC) is approximately 95 fs from 10 Hz to 1 MHz.

3.1 Microwave Techniques

Theoretically, jitter is defined as the short-term non-cumulative variations of the significant instants of a signal from their ideal positions in time [42]. Generally, digital storage oscilloscopes (DSO), spectrum analyzers, and phase noise measurement test sets are used for jitter measurements. A detailed presentation of microwave techniques for measuring noise in Ti:sapphire laser can be found in [19].

3.1.1 Spectrum Analyzer Measurements

Among the most popular methods for noise characterization is to use a photodiode to convert the optical pulse stream into a rf signal and to measure it with a rf spectrum analyzer. As long as the noise of the spectrum analyzer is lower than that of the optical signal, this technique is valid and desirable since it is easy and fast.

Converting the spectrum analyzer measurements into amplitude and timing jitter for actively modelocked lasers was presented by von der Linde [36]. The interpretation of the power spectrum for harmonically modelocked lasers is presented in Section 2.5.

The phase noise for a state-of-the-art spectrum analyzer is shown in Fig. 3-1. Integrating the phase noise curve for the 5 GHz carrier frequency from 10 Hz to 1 MHz yields 95 fs (783 fs if integrated from 1 Hz to 1 MHz). This implies that most of the timing jitter measured lasers using spectrum analyzers, such as Yu's quantum-noise limited stretched-pulse fiber laser [43], was due to the noise of the spectrum analyzer. Note that for a fixed timing jitter, the phase noise increases by 6 dB for every factor of 2 increase in the carrier frequency.[1] Physically, this means that for a fixed timing jitter, the phase displacements are larger relative to the carrier cycle.

3.1.2 Sampling Scope Measurements

Measuring jitter with a DSO has several limitations.

1. Amplitude noise is converted to phase noise on the input of the DSO and thus contributes to the overall jitter reading.

2. The jitter is measured relative to the time base of the DSO, which also has a jitter characteristic. That means that the measured value depends upon the jitter of the DSO and the oscillator under test. If the DSO's timebase jitter is higher than the oscillator jitter, it is the DSO's jitter rather than the oscillator jitter that will be measured.

[1] This assumes that the doubler adds no noise.

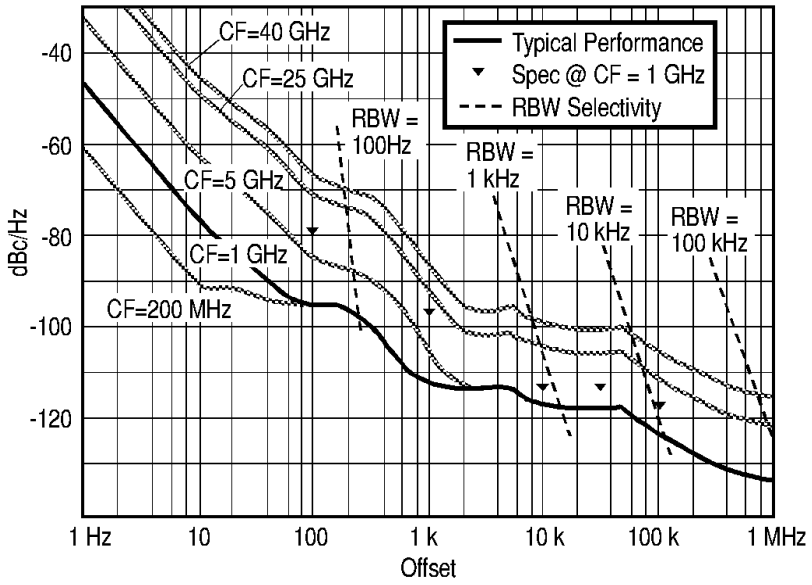

Figure 3-1: Agilent 8585EC spectrum analyzer phase noise [2]. CF = center frequency.

3. The short-term jitter of sampling scopes is large compared to the noise of modelocked lasers. For the state-of-the-art Tektronix sampling oscilloscope (CSA8000B), the short-term jitter is 0.8 ps RMS +5 ppm (typical) and $<$ 1.2 ps RMS +10 ppm (max.). When locked to a 10 MHz reference, the long-term jitter is 1.6 ps RMS+0.04 ppm of position (typical), and $<$ 2.5 ps RMS +0.01 ppm of position (max.).

4. Limited spectral information is given by the DSO measurement. The measured histogram yields a timing jitter number that does not indicate whether the noise is due to 60 Hz pickups, vibration spurs, radio pickups, or quantum noise.

The advantages of using a sampling oscilloscopes are:

1. One can see the signal in the time domain and hence can observe pulse-dropouts in the eye diagram.

2. The histogram functionality allows one to find the probability density function of both amplitude and phase noise.

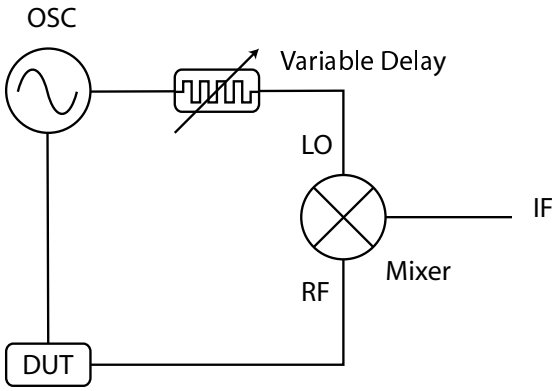

Figure 3-2: Residual phase noise measurement setup.

3.1.3 Residual Phase Noise Measurements

A residual phase noise measurement measures the inherent phase noise of the device-under-test and removes the phase noise of the driving oscillator. A typical residual phase noise measurement setup is shown in Fig. 3-2. The variable delay is set so that the signals to the LO and RF ports are in quadrature. In this configuration, the mixer acts as a phase detector. The time delay from the oscillator to the LO port should closely match the length of the oscillator to the RF port for best oscillator noise rejection.

The advantage of a residual phase noise measurement over an absolute phase noise measurement is that a relatively noisy microwave oscillator can be used to drive the modelocked laser and still be able to uncover the fundamental quantum-noise of the laser. On the other hand, it is difficult to obtain the residual phase noise of a harmonically modelocked laser for reasons detailed in Section 3.1.4.

The phase detector in the residual phase noise measurement is typically a double-balanced mixer. The mixer is made into a phase detector by phase delaying the two input signals until they are in quadrature. Typically, the mixer is operated so that the IF output port is at 0 V DC. Due to the fact that the diodes in the mixer are not perfectly matched, the phase detector may be slightly more sensitive to negative than positive voltage. For example, in our measurements, the IF output port voltage swung between 280 mV and -300 mV. This implies that there is an optimal point

when the phase is delayed so that the IF output voltage is -10 mV. The best AM noise rejection occurs at the optimal point. This asymmetry in the mixer can be pronounced, especially, when the RF input power is low. At the sweet spot, one should be able to obtain 30 dB AM rejection. This could be a reason why some groups only get 10-20 dB AM rejection in their phase detector.

The delays between the LO and RF ports should be matched since the noise rejection worsens as f^2. If the input voltages to the mixer LO and RF ports are $A\sin\omega t$ and $A\cos(\omega(t-\Delta t))$, respectively, then the IF voltage is $AB\omega\Delta t$, where Δt is the time delay between both arms. The IF power is $(AB)^2\omega^2(\Delta t)^2$. There is no noise suppression when $\omega\Delta t = \pi/2$. In other words, when $f = 1/4\Delta t$ then $L(f) = 0$ dBc/Hz. Fig. 3-3 shows a plot of the oscillator's phase noise, the residual oscillator noise at the IF port of the mixer, and the suppression function $(4\Delta t f^2)$. The oscillator noise is significantly suppressed in a residual phase noise measurement. For this plot, we assumed that $\Delta t = 33$ ns, which corresponds to 10 m of free-space propagation delay. At offsets greater than 20 kHz, the measurement noise floor is at -130 dBc/Hz due to finite rejection of the oscillator noise. If Δt is decreased, the rejection curve translates to the right, and the residual oscillator noise levels-off to a lower phase noise value at a lower frequency.

3.1.4 Validity of Residual Phase Noise Measurement

Equation (eq:theory-brief-psd) shows how the microwave oscillator noise contributes to the output timing jitter of the laser. It has been argued that residual phase noise measurements do not make sense for nonlinear devices such as modelocked lasers. However, our analysis [44] shows exactly when the residual phase noise measurement is valid. In other words, it shows us when the microwave oscillator noise is sufficiently suppressed, so that the residual noise is all that is left.

Equation (eq:theory-brief-psd) shows that the timing jitter psd contains a term that has the cavity response (a simple Lorentzian with a roll-off at $2\gamma_0^{\Re}$) multiplied by the oscillator phase noise. The residual phase noise measurement is valid for angular frequencies less than $2\gamma_0^{\Re}$, but the measurement does not suppress microwave phase

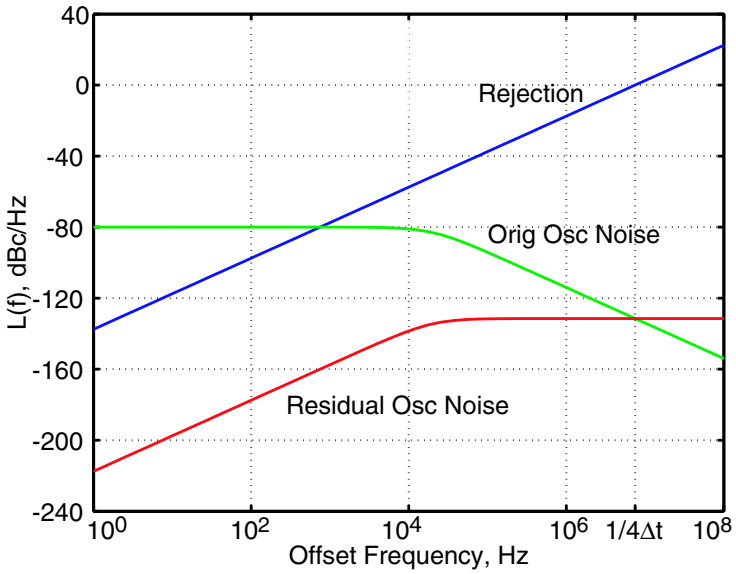

Figure 3-3: Residual phase noise measurement and the suppression of the oscillator noise.

noise at frequencies greater than $2\gamma_0^{\Re}$ since the cavity response of the laser filters the oscillator phase noise. Since $2\gamma_0^{\Re}$ is relatively large (1 to 10 MHz) compared to the bandwidth of the microwave oscillator phase noise in semiconductor lasers, the residual phase noise measurement is often valid. For EDFLs, $2\gamma_0^{\Re}$ can be small, and hence a residual phase noise measurement may not eliminate all of the oscillator noise, but at least give a good upper bound to the noise.

We show that a residual phase noise measurement of an actively modelocked laser is residual for offset frequencies that are less than the laser cavity response time but absolute for larger offset frequencies. It is found that harmonically modelocked lasers exhibit less oscillator phase noise suppression than fundamentally modelocked lasers.

A residual phase noise measurement is a sensitive technique that is able to measure the timing jitter of ultralow-noise modelocked lasers [45, 25] with sensitivities that exceed tens of femtoseconds. This is an important measurement technique since it can reveal the inherent spontaneous emission noise of a modelocked laser and remove the contribution due to the driving microwave oscillator. It has been found experimentally by several groups that the residual phase noise measurement of har-

monically modelocked lasers depends on the quality of the driving oscillator. In other words, the measurement is not so "residual", but rather depends on the noise of the microwave oscillator. The goal of this article is to show why this happens, and for what frequency offsets the residual phase noise measurement is valid.

At first glance, it may seem like residual phase noise measurements have no meaning for modelocked lasers, especially soliton modelocked lasers, since they are nonlinear devices. As long as the oscillator noise is small, as for any well-designed system, perturbation theory shows exactly how the oscillator noise is filtered by the laser cavity.

Oscillator noise can be incorporated into the theory of noise in actively modelocked lasers [12, 26] and actively modelocked soliton lasers [10] by making the change in the master equation $M_{AM}[1-\cos(\omega_M(t+\Delta t))] \approx M_{AM}(\omega_M t)^2 - M_{AM}(2\omega_M t\Delta t)/2$, where M_{AM} is the modulation depth and ω_M is the repetition rate of the modulator. The oscillator noise shows up in the power spectral density of the timing jitter as

$$\langle|\Delta t(\Omega)|^2\rangle = C(\Omega)\langle|S_{OSC}(\Omega)|^2\rangle \tag{3.1}$$

where $\langle|S_{OSC}(\Omega)|^2\rangle$ is the phase noise of the microwave oscillator, and $C(\Omega)$ is the laser cavity response. For actively modelocked lasers with negligible dispersion, the cavity response is Lorentzian

$$C(\Omega) = \frac{c_1}{\Omega^2 + \Omega_0^2}, \tag{3.2}$$

where c_1 and Ω_0 are constants. On a log-log scale, this function is flat up until the cutoff frequency of the cavity at Ω_0 which is proportional to $M_{AM}\omega_M^2\ 2tau^2/T_R$, where τ is the pulse width and T_R is the repetition period of the cavity. As the cavity length is increased, the cutoff frequency decreases.

A residual phase noise measurement compares the output pulses from the modelocked laser to the driving microwave oscillator. Since the laser cavity filters out the oscillator noise at offset frequencies above Ω_0, all of the oscillator noise at the LO port of the mixer above Ω_0 appears in the "residual phase noise measurement." Therefore, the measurement is truly residual for offset frequencies less than Ω_0, but absolute for

frequencies above Ω_0. For our 9 GHz fundamentally modelocked semiconductor laser, Ω_0 is typically on the order of 10 MHz, but for our 9 GHz Erbium-doped fiber laser (EDFL) operating at the 25000th harmonic, Ω_0 is typically in the range of kilohertz. Since the oscillator noise of the Agilent 83732B synthesizer extends out to 20 kHz before it rolls off at 20 dB/decade (-80 dBc/Hz from 100 to 10 kHz), it is difficult to obtain a true residual phase noise measurement for an EDFL.

Residual phase noise measurements of a 9 GHz fundamentally modelocked semiconductor laser and a 9 GHz harmonically modelocked fiber laser operated at the 22500th harmonic were performed with a quiet sapphire loaded crystal oscillator (integrated timing jitter of 5 fs from 10 Hz to 10 MHz) and with a noisier Agilent 83732B microwave synthesizer (integrated timing jitter of 300 fs from 10 Hz to 10 MHz). The residual phase noise measurements for the fundamentally modelocked laser are shown in Fig. 3-4 and for the harmonically modelocked laser in Fig. 3-5. The figures show that the residual phase noise measurement for the fundamentally modelocked laser is not affected by the noise of the microwave oscillator, whereas the "residual" phase noise measurements of the EDFL depend on the noise of the microwave oscillator. One can easily discern the 20 kHz roll-off of the synthesizer phase noise in the EDFL phase noise plot. In addition, the phase noise suppression from 10 to 1 kHz is most likely due to the cavity length stabilization circuit, which adjusts the cavity length with a fiber-wound PZT.

We have shown that a residual phase noise measurement of a modelocked laser is residual for frequency offsets that are slower than the laser cavity response time. For higher offset frequencies, the measurement yields absolute phase noise. This implies that quiet microwave oscillators are needed to measure the intrinsic phase noise of harmonically modelocked lasers.

3.1.5 Amplitude Noise Measurements

The AM noise was measured by using a mixer in which both inputs were set in-phase. The level-7 mixer was found to be most AM sensitive when the LO power was 10 dBm and the RF power was 0 dBm. Typical output IF voltages range from -180 mV to

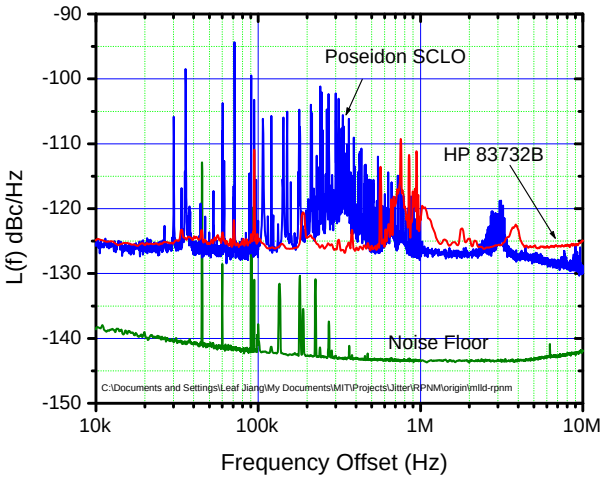

Figure 3-4: Residual phase noise of fundamentally modelocked semiconductor laser driven with the Agilent 83732B synthesizer and Poseidon Scientific Instruments SCLO.

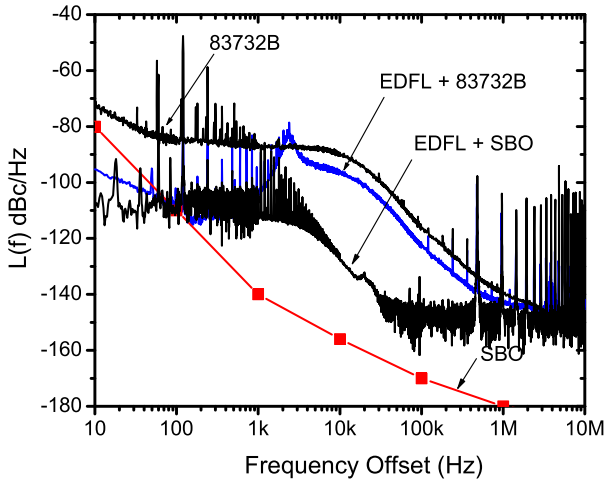

Figure 3-5: Residual phase noise of harmonically modelocked Erbium-doped fiber laser driven with the Agilent 83732B synthesizer and Poseidon Scientific Instruments SCLO.

-120 mV. The asymmetry is due to the asymmetry of the turn-on voltage of the diodes in the double-balanced mixer.

Calibration can be obtained in two ways. One way involves sending a known AM tone on top of the 10 GHz carrier. When it is difficult to use an AM tone, or the AM tone introduces extra unwanted AM noise, then calibration can be done as follows:

The normalized version of the AM noise, $m(f)$, analogous to $L(f)$, is defined as the ratio of the spectral density of one amplitude-modulated sideband to the total signal power [46, p.254]. Mathematically, this can be expressed as

$$m(f) = 20\log_{10}\left(\frac{V_c(f)}{V_{c0}}\right) - 3 \tag{3.3}$$

where V_{c0} is the voltage of the carrier signal without noise and $V_c(f)$ is the rms amplitude noise at frequency f. The carrier voltage is related to the measured IF voltage by

$$K_{AM}\frac{V_c(f)}{V_{c0}} = \frac{V_{IF}(f)}{V_{IF0}}. \tag{3.4}$$

The calibration constant, K_{AM}, can be found by attenuating the carrier by a known amount, say 1 dB, and measuring the change in the IF voltage. The calibration constant is

$$K_{AM} = \frac{\Delta V_{IF}/V_{IF0}}{\Delta V_c/V_{c0}}, \tag{3.5}$$

where ΔV_{IF} is the change in the IF voltage by adding a known attenuation, ATT, and ΔV_c is the change in the carrier voltage due to the attenuation. The attenuation is related to the change in the carrier power by

$$\frac{\Delta V_c}{V_{c0}} = 1 - 10^{-ATT/20} \tag{3.6}$$

where ATT is the attenuation in units of dB (e.g. $ATT = 1$ means -1 dB). Putting equations (3.3), (3.5), and (3.6) together, we get

$$\begin{aligned} m(f) &= 20\log_{10} V_{IF}(f) - 20\log_{10} V_{IF0} - 20\log_{10} K_{AM} - 3 && (3.7)\\ &= 20\log_{10} V_{IF}(f) - 20\log_{10}\Delta V_{IF} + 20\log_{10}\left(1 - 10^{-ATT/20}\right) - 3 && (3.8) \end{aligned}$$

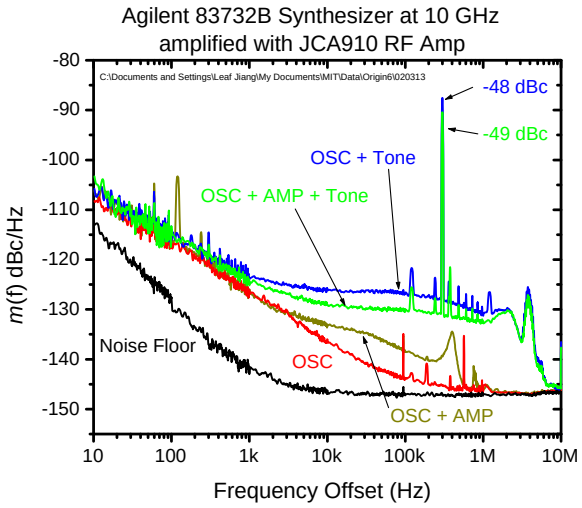

Figure 3-6: AM noise of Agilent 83732B synthesizer at 10 GHz.

For example, if $20\log_{10} V_{IF}(300\text{ kHz}) = -62$ dBVrms, $\Delta V_{IF} = 16$ mV, and $ATT = 1$ dB, then $m(f) = -48$ dBc/Hz.

Fig. 3-6 shows the amplitude noise for an Agilent 83732B synthesizer at 10 GHz before and after amplification by a JCA910 RF amplifier. The tone refers to the case when we insert a 300 kHz tone in the linear AM modulation port of the synthesizer. One can see that turning on the linear AM modulation port increases the amplitude noise up to its modulation bandwidth of about 1 MHz. The integrated AM noise is shown in Fig. 3-7.

Tracking down pickups in AM or PM noise measurements is often tricky. For example, the AM noise measurement shown in Fig. 3-8 shows large pickups from 100 kHz to 10 MHz. These pickups were removed by twisting a BNC L-connector on the IF port! These rf pickups were often evident in our phase noise measurements.

Some published work on ultralow-noise lasers [24] does not correctly normalize the spurs. The spurs should not be divided by the resolution bandwidth of the spectrum analyzer or vector signal analyzer, which makes the spurs look smaller.

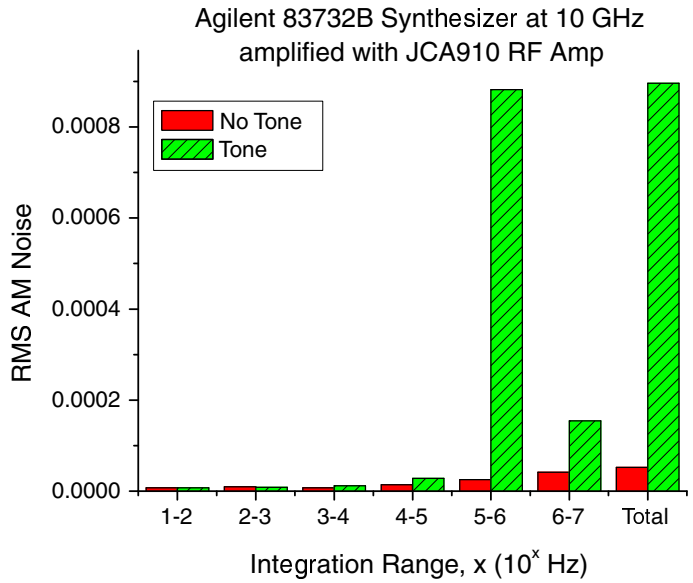

Figure 3-7: Integrated AM noise for the case of just the oscillator output, and the oscillator with the 300 kHz tone applied.

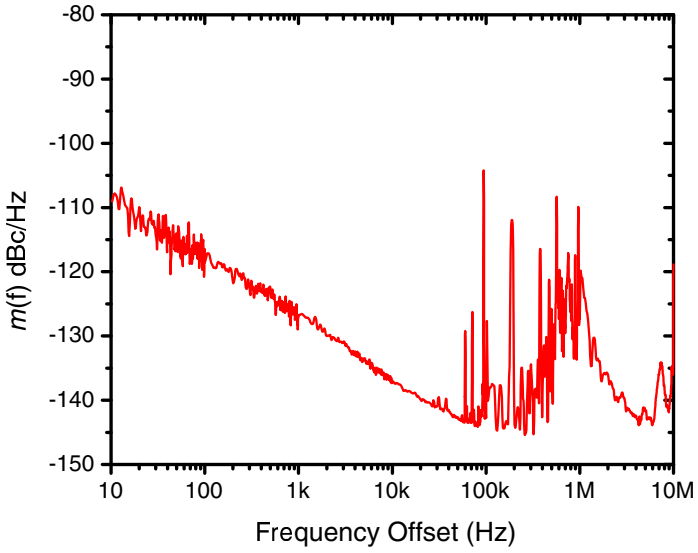

Figure 3-8: AM noise of Agilent 83732B synthesizer at 10 GHz with electrical pickups.

AM Bleed Through

The measured phase noise at low offsets can also be due to amplitude noise that bleeds through the phase detector. For MITEQ's DM0812LW2 8-12 GHz mixer, the RF-IF port AM rejection is 30 dB and the LO-IF rejection is 35 dB.

As an example, consider DePriest's external-cavity semiconductor diode ring laser actively modelocked at 10 GHz [27]. The AM laser noise at 10 kHz offset was reported to be −120 dBc/Hz. Assuming that the input power to the rf port of the mixer is 0 dBm, then the output AM noise power at the IF port at 10 kHz is $0 - 120 = -120$ dBm/Hz. Further, if the phase detector gain constant is $20 \log_{10} \kappa_\phi = -15$ dB, and the real residual phase noise is -110 dBc/Hz at 10 kHz offset, then the output power at the IF port due to phase noise is $-110 - -15 - 3 = -110 + 12 = -98$ dBm/Hz. Therefore, the amplitude noise bleed through must be negligible at 10 kHz since it is 22 dB smaller than the phase noise signal.

At a frequency offset of 10 Hz, the amplitude noise is reported to be -90 dBc/Hz and the bleed-through amplitude noise power at the IF port of the mixer is -90 dBm/Hz. The measured residual phase noise at a 10 Hz offset is reported to be -100 dBc/Hz. This indicates that the output power at the IF port due to phase noise is estimated at $-100 + 12 = -88$ dBm/Hz, which is very close to the -90 dBm/Hz due to AM bleed-through. This means that the measured residual phase noise at 10 Hz may not really be phase noise, but rather amplitude noise that is not rejected by the phase detector.

The approximate formula that expresses the AM noise contribution to the residual phase noise measurement is

$$L_{AM}(f) = S_{AM}(f) - 30 - -15 - 3 = S_{AM}(f) - 18 \text{ dB} \tag{3.9}$$

where S_{AM} is the normalized amplitude noise power in units of dBm/Hz, 30 is the RF-IF rejection, −15 is the phase detector gain constant in dB (κ_ϕ), and 3 is the conversion from a double-sideband measurement to a single-sideband measurement.

The amplitude noise from the HP83732B synthesizer at 10 GHz is better than

-150 dBc/Hz for frequency offsets greater than 5 MHz. This corresponds to an amplitude noise of $S_{AM}(f > 5\text{ MHz}) = -136$ dBm/Hz when the carrier power is 14 dBm. The residual phase noise measurement noise floor due to amplitude noise bleed through is $-136 - 35 - -15 - 3 = -159$ dBc/Hz. The noise floor for offsets greater than 5 MHz is not due to the amplitude noise of the synthesizer since it is at approximately -150 dBc/Hz. The amplitude noise of the HP83732B synthesizer at 10 GHz was measured and is plotted in Fig. 3-6.

Current and Voltage Supply Noise

The noise of the current supply and voltage noise shows up directly in the timing jitter power spectrum through two mechanisms

- Current supply noise: A change in the injection current causes a change in the carrier density of the gain section, which results in a change of the group velocity and cavity repetition rate. Therefore, $\Delta I \propto \frac{\Delta f_{cav}}{f_{cav}} \propto \frac{\Delta T}{T}$, where ΔI is the change in the injection current, f_{cav} is the cavity repetition rate, and T is the cavity repetition period.

- Voltage supply noise: A change in the saturable absorber bias voltage causes a change in the carrier density of the saturable absorber section, which results in a change of the group velocity and cavity repetition rate. Therefore, $\Delta V \propto \frac{\Delta f_{cav}}{f_{cav}} \propto \frac{\Delta T}{T}$, where ΔV is the change in the applied voltage, f_{cav} is the cavity repetition rate, and T is the cavity repetition period.

To evaluate the voltage supply noise, we tuned the saturable absorber bias current around its bias point (typically -1.5 V) by a small amount and measured the change of the repetition rate of the modelocked laser with a rf spectrum analyzer. Experimentally, we find that the cavity repetition rate tunes by 72.9 MHz/V when fundamentally modelocked at 10 GHz. This implies that $\Delta T = \kappa_v \, \Delta V$ and $\kappa_v = 7.29 \times 10^{-13}$ s/V = 729 fs/V. The power spectral density of the timing jitter is related to the power spectral density of the voltage fluctuations by $S_T(f) = \kappa_v^2 S_V(f)$. The SSB phase

noise due to the voltage fluctuations is

$$L(f) = \left(\frac{2\pi}{T}\right)^2 S_T(f) = \left(\frac{2\pi}{T}\right)^2 \kappa_v^2 S_V(f). \tag{3.10}$$

The power spectral density of the thermal noise from a 50 Ω resistor is $S_V(f) = (0.9\text{ nV})^2 \approx 10^{-18}\text{ V}^2$, and the resulting SSB phase noise due to the thermal noise from the 50 Ω resistor is $L(f) = \left(\frac{2\pi}{100\text{ ps}}\right)^2 (7.29\times10^{-13}\text{ s/V})^2(0.9\text{ nV})^2 = 1.7\times10^{-21} = -208$ dBc/Hz. Hence, broadband thermal noise from the saturable absorber voltage source is negligible. One must also consider the flicker noise of the voltage source. Fig. 3-9 shows that $S_V(10\text{ Hz}) = 10^{-110/20}\text{ V}^2$. This amount of voltage noise would cause a phase noise of $L(10\text{ Hz}) = \left(\frac{2\pi}{100\text{ ps}}\right)^2 (7.29\times10^{-13}\text{ s/V})^2(10^{-110/20}\text{ V}^2) = 2.1\times10^{-14} = -137$ dBc/Hz. Fig. 3-10 shows that the experimentally measured value is $L(10\text{ Hz}) = -90$ dBc/Hz, which is 47 dB higher than the theoretically predicted value. Therefore, the excess noise at the low frequency offsets less than 5 kHz in Fig. 3-10 is probably due to the ground loops caused by the MLLD mount between the saturable absorber, injection current terminal, and the optical cable. When we measure the phase noise of our temperature-controlled MLLD, which is electrically isolated from the optical table, we do not observe such a large amount of low frequency noise (see Fig. 2-9 for comparison).

The AM noise from the current and voltage supplies that were used to drive the modelocked semiconductor laser are shown in Fig. 3-9. The noise floor is given by the vector signal analyzer with the input range set to -30 dBm. The current supply was an ILX LDZ-3207B current source at 65 mA into a 50 Ω load. The current source noise is only slightly larger than the noise floor except for some electrical pickups at higher offsets. The voltage supply consisted of two AA alkaline batteries and 10-turn potentiometer to drop the applied voltage from -3 V to -1.5 V to a 50 Ω load. It is surprising that the battery noise dominates at low frequency offsets, and the enhanced noise may be from the potentiometer. Carbon film resistors are known to be noisier than wire-wound resistors. The AM noise of the voltage supply closely follows the shape of the noise floor and laser phase noise in Fig. 3-10 for offsets less than 1 kHz.

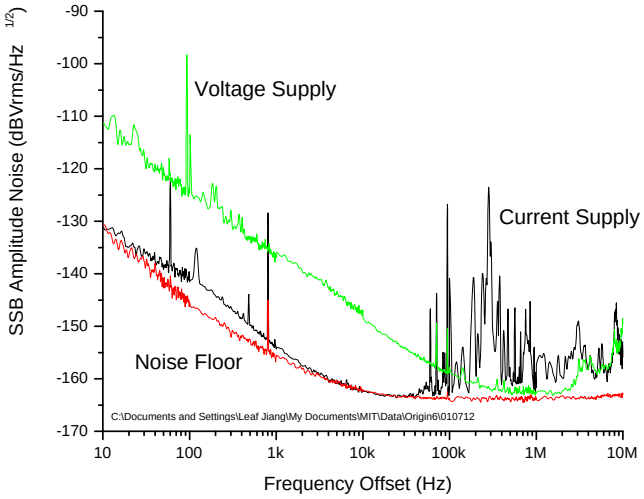

Figure 3-9: AM noise due to the current and voltage supply. The AM noise rolls off at 13 dB/decade.

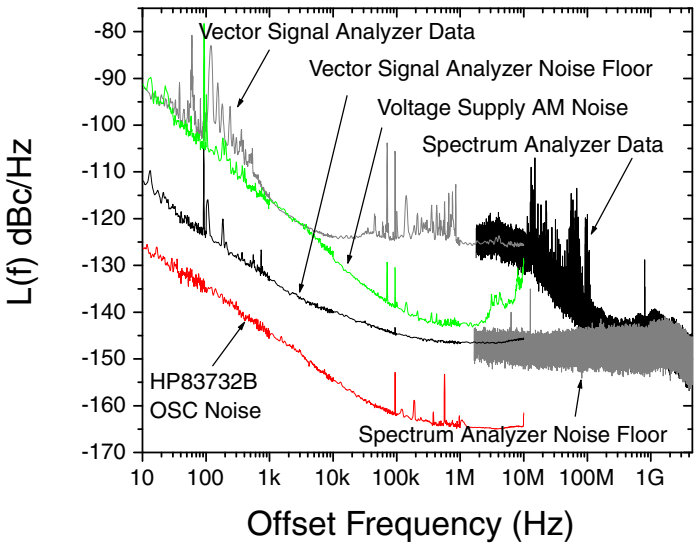

Figure 3-10: AM noise of voltage supply is plotted next to the residual phase noise measurement of a modelocked semiconductor laser. The AM bleed-through noise of the HP83732B synthesizer is also shown and is small. The exact AM-to-PM conversion factor for the voltage source noise is not known, so the line was scaled arbitrarily.

3.2 Optical Techniques

Optical cross-correlations are useful for characterizing the timing jitter of high-repetition rate modelocked lasers [47]. Sub-kilometer fiber delay lengths allow us to find correlations between pulses that are up to tens-of-thousands of cavity round-trips away. The goal of this section is to show how optical cross-correlations can be used to determine the high-frequency timing jitter and pulse-to-pulse correlations. For optical sampling applications, it is important to measure the timing jitter of a modelocked laser from 0 Hz to half its repetition rate. Since rf techniques can typically measure the phase noise of a fundamentally modelocked laser only up to several hundred megahertz before the phase noise falls below the noise floor, optical techniques are needed to characterize the jitter at higher offsets. We compare our optical cross-correlation results to radio-frequency measurements and show that they yield the same values for jitter at lower frequency offsets as well. Next, we show that the probability density function of the timing jitter of a semiconductor modelocked lasers can be found by deconvolving it from the cross-correlation measurements with the aid of pulse characterization techniques. Finally, we show how optical cross-correlations simplify timing jitter measurements in recirculating-loop experiments.

Optical cross-correlations using a nonlinear crystal and second harmonic generation provide a direct, time-domain method for characterizing high-frequency timing fluctuations and pulse-to-pulse timing jitter. By changing the length of a low-loss fiber in one arm of the cross-correlator, the integrated timing jitter can be measured accurately. The increase in the width of the cross-correlation over that of the autocorrelation is due to timing jitter. Amplitude noise is conveniently averaged out. Broadening due to dispersion in the fiber delay arm can be accounted for with an additional autocorrelation. Pulses at high repetition rates (> 40 GHz), often encountered in optical time-division multiplexed transmission [17] or passively modelocked monolithic semiconductor lasers [31], are ideal candidates for optical cross-correlations.

The use of optical cross-correlations to measure timing jitter is similar to the delay-line/mixer-frequency discriminator method used in microwave systems [48]. They

have been used largely for comparing the relative jitter between two pulse sources [49]. The use of optical cross-correlations to measure the timing jitter of a single source lost popularity from around 1986, when von der Linde [36] and Rodwell [50] introduced spectral methods which were experimentally easier. They argued correctly that to measure the timing jitter down to low frequency offsets requires impractically long lengths of fiber delay [37]. On the other hand, optical cross-correlations remain very useful for characterizing timing jitter at high frequency offsets where the timing noise is typically below the noise floor of the RF analyzer.

3.2.1 Cross-Correlation Measurements

A typical cross-correlation setup is shown in Fig. 2-14. The input pulses are split into two arms and then recombined at a nonlinear crystal so that the first pulse overlaps with the nth pulse. A fiber delay line is low loss and hence can be kilometers long. Due to the long spans of fiber, its dispersion may become significant. For that reason, three measurements are required for each delay, T. (1) An autocorrelation of pulses directly from the laser yields information about the pulse width. (2) An autocorrelation of the pulses after they propagate through the fiber of length L determines the effect of dispersion. (3) A crosscorrelation with the fiber of length L in one arm yields a curve that is the correlation of the dispersed pulse autocorrelation with the timing jitter probability density function(pdf).

Frequency Sensitivity and Relation to RF Measurements

As shown below, the frequency sensitivity of a cross-correlation measurement with one arm delayed by T is $1/4T$ to ∞ Hz. This is a good approximation when the spectral noise density is smooth over a frequency interval of $1/T$. The sensitivity to timing fluctuations slower than $1/4T$ decreases as $1/f^2$.

The optical cross-correlation measurement yields the standard deviation, $\sigma_{pp}(T)$, of $\Delta J(T) = J(t) - J(t-T)$, where $J(t)$ is the pulse displacement at time t. The

autocorrelation function of $\Delta J(T)$ is

$$\begin{aligned} & R_{\Delta J \Delta J}(T) \\ &= \langle \Delta J(t) \Delta J(t-T) \rangle \\ &= 2R_{JJ}(T) - R_{JJ}(t-T) - R_{JJ}(t+T), \end{aligned} \tag{3.11}$$

where $R_{JJ}(T) = \langle J(t)J(t-T) \rangle$ is the autocorrelation function of the jitter. The power spectral density of $\Delta J(T)$ is the Fourier transform of (3.11),

$$S_{\Delta J}(\Omega) = 2\left[1 - \cos \Omega T\right] S_J(\Omega), \tag{3.12}$$

where $S_J(\Omega)$ is the power spectral density of the timing jitter. The power spectral density of $\Delta J(T)$ is equal to the power spectral density of the timing jitter multiplied by a sinusoid. The variance of $\Delta J(T)$ is [50] [10]

$$\sigma_{pp}^2(T) = \int_{-\infty}^{\infty} S_{\Delta J}(\Omega) \frac{d\Omega}{2\pi} = \int_{-\infty}^{\infty} 2\left[1 - \cos \Omega T\right] S_J(\Omega) \frac{d\Omega}{2\pi}. \tag{3.13}$$

where we use the subscript *pp* to denote that it is the pulse-to-pulse variance. Therefore, for the pulse-to-pulse delay T, the cross-correlation measurement loses sensitivity to timing fluctuations slower than about $1/4T$ Hz. In addition, the cross-correlation is not sensitive to timing fluctuations at multiples of $1/T$ Hz since the timing jitter cancels out in the cross-correlator. In order to interpret the cross-correlation measurement as an integration of the jitter faster than $1/4T$ Hz, the power spectral density of the noise must have features that are broader than $1/T$ Hz. This is usually no problem for spontaneous emission noise or other sources of broad-band white noise, but may be problematic for radio station pickups and other spurs. The spurs in the timing jitter spectral density located at frequencies that are multiples of $1/T$ are not counted in the integrated jitter.

Pulse-to-pulse versus pulse-to-clock An optical cross-correlation measures the timing jitter between pulse 1 and pulse N, whereas an absolute or residual phase noise

measurement yields the jitter of the laser pulses relative to a microwave oscillator, or in other words, the pulse-to-clock jitter. For an actively modelocked laser, where the timing jitter is bounded relative to the driving microwave clock signal, the pulse 1 to pulse N jitter is related to the pulse-to-clock jitter. The timing jitter of pulse 1 relative to the driving microwave clock is σ_{pc} and the timing jitter of pulse N relative to the clock is also σ_{pc}. For long delays (N large), the timing fluctuations between pulse 1 and pulse N are uncorrelated. This implies that the timing fluctuations between pulse 1 and pulse N are equal to $\sigma_{pp}^2 = 2\sigma_{pc}^2$ when N is large.

Error Bars

The RMS timing jitter (for a given delay T corresponding to an integration range of approximately $1/4T$ to ∞ Hz) is then given by the expression,

$$\sigma_{pp} = \sqrt{\sigma_{XC}^2 - \sigma_{AC}^2}, \tag{3.14}$$

where we assume Gaussian pulse shapes and Gaussian pdf. Here, $\sigma_{AC}^2 = (\sigma_{AC1}^2 + \sigma_{AC2}^2)/2$ where σ_{AC1}^2 is the standard deviation of the autocorrelation of the laser output and σ_{AC2}^2 is the standard deviation of the autocorrelation after the dispersive fiber delay line. Therefore, the pulse-to-pulse timing jitter is equal to the broadening of the cross-correlation over the adjusted autocorrelation width. Assume that there is a measurement error of δ_{XC} in the cross-correlation width and δ_{AC} in the autocorrelation width. Since both measurements are usually done with the same experimental apparatus it is safe to equate these two errors, $\delta \equiv \delta_{XC} = \delta_{AC}$. The total timing jitter, including the error, is

$$\begin{aligned}
\sigma_{pp,tot} &\equiv \sigma_{pp} + \delta_{pp} \\
&= \sqrt{(\sigma_{XC} + \delta_{XC})^2 - (\sigma_{AC} + \delta_{AC})^2} \\
&\approx \sigma_{pp}\sqrt{1 + 2\frac{\sigma_{XC} + \sigma_{AC}}{\sigma_{pp}^2}\delta} \\
&\approx \sigma_{pp}\left(1 + \frac{\sigma_{XC} + \sigma_{AC}}{\sigma_{pp}^2}\delta\right)
\end{aligned} \tag{3.15}$$

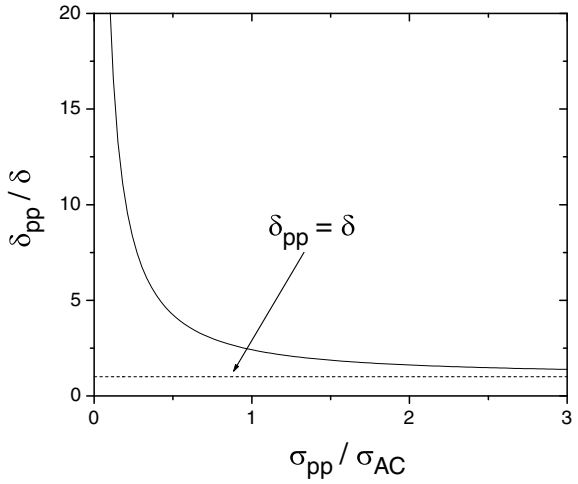

Figure 3-11: Error in measuring the RMS timing jitter increases rapidly as the timing jitter width decreases below the autocorrelation width. For example, if the experimental error in measuring the auto and cross-correlations is $\delta = 50$ fs and if the RMS timing jitter is one-tenth the standard deviation of the autocorrelation ($\sigma_{pp}/\sigma_{AC} = 1/10$), then the error in the recovered value of the timing jitter is $\delta pp = 20\delta = 1$ ps.

where the terms in δ^2 are neglected and the approximation $\sqrt{1+x} \approx 1 + x/2$ is used. This approximation is valid as long as $x \ll 1$ or equivalently $(\delta/\sigma_{pp}) \ll \sigma_{pp}/2(\sigma_{XC}+\sigma_{AC})$. As the timing jitter increases relative to the autocorrelation width, the measurement error can be larger for the above approximation to still hold. The error in measuring the RMS timing jitter is

$$\delta_{pp} = \left(\frac{\sigma_{XC} + \sigma_{AC}}{\sqrt{\sigma_{XC}^2 - \sigma_{AC}^2}} \right) \delta. \tag{3.16}$$

We can use this equation to plot σ_{pp}/σ_{AC} versus δ_{pp}/δ as shown in Fig. 3-11. Accurate correlations are necessary when the timing jitter is much smaller than the autocorrelation width. At first glance at Fig. 3-11, it may seem that it would be difficult to measure the timing jitter to less than one-tenth the autocorrelation width. But with high dynamic-range autocorrelations (20-30 dB), it is possible to reduce δ significantly below the step spacing since the Gaussian can be fit over a larger time span.

The error given by (3.16) indicates a nonlinear dependence on the auto and cross-

correlation widths. For example, for Gaussian pulses with $\sigma_{XC} = 4400$ fs, $\sigma_{AC} = 4000$ fs, and $\delta = 170$ fs (corresponding to a 50 μm step of a fine-delay stage), the timing jitter error is $\delta_{pp} = 408$ fs.

3.2.2 Measurement of Timing Jitter in Modelocked Laser Diodes

The timing jitter of a modelocked semiconductor laser was measured using both an RF spectrum analyzer and with cross-correlation measurements. The semiconductor laser shown in Fig. 2-11 was either passively or hybridly modelocked. The external cavity laser contained a 5 nm bandpass filter, a $> 99\%$ reflective dielectric mirror, a semiconductor chip with a 500 μm gain section and a 50 μm saturable absorber section. The injection current was 55 mA, the saturable absorber was reverse biased at -1.92 V and driven at the fundamental cavity harmonic of 9.348 GHz with 22 dBm of power for hybrid modelocking, the fiber coupled power was 0.4 mW, the center wavelength was 1547 nm, the 3-dB optical spectrum bandwidth was 1.42 nm, the pulsewidth was 2.5 ps, and the time-bandwidth product was 0.47 (near the transform limit for Gaussian pulses at 0.44).

The radio frequency spectrum of the directly detected pulses from the laser is shown in Fig. 3-12 and the results of the cross-correlation measurements are shown in Fig. 3-13. The RF spectrum measurements and cross-correlation measurements reveal the same values for the timing jitter: 700 fs when hybridly modelocked and RMS timing kicks ($\Delta\sigma_{pp} = \sqrt{2D^2T_R}$ from equation (3.20)) of 18 fs/round-trip when passively modelocked. Notice that an RMS timing jitter value does not make much sense for passively modelocked lasers since there is no active re-timing of the pulses and hence they undergo a random walk in position.

The solid lines in Fig. 3-12 and 3-13 correspond to theoretical curves. For actively modelocked lasers that are not dominated by Gordon-Haus jitter, the power spectral

density of the timing jitter has the form [51]

$$S_J(\Omega) = \frac{\sigma_{pc}^2 \Omega_{FWHM}}{\Omega^2 + \left(\frac{\Omega_{FWHM}}{2}\right)^2}, \tag{3.17}$$

which integrates to $\int_{-\infty}^{\infty} S_J(\Omega) d\Omega/2\pi = \sigma_{pc}^2$. Using equation (3.17) in (3.13) and noting that $\sigma_{pp}^2(T) = 2\sigma_{pc}^2$ yields the variance

$$\sigma_{pc}^2(T) = \sigma_{pc}^2 \left[1 - \exp\left(-\frac{\Omega_{FWHM} T}{2}\right)\right]. \tag{3.18}$$

For the hybridly modelocked laser $\Omega_{FWHM} = 2\pi \times 2 \times 10^6$ and $\sigma_{pc} = 700$ fs (obtained by fitting to the data). For passively modelocked lasers, the power spectral density is

$$S_J(\Omega) = \frac{2D^2}{\Omega^2}, \tag{3.19}$$

where D is a diffusion constant. This expression can be integrated according to equation (3.13) to find the variance

$$\sigma_{pc}^2 = D^2 T. \tag{3.20}$$

For the passively modelocked laser $D = 1.26 \times 10^{-10}$ Hz$^{1/2}$ (obtained by fitting to the data, $D^2 = (2\text{ps})^2/250\mu\text{s}$). To convert from a power spectral density of timing jitter to a power spectral density of phase, the following relation was used

$$S_\phi(\Omega) = \left(\frac{2\pi}{T_R}\right)^2 S_J(\Omega), \tag{3.21}$$

where T_R is the round-trip time of the cavity.

The pulse-to-pulse jitter of the hybridly modelocked laser is proportional to the derivative of equation (3.18), $\Delta\sigma_{pc}^2 = T_R \frac{d\sigma_{pc}^2}{dT}\Big|_{T=0} = T_R \sigma_{pc}^2 \frac{\Omega_{FWHM}}{2} = 100$ ps $\times (700$ fs$)^2$ $\times \frac{2\pi \times 2 \text{ MHz}}{2} = 3.08 \times 10^{28}$ s^2, or $\Delta\sigma_{pp} = \sqrt{2}\Delta\sigma_{pc} = 25$ fs. For comparison, the pulse-to-pulse jitter of the passively modelocked laser is 18 fs, which is lower than that of the hybridly modelocked laser, presumably since the losses in the monolithic

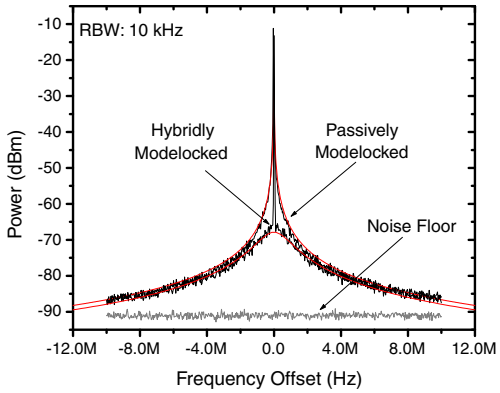

Figure 3-12: RF spectrum analyzer measurement of the laser noise. The frequency offset is referenced from the first harmonic at 9.3 GHz. The noise floor is measured by blocking the light that is incident upon the photodetector.

passively modelocked laser are smaller than the losses in the external-cavity hybridly modelocked laser. A free-space coupling loss of 3 dB in the external-cavity hybridly modelocked laser would account for the difference between the two numbers.

Timing Jitter Probability Density Function

The timing jitter probability density function (pdf) can be deconvolved from the cross-correlation. Without dispersion, the cross-correlation is equal to the timing jitter pdf convolved with the autocorrelation. The presence of dispersion in the delay lines makes the deconvolution more difficult since it becomes necessary to fully characterize the pulse in phase and amplitude. After characterizing the pulses, we can compute the shape of the cross-correlation without timing jitter. The timing jitter pdf is the deconvolution of the measured cross-correlation with the computed cross-correlation without jitter.

The first step is to characterize the pulse. There are many techniques to do this, but we chose to measure the autocorrelations after propagation through different amounts of dispersion and use a genetic algorithm to reconstruct the amplitude and phase of the pulses [52]. See Appendix C for more details on pulse characterization.

The pdf of the timing jitter for the external-cavity hybridly modelocked semicon-

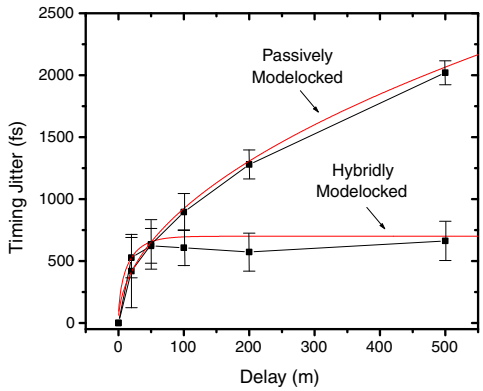

Figure 3-13: Timing jitter as a function of pulse-to-pulse delay measured with the cross-correlation scheme. The error bars, given by $\pm\delta_{pp}$, are computed from equation (3.16) with $\delta = 50$ fs.

ductor laser shown in Fig. 3-14 is nearly Gaussian in shape, and hence the pdf can be described with a single number, the standard deviation. The slight tail in the right side of the cross-correlation is presumably due to a small satellite pulse due to a Fabry-Perot reflection in one arm of the cross-correlator.

Cross-correlation measurements can reveal asymmetries in the timing jitter pdf whereas the power spectral density of the directly detected signal does not yield any information about the shape of the pdf. The timing jitter pdf of the 45 GHz passively modelocked laser diode was observed to have an interesting shape under certain operating conditions. Fig. 3-15 shows the autocorrelations of the pulses from the passively modelocked laser diode and the cross-correlations after propagation through various lengths of SMF-28 fiber. Since the autocorrelations are much narrower than the cross-correlations, the pdf of the timing jitter is essentially given by the cross-correlations. The pdf is asymmetric and more heavily weighted on the leading edge of the pulse. This asymmetry occurs at low saturable absorber bias voltages. Since the bias is low, gain saturation plays a larger role than saturable absorption in the pulse dynamics. ASE kicks to the pulse in the forward direction tend to be favored over ASE kicks in the backward direction due to gain saturation, hence leading to an asymmetric pdf more heavily weighted on the leading edge of the pulse.

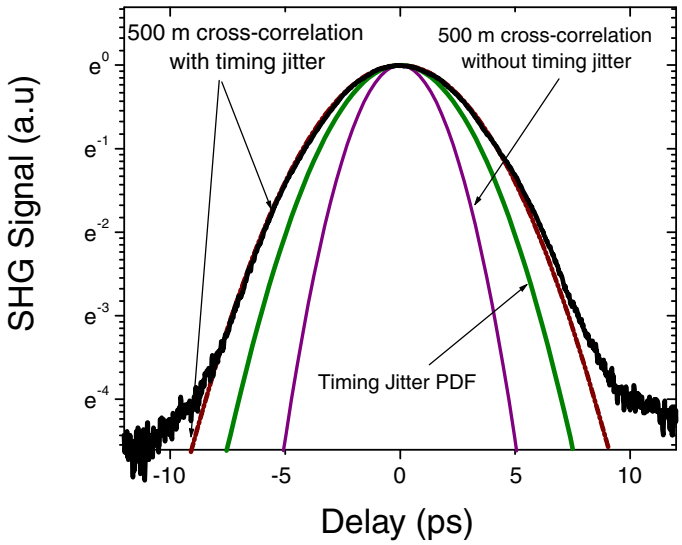

Figure 3-14: The probability density function of the timing jitter of 5 GHz MLLD for timing fluctuations faster than 200 kHz (500 m fiber delay).

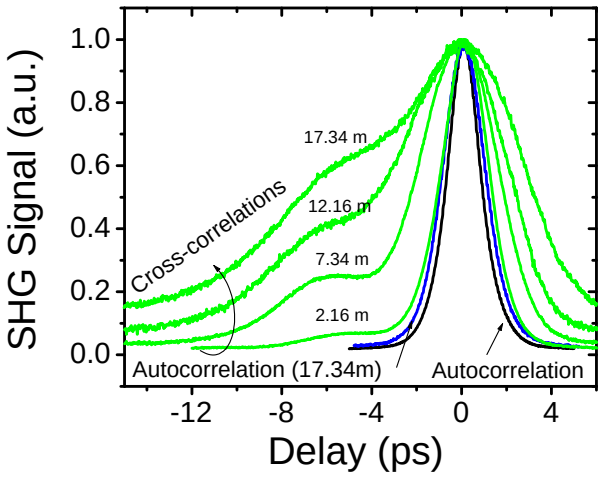

Figure 3-15: The autocorrelations and cross-correlations of a 45 GHz passively modelocked laser diode. The probability density function of the timing jitter is approximately given by the cross-correlations and is asymmetric.

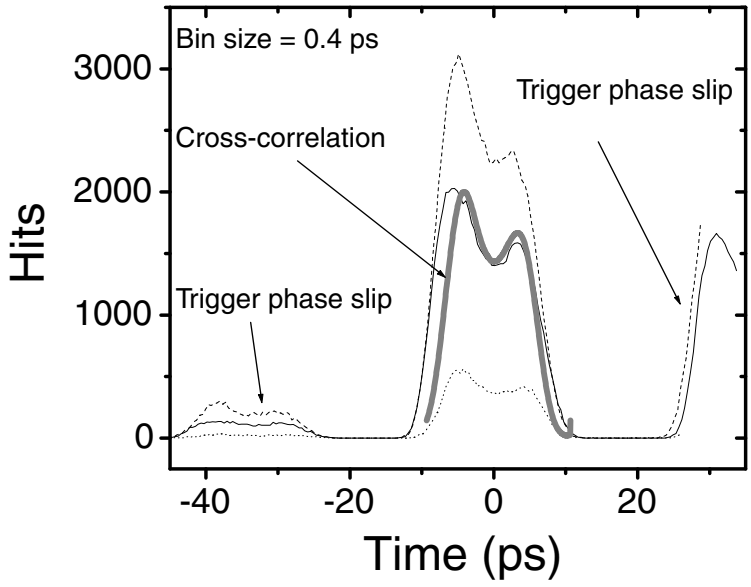

Figure 3-16: Timing displacements of speaker measured with sampling scope and cross-correlation. The sampling scope traces, shown with narrow black lines (dotted, dashed, and solid), were taken at even intervals over a few minutes. The pdf of the timing jitter is approximately equal to the cross-correlation trace (shown in bold gray line) since the pulse width is very narrow compared to the cross-correlation width.

unfavorable combinations of saturable absorber and injection current biases, for which the timing jitter kicks can be very large. When the saturable absorber

Fig. 3-16 shows the difficulty in measuring the timing jitter with sampling scopes. Most modern high-speed sampling scopes have the capability to record a histogram of the points that appear inside a user-defined rectangle. The timing jitter can be measured by centering this rectangle on either the leading or falling edge of the directly detected pulses and recording the temporal position of the edge. Sampling scopes typically have large triggering jitters (> 1 ps) and phase slips of the trigger cause problems with the histogram. In addition, the statistics change depending on the length of the measurement. The timing jitter shown in Fig. 3-16 is a simulated jitter caused by driving the speaker in Fig. 2-14 with a square wave and using 3 ps pulses from the 5 GHz hybridly MLLD. For the sampling scope, the beam is picked off before the nonlinear crystal and directly detected. The sampling scope and cross-correlation measurements qualitatively agree, but the jitter in the triggering circuitry

of the sampling scope is a limiting factor. The cross-correlation measurement shows that the FWHM of the timing displacement produced by the speaker was 13 ps.

3.2.3 Measurement of Pulse-to-Pulse Timing Jitter in Dispersion Managed Recirculating Loop

A recirculating loop is a convenient experimental setup to examine the evolution of the timing jitter in long distance propagation after many round-trips through amplification, filtering, and switching stages. In addition, recirculating loops can be used to inspect the timing jitter in a fiber ring laser after each round-trip.

The difficulty of measuring the timing jitter of pulses in a dispersion managed loop is due to the fact that there is a packet of pulses that constantly switch in and out of the loop [47]. The timing jitter of these switches is rather large, and the synchronization of the switches with either an RF spectrum analyzer or sampling scope is not trivial. The characterization of the timing jitter of the pulses from a recirculating loop can be done with optical cross-correlations, which conveniently remove the problem of synchronization with the acoustooptic switches and the associated electronic jitter. In addition, the amplified spontaneous emission noise can be separated from electronic and low frequency jitter sources by cross-correlating neighboring pulses.

Fig. 3-17 shows the dispersion managed loop which consisted of 85 km Lucent All-Wave fiber (17 ps/nm/km) followed by 15 km dispersion compensating fiber (-99 ps/nm/km). The net zero dispersion wavelength of the recirculating loop was at 1546 nm. The laser used was an external-cavity actively mode-locked laser emitting 20 ps pulses at 10 GHz repetition rate. The output of the recirculating loop goes directly to a background free SHG intensity autocorrelator. The delay stage in the autocorrelator has a range of several hundred picoseconds, which allows us to measure the pulse 1 to pulse 2 cross-correlation and the autocorrelation of a 10 GHz repetition rate pulse train. The wavelength of the modelocked erbium-doped fiber laser was tuned to match either the zero dispersion point or a non-zero dispersion value. It is found experimentally that the timing jitter variance grows linearly with

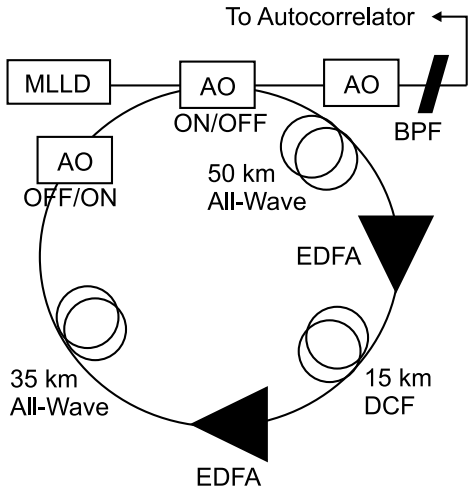

Figure 3-17: Dispersion-managed recirculating loop. MLLD is mode-locked laser diode. AO is acousto-optic modulator. BPF is bandpass filter. EDFA is erbium-doped fiber amplifier. DCF is dispersion compensating fiber. Courtesy of Sam T. Wong.

distance at net zero dispersion, and grows as distance cubed at net non-zero dispersion, in agreement with Gordon and Haus's theory [53]. This dependence can be seen in our plot of the rms timing jitter versus propagation distance in Fig. 3-18. The slight deviations from the theoretically expected L and L^3 dependence may be due to deviations of the launched pulses from a perfect hyperbolic secant shape. The error bars are derived from equation (3.16) with $\delta = 500$ fs. The timing jitter for the zero dispersion case is initially greater than the non-zero dispersion case for distances less than 1500 km. The filters after the EDFAs were not centered at the zero-dispersion wavelength, and hence the zero-dispersion propagation experienced greater loss than the non-zero dispersion case.

3.2.4 Conclusions

Optical cross-correlations present a useful tool for characterizing timing jitter in recirculating loop experiments, and for modelocked laser noise. They allow measurement of the high-frequency timing jitter with higher resolution than RF techniques. In addition, optical cross-correlations can be used to find the probability density func-

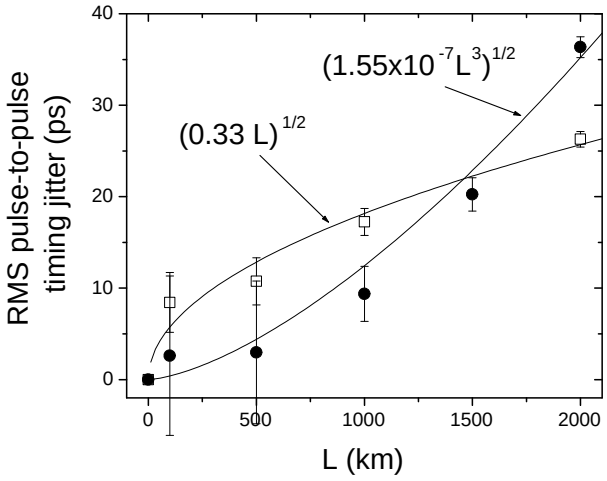

Figure 3-18: Timing jitter as a function of propagation distance for net zero dispersion at 1546 nm (empty squares) and net non-zero dispersion (filled circles). Courtesy of Sam T. Wong.

tion of the timing jitter with higher resolution than sampling scopes. Finally, the concept of pulse-to-pulse and pulse-to-clock jitter and the correspondence between cross-correlation measurements and spectral measurements were clarified.

3.3 Quantum-Limited Noise Performance of a Modelocked Semiconductor Laser

Low noise operation of a 9 GHz hybridly modelocked laser diode is demonstrated [25]. The integrated timing jitter was 47 fs (10 Hz to 10 MHz) and 86 fs (10 Hz to 4.5 GHz) with a pulse width of 6.7 ps.

The timing jitter of modelocked lasers is typically determined by measuring the noise skirts around the directly detected laser output on a radio frequency spectrum analyzer [36], a classic residual phase noise measurement [23], with phase-encoded optical sampling [41], or through optical cross-correlations [54, 55]. For the low noise lasers studied for this work at 9 GHz repetition rate, a residual phase noise mea-

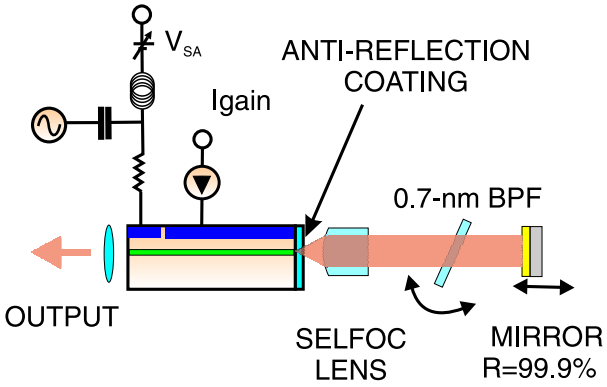

Figure 3-19: The hybridly modelocked semiconductor laser used in our experiments.

surement is the most appropriate since it is generally the most sensitive of the three techniques.

The modelocked laser diode (MLLD) used in our noise measurements is shown in Fig. 3-19. The semiconductor chip consisted of two sections [31], a 50 μm saturable absorber section and a 500 μm gain section. The laser diodes were fabricated from a double channel planar buried heterostructure laser diode wafer, which were graded index, separate confinement heterostructures having five InGaAs-InGaAsP strained-layer quantum wells. The gain section was biased at 65 mA and the saturable absorber section was reverse biased at -1.4 V. The saturable absorber was modulated externally with a low noise Poseidon Scientific Shoe Box Oscillator (SBO) at 9 GHz, amplified to give 24 dBm of RF power. The cavity length was set so that the round-trip frequency matched the RF drive frequency (fundamentally modelocked).

The residual phase noise measurement setup is shown in Fig. 3-20 and consists of the SBO microwave oscillator, the device under test (DUT), and a delay arm to set the microwave phase into quadrature so that the mixer output is proportional to the phase difference between both arms. The DUT consists of the MLLD and photodetector for the laser noise measurement or an attenuator with equivalent loss for the noise floor measurement. The mixer output is then observed on a vector signal analyzer for low frequency offsets (0-10 MHz) and on a radio frequency spectrum analyzer for high offsets (10 MHz-4.5 GHz). The delays through both arms were closely matched

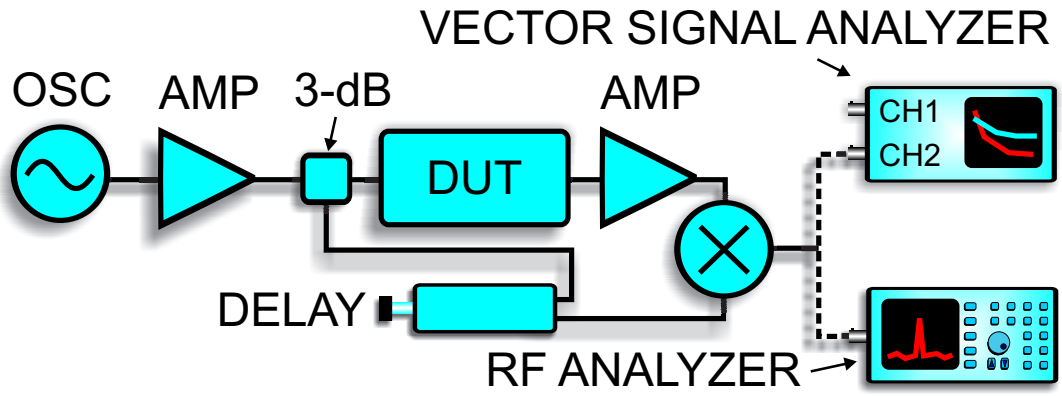

Figure 3-20: Residual phase noise experimental setup. The device under test (DUT) is the hybridly modelocked laser diode and photodetector. OSC = Poseidon Shoebox oscillator or HP83732B synthesizer.

to suppress the oscillator noise. Experimentally, we found it important to connect the radio frequency spectrum analyzer directly to the IF mixer output, otherwise the cables and splitter to the vector signal analyzer filter the noise signal at high offsets. The RF spectrum analyzer measurement was calibrated by measuring the noise down to 1 MHz where it overlapped the frequency range of the vector signal analyzer measurement. It should be emphasized that detecting the noise after the mixer with an RF spectrum analyzer for high offsets allows higher sensitivity than measuring the noise directly after a photodiode. In the latter case, the measurement is limited by the noise of the spectrum analyzer, but in the former case, the carrier signal is removed and hence the noise of the spectrum analyzer does not limit the measurement. Carrier removal improves the sensitivity since the dynamic range of the instrument is spent on the laser noise rather than on the signal plus laser noise. Fig. 3-21 shows the oscillator noise internal to our Agilent 8565EC spectrum analyzer around 9 GHz. Integrating the curve from 3.3 kHz to 500 kHz yields 109 fs of timing jitter, which indicates that a measurement of the power spectrum with the RF spectrum analyzer after a photodiode is not sensitive enough to measure the noise of our MLLD.

The single-sided phase noise is shown in Fig. 3-22. Spurs due to 60 Hz and harmonics thereof are apparent. Vibration spurs at harmonics of 20 Hz and 55 Hz

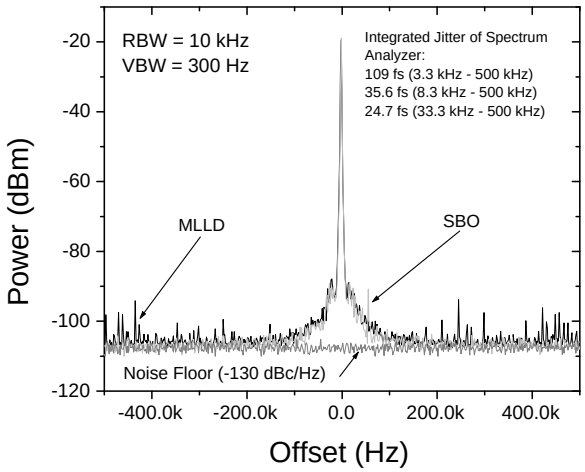

Figure 3-21: Noise of Agilent 8565EC spectrum analyzer. The offset is referenced to 9 GHz. The reference level and analyzer settings were kept constant for the three measurements: (1) MLLD is the curve corresponding to the power spectrum of the current after directly detecting the output of our modelocked laser diode with a Discovery DSC40S photodiode. (2) The SBO curve is when we plugged the Poseidon SBO low noise oscillator directly into the spectrum analyzer so that it would reveal the analyzer noise. (3) The noise floor of the analyzer without any input. The flat level corresponds to -130 dBc/Hz on our residual phase noise plots.

due to AC fans and other ambient vibrations are also visible. At higher offsets, radio stations pickups appear in the 10-100 MHz decade. A spur due to wireless telephones is visible in the 100 MHz to 1 GHz decade. In addition, contributions of noise due to the fast gain dynamics in the semiconductor laser at the relaxation oscillation frequency are also evident in this decade [26]. In the 100 kHz to 1 MHz decade, the spurs in the laser noise are due to the switching power supply in the ILX-3207B current source. For offsets less than 1 kHz, the laser noise increases by approximately 13 dB/decade. A direct measurement of the noise of the voltage supply to the saturable absorber and current source reveals an increase by 13 dB/decade for offsets less than 1 kHz, which indicates that the low-frequency noise is due to the current source driver and voltage supply. For offsets greater than 5 kHz, the noise reduces to that produced by the fundamental amplified spontaneous emission (ASE) quantum noise since the curve follows the theoretically predicted Lorentzian shape. Since the noise less than 5 kHz contributes a small fraction of the integrated timing jitter, the predominant source of the total value is ASE. Fig. 3-23 shows the integrated timing jitter in each decade. The timing jitter from 10 Hz to 4.5 GHz is 86 fs, or 154 fs if all spurs are included.

Since the integrated residual timing jitter of the MLLD is 86 fs, the driving rf oscillator must have a phase noise less than this value so that the absolute phase noise is mainly dominated by the laser noise. The SBO used in these measurements had 5.6 fs of timing jitter (10 Hz to 10 MHz), which allows quantum-limited noise performance of the MLLD. Fig. F-3 shows the single-side band phase noise of different oscillator technologies at 10 GHz (SAW, DRO, sapphire loaded crystal oscillator). The integrated timing jitter (10 Hz to 10 MHz) is shown on the plots and indicates that a sapphire-loaded crystal oscillator is necessary to reach quantum-limited noise performance (see appendix F for a discussion on X-band oscillators). Quantum-limited noise performance means that the noise is dominated by spontaneous emission noise and not the microwave oscillator noise. Since the noise that is less than 5 kHz contributes less than 5 fs of jitter, see Fig. 3-23, and the spontaneous emission noise above 5 kHz contributes approximately 85 fs of jitter, the noise of the MLLD is

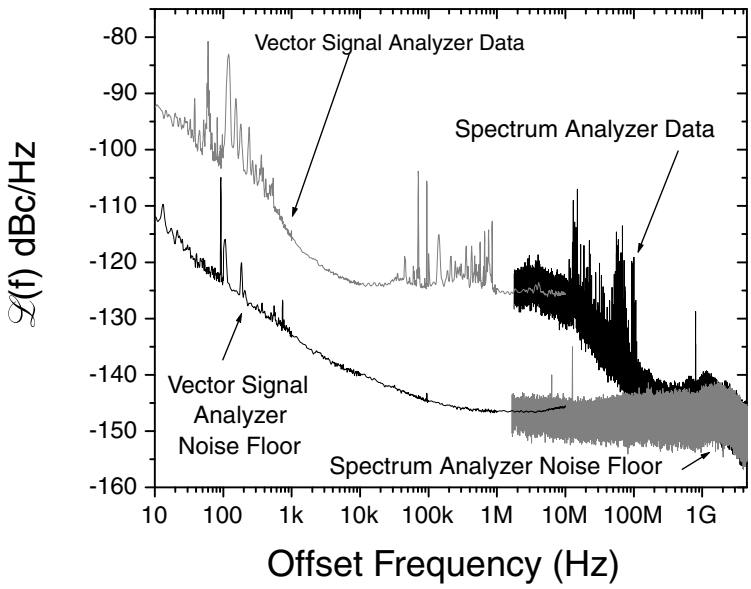

Figure 3-22: Single-sideband phase noise of the hybridly modelocked laser diode and corresponding noise floor. The plot is pieced together from vector signal analyzer measurements at low offsets and radio frequency spectrum analyzer measurements at high offsets. The measurement noise floor was obtained by bypassing the modelocked laser and substituting it with an equivalent microwave loss (51 dB in this case) and was given by the thermal noise of the amplifiers after the photodiode. The mixer IF bandwidth was 2 GHz, which was wide enough to view the noise energy before it dipped below the measurement noise floor.

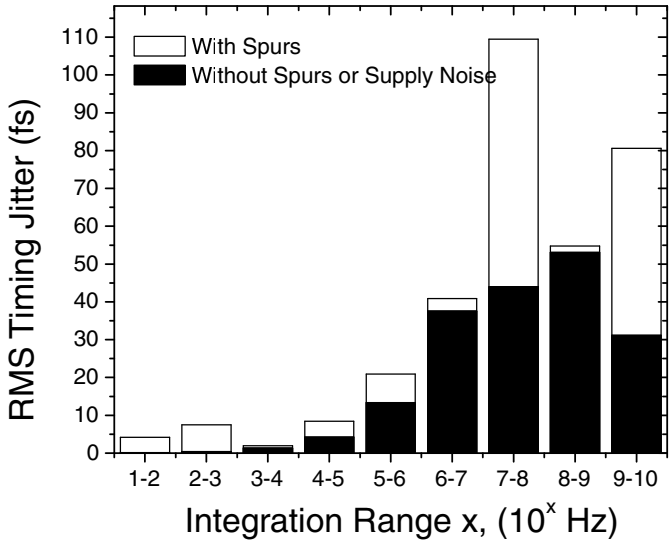

Figure 3-23: The integrated timing jitter in each decade of the phase noise shown in Fig. 3-22. The square root of the sum of the squares of the numbers above yields the jitter over multiple decades. For example, the noise without the switching power supply spurs from 1 kHz to 10 MHz is $\sqrt{1.33^2 + 4.22^2 + 13.34^2 + 37.60^2} = 40.14$ fs. In the last decade, from 1 GHz to 4.5 GHz, the white bar corresponds to the timing jitter where we assume that the noise is equal to the noise floor and the black bar corresponds to a theoretically expected -20 dB/decade rolloff.

quantum-limited.

Chapter 4

Reduction of Timing Jitter

The timing jitter of the actively modelocked semiconductor laser was reduced using three different techniques

1. Photon seeding
2. Electronic feedback
3. Timing jitter eater (phase modulation and dispersion)

The following three sections will discuss the noise reduction techniques in detail. The last method is applied outside the laser cavity and the input does not necessarily need to be from a modelocked source. We will show that this technique actually works better for pulses with narrow spectra.

4.1 Photon Seeding

In this section, we demonstrate improvement of the noise performance of a modelocked semiconductor laser using coherent photon seeding [56]. We show that the timing jitter can be reduced without increasing the pulse width.

Photon seeding has been shown to reduce timing jitter in modelocked semiconductor lasers [57, 58] and in gain-switched semiconductor lasers [59].[1] Reduction of

[1]The modelocked laser is different than the gain-switched laser in that the amount of new photons

timing jitter is crucial for high-speed optical sampling systems [18] in which it is important to have both short pulses and low-timing jitter. These two requirements on optical sampling streams are difficult to achieve simultaneously [25]. In this section, we demonstrate improved noise performance though coherent photon seeding (CPS) without significant pulse broadening.

Improved timing jitter performance from CPS has been attributed to the suppression of noise initially located just ahead of the pulse. This noise migrates into the pulse and causes severe perturbations of the pulse profile due to the random phase and amplitude of the spontaneous emission [60]. Numerical simulations have shown that the pulses suffer large scale perturbations originating from the weak spontaneous emission noise background and that the power of the seeding pulse should be large enough to swamp the noise background, but small enough so as to not affect the pulse forming dynamics of the laser [61].

4.1.1 Experiments

The experimental setup for the external-cavity, hybridly modelocked semiconductor laser with feedback is shown in Fig. 4-1. The laser consists of a 5 nm optical bandpass filter, a saturable absorber section biased at -2.10 V, a gain section biased at 55 mA, and an end mirror of reflectivity greater than 99%. The mirror on the output port of the laser is a cleaved facet with a reflectivity of about 30%. Hybrid modelocking is achieved by modulating the saturable absorber section at the fundamental repetition rate of the cavity. In this case, the RF modulation is at 9 GHz with 25 dBm average power. The pulse width at the output of the laser is 2.5 ps, as determined by fitting the background-free intensity autocorrelation of the pulses with a Gaussian shape;

added per pulse is greater for gain-switched lasers than for modelocked lasers. Therefore, the turn-on jitter of gain-switched lasers can be very large since each pulse starts from spontaneous emission, 2 ps for example [21]. Therefore the reduction of the timing jitter through photon seeding in gain-switched lasers can be very large (by a factor of > 4 in [21]). We show that for a modelocked laser, when the amount of added ASE photons per pass is large (as with a 5 nm optical BPF), the timing jitter can still be reduced by a factor of 2-3 with photon seeding. When we replace the 5 nm filter with a 0.7 nm filter, then the ASE spectral bandwidth is reduced, the amount of noise photons added per pass is small, and photon seeding does not lead to an observable reduction in the timing jitter.

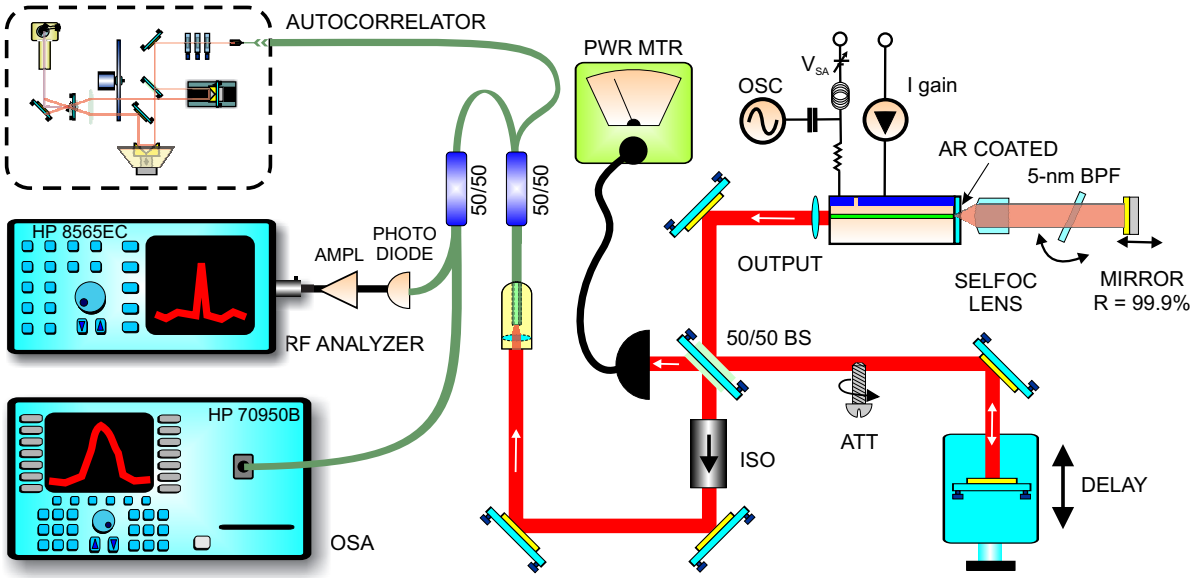

Figure 4-1: Experimental setup for photon seeding.

and the 3-dB width of the optical spectrum is measured to be 1.55 nm. Hence, the time bandwidth product (TBWP) is 0.52, indicating slightly chirped output (TBWP = 0.44 for transform-limited Gaussian pulses). An OZ Optics collimator is used to couple the light from free-space into single-mode fiber. The signal is then measured simultaneously with an optical spectrum analyzer, a background-free intensity autocorrelator, and an RF spectrum analyzer.

Photon seeding is achieved by reflecting part of the output back into the laser cavity. The relative delay between the seed pulse and main cavity pulse is adjusted with a gold mirror attached to a micrometer translation stage that follows the 50/50 beamsplitter shown in Fig. 4-1. Although we do not know the absolute position of the seed pulse relative to the main pulse, the relative delay can be obtained from the micrometer's calibrated tick marks.

The optical intensity autocorrelation, optical spectrum, and RF spectrum of the pulses as a function of delay between the main and seed pulses are shown in Fig. 4-2. The intensity autocorrelations and optical spectra are almost invariant with photon seeding. This indicates that the pulse shape is not significantly changed with photon

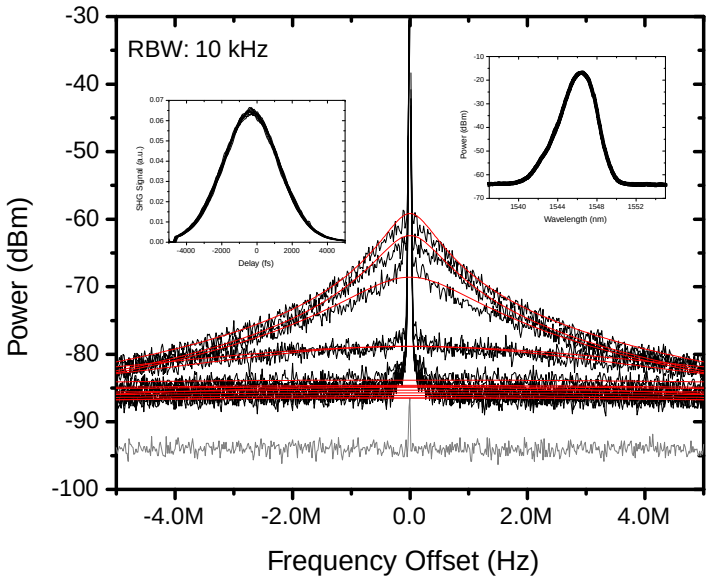

Figure 4-2: The RF spectra, intensity autocorrelations (left inset), and optical spectra (right inset) of the modelocked laser. The RF spectra are centered at the second harmonic (18 GHz). The RF carrier power at the second harmonic was measured separately using a wider resolution bandwidth and was -15.50 to -17.00 dBm depending on the feedback level (10^{-3} to 10^{-2}) and delay. The RF spectrum plots are for different feedback delays and correspond to the points in the inset plot of Fig. 4-3. The gray line is the noise floor of the RF measurement.

seeding. The RF spectrum, on the other hand, shows a large improvement with optimum CPS. The RF noise power is suppressed by approximately 20 dB near the carrier.

By measuring higher harmonics [36], it is found that most of the noise is due to timing jitter and not amplitude noise. The timing jitter is estimated by fitting a Lorentzian function to the data according to

$$\begin{aligned} P_{RF}(\Omega) &= 10\log_{10}\left[\left(\frac{2\pi n}{T_R}\right)\frac{\sigma_{pc}^2\Omega_{FWHM}}{\Omega^2+(\Omega_{FWHM}/2)^2}(RBW)\right] \\ &\quad +P_c - 2.0 \text{ dBm}, \end{aligned}$$

where T_R is the cavity repetition-rate, RBW is the resolution bandwidth setting of the RF spectrum analyzer, P_c is the power of the carrier in units of dBm, and n is the harmonic number (for our data, $n = 2$). The two fitting parameters are the RMS pulse-to-clock jitter σ_{pc} and the full-width at half maximum Ω_{FWHM}. The 2.0 dBm term corrects the effect of envelope detection, log averaging, and shape of the resolution filter on the measurement of noise with the RF spectrum analyzer [62]. The timing jitter is plotted as a function of delay and feedback in Fig. 4-3.

The inset plot in Fig. 4-3 shows the timing jitter plotted as a function of the seed-to-main pulse delay. This pattern repeats when the delay stage is moved by multiples of the laser cavity length, 16.67 mm, which shows that this is a photon seeding effect that depends on the relative seed-to-main pulse position. The timing jitter improves from 0.75 ps to 0.3 ps over a span of 600 μm (4 ps), presumably when the seed pulse proceeds the main pulse. Each point in the inset plot of Fig. 4-3 corresponds to a different optimal feedback power. The feedback power needed to obtain the points in the center of the 0.3 ps timing jitter region is smaller than the feedback power of the points at the edge of that region by an order of magnitude. Larger feedback powers are needed to obtain the same timing jitter performance as the seed pulse is moved away from its optimal position. The minimum value of timing jitter is 0.22 ps and is obtained at a delay of 300 μm.

Fig. 4-3 shows the timing jitter of the laser plotted as a function of the feedback

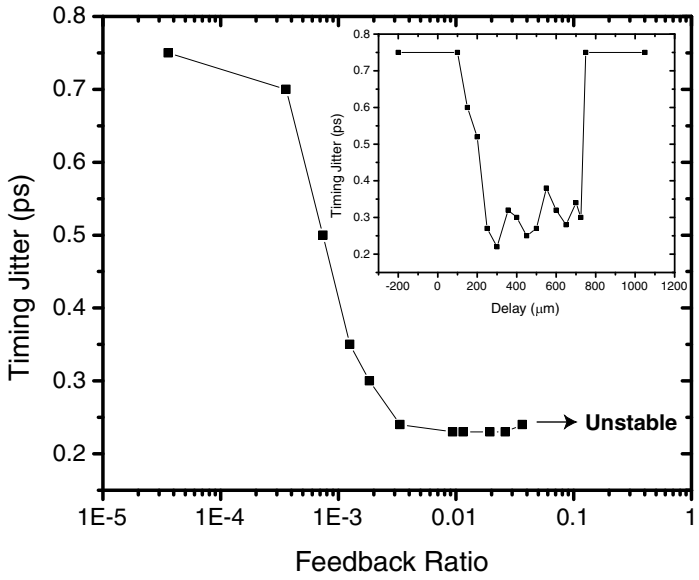

Figure 4-3: Timing jitter is plotted as a function of feedback ratio for a delay of 300 μm. The inset shows the timing jitter as a function of seed-to-main pulse delay. The double-pass delay is twice the value of the x-axis. Hence, a delay of 150 μm corresponds to double-pass delay of 300 μm or 1 ps.

ratio. The feedback power is controlled by spatially blocking part of the beam using a micrometer screw. The feedback ratio is equal to the feedback power into the laser cavity divided by the unseeded output power of the laser.[2] In this case, the delay between the main and seed pulse is fixed at 300 μm. At feedback ratios less than 10^{-4}, the laser noise performance approaches that of the unseeded case. The timing jitter decreases as the feedback ratio is increased up to 0.03. When the feedback power is increased past this value, the laser becomes unstable and falls out of modelocking[3], which indicates that for a given delay, there is an optimal feedback ratio.

[2]The power was measured from a port of the free-space 50/50 beam splitter. The power measurement was multiplied by the 30%, which corresponds to the facet reflectivity. The error in the measurement of the feedback level is due to divergence of the collimated output beam. Since the return beam waist does not diverge by more than a factor of two, the feedback measurement is accurate to within a factor of 4.

[3]At high feedback levels, the seed pulse is amplified and saturates the gain. The main pulse, which follows the seed pulse, does not experience any gain, and the result is that the pulse is temporally shifted forward in time after each round-trip. Eventually, the pulse crawls under the modulation envelope and is extinguished.

4.1.2 Results

The effectiveness of CPS depends on how well the amplified spontaneous emission (ASE) noise background is reduced through other processes. For example, the addition of an optical bandpass filter (BPF) in the laser cavity reduces the timing jitter noise by broadening the laser pulses [25]. The broadened pulses are more strongly retimed by the active modulation envelope and the narrow filtering reduces the Gordon-Haus jitter [53]. To observe the effectiveness of CPS as a function of ASE reduction by optical bandpass filtering, we replaced the 5 nm BPF with a 0.7 nm BPF. The pulse width[4] increased from 2.5 ps to 6.7 ps and the timing jitter, without CPS, decreased from 750 fs to 86 fs (10 kHz to 5 GHz) [25]. When we tried CPS on the laser with the 0.7 nm BPF, we did not observe any improvement in the timing jitter. This indicates that when the spontaneous emission induced noise is already greatly suppressed with tight optical filtering, then CPS will not significantly improve the noise any further.

The length of the feedback loop affects the CPS. As the length of the feedback loop is increased past the coherence length of the laser, more feedback power is needed to obtain the same noise performance. The length of the feedback arm, the distance from the cleaved facet of the laser to the gold mirror, was 70 cm in these experiments. When we increased the feedback loop to 17 m, feedback ratios greater than 0.01 were necessary to reduce the noise of the laser.

It is difficult to achieve both low timing jitter and short pulse widths simultaneously since the RMS timing jitter scales as $1/\tau^2$ according to actively modelocked laser theory, where τ is the intracavity pulse width [25]. Fig. 4-4 shows the relationship between timing jitter and pulse width for three configurations of the hybridly modelocked semiconductor laser. The solid lines are proportional to $1/\tau^2$. A line that is lower on the plot represents a laser with a better figure of merit. Point B corresponds to the unseeded modelocked laser with a 5 nm intracavity optical BPF.

[4]For actively modelocked lasers, the pulse width is proportional to $1/\sqrt{\Omega_f}$, where Ω_f is the optical filter bandwidth. Therefore, the ratio of the pulse widths of two lasers with different optical BPF bandwidths is $\frac{\tau_1}{\tau_2} = \sqrt{\frac{\Omega_{f2}}{\Omega_{f1}}}$. We find that $\frac{\tau_1}{\tau_2} = \frac{2.5 \text{ ps}}{6.7 \text{ ps}} = 0.373$ and $\sqrt{\frac{\Omega_{f2}}{\Omega_{f1}}} = \sqrt{\frac{0.7 \text{ nm}}{5 \text{ nm}}} = 0.374$, which means that the trends in the pulse width closely follow actively modelocked laser theory.

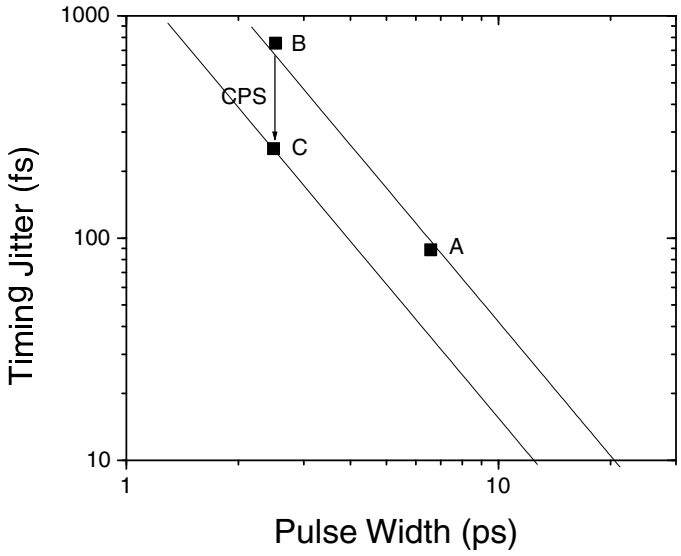

Figure 4-4: The timing jitter is plotted as a function of pulsewidth. The RMS timing jitter value is integrated over 10 kHz-5 GHz.

Point A corresponds to the unseeded modelocked laser with a 0.7 nm BPF and lies approximately on the same line. Point C corresponds to the 5-nm BPF modelocked laser with seeding. CPS improves the figure of merit of the laser.

CPS is a technique that not only applies to hybridly or actively modelocked lasers, but also to passively and regeneratively modelocked lasers. Fig. 4-5 shows the integrated timing jitter for another semiconductor laser device which is modelocked hybridly, regeneratively, and passively. In all cases, the timing jitter is shown to improve with photon seeding.

In summary, the timing jitter of a hybridly modelocked semiconductor laser was reduced from 0.75 to 0.22 ps using CPS. There was no penalty to the pulse width of the laser indicating that CPS may be useful in obtaining short pulses and low noise simultaneously.

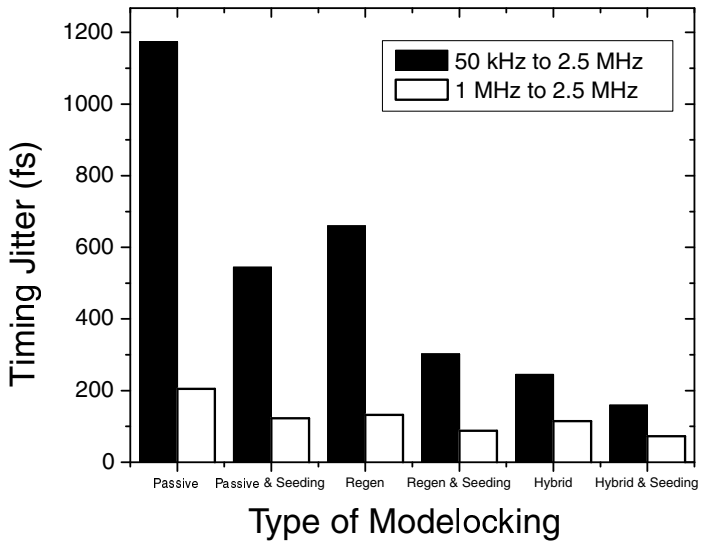

Figure 4-5: Integrated jitter with and without seeding for various types of modelocking.

4.2 Electronic Feedback

State-of-the-art fixed frequency microwave oscillators such as the Poseidon Shoe Box Oscillator and OEwaves optoelectronic oscillator have superior timing jitter compared to that of actively modelocked lasers. Therefore it would be desirable to build a feedback circuit so that the noise of the modelocked laser more closely follows the noise of the quiet microwave oscillator. This requires that the feedback circuit has enough bandwidth, gain, and low enough noise. In addition, the cavity length control also needs to be broad-band. We will show that our technique theoretically allows for broad-band operation.

4.2.1 Previous Work

The mixer output from the residual phase noise measurement can be used as an error signal to correct the timing jitter by adjusting the cavity length to match the oscillator's frequency. The maximum bandwidth over which the noise can be reduced is fundamentally limited by the round-trip time of the cavity plus the length from the

output of the laser to the detector, then the mixer, through the feedback circuit, and back to the cavity length control mechanism. The feedback length is approximately 3 meters of fiber and RF cabling. This corresponds to a minimum delay of 10 ns or 100 MHz. To reduce this feedback length, we can use the gain section or saturable absorber section as a detector and feedback this signal to the length control element in the laser [63]. We will see shortly that the feedback length, although it gives the ultimate limit to the bandwidth over which the noise cancellation is effective, is not the limiting factor in most experiments. For fiber lasers, whose length is controlled through a PZT, the speed at which the cavity length can be adjusted is the speed at which a high impedance PZT can be modulated. The response of a PZT is on the order of kHz to tens of kHz. Another technique used to control the error signal is to have the oscillator follow the cavity by using a microwave phase shifter [28]. This is not timing jitter reduction since the oscillator signal is made to follow the noise of the laser.

Here we report on controlling the cavity length through an applied voltage to the saturable absorber and/or gain section of a modelocked laser diode. This feedback mechanism has the capability of changing the cavity length over a very large bandwidth. In gain-switched diode lasers, Williams et al. demonstrated that an optoelectronic feedback loop from the gain section to the saturable absorber section was able to reduce the uncorrelated jitter from 6 to 2.5 ps [63].

4.2.2 Feedback Theory

Given the laser response to the saturable absorber, the question is whether it is possible to build a feedback circuit that will reduce the noise of the laser. The limitations of the electronic feedback are: (1) the noise of the microwave oscillator used for the phase comparison, (2) the circuit noise or noise figure of the feedback amplifiers which increases for increasing gain, (3) the capacitive load of the saturable absorber, and (4) the small cavity length change with voltage. A block diagram of the electronic feedback control of the saturable absorber bias is shown in Fig. 4-6 and includes the addition of noise sources. The noise originates from the spontaneous

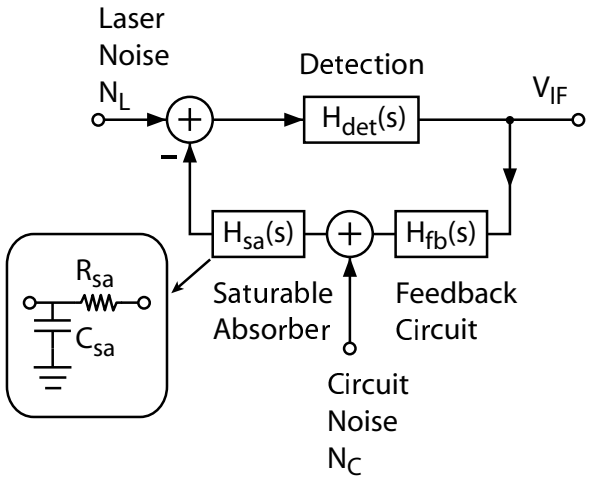

Figure 4-6: Block diagram of electronic feedback control of the saturable absorber bias.

emission in the laser, N_L, and from thermal plus flicker noise in the feedback circuit, N_C. The saturable absorber is modelled by a simple RC circuit with resistance R_{sa} and capacitance C_{sa}. The series resistance is purposefully patterned into the microwave feed and is equal to 50 Ω. The capacitance of the saturable absorber was measured with a capacitance meter at 500 nF. The transfer function of the saturable absorber is

$$H_{sa}(s) = \frac{1}{1 + sR_{sa}C_{sa}}. \tag{4.1}$$

The feedback circuit is constructed from a series of op-amp followers of voltage gain A_v and 3-dB bandwidth of s_0. The transfer function of the feedback circuit is modelled as

$$H_{fb}(s) = \frac{A_v s_0}{s + s_0}. \tag{4.2}$$

The detection circuitry consists of the laser cavity, photodiode, and phase detected output of the mixer. This can be modelled simply as a DC gain or loss according to

$$H_{det}(s) = d. \tag{4.3}$$

The total transfer function from N_L to V_{IF} is

$$H_L(s) = \frac{V_{IF}}{N_L} = \frac{H_{det}(s)}{1 + H_{det}(s)H_{fb}(s)H_{sa}(s)} \tag{4.4}$$

$$= \frac{d(s + \frac{1}{R_{sa}C_{sa}})(s + s_0)}{s^2 + \left(s_0 + \frac{1}{R_{sa}C_{sa}}\right) s + \frac{(1+A_v d)s_0}{R_{sa}C_{sa}}} \tag{4.5}$$

$$= \frac{d(s + \frac{1}{R_{sa}C_{sa}})(s + s_0)}{(s + p_1)(s + p_2)}. \tag{4.6}$$

When $d = 1$, equation (4.6) has the form

$$H_L(s) = \frac{1}{1 + H_{FB}(s)}, \tag{4.7}$$

where $H_{FB}(s) = H_{sa}H_{fb}$ has at least one more pole than zero (equal to the condition of finite bandwidth). At high frequencies, $s \to \infty$, the transfer function approaches unity $H_L(s) \to 1$. At low frequencies, $s \to 0$, the transfer function approaches the inverse of the feedback transfer function $H_L(s) \to 1/H_{FB}(s)$. In addition, the noise suppression goes to zero when $H_{FB}(s) = 1$. Fig. 4-7 shows the transfer functions $H_L(s)$ and H_{FB} for the values of $s_0 = 10$ MHz, $R_{sa} = 50\ \Omega$, $C_{sa} = 500$ nF, $A_v = 7$, and $d = 1$. The noise is suppressed by 18 dB ($20 \log_{10} A_v$) from 0 Hz to 50 kHz. The suppression is proportional to the feedback gain A_v. Increasing the gain, increases the noise suppression. The noise suppression bandwidth is limited by the capacitance of the saturable absorber and suppression degrades by 3-dB at 6.4 kHz. This value corresponds exactly to $1/2\pi R_{sa}C_{sa}$. In summary, the area of the noise suppression equals the time-bandwidth product of the feedback amplifier. To obtain good noise suppression, one needs a large gain over a broad bandwidth.

For stable operation and to avoid oscillations, the loop gain must be less than one when the phase change is 180 degrees. Fig. 4-7 shows that the phase of $H_L(s)$ never shifts by 180 degrees and hence is stable.

The transfer function from N_C to V_{IF} (with $d = 1$) is

$$H_C(s) = H_{sa}(s)H_L(s). \tag{4.8}$$

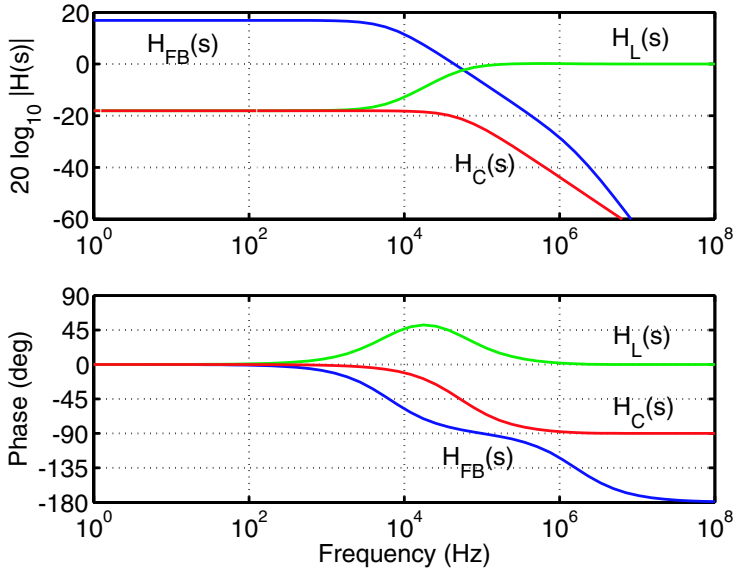

Figure 4-7: Transfer function $H_L(s)$ from the laser noise input to the mixer IF port output. The total feedback transfer function $H_{FB}(s)$ and the transfer function $H_C(s)$ are also plotted.

Fig. 4-7 shows $H_C(s)$ plotted for the feedback parameters listed in the previous paragraph. Feedback is worthwhile when the noise of the feedback amplifiers is small relative to the laser noise so that the output noise is dominated by the laser noise. Mathematically, this implies that $|H_C(j\omega)|^2 S_{N_C}(j\omega) < |H_L(j\omega)|^2 S_{N_L}(j\omega)$. For frequencies less than s_0 and $1/2\pi R_{sa}C_{sa}$, this implies that $S_{N_C}(j\omega) < S_{N_L}(j\omega)$. In other words, at best, we can only suppress the noise down to the noise of the rf oscillator and the feedback gain needs to be large enough without introducing too much noise of its own.

4.2.3 Feedback to Saturable Absorber

The output of a residual phase noise measurement was used as the error signal that was fed back to the saturable absorber bias. The cavity tunes by 14.58 MHz for every 0.2 V change in the saturable absorber bias voltage.[5] As the voltage is tuned,

[5] A 1 MHz change in a 10 GHz cavity implies that the cavity length change is 3 cm $\times$ 1 MHz/10 GHz = 3μm. This corresponds to a change of only 10 fs.

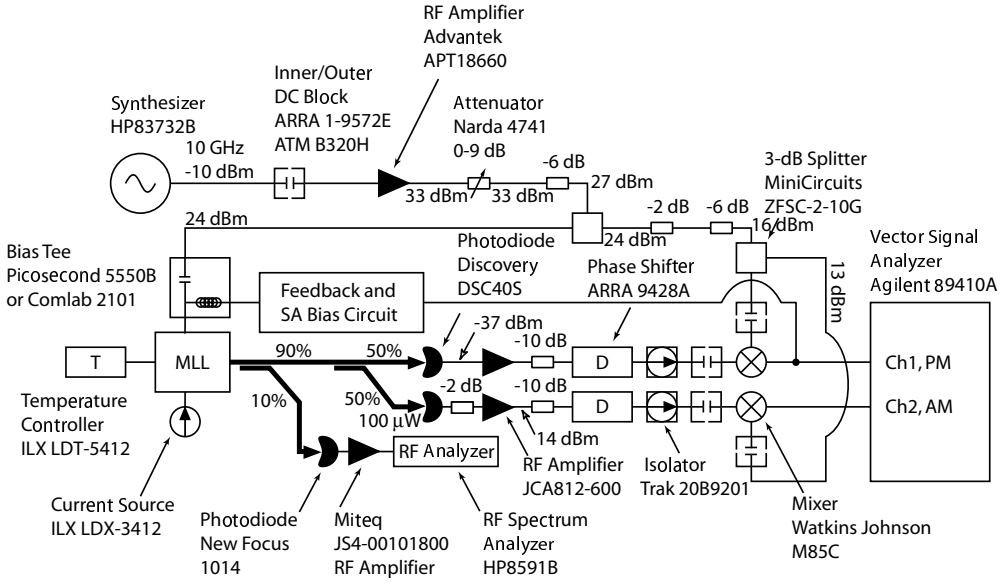

Figure 4-8: Experimental setup for electronic feedback noise cancellation.

the carrier density is changed and this results in a change of the group velocity of the material. Therefore, it is possible to re-time the pulses by tuning the saturable absorber bias. The diagram of electronic feedback setup is shown in Fig. 4-8 and the electronic circuit is shown in Fig. 4-9.

The residual phase noise measurements with the phase noise reduction circuit are shown in Fig. 4-10.[6] The plots show that the feedback circuit reduces the noise by 20 dB for offsets less than 60 kHz. These numbers match well with the theoretical model in section 4.2.2. The integrated timing jitter is shown in Fig. 4-11 and 4-12. There is no overall improvement is obtained in the integrated jitter, but fine-tuning of the feedback circuit to prevent the overshoot of its transfer response or increasing the bandwidth of the feedback may lead to improved integrated jitter performance.

Even though the feedback amplifier had a bandwidth of 10 MHz, the noise reduction bandwidth was only 60 kHz due to the capacitance of the saturable absorber section. The capacitance of the saturable absorber terminal on the temperature con-

[6]The modulation depth is not changed by feedback to the saturable absorber bias since the modulation depth depends on the DC value of the saturable absorber bias. The error signal fed back to the saturable absorber was very small, and the DC value was always fixed around -1.850 V.

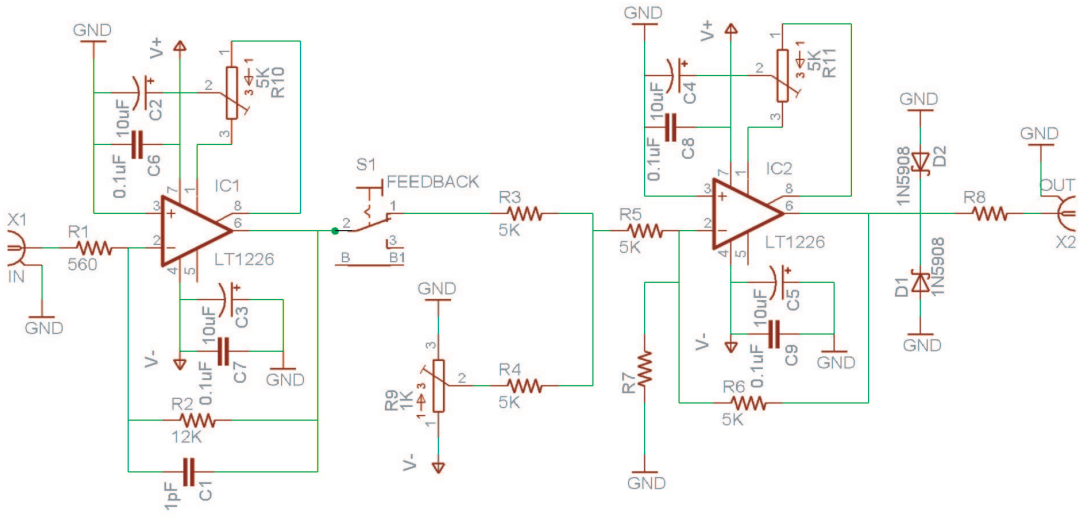

Figure 4-9: The noise reduction feedback circuit whose output is connected to the modelocked laser saturable absorber section. The input is the error signal from the IF port of the phase detector and output is fed to the DC port of the bias tee that connects to the saturable absorber.

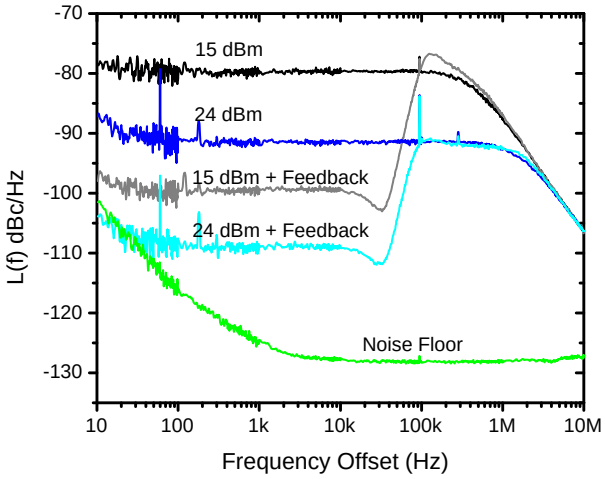

Figure 4-10: Timing jitter noise of temperature controlled external-cavity MLLD with and without electronic feedback. The power level refers to the microwave power applied to the saturable absorber.

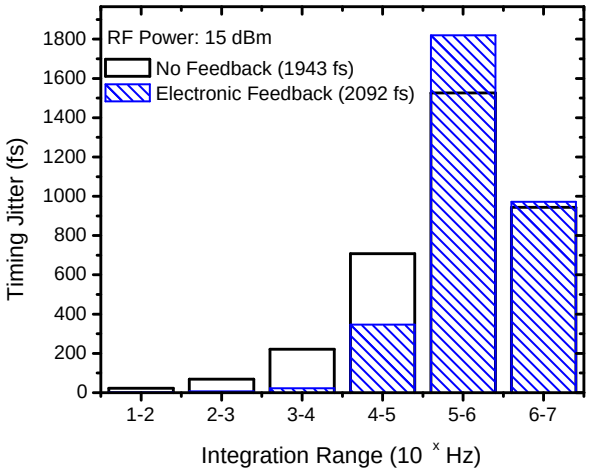

Figure 4-11: Integrated timing jitter for the temperature controlled external-cavity MLLD when the saturable absorber is driven with 15 dBm of microwave power.

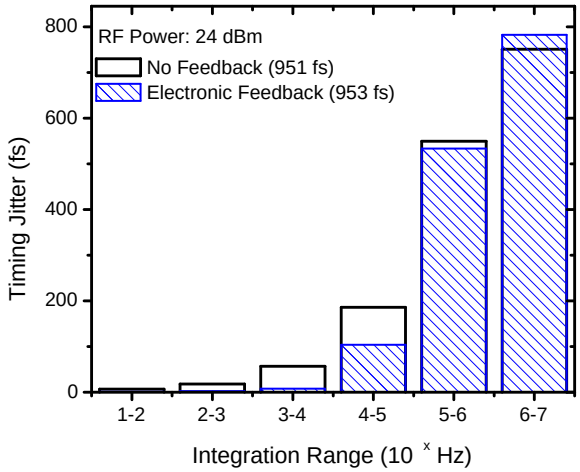

Figure 4-12: Integrated timing jitter for the temperature controlled external-cavity MLLD when the saturable absorber is driven with 24 dBm of microwave power.

trolled semiconductor laser was measured with a capacitance meter at 580 nF.[7] The capacitance of the gain section terminal was measured at 43 nF. The large capacitance of the saturable absorber terminal is the reason for limited noise reduction bandwidth. If the capacitance of these terminals could be reduced, then the noise reduction bandwidth could be much larger.

Changing the saturable absorber bias also has the unwanted effect of modulating the pulse amplitudes. The amplitude noise increases by approximately 5 dB in the frequency offsets in which the timing jitter improves (< 60 kHz). One work-around to this problem is to also drive the current section with the error signal. Whenever, the error signal makes the saturable absorber lossier, the current section would yield more gain to offset the increased loss. In addition, the timing shifts from the gain section would be in the correct direction. At low frequencies, less than a gigahertz, the frequency response both terminals should be flat.

4.2.4 Feedback to External SOA

The error signal from the residual phase noise measurement can also be fed forward to a semiconductor optical amplifier (SOA) placed after the modelocked laser. The error signal controls the carrier density, which in turn controls the group velocity of the pulses traversing the SOA.

Fig. 4-13 shows the residual phase noise of the laser at the output of the SOA. The noise reduction is approximately 5-8 dB over the range 10 kHz to 100 kHz. The noise at frequency offsets less than 2 kHz are plagued by a forrest of 60 Hz tones and are presumably due to ground loops.[8] The noise enhancement or Q-ing around 450 kHz is indicative of not having enough phase margin. Hence, the output is close to oscillating. The limitation on the noise reduction bandwidth is due to the bandwidth of the modulation port of the current source.

[7]The saturable absorber capacitance for the non-temperature controlled free-space external-cavity MLLD was 620 nF.

[8]Even though the phase noise looks smooth in the 1 kHz to 10 kHz decade when the feedback is on, these are actually 60 Hz harmonics which can be seen when the resolution bandwidth is decreased.

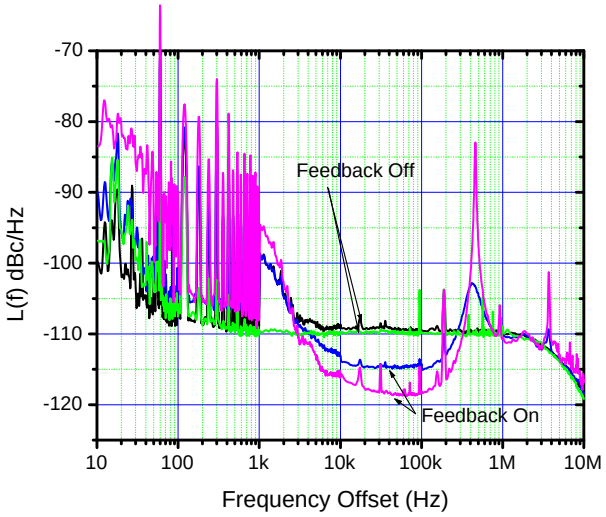

Figure 4-13: Residual phase noise of modelocked semiconductor laser after propagation through SOA.

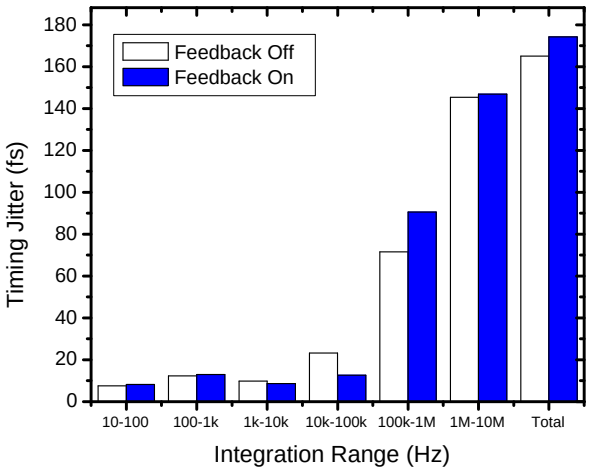

Figure 4-14: Integrated timing jitter of the phase noise curved in Fig.4-13.

The phase noise of the modelocked semiconductor laser can be reduced with feedback to the saturable absorber port or to an external SOA. Excellent low frequency noise suppression can be obtained, which may be important for optical clock applications.

4.3 Timing Jitter Eater

The idea of using external modulators to re-time pulses dates back to the work of Nakazawa in 1991 [64, 65]. His concept, called synchronous modulation, allowed him to transmit 10 Gbit/s soliton pulses trains over unlimited distances. Smith et al. later demonstrated that the timing jitter of a soliton pulse train could be reduced by a factor of 5-20 with single phase modulator [66, 67, 68]. King et al. soon afterwards filed a patent for using a modulator in a receiver at the end of a transmission line [69]. Their patent mentioned the use of electro-absorption modulators followed by dispersive fiber but did not contain any performance data.

Here, we demonstrate the use of a phase modulator followed by dispersive fiber for re-timing any optical pulse (not just solitons) [70]. This problem is more formidable in the sense that soliton pulses keep their shape after propagation through dispersive fiber, whereas Gaussian pulses spread and eventually wash out. We show that choosing an appropriate pre-chirp fiber can ameliorate the pulse spreading problem, and it introduces another parameter for optimizing the timing jitter eater. The parameter space of the timing jitter eater is somewhat counter-intuitive and we will show that there exists a surprising choice of fiber dispersion that yields excellent timing jitter suppression while minimizing pulse spreading. We also investigate the applicability of the timing jitter eater to optical sampling systems and find optimal parameters for this application. In addition, we experimentally demonstrate that a 12 dB reduction in the phase noise is easily attainable for telecommunication applications.

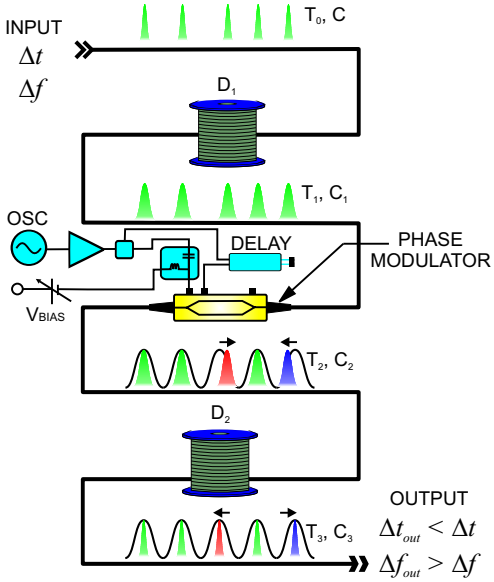

Figure 4-15: Diagram of the timing jitter eater. Pulse broadening due to fiber dispersion is also illustrated.

4.3.1 How it Works

The setup used to reduce the timing jitter of a modelocked laser is shown in Fig. 4-15. A train of pulses with a given amount timing jitter $\langle \Delta t^2 \rangle$ and frequency noise $\langle \Delta f^2 \rangle$ is shown at the top of the figure. The pulses are then sent through pre-chirp fiber and then through a phase modulator. The offset phase of the phase modulator is chosen so that correctly timed pulses do not get chirped. Pulses that are mis-timed so that they arrive too early in the modulator are positively (or negatively; depends on the cycle of the phase modulator). Pulses that are too late are negatively (or positively) chirped. If the sign of the dispersion is chosen so that the positively chirped pulses are delayed and the negatively chirped pulses are advanced, then at the end of the dispersive fiber, the timing jitter is reduced. The frequency noise, on the other hand, increases since each mistimed pulse has a slightly different carrier frequency due to the modulator. [9]

[9] The tradeoff between timing and frequency noise cannot be thought of as an uncertainty principle effect. In principle, assuming that the phase modulator has no noise, the timing jitter of the output can be reduced to zero. Therefore, the product $\Delta t \Delta f$ is not conserved.

Adding dispersive pre-chirp fiber before the phase modulator yields an extra parameter for controlling the output pulse width. Introducing the pre-chirp fiber allows us to better optimize both the timing jitter reduction and pulse width spreading.

4.3.2 Theory – Timing Jitter Reduction

An expression for the timing jitter reduction will be derived in this section. The phase modulator multiplies the pulses by $\exp[j\phi(t)]$, where $\phi(t) = M\cos\omega_M t$ and the applied chirp is $\omega = -\frac{d\phi}{dt} = M\omega_M \sin\omega_M t \approx M\omega_M^2 t$. If the pulse is initially displaced by Δt_{in}, then the modulator applies a pulse-position-dependent frequency shift to the optical pulses according to

$$\Delta\omega = M\omega_M^2 \Delta t_{in}. \tag{4.9}$$

The pulse then propagates through dispersive fiber with dispersion $\beta_2^{(post)} L$ (units: ps^2), and if the sign of the dispersion is chosen correctly, the pulses are re-timed. The dispersion parameter β_2 is related to the group velocity by

$$\beta_2 = \frac{d}{d\omega}\left(\frac{1}{v_g}\right) = -\frac{1}{v_g^2}\frac{dv_g}{d\omega}. \tag{4.10}$$

Therefore a frequency shift of $\Delta\omega$ will result in a group velocity change of

$$\Delta v_g = -v_g^2 \beta_2 \, \Delta\omega. \tag{4.11}$$

After the pulses propagate through a fiber with length L, the pulses are re-timed according to

$$\Delta t_{fiber} = -\frac{L}{v_g^2} \, \Delta v_g. \tag{4.12}$$

which is the differential of $t = L/v_g$. Substituting equation (4.9) into equation (4.10) and the result into equation (4.11) and the result into equation (4.12), yields

$$\Delta t_{fiber} = M\omega_m^2 \beta_2 L \, \Delta t_{in}. \tag{4.13}$$

The resulting pulse displacement at the output of the fiber is

$$\Delta t_{out} = \Delta t_{in} + \Delta t_{fiber} = (1 + M\omega_m^2 \beta_2 L)\Delta t_{in}. \tag{4.14}$$

Therefore, if M and β_2 have opposite signs, then the timing jitter at the output can be reduced. The timing jitter reduction is equal to

$$R \equiv \frac{\Delta t_{out}}{\Delta t_{in}} = 1 + M\omega_M^2 \beta_2^{(post)} L. \tag{4.15}$$

The timing jitter power spectral density and phase noise of the pulses are decreased by a factor of R^2.

To maximize the timing jitter reduction, the dispersion, modulation depth, and modulation frequency must be made large. The downside of increased dispersion is pulse broadening, which will be discussed in the next section.

4.3.3 Theory – Pulse Width

The equations that govern the pulse width assume that the launched pulse has a linearly-chirped Gaussian shape, the fiber nonlinearity is ignored, and only second-order dispersion (β_2) in the fiber is considered. For this specific case, we can derive analytic solutions.

The Kerr nonlinear effect in a fiber may be important for large input powers. Kerr nonlinearities give rise to soliton-like effects in anomalous dispersive fiber, i.e. it holds the pulse together. Therefore, high input powers and anomalous dispersion fiber should provide even better performance over the linear propagation case since longer lengths of dispersive fiber can be used without excessive pulse broadening.

The electric-field from the laser can be written as

$$E(t) = E_0 \exp\left(-\frac{1 + jC_0}{2}\left(\frac{t}{T_0}\right)^2\right) \tag{4.16}$$

where C_0 is the linear chirp and $T_{FWHM} = 1.6651 T_0$. This field is then propagated in the system illustrated in Fig. 4-16. Since we choose to represent the carrier as

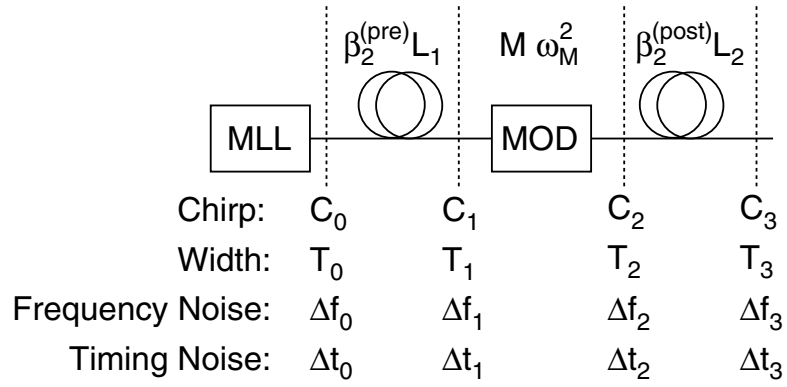

Figure 4-16: Experimental setup of the timing jitter eater.

$\exp(-j\omega_0 t)$ in the electric-field, the chirp on the pulse is

$$\omega = -\frac{\partial \phi}{\partial t} \tag{4.17}$$

The basic equations are (see Fig. 4-16 for the variable definitions):

$$T_1 = T_0\sqrt{\left(1+\frac{C_0\mathcal{D}_1}{T_0^2}\right)^2+\left(\frac{\mathcal{D}_1}{T_0^2}\right)^2} \tag{4.18}$$

$$C_1 = T_1^2\frac{C_0T_0^2+\mathcal{D}_1(1+C_0^2)}{(T_0^2+C_0\mathcal{D}_1)^2+\mathcal{D}_1^2} \tag{4.19}$$

$$T_2 = T_1 \tag{4.20}$$

$$C_2 = C_1 + M\omega_M^2T_1^2 \tag{4.21}$$

$$T_3 = T_2\sqrt{\left(1+\frac{C_2\mathcal{D}_2}{T_2}\right)^2+\left(\frac{\mathcal{D}_2}{T_2^2}\right)^2} \tag{4.22}$$

$$C_3 = T_3^2\frac{C_2T_1^2+\mathcal{D}_2(1+C_2^2)}{(T_1^2+C_2\mathcal{D}_2)^2+\mathcal{D}_2^2} \tag{4.23}$$

$$R^2 = \left(1+M\omega_M^2\mathcal{D}_2\right)^2+(\mathcal{D}_1+\mathcal{D}_2)^2F^2 \tag{4.24}$$

where $\mathcal{D}_1 = \beta_2^{(pre)}L_1$, $\mathcal{D}_2 = \beta_2^{(post)}L_2$, and $F = \Delta\omega_0/\Delta t_0$ is the ratio of the input angular frequency noise (rms value) to the input rms timing jitter.

Mathematically, the phase modulator multiplies the electric field by

$$\exp(jM\cos(\omega_M t)) \tag{4.25}$$

where ω_M is the angular frequency of the modulator and

$$M = \frac{V_p}{V_\pi}\pi \tag{4.26}$$

is the modulation depth. The peak voltage V_p relates the average applied RF power by $V_{rms} = V_p/\sqrt{2}$. The phase modulator applies a chirp to the input electric field. The output pulse width is unchanged, but the new chirp is $C_2 = C_1 + M\omega_M^2 T_1^2$.

In addition, the input pulse contains some frequency noise which can turn into timing jitter if the overall dispersion is large. This term shows up in the last part of equation (4.24).

The basic equations (4.18) through (4.24) can be solved simultaneously for $\mathcal{D}_1$ and $\mathcal{D}_2$. There are four solutions [10] when the input pulse is transform limited,

[10] The solutions are

$$\mathcal{D}_1 = -T_0\sqrt{T_1^2 - T_0^2} \tag{4.27}$$

$$\mathcal{D}_2 = -T_0\frac{-\sqrt{T_1^2 - T_0^2} + M\omega_M^2 T_0 T_1^2 + \sqrt{-T_0^2 + M^2\omega_M^4 T_0^4 T_3^2 + \left(T_3 - M\omega_M^2 T_0 T_3\sqrt{T_1^2 - T_0^2}\right)^2}}{1 - 2M\omega_M^2 T_0\sqrt{T_1^2 - T_0^2} + M^2\omega_M^4 T_0^2 T_1^2} \tag{4.28}$$

$$\mathcal{D}_1 = T_0\sqrt{T_1^2 - T_0^2} \tag{4.29}$$

$$\mathcal{D}_2 = -T_0\frac{\sqrt{T_1^2 - T_0^2} + M\omega_M^2 T_0 T_1^2 + \sqrt{-T_0^2 + M^2\omega_M^4 T_0^4 T_3^2 + \left(T_3 + M\omega_M^2 T_0 T_3\sqrt{T_1^2 - T_0^2}\right)^2}}{1 + 2M\omega_M^2 T_0\sqrt{T_1^2 - T_0^2} + M^2\omega_M^4 T_0^2 T_1^2} \tag{4.30}$$

$$\mathcal{D}_1 = -T_0\sqrt{T_1^2 - T_0^2} \tag{4.31}$$

$$\mathcal{D}_2 = -T_0\frac{-\sqrt{T_1^2 - T_0^2} + M\omega_M^2 T_0 T_1^2 - \sqrt{-T_0^2 + M^2\omega_M^4 T_0^4 T_3^2 + \left(T_3 - M\omega_M^2 T_0 T_3\sqrt{T_1^2 - T_0^2}\right)^2}}{1 - 2M\omega_M^2 T_0\sqrt{T_1^2 - T_0^2} + M^2\omega_M^4 T_0^2 T_1^2} \tag{4.32}$$

and

$$\mathcal{D}_1 = T_0\sqrt{T_1^2 - T_0^2} \tag{4.33}$$

$C_0 = 0$, of which only two lead to noise reduction for $M > 0$. The four solutions can be understood graphically from Fig. 4-17, which plots the pulse width T versus the chirp parameter C. The output pulse width is related to its transform-limited value[11] by $T_0\sqrt{1+C^2}$. Therefore, dispersion shifts the operating point along the solid "parabolic-looking" lines in Fig. 4-17. The phase modulator serves to translate the operating point horizontally by an amount given by equation (4.21). The dashed lines indicate lines of constant dispersion, $T = D\frac{1+C^2}{C}$. Starting at the point ($C = 0$,$T = T_{in}$), there are four paths to get to T_{out} which correspond to the four solutions. Path 1, 2, 3, and 4 correspond to equations (4.33), (4.31), (4.27), and (4.29), respectively. Path 3 and 4 have the right sign of dispersion in the post-chirp fiber. It turns out that although the post-chirp dispersion in path 3 is greater than path 4, it actually is too large and causes over-compensation. Therefore, path 4 is the desirable solution.

The three constraints used to obtain the solutions are (1) $C_0 = 0$ since we can easily pre-chirp the pulse so that it is transform-limited; (2) T_1 (or T_{mod} in Fig. 4-17) is limited to the parabolic region of the sinusoidal modulation envelope. This constrains the width to $T_1 < 0.3 \times \frac{2\pi}{\omega_M}$; (3) T_3 (or T_{out} in Fig. 4-17) is set to some target value.

Fig. 4-18 shows the greatest calculated noise reduction possible using a pre-chirp fiber, a single phase modulator with $M = 3.6$ at 10 GHz, and post-chirp fiber. Fig. 4-19 shows the same plot on a logarithmic scale. The noise reduction is plotted as a function of the output pulse width (FWHM) for different input pulse widths (FWHM). Oscillator noise and input frequency noise were ignored in this calculation for simplicity. Perfect timing jitter suppression occurs at $R = 0$. Perfect noise suppression is possible with 6.5 ps pulses, although the output pulse width must be 30 ps. Fig. 4-20

$$\mathcal{D}_2 = -T_0\frac{\sqrt{T_1^2-T_0^2}+M\omega_M^2T_0T_1^2-\sqrt{-T_0^2+M^2\omega_M^4T_0^4T_3^2+\left(T_3-M\omega_M^2T_0T_3\sqrt{T_1^2-T_0^2}\right)^2}}{1+2M\omega_M^2T_0\sqrt{T_1^2-T_0^2}+M^2\omega_M^4T_0^2T_1^2} \quad (4.34)$$

where equations (4.27) and (4.29) lead to a noise reduction when $M > 0$. Equations (4.31) and (4.33) are the solutions that lead to timing jitter reduction when $M < 0$.

[11] Simplify the basic equations for $C = 0$. One obtains $T_1 = T_0\sqrt{1+C^2}$ and $C_1 = D/T_0^2$.

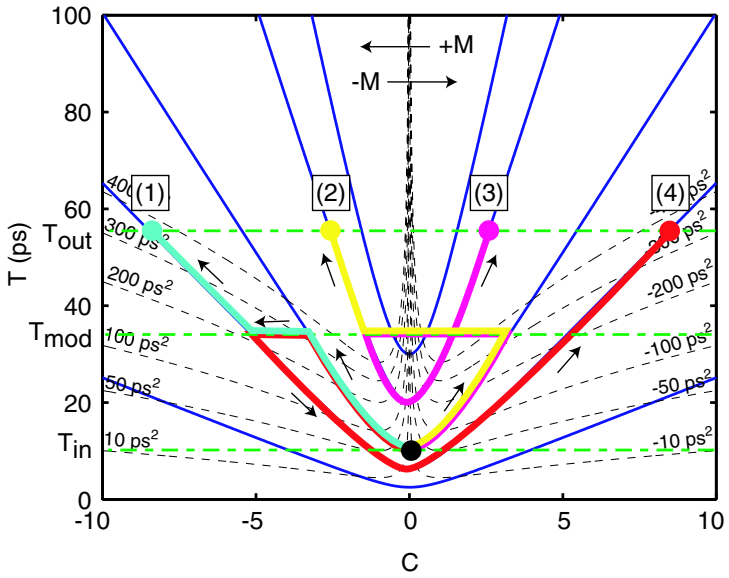

Figure 4-17: Graphical analysis of solutions. Plot of pulse width versus chirp parameter.

shows that the optimal solution has normal dispersion pre-chirp fiber. The post-chirp fiber is anomalous dispersion, and is shown in Fig. 4-21. This configuration is ideal for minimizing frequency-to-timing noise conversion since the total dispersion of the system is close to zero.

Fig. 4-19 indicates a very interesting consequence of dispersion penalty and the spectral broadening of the modulator. The plot shows that, compared to input pulse widths of 10 ps, input pulse widths of 20 ps can have much better jitter reduction and have much narrower output pulse widths. In addition, a modelocked laser that produces 20 ps pulses is much quieter than a laser that produces 10 ps pulses.

The dashed lines in Fig. 4-18, 4-19, and 4-21 correspond to the best that can be done with no pre-chirp fiber. The graphs show that better timing jitter and lower output pulse widths reduction can be obtained with pre-chirp fiber. However, if one wants to attain perfect timing jitter suppression, the pre-chirp fiber is not necessary.

Increasing the modulation rate improves the timing jitter reduction quadratically. Increasing the modulation rate by a factor of 2 (from 10 GHz to 20 GHz), moves the $R = 0$ intercept in Fig. 4-18 from $T_{out} = 30$ ps to $T_{out} = 30/4 = 7.5$ ps.

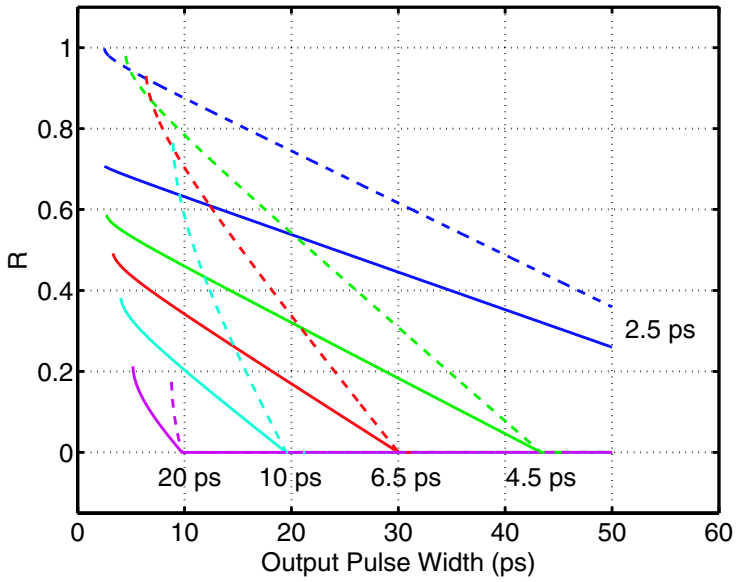

Figure 4-18: Noise reduction using a timing jitter eater with a single phase modulator with $M = 3.6$ for input pulse widths from 2.5 to 20 ps. The dashed line corresponds to no pre-chirp fiber.

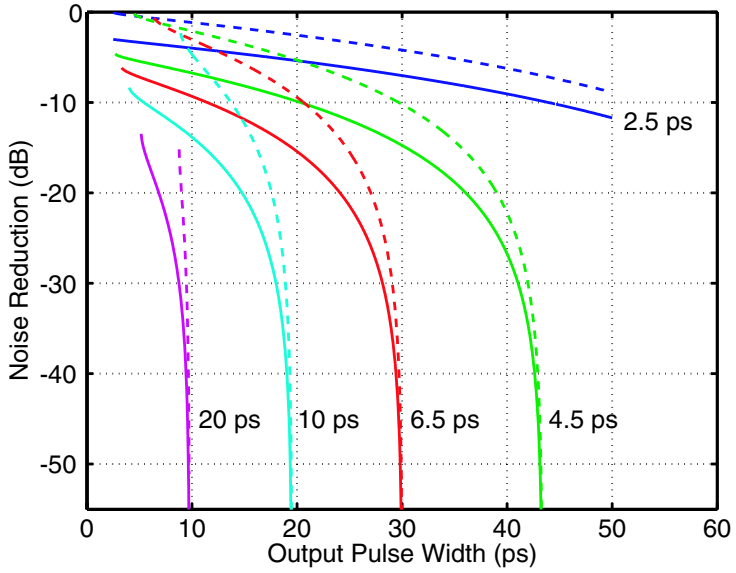

Figure 4-19: Noise reduction using a timing jitter eater plotted on a logarithmic scale.

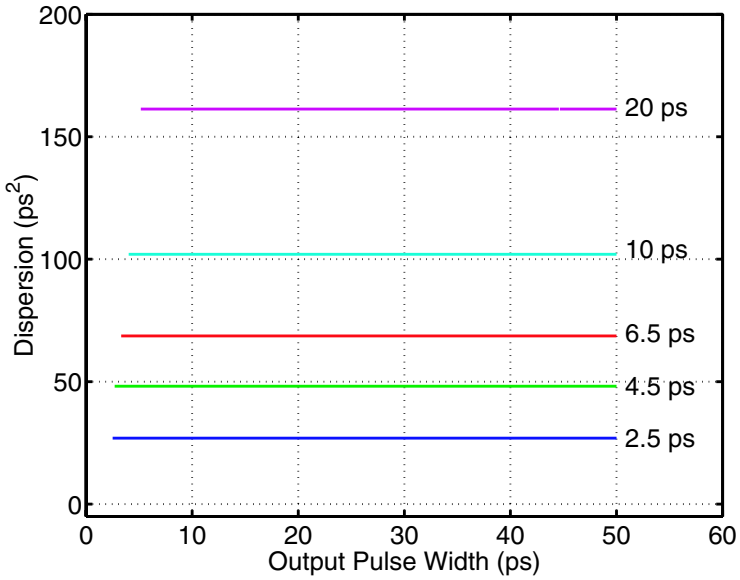

Figure 4-20: Necessary pre-chirp fiber dispersion corresponding to the solid lines in Fig. 4-18.

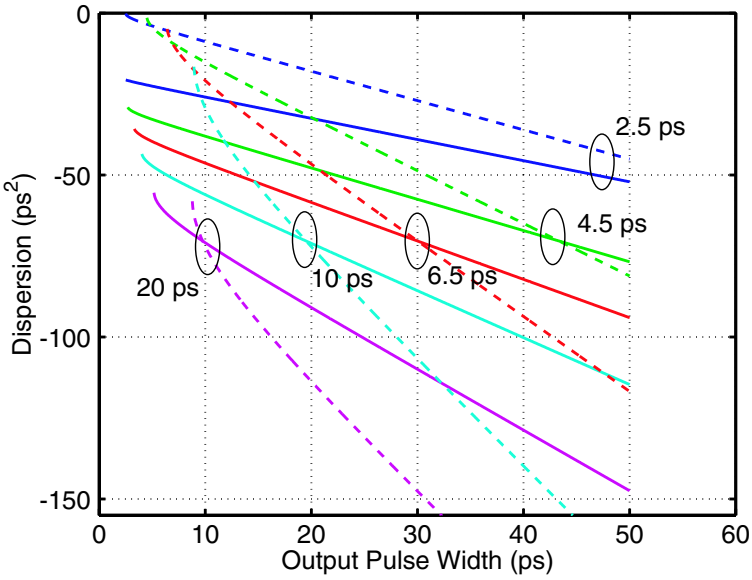

Figure 4-21: Necessary post-chirp fiber dispersion corresponding to Fig. 4-18.

T_0 (ps)	FWHM (ps)	erfc $\left(\frac{T_m}{2T_0}\right)$	N	2^{-N}
10	17	1.5×10^{-12}	39	1.5×10^{-12}
20	33	4.1×10^{-4}	11	4.1×10^{-4}
30	50	1.8×10^{-3}	5.8	1.8×10^{-3}
40	67	7.7×10^{-2}	3.7	7.7×10^{-2}
50	83	1.6×10^{-1}	2.7	1.6×10^{-1}

Table 4.1: Pulse width and bits of resolution.

Optical Sampling Applications

To avoid intersymbol interference (ISI) in optical sampling applications, the output pulse width must not become too large relative to its bit-slot time-interval. In fact, if the pulse energy is normalized to 1, the amount of energy that spills into the neighboring time-slot from both sides is[12] erfc $\left(\frac{T_m}{2T_0}\right)$, where T_m is the bit-slot time-interval and T_0 is the pulse width that is related to the optical intensity by $\frac{1}{\sqrt{\pi}}e^{-t^2/T_0^2}$. With a pulse width of T_0, ISI limits[13] the number of bits of resolution to $N < -\log_2\left[\text{erfc}\left(\frac{T_m}{2T_0}\right)\right]$. Table 4.1 shows the number of bits of resolution attainable with a given pulse width. The table shows that it is desirable to keep the output pulse widths (FWHM) under 33 ps.

Telecommunications Applications

To retain the receiver sensitivity improvement of 2 dB over NRZ, the pulse must be less than half the time-slot [71]. At 10 GHz, this implies that the pulse width should be less than 50 ps, which is a very lax requirement on the timing jitter eater apparatus.

[12] $\text{erfc}(x) = 1 - \text{erf}(x) = \frac{2}{\sqrt{\pi}T_0}\int_x^\infty e^{-t^2}dt$

[13] The amount of energy that spills into the neighboring slot should be less than the energy needed to move by one quantization level.

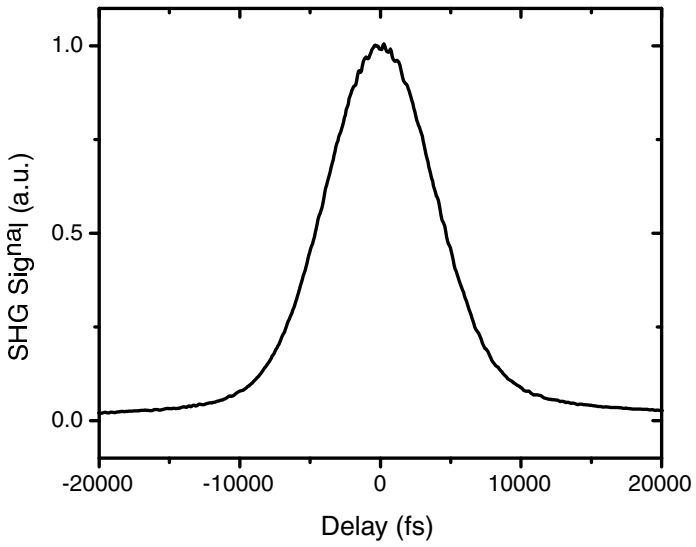

Figure 4-22: Autocorrelation of modelocked semiconductor laser output.

4.3.4 Experiments

The laser source used in our experiments is an external cavity semiconductor laser which is hybridly modelocked (see Fig. 2-11). The pulsewidth is 6.7 ps (intensity FWHM), the fundamental cavity repetition rate is 10 GHz, and the carrier wavelength is 1547 nm. The autocorrelations and optical spectrum are shown in Fig. 4-22 and Fig. 4-23, respectively. The optical spectrum has a 3-dB width of 0.72 nm.

The laser contains a saturable absorber and gain section integrated on a single chip. The saturable absorber was biased at -1.5 V and modulated at 10 GHz with 11 dBm of RF power. The gain section was driven with a DC current source at 65 mA. The laser cavity contained an optical bandpass filter with a 3-dB width of 0.7 nm centered at 1547 nm.

The fiber coupled power is 0.5 mW and the output was subsequently amplified with an erbium-doped fiber amplifier (EDFA) to 5 mW.

Three experimental configurations were investigated:

1. No pre-chirp fiber, large modulation depth, and 10 km SMF-28 post-chirp fiber.

2. No pre-chirp fiber, small modulation depth, and 10 km SMF-28 post-chirp fiber.

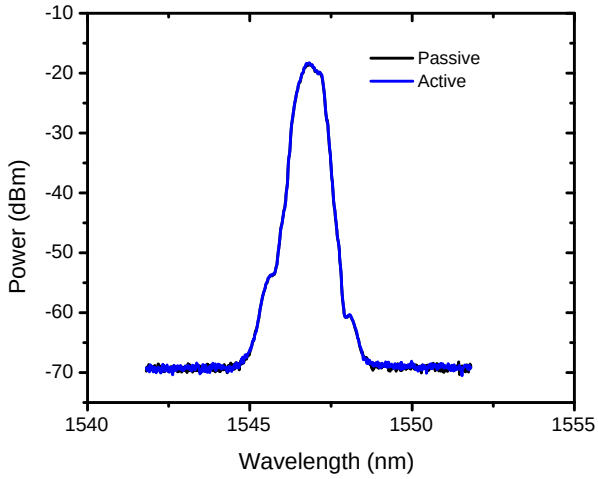

Figure 4-23: Optical spectrum of modelocked semiconductor laser.

3. No pre-chirp fiber, large modulation depth, and 4 km SMF-28 post-chirp fiber.

Configuration 1 represents the case where the phase modulation plus dispersion overcompensates the timing jitter. The rf spectrum analyzer measurements of the signal with and without phase modulation are shown in Fig. 4-24. The plot shows a 6 dB reduction of the phase noise at a 720 kHz offset.[14] The peak amplitude of the rf spectrum increases when the phase modulator is turned on since it results in decreased output pulse width and hence more spectral energy at 10 GHz.

The modulation strength was subsequently reduced to prevent overcompensation, and this setting corresponds to configuration 2. The rf spectrum analyzer measurements are shown in Fig. 4-25.[15] The plot shows improved performance with a 10.9 dB reduction of the phase noise at a 1 MHz offset.[16]

[14]Best results occur when fine microwave delay line that connects to the phase modulator is set at 294.5 degreeds. When the fine delay line is set at 104.5 and 134 degrees, the noise reduction is 44 and 39 dB, respectively.

[15]Residual phase noise measurements are difficult with this system since the delay between the two arms to the mixer is several kilometers. This implies that the residual phase noise suppression would only be good for offsets less than several kilohertz. See Fig. 3-3 and corresponding section for more details.

[16]Best results occur when fine microwave delay line that connects to the phase modulator is set at 147.5 degreeds. When the fine delay line is set at 327.5 degrees, the noise reduction is 46.3 dB.

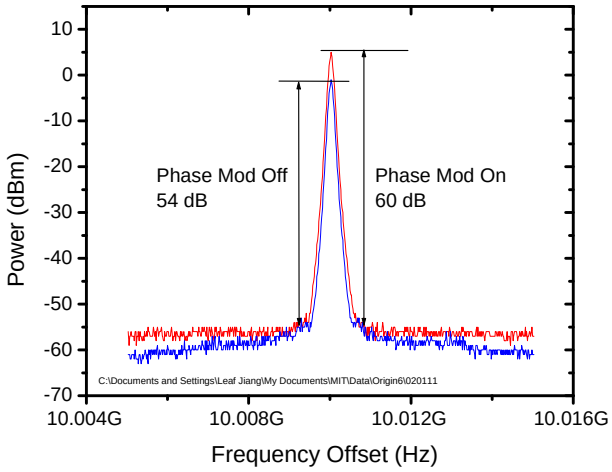

Figure 4-24: RF spectrum analyzer measurements of configuration 1.

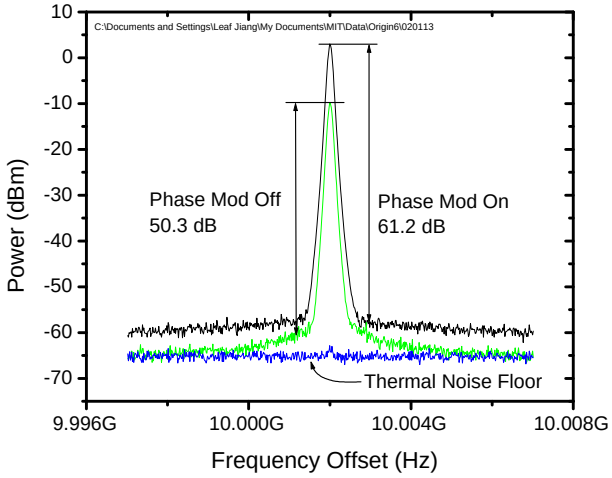

Figure 4-25: RF spectrum analyzer measurements of configuration 2.

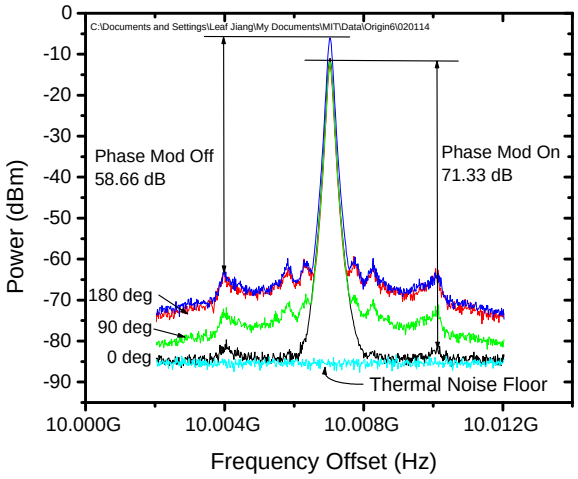

Figure 4-26: RF spectrum analyzer measurements of configuration 3.

Although configuration 2 shows good noise suppression, the output pulses are 90 ps in duration. To obtain shorter output pulses and still retain good noise suppression, we tried configuration 3. The post-chirp fiber length was shorted to 4 km and the modulation depth of the modulator was increased. The rf spectrum analyzer measurements of the output pulses are shown in Fig. 4-26. The plot shows 12.67 dB noise reduction at an offset of 2.984 MHz. The output pulse width was 45 ps.[17]

In summary, the noise reduction results of the three experimental configurations are shown in Table 4.2, which illustrates that the trends predicted by equation (4.15) are correct.

[17]Best results occur when fine microwave delay line that connects to the phase modulator is set at 0 degreeds. When the fine delay line is set at 90 and 180 degrees, the noise reduction is 61.5 and 51.44 dB, respectively.

Config.	M	$\mathcal{D}_2$ (ps^2)	R	R^2	Theoretical Noise Reduc. $10\log_{10}(R^2)$ (dB)	Experimental Noise Reduc. (dB)	Input Pulse Width (ps)	Output Pulse Width (ps)
1	1.9	-200	-0.50	0.25	6	6	6.7	90
2	0.9	-200	0.29	0.08	10.9	10.9	6.7	90
3	1.95	-100	0.23	0.05	12.67	12.67	6.7	45

Table 4.2: Noise reduction results.

4.3.5 Limitations

RF Oscillator Noise

The microwave oscillator driving the phase modulator has finite timing jitter or phase noise. Therefore, one can only squeeze down to the oscillator noise level. The oscillator used in our measurements was an HP83732B synthesizer with 300 fs integrated timing jitter from 10 Hz to 10 MHz. Sapphire fixed frequency oscillators exhibit good phase noise performance with integrated timing jitter of only 5.6 fs from 10 Hz to 10 MHz. See Fig. F-3 for the single-sideband phase noise plots of these oscillators.

It has been suggested that a potential limitation of the timing jitter eater is the broadband thermal noise due to the modulator. The output timing jitter from a modelocked laser typically follows a Lorentzian spectral shape. Noise at large offset frequencies are filtered by the transfer response of the laser cavity. For the timing jitter eater, potentially all the high frequency noise from the RF oscillator transfers to the optical signal via the phase modulator. It may seem possible that this can worsen the timing jitter at higher frequency offsets. This effect is pictorially illustrated in Fig. 4-27.

It is emphatically not true that thermal noise of the modulator worsens the timing

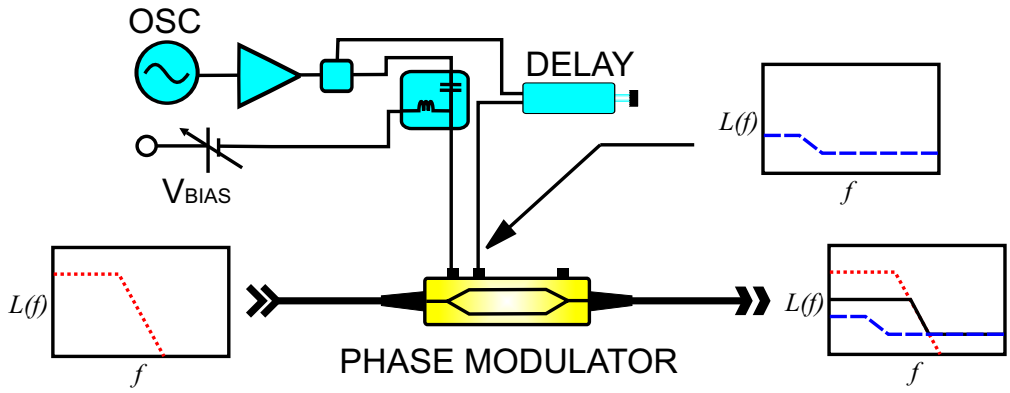

Figure 4-27: Noise at high frequency offsets can be worsened by the phase modulator.

jitter. The timing jitter due to thermal noise from the modulator is[18]

$$\Delta t_{th} = (M\omega_M \beta_2 L)\Delta\phi_{th}. \tag{4.35}$$

For typical values of $M = 3.6$, $\omega_M = 2\pi \times 10$ GHz, $\beta_2 L = 100$ ps^2, and $\Delta\phi_{th} = 6 \times 10^{-6}$ rad,[19] the rms jitter is a mere 0.14 fs.

Frequency-to-Timing Conversion

The linewidth of the laser operating in passive and active modelocking was characterized using a self-heterodyne technique. The laser output was split into two arms. One arm contained an AOM modulated at 40 MHz to impose a doppler shift on the light and the other arm contained 500 m of Corning LEAF fiber to decorrelate the phases. The two arms were then recombined on a photodiode and the current was observed on an electrical spectrum analyzer (ESA). The ESA reveals the convolution of the

[18] The phase of the modulator with thermal noise can be written as $\phi(t) = M\cos[\omega_M t + \phi_{th}(t)]$. The frequency chirp applied to the pulses, assuming that the pulses initially have no timing jitter, is $\omega(t) = d\phi/dt \approx M\omega_M\phi_{th}(t)$. The rms frequency shift is related to the rms phase shift due to thermal noise by $\Delta\omega = M\omega_M\Delta\phi_{th}$. The rms timing jitter from the thermal noise is $\Delta t_{th} = -\frac{L}{v_g^2}(-v_g^2\beta_2)M\omega_M\Delta\phi_{th}$.

[19] The maximum matched thermal noise power is kTB or -174 dBm. If noise is split equally between amplitude and phase fluctuations, then the thermal phase noise power is -177 dBm. Since the 10 GHz carrier power is 27 dBm, the double-sideband phase noise due to thermal noise is -204 dBc/Hz. The rms phase fluctuation is $\Delta\phi_{th} = \sqrt{10^{-204/10} \times 10^{10}} = 6 \times 10^{-6}$ rad.

linewidth with itself centered at 40 MHz, as shown in Fig. 4-28. Therefore, taking half the width of the observed spectrum yields the linewidth of the laser. The linewidth of the passively modelocked laser fits well to a Lorentzian, but the linewidth of the actively modelocked laser fits better to a Gaussian function. Frequency fluctuations cause a smearing of the Lorentzian linewidth and often results in a Gaussian-looking linewidth. The active modulation of the saturable absorber not only modulates the amplitude, but also modulates the phase as well since in semiconductor lasers, the gain and index are related to the modulated carrier density. This is presumably why the linewidth looks Gaussian. In any case, the resulting linewidth indicates the input frequency noise to our system, which is an important parameter for the design of a timing-jitter eater.

The results, shown in 4-28, indicate that the frequency noise bandwidth is less than 2 MHz. Using our experimental values in equation (4.24) indicates that this is a negligible effect. To double-check, we measured the phase noise of the laser and compared it to the phase noise after propagation through 2.2 km of fiber. The resulting phase noise plots in Fig. 4-29 show that the frequency-to-timing jitter conversion is indeed negligible after propagation through 2.2 km of SMF-28 fiber.

The value of $F = \Delta\omega_0/\Delta t_0$, in equation (4.24), can be derived for AM actively modelocked fiber lasers from the noise theory in appendix B. Dividing equation (B.118) by equation (B.117) yields

$$F = \sqrt{\frac{\sigma_{p,pc}^2}{\sigma_{t,pc}^2}} = \frac{1}{\tau^2}. \tag{4.36}$$

For pulses with a FWHM of 6.7 ps, $F = 6.2 \times 10^{22}$ s^{-2}. Experimentally, we find that for our semiconductor modelocked laser, $F = 2\pi \times 4 \times 10^6$ Hz/50 fs $= 5 \times 10^{20}$ s^{-2}. This number is two orders of magnitude smaller than the theoretical value.

Polarization Dependence

The phase modulator is polarization dependent. The input polarization must be adjusted to obtain maximum phase modulation depth. Rather than a lithium niobate

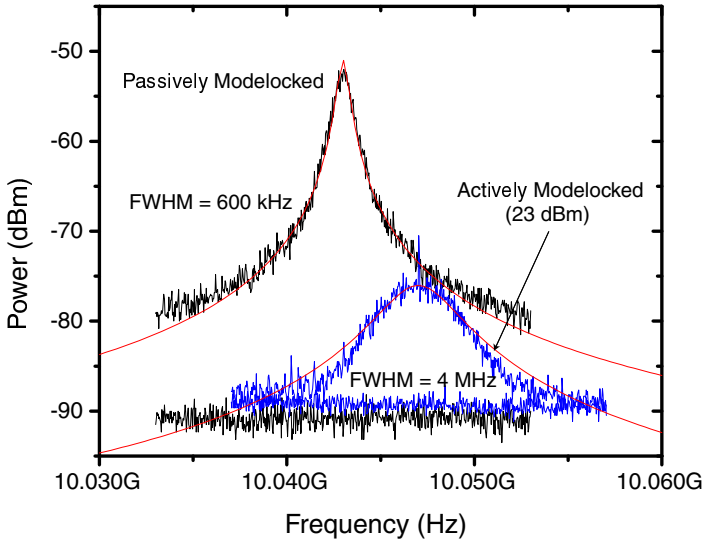

Figure 4-28: Linewidth of modelocked semiconductor laser.

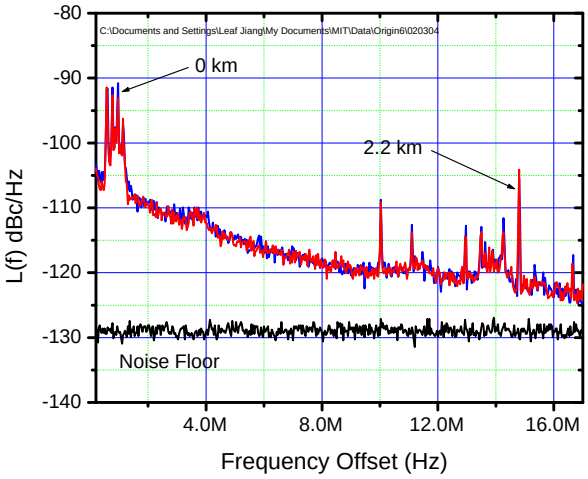

Figure 4-29: Absolute phase noise of modelocked semiconductor laser after propagation through 0 and 2.2 km of SMF-28 fiber. The two phase noise plots are almost indistinguishable.

modulator, a polarization insensitive electro-absorption modulator that exploits the Franz-Keldysh effect in an InGaAsP p-i-n ridge waveguide structure can be employed that results in both amplitude and phase modulation [72, 69]. The ridge width and active waveguide layer thicknesses can be tailored to minimize polarization dependent loss.

4.3.6 Conclusions

We have experimentally demonstrated that it is possible to reduce the timing jitter by 12 dB with a single phase modulator plus dispersive fiber. Dispersion is necessary for timing jitter reduction but has the undesired effect of broadening the output pulses. For example, our input pulses were broadened from 6.7 ps to 45 ps. Pulse width broadening can be mitigated by using longer pulses that have narrower spectra. For example, 4-19, shows that it is possible to obtain 10 ps pulse output with 20 ps input pulses. In addition, the dispersive pulse broadening of the post-chirp fiber can be reduced by using soliton pulses.

Chapter 5

Conclusion

5.1 Achievements

The salient points of this thesis are:

1. The noise of actively modelocked semiconductor lasers were measured accurately and compared to our noise theory. It was found that the actively modelocked noise theory does an excellent job in predicting actual modelocked laser noise performance. The phase noise was measured as a function of modulation depth, cavity length, cavity loss, modulation rate.

2. Optical cross-correlations were demonstrated to be a valuable tool for understanding the timing jitter correlations in high-repetition-rate modelocked lasers and for measuring the high frequency noise. A cross-correlator was designed and built that allowed arbitrary fiber length delays. The correlated jitter from pulse 1 to pulse N were measured and compared to theory for actively and passively modelocked semiconductor lasers. The cross-correlation technique was shown to be useful for measuring the timing jitter in a recirculating loop experiment and for predicting the probability density function of the timing jitter.

3. The applicability and limitations of phase noise measurements and optical cross-correlations were investigated. It was discovered why residual noise measurements depended on the noise of the oscillator. The region of validity for residual

phase noise measurements and resolution of optical cross-correlations on pulse width were determined.

4. A model for noise of harmonically modelocked lasers was developed and subsequently verified with cross-correlation and residual phase noise measurements. The model revealed how to correctly interpret the rf phase noise measurements and how the supermodes relate to the laser noise.

5. A method to measure the noise in harmonically modelocked lasers and isolate the amplitude and timing jitter contributions with finite-bandwidth detection electronics was discovered. This method allows one to measure the amplitude and timing jitter of a 10 GHz modelocked laser with a detector and spectrum analyzer with only 10 GHz of bandwidth.

6. Quantum-limited noise performance of a modelocked semiconductor laser was demonstrated. The cavity design was critical and the theory showed how to scale laser parameters to achieve low noise performance. It is currently the record for the quietest semiconductor laser performance (best absolute phase noise).

7. Several salient features of the noise theory were identified: the difficulty of obtaining short pulses and low noise, region of validity for residual phase noise measurements, and the rms jitter as a function of laser cavity parameters.

8. The noise of an actively modelocked laser was reduced with photon seeding. The noise of the laser decreased without penalty to the width of the pulses.

9. Novel electronic feedback techniques were employed to further reduce the noise of our actively modelocked lasers. It was the first time that someone used a feedback path to the saturable absorber and an external SOA.

10. A timing jitter eater, consisting of a phase modulator and dispersive fiber, was demonstrated to reduce the phase noise spectrum by over 20 dB.

11. New algorithms were developed to characterize the amplitude and phase profiles of an optical pulse. Combining the algorithms with optical cross-correlations, we were able to reconstruct the timing jitter probability density functions. In addition, a new SOA sampling technique using gain saturation was invented.

5.2 Future Research

Now that we have a better understanding of noise in modelocked lasers and that we can measure the noise accurately, the next step is to find ways to reduce the noise of these lasers even further. The following list are good projects for future research

- Build a timing jitter eater using solitons. Solitons do not have the problem of pulse broadening. Therefore, better timing jitter reduction for a given output pulse width should be possible with solitons. The limitation is given by the input frequency noise and the noise of the rf oscillator that drives the phase modulator.

- Build a feedback loop to lock the noise of a semiconductor or fiber modelocked laser to a quiet sapphire crystal oscillator. The feedback might be done through a fast phase shifter to the rf drive port. This could potentially bring the timing jitter down from 50 fs to 5 fs (10 Hz to 10 MHz).

- Investigate the noise of other optical pulse sources: (1) modulation of a cw signal followed by amplification and dispersion decreasing fiber (DDF), (2) beating of two cw signals followed by amplification and DDF. These sources can be followed by a nonlinear optical loop mirror, which cleans up the energy between pulses.

- In an Erbium-doped fiber laser, it is difficult to reduce the dispersion of the cavity to reduce the timing jitter. In this case, it would be beneficial to place the amplitude modulator where the pulse is the broadest. This would increase the effective modulation depth and decrease the timing jitter of the laser. The pulse is broadest when it is chirped, and therefore, amplitude modulation would

also have the additional effect of filtering by removing pulse tails that contain the reddest and bluest parts of its optical spectrum.

- Investigate and minimize the noise at low frequency offsets for optical clock applications.

- Increase the modulation curvature driving the modelocked laser. Since the noise of the Poseidon Shoebox oscillator is lower than that of the laser, one can use frequency doublers to increase the modulation curvature and decrease the noise of the laser.

- The timing jitter of the laser decreases for higher pulse powers. This implies that it would be interesting to look into designing semiconductor or fiber lasers that have high output powers.

Appendix A

Derivation of Master Equation

The master equation describes the evolution of the electric-field in the cavity. It is a time-domain analysis that considers a circulating pulse that is acted upon by lumped elements: gain, GVD, optical filtering, amplitude modulation, phase modulation, saturable absorption, Kerr nonlinearity, etc. This model was originated by Haus [73, 74, 75], but here we carefully go through the derivation to show the correspondence to physical parameters and outline the range of practical values.

The lumped element model is valid as long as the effects of each element are small. The round-trip model for the modelocked laser is shown in Fig. A-1. The following sections will address propagation through each element. The elements considered in our model are

1. Amplitude and phase modulation
2. GVD
3. Gain
4. Loss
5. Saturable absorption
6. Kerr nonlinearity

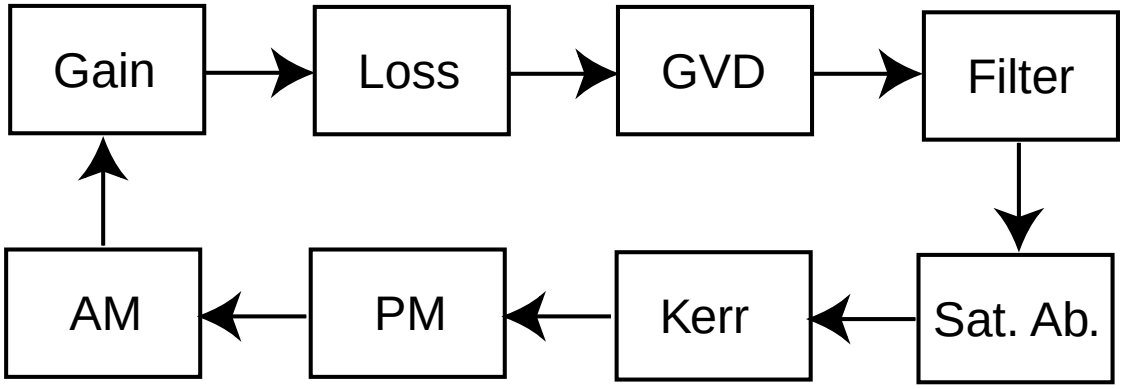

Figure A-1: The round-trip lumped element model of a modelocked laser.

The electric-field is denoted by $a(t)$ and is normalized so that its integral over time equals the pulse energy,

$$w_0 = \int_{-\infty}^{\infty} |a(t)|^2 dt. \tag{A.1}$$

Therefore $a(t)$ has units of $\sqrt{\text{power}} = \sqrt{\text{energy/time}}$.

We want to find $\hat{O}$ so that $a_{out}(t) = a_{in}(t)\exp(\hat{O}(t))$ for each lumped element enumerated above. Reason:

$$\begin{aligned} a_{n+1}(t) &= \exp[\hat{O}_1(t) + \hat{O}_2(t) + \hat{O}_3(t)]a_n(t) + S_n(t) \\ &= \exp[\hat{O}(t)]a_n(t) + S_n(t) \end{aligned} \tag{A.2}$$

where $\hat{O}(t)$ is equal to $\hat{O}_1(t) + \hat{O}_2(t) + \hat{O}_3(t)$ and n is the number of round-trips the pulse propagated in the cavity. The quantity $S_n(t)$ is the noise added to the electric-field per round-trip that can be from spontaneous emission, cavity length fluctuations, and noise from the current and voltage supplies. Subtracting $a_n(t)$ from both sides of equation A.2 yields

$$\begin{aligned} a_{n+1}(t) - a_n(t) &= \left[\exp(\hat{O}(t)) - 1\right] a_n(t) + S_n(t) \\ &\approx \hat{O}(t)a_n(t) + S_n(t) \end{aligned} \tag{A.3}$$

where the approximation $\exp(\hat{O}(t)) \approx 1 + \hat{O}(t)$ was used and is valid only when $-1 \ll \hat{O}(t) \ll 1$. The discrete equation of motion, equation A.3, can be converted into a continuous time equation by using the general relation

$$f(x + \Delta x) - f(x) \approx \Delta x \frac{\partial f}{\partial x} \tag{A.4}$$

for the electric-field. This relation implies that

$$a_{n+1}(t) - a_n(t) \approx T_R \frac{\partial a(t,T)}{\partial T}, \tag{A.5}$$

where $n = T/T_R$. Substituting equation A.5 in equation A.3 and making the substitutions $a_n(t) \rightarrow a(t,T)$ and $S_n(t) \rightarrow S(t,T)$, equation A.3 becomes

$$T_R \frac{\partial a(t,T)}{\partial T} \approx \hat{O}(t) a(t,T) + S(t,T). \tag{A.6}$$

To agree with the notation in Haus and Mecozzi's paper [10], we rescale the noise so that $S(t,T) \rightarrow T_R S(t,T)$ and equation A.6 becomes

$$T_R \frac{\partial a(t,T)}{\partial T} = \hat{O}(t) a(t,T) + T_R S(t,T). \tag{A.7}$$

where the approximation sign was changed to an equal sign for notational convenience. The electric-field $a(t,T)$ has the units of $\sqrt{\text{Power}}$ and the Haus-Mecozzi $S(t,T)$ has the units of $\sqrt{\text{Power}}$/time.

The operator $\hat{O}(t)$ in equation A.7 represents the sum of the effects of amplitude modulation, phase modulation, gain, loss, GVD, Kerr nonlinearity, and saturable absorption per round-trip:

$$\hat{O}(t) = \hat{O}_{gain}(t) + \hat{O}_{loss}(t) + \hat{O}_{GVD}(t) + \hat{O}_{AM}(t) + \hat{O}_{PM}(t) + \hat{O}_{Kerr}(t) + \hat{O}_{SA}(t). \tag{A.8}$$

The following sections will show that

$$\hat{O}_{gain}(t) = g\left(1+\frac{1}{\Omega_g^2}\frac{\partial^2}{\partial t^2}\right) \quad (A.9)$$

$$\hat{O}_{L,mirror}(t) = \frac{\ln R_1 + \ln R_2}{2} \quad (A.10)$$

$$\hat{O}_{L,material}(t) = -\alpha_i L \quad (A.11)$$

$$\hat{O}_{GVD}(t) = jD\frac{\partial^2}{\partial t^2} \quad (A.12)$$

$$\hat{O}_{filter}(t) = \frac{1}{\Omega_f^2}\frac{\partial^2}{\partial t^2} \quad (A.13)$$

$$\hat{O}_{L,filter} = 1+\ln(1/2) \approx 0.3068528 \quad (A.14)$$

$$\hat{O}_{AM}(t) = \frac{M_{AM}}{2}(1-\cos(\omega_M t)) \approx \frac{M_{AM}\omega_M^2 t^2}{4} \quad (A.15)$$

$$\hat{O}_{L,AM}(t) = \ln\left[\sqrt{\frac{1}{2}+M_{AM}}\right] \quad (A.16)$$

$$\hat{O}_{PM}(t) = j\frac{M_{PM}}{2}(1-\cos(\omega_M t)) \approx j\frac{M_{PM}\omega_M^2 t^2}{4} \quad (A.17)$$

$$\hat{O}_{Kerr}(t) = -j\delta|a(t)|^2 \quad (A.18)$$

$$\hat{O}_{L,SA,slow} = -\frac{L_A}{2} \quad (A.19)$$

$$\hat{O}_{SA,slow} = -\frac{L_A w(t)}{2w_A} \quad (A.20)$$

$$\hat{O}_{L,SA,fast} = -\frac{L_A}{2} \quad (A.21)$$

$$\hat{O}_{SA,fast} = \gamma|a(t)|^2, \quad (A.22)$$

where the total loss is

$$\begin{aligned}\hat{O}_{loss}(t) &= \hat{O}_{L,filter}(t)+\hat{O}_{L,AM}(t)+\hat{O}_{L,SA}(t)+\hat{O}_{L,mirror}(t)+\hat{O}_{L,material}(t)\\ &\equiv -l. \end{aligned} \quad (A.23)$$

Typically l = -0.307 (filter) + 0.607 (mirror) + 0.650 (material) + (0.2554 to -0.4229) (AM, M_{AM} = 0.1 to 1.83) + (0.345 to 0.460) (Fast SA) = 0.8721 to 1.6554.

Substituting equations A.8, A.22 and A.23 into equation A.7 gives the more fa-

miliar form for the master equation (assuming a fast saturable absorber)

$$\begin{aligned} T_R\frac{\partial a(t,T)}{\partial T} &= \left\{-l+g\left(1+\frac{1}{\Omega_g^2}\frac{\partial^2}{\partial t^2}\right)\right. \\ &\quad +\frac{1}{\Omega_f^2}\frac{\partial^2}{\partial t^2}+jD\frac{\partial^2}{\partial t^2} \\ &\quad -\frac{M_{AM}+jM_{PM}}{2}\left[1-\cos(\omega_M t)\right] \\ &\quad \left.+(\gamma-j\delta)|a(t,T)|^2\right\}a(t,T)+T_R S(t,T). \end{aligned} \tag{A.24}$$

The cosinusoidal terms in equation A.24 can be approximated by expanding them to second order. The master equation is now

$$\begin{aligned} T_R\frac{\partial a(t,T)}{\partial T} &= \left\{-l+g\left(1+\frac{1}{\Omega_g^2}\frac{\partial^2}{\partial t^2}\right)\right. \\ &\quad +\frac{1}{\Omega_f^2}\frac{\partial^2}{\partial t^2}+jD\frac{\partial^2}{\partial t^2} \\ &\quad -\frac{M_{AM}+jM_{PM}}{4}(\omega_M t)^2 \\ &\quad \left.+(\gamma-j\delta)|a(t,T)|^2\right\}a(t,T)+T_R S(t,T). \end{aligned} \tag{A.25}$$

A.1 Propagation Through an Amplitude Modulator

A Mach-Zehnder modulator biased for "push-pull" operation has opposite phase shifts in the upper and lower arms as shown in Fig. A-2. "Push-pull" operation allows for pure amplitude modulation without residual phase modulation. The output power is related to the input power by

$$\begin{aligned} P_{out} &= \left|\frac{1}{2}\exp\left(j\frac{V/2}{V_\pi}\pi\right)+\frac{1}{2}\exp\left(j\frac{-V/2}{V_\pi}\pi\right)\right|^2 P_{in} \\ &= \cos^2\left(\frac{V/2}{V_\pi}\pi\right)P_{in} \\ &= \frac{1}{2}\left[1+\cos\left(\frac{V}{V_\pi}\pi\right)\right]P_{in}. \end{aligned} \tag{A.26}$$

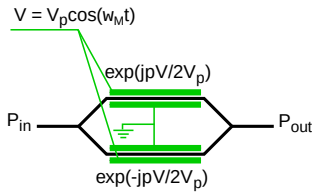

Figure A-2: Mach-Zehnder modulator.

The voltage V is the voltage applied between the upper and lower arm of the modulator. The voltage required to move the device from "maximum on" to "maximum off" is V_π. Setting the DC bias to half transmission, $V \rightarrow V - V_\pi/2$, see Fig. A-3, leads to the appropriate input-output relation for amplitude modulation:

$$P_{out} = \frac{1}{2}\left[1 - \sin\left(\frac{V}{V_\pi}\pi\right)\right] P_{in}. \tag{A.27}$$

For an applied microwave signal of angular frequency ω_M, the voltage is

$$V = V_p \cos(\omega_M t) \tag{A.28}$$

where the average microwave power into 50 Ω is

$$\begin{aligned} P_{dBm} &= 10\log_{10}\left(\frac{V_{rms}^2}{10^{-3}R}\right) \\ &= 10\log_{10}\left(\frac{V_p^2}{2\times 10^{-3}R}\right) \\ &= 20\log_{10} V_p + 10. \end{aligned} \tag{A.29}$$

Table A.1 shows the peak voltage for a given average power. The internal 50 Ω termination resistor inside the modulator is typically 1/4 or 1/2 Watt (corresponding to 24 or 27 dBm, respectively). The maximum peak voltage allowed in our EO Space phase modulator is 10 V which corresponds to an average power of 30 dBm.

P_{dBm}	V_p	P_{dBm}	V_p
4 dBm	0.50 V	26 dBm	6.31 V
10 dBm	1.00 V	27 dBm	7.08 V
16 dBm	2.00 V	28 dBm	7.94 V
20 dBm	3.16 V	29 dBm	8.91 V
22 dBm	3.98 V	30 dBm	10.00 V
23 dBm	4.47 V	31 dBm	11.22 V
24 dBm	5.01 V	32 dBm	12.59 V
25 dBm	5.62 V	34 dBm	15.85 V

Table A.1: Table of average power and peak voltage.

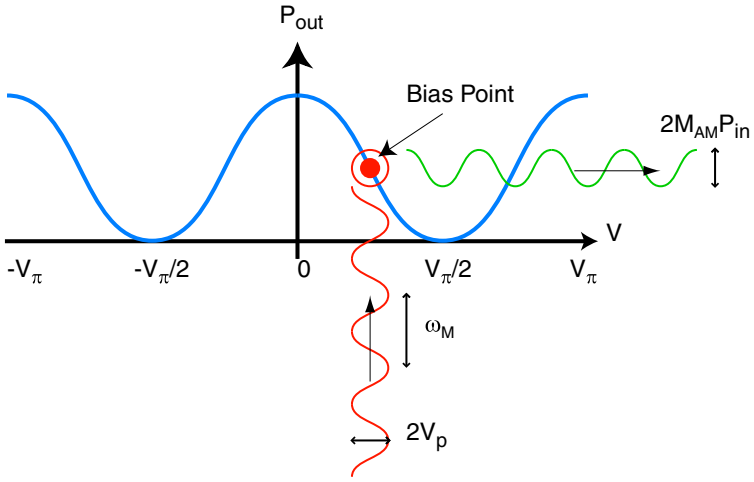

Figure A-3: Bias of Mach-Zehnder modulator for amplitude modulation.

Substituting equation A.28 into equation A.27 yields

$$\begin{aligned} P_{out} &= \frac{1}{2}\left[1-\sin\left(\frac{\pi V_p\cos(\omega_M t)}{V_\pi}\right)\right]P_{in} \\ &\approx \frac{1}{2}\left[1-\frac{\pi V_p\cos(\omega_M t)}{V_\pi}\right]P_{in} \\ &= \frac{1}{2}\left[1-2M_{AM}\cos(\omega_M t)\right]P_{in} \\ &= -\left[\frac{1}{2}+M_{AM}\right]P_{in}\times\left[1+M_{AM}(1-\cos(\omega_M t))\right]P_{in} \\ &\approx \exp\left\{\ln\left[-\left(\frac{1}{2}+M_{AM}\right)\right]\right\}P_{in}\times\exp\left[M_{AM}(1-\cos(\omega_M t))\right]P_{in} \end{aligned} \quad (A.30)$$

where the small angle approximation for sin was used, and

$$M_{AM}=\frac{V_p}{2V_\pi}\pi. \quad (A.31)$$

The factor of 2 in the denominator is a bit strange, but we keep this for consistency with the notation in the literature. The electric-field is equal to the square-root of equation A.30

$$\begin{aligned} a_{out} &= \exp\left\{\frac{1}{2}\ln\left[-\left(\frac{1}{2}+M_{AM}\right)\right]\right\}a_{in}\times\exp\left[\frac{1}{2}M_{AM}(1-\cos(\omega_M t))\right]a_{in} \\ &= \exp\left\{\frac{1}{2}\ln\left[\frac{1}{2}+M_{AM}\right]+\frac{1}{2}\ln(-1)\right\}a_{in}\times\exp\left[\frac{M_{AM}}{2}(1-\cos(\omega_M t))\right]a_{in} \\ &= \exp\left\{\ln\left[\sqrt{\frac{1}{2}+M_{AM}}\right]+\frac{j\pi}{2}\right\}a_{in}\times\exp\left[\frac{M_{AM}}{2}(1-\cos(\omega_M t))\right]a_{in} \\ &= \exp\left[\hat{O}_{L,AM}(t)\right]a_{in}\times\exp\left[\hat{O}_{AM}(t)\right]a_{in} \end{aligned} \quad (A.32)$$

where the constant phase factor $j\pi/2$ was removed,

$$\boxed{\hat{O}_{L,AM}(t)=\ln\left[\sqrt{\frac{1}{2}+M_{AM}}\right]} \quad (A.33)$$

is the lumped element operator for the inherent loss of the amplitude modulator, and

$$\boxed{\hat{O}_{AM}(t)=\frac{M_{AM}}{2}(1-\cos(\omega_M t))} \quad (A.34)$$

is the lumped element operator for the pulse carving effect of the amplitude modulator. Equation A.32 has the same form as equation A.2, which allows us to identify the lumped element operators for the amplitude modulator.

Typical values for V_π for lithium niobate at 10 GHz are 6 V (EO Space) and 11 V (JDS-Uniphase). Maximum applied average power to an internally terminated modulator is usually 27 dBm or equivalently $V_p = 7$ V. Typical values for M_{AM} range from 0 to 1 ($V_p = 7$ V, $V_\pi = 11$ V) to 1.83 ($V_p = 7$ V, $V_\pi = 6$ V). The corresponding values for the lumped-element loss due to the modulator are $\hat{O}_{L,AM} = -0.3466, 0.2027,$ and 0.4229.

A.2 Propagation Through a Phase Modulator

The phase shift applied to an electric signal is

$$a_{out} = \exp\left[j\frac{V}{V_\pi}\pi\right] a_{in} \tag{A.35}$$

For a phase modulator, V_π is defined as the applied voltage required to change the delay of the phase modulator by one-half an optical cycle. This parameter is normally measured at a low frequency and is frequency dependent. Appendix E describes how we measure V_π of our phase modulators. If the applied voltage is sinusoidal according to equation A.28, then equation A.35 can be written as

$$a_{out} = \exp\left[j\frac{M_{PM}}{2}\cos(\omega_M t)\right] a_{in} \tag{A.36}$$

where

$$M_{PM} = \frac{V_p}{V\pi}2\pi. \tag{A.37}$$

Notice that the definition of M_{PM} differs from the definition of M_{AM} by a factor of 4, see equations A.31 and A.37. We can adjust the DC offset to the phase modulator (we add the constant phase of $M_{PM}/2$ to the argument of the exponential) and phase

delay the co-sinusoidal modulation ($\omega_M t \rightarrow \omega_M t - \pi$) so that equation A.36 becomes

$$a_{out} = \exp\left[j\frac{M_{PM}}{2}(1-\cos(\omega_M t))\right] a_{in} \tag{A.38}$$

Comparing equation A.2 and equation A.38, the lumped element operator for propagation through a phase modulator is

$$\boxed{\hat{O}_{PM}(t) = j\frac{M_{PM}}{2}(1-\cos(\omega_M t)).} \tag{A.39}$$

Typical values for M_{PM} range from 0 to 4 ($V_p = 7$ V, $V_\pi = 11$ V) to 7.33 ($V_p = 7$ V, $V_\pi = 6$ V).

A.3 Propagation Through the Loss Section

The circulating cavity pulse experiences loss from the material loss of semiconductor, mirrors, coupling loss to and from the semiconductor chip to the external cavity, and insertion loss of optical bandpass filter.

The output electric-field relates to the input electric-field according to

$$a_{out}(t) = \exp(-l) a_{in}(t). \tag{A.40}$$

Hence, comparing equation A.40 to equation A.2, we find that the lumped element operator for the total cavity loss is

$$\hat{O}_{loss} = -l. \tag{A.41}$$

The total loss is from the amplitude modulator (equation A.33), the optical bandpass filter (equation A.54), the saturable absorber (equation A.63 and A.71), the mirrors, and intrinsic material loss.

Fig. A-4 shows a typical laser cavity with left and right mirror reflectivities of R_1 and R_2. In addition, there is a lossy element of length L inside the cavity. The optical

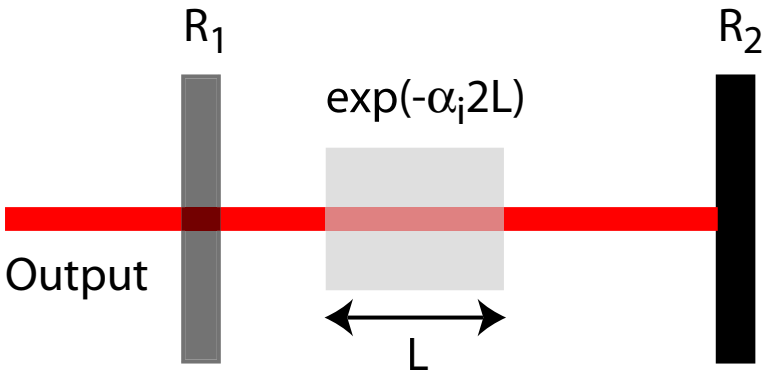

Figure A-4: Cavity loss due to mirrors and intrinsic loss of gain medium.

power after one round-trip is decreased by the loss elements according to

$$P_{out}(t) = R_1 R_2 \exp(-\alpha_i 2L) P_{in}(t), \tag{A.42}$$

The lumped-element operator associated with the mirror loss is

$$\hat{O}_{L,mirror} = \frac{\ln R_1 + \ln R_2}{2}. \tag{A.43}$$

The NEC EC-MLLD has mirror reflectivities of $R_1 = 0.30$ and $R_2 = 0.99$, and its corresponding lumped-element operator is $\hat{O}_{L,mirror} = -0.60701157$.

The lumped-element operator associated with the intrinsic material loss is

$$\hat{O}_{L,material} = -\alpha_i L \tag{A.44}$$

where α_i is the material loss, and L is the length of the loss element. The NEC MLLD parameters[1] are $\alpha_i = 13$ cm^{-1} and $L = 500\mu$m. For these parameters, $\hat{O}_{L,material} = -0.65$.

[1]Loss[dB/cm] = 4.34294482 α_i[1/cm] $\times L$[cm] or equivalently, α_i[1/cm] $\times L$[cm] = 0.2302585 Loss[dB/cm]. Therefore, 10 dB/cm translates into $\alpha_i = 2.3$ cm^{-1} and 56.42 dB/cm translates into $\alpha_i = 13$ cm^{-1}.

A.4 Propagation Through the Gain Section

The laser gain is assumed to have a Lorentzian shape, so that the input and output optical powers are related by

$$\begin{aligned}\tilde{P}_{out}(\Omega) &= \exp\left[\frac{2g}{1+\left(\frac{\Omega}{\Omega_g}\right)^2}\right]\tilde{P}_{in}(\Omega) \\ &= \exp\left[\frac{g}{1+j\frac{\Omega}{\Omega_g}}+\frac{g}{1-j\frac{\Omega}{\Omega_g}}\right]\tilde{P}_{in}\end{aligned} \tag{A.45}$$

where $\Omega = 0$ is the center angular frequency of the pulse and the Lorentzian gain spectrum, and Ω_g is the half-width at half-maximum (HWHM) of the gain spectrum. For a round-trip gain of 15 dB (the single-pass gain is 15 dB but is saturated after the pulse goes through the gain medium once, see Appendix G), $g = 1.7269$. Table A.2 shows the g's for a given round-trip gain. The optical power is related to the normalized electric-field by

$$\tilde{P}(\Omega) = T_R\tilde{a}(\Omega)\tilde{a}^*(\Omega). \tag{A.46}$$

Using equation A.46 in equation A.45, we find that

$$\tilde{a}_{out}(\Omega) = \exp\left[\frac{g}{1+j\frac{\Omega}{\Omega_g}}\right]\tilde{a}_{in}(\Omega). \tag{A.47}$$

For semiconductor and erbium fiber lasers, the laser medium linewidth is usually larger than the inverse pulsewidths, i.e. $\Omega/\Omega_g \ll 1$. For this case, the exponent can be expanded to second-order, $1/(1+x) \approx 1 - x + x^2$, so that equation A.47 can be approximated as

$$\tilde{a}_{out}(\Omega) = \exp\left[g\left(1 - j\frac{\Omega}{\Omega_g} - \left(\frac{\Omega}{\Omega_g}\right)^2\right)\right]\tilde{a}_{in}(\Omega). \tag{A.48}$$

Notice that we are multiplying $\tilde{a}_in(\Omega)$ by $\exp(-j\Omega g/\Omega_g)$ which is just a constant delay in the time domain. It is equal to the propagation time through the gain

Round-trip Gain (dB)	g
5	0.5756
10	1.1513
15	1.7269
20	2.3026
25	2.8782
30	3.4539

Table A.2: The relation between g and the round-trip gain in units of dB.

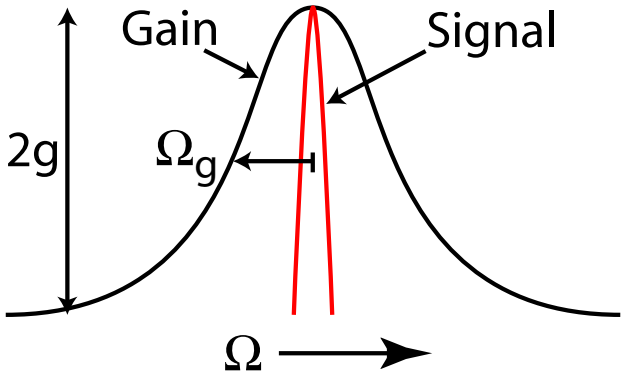

Figure A-5: Gain filtering of the optical spectrum. The gain bandwidth is assumed to have a Lorentzian shape and much wider than the signal spectrum.

medium. Hence, we can conveniently ignore this term. If we inverse Fourier transform equation A.48, use the Fourier transform relations $-j\Omega \rightarrow \partial/\partial t$ and $-\Omega^2 \rightarrow \partial^2/\partial t^2$, and ignore the constant time delay term, we obtain

$$a_{out}(t) = \exp\left[g\left(1 + \frac{1}{\Omega_g^2}\frac{\partial^2}{\partial t^2}\right)\right] a_{in}(t). \tag{A.49}$$

Comparing equation A.49 to equation A.2, it is apparent that

$$\boxed{\hat{O}_{gain} = g\left(1 + \frac{1}{\Omega_g^2}\frac{\partial^2}{\partial t^2}\right).} \tag{A.50}$$

A.5 Propagation Through Optical Bandpass Filter

The effect of the optical bandpass filter is exactly the same as gain filtering. Fig. A-6 shows the filter and signal power spectrum. The lumped element operator for propagation through the optical bandpass filter can be obtained by replacing Ω_g with Ω_f and $2g$ with 2 in equation A.50

$$\boxed{\hat{O}_{filter} = \left(1 + \frac{1}{\Omega_f^2}\frac{\partial^2}{\partial t^2}\right).} \tag{A.51}$$

The weird normalization so that the output power is equal to twice the input power at the center of the filter is to keep consistent notation with [10]. Therefore, we need to add a lumped loss operator so that the input and output powers are equal at the center of the optical filter. The following operator provides a reduces the optical power by a factor of two:

$$\boxed{\hat{O}_{L,filter} = \ln(1/2) \approx -0.693147.} \tag{A.52}$$

For convenience, we move the constant term from the lumped-element operator in equation A.51 to the lumped-element operator in equation A.52 so that the new operators are

$$\boxed{\hat{O}_{filter} = \frac{1}{\Omega_f^2}\frac{\partial^2}{\partial t^2}.} \tag{A.53}$$

and

$$\boxed{\hat{O}_{L,filter} = 1 + \ln(1/2) \approx 0.3068528.} \tag{A.54}$$

Therefore, the "loss" operator $\hat{O}_{L,filter}$ is really a gain operator since it is a positive value.

According to the device parameters for the NEC MLLDs, whose parameters are listed in Appendix G, the FWHM gain bandwidth is 50-60 nm. This is much larger than the bandwidth of the optical bandpass filters (typically 0.7 or 5 nm), and therefore, we can ignore the gain filtering terms and keep the optical filtering terms.

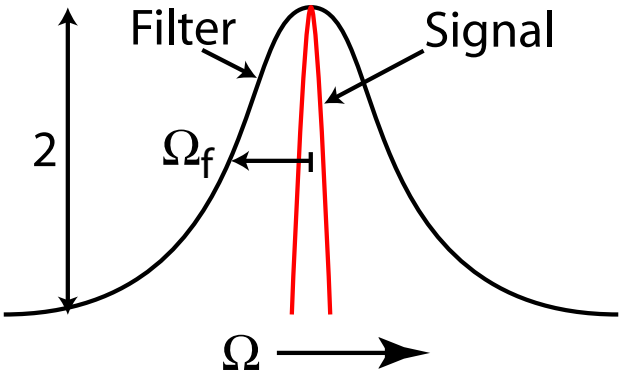

Figure A-6: Spectrum of Lorentzian optical bandpass filter and the pulse spectrum. The pulse spectrum is much narrower than the filter bandwidth.

A.6 Propagation Through the Saturable Absorber

A saturable absorber is an intensity dependent medium that passes high powers more easily than low powers. This thresholding of the optical signal selects for pulsed operation in the laser cavity. A saturable absorber can be created by a reversed biased diode in the case of a semiconductor laser [76] or highly engineered quantum well dielectric stack mirror for fiber lasers [34, 77].

A closed form solution for the theory of fast and slow saturable absorbers in modelocked lasers was discovered by Haus in 1975 [75, 74]. The theory begins by writing an equation that describes the evolution of the carrier population in the saturable absorber,

$$\frac{\partial n}{\partial t} = -\frac{n - n_e}{T_A} - \frac{2\sigma_A}{A_A}\frac{|a(t)|^2}{\hbar\omega_0}n \tag{A.55}$$

where $n = n_l - n_u$ is the difference between the lower and upper levels, T_A is the relaxation time of the saturable absorber, $|a(t)|^2$ is the energy of the pulse, T_R is the round-trip time of the cavity, σ_A is the optical cross-section of the absorbing particles, and A_A is the beam cross-section in the saturable absorber. Here it was assumed that the saturable absorber behaves like a two-level system with equal relaxation times of the upper and lower levels. If the saturable absorber behaved like a three-level systems with a fast relaxation of the upper level (as in Erbium fiber), the $2\sigma_A$ would have to

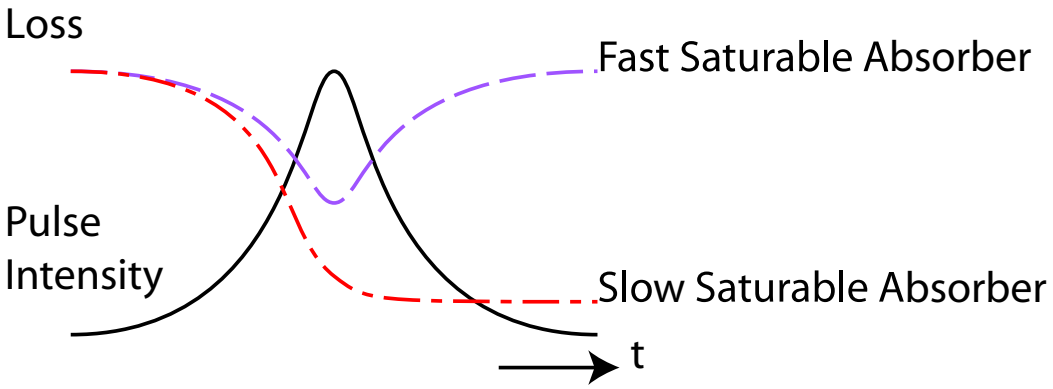

Figure A-7: Loss plotted as a function of time for fast (dashed line) and slow (dash-dot line) saturable absorbers.

be replaced with σ_A.

The next two subsections will consider slow and fast saturable absorbers. These two cases yield two different approximations to equation A.55. Fig. A-7 schematically shows the difference between fast and slow saturable absorbers. In the case of a fast absorber, the loss follows the pulse intensity, whereas for a slow absorber, the loss follows the integral of the intensity.

A.6.1 Slow Saturable Absorber

For a slow saturable absorber, the relaxation time T_A is much longer than the rate of change of the optical intensity and equation A.55 can be approximated as

$$\frac{\partial n}{\partial t} = -\frac{2\sigma_A}{A_A}\frac{|a(t)|^2}{\hbar\omega_0}n. \tag{A.56}$$

In this case, n can be solved exactly as

$$n = n_e \exp\left(-\frac{w(t)}{w_A}\right) \tag{A.57}$$

where

$$w(t) \equiv \int^t |a(t)|^2 dt \tag{A.58}$$

is the cumulative energy in the pulse,

$$\frac{1}{w_A} \equiv \frac{2\sigma_A}{\hbar\omega_0 A_A} \tag{A.59}$$

is the inverse saturation energy, and n_e is the starting population. It was assumed that the saturable absorber relaxes completely between pulses, $T_A \ll T_R$, so that the starting population equals the equilibrium population n_e.

The loss of the saturable absorber is proportional to n,

$$L(t) = L_A \exp\left(-\frac{w(t)}{w_A}\right). \tag{A.60}$$

where L_A is the non-saturable or linear loss. The constants L_A and w_A can be obtained from pump-probe measurements. The input/output optical power relationship is

$$\begin{aligned} P_{out} &= [1 - L(t)]P_{in} \\ &\approx \exp[-L(t)]P_{in} \\ &= \exp\left[-L_A \exp\left(-\frac{w(t)}{w_A}\right)\right] P_{in} \\ &\approx \exp\left[-L_A\left(1 - \frac{w(t)}{w_A}\right)\right] P_{in} \end{aligned} \tag{A.61}$$

Taking the square-root of the equation above, the input and output electric-fields are

$$\begin{aligned} a_{out} &= \exp\left[-\frac{L_A}{2}\exp\left(-\frac{w(t)}{w_A}\right)\right] a_{in} \\ &\approx \exp\left[-\frac{L_A}{2}\left(1 - \frac{w(t)}{w_A}\right)\right] a_{in}. \end{aligned} \tag{A.62}$$

Comparing equation A.62 with equation A.2, we find that the lumped element operators for a slow saturable absorber are

$$\boxed{\hat{O}_{L,SA,slow} = -\frac{L_A}{2},} \tag{A.63}$$

and

$$\boxed{\hat{O}_{SA,slow} = -\frac{L_A w(t)}{2w_A}.} \tag{A.64}$$

A.6.2 Fast Saturable Absorber

For a fast saturable absorber, the relaxation time T_A is shorter than the rate of change of the optical intensity. Hence the population difference is an instantaneous function of intensity, or in other words, the carrier population reaches steady-state instantaneously. Therefore, letting $\partial n/\partial t = 0$ for equation A.55 yields

$$n(t) = n_e \left(1 - \frac{|a(t)|^2}{P_A}\right). \tag{A.65}$$

where

$$P_A = \frac{w_A}{T_A} = \frac{2\sigma_A T_A}{A_A}\frac{|a(t)|^2}{\hbar\omega_0}. \tag{A.66}$$

The loss is proportional to n. Hence, the absorption of a pulse after a single passage is

$$L(t) = L_A \left(1 - \frac{|a(t)|^2}{P_A}\right), \tag{A.67}$$

where L_A is the non-saturable or linear loss of the saturable absorber. The input/output relationship for the optical power is

$$\begin{aligned} P_{out} &= [1 - L(t)]P_{in} \\ &= \left(1 - L_A + L_A\frac{|a(t)|^2}{P_A}\right)P_{in} \\ &\approx \exp\left(-L_A + L_A\frac{|a(t)|^2}{P_A}\right)P_{in} \\ &= \exp\left(-L_A + 2\gamma|a(t)|^2\right)P_{in} \end{aligned} \tag{A.68}$$

where it is assumed that $|a(t)|^2/P_A \ll 1$ so that $\exp(x) \approx 1 + x$, and

$$\gamma \equiv \frac{L_A}{2P_A}. \tag{A.69}$$

The corresponding input/output relationship for the electric-fields is equal to the square-root of equation A.68,

$$a_{out} = \exp\left(-\frac{L_A}{2} + \gamma|a(t)|^2\right) a_{in}. \tag{A.70}$$

Comparing equation A.70 with equation A.2, we find that the lumped element operators for a fast saturable absorber are

$$\boxed{\hat{O}_{L,SA,fast} = -\frac{L_A}{2},} \tag{A.71}$$

and

$$\boxed{\hat{O}_{SA,fast} = \gamma|a(t)|^2.} \tag{A.72}$$

Appendix G lists the unsaturated SA absorption coefficient as 230 cm^{-1} and the length of the SA section is 30-40 μm. These values imply that $\hat{O}_{L,SA,fast} = -\frac{230\times(30-40\times10^{-4})}{2} = -0.345$ to -0.460.

A.6.3 Semiconductor Laser Saturable Absorber

Pump-probe measurements are used to characterize the saturable absorbers in our MLLDs. Fig. A-8 shows the transmission versus time for different reverse biases for our MLLD. The plot shows that the recovery time of the saturable absorbers have two time scales: a fast time scale of 8 ps and a slow time scale of 21 ps. These time scales are long compared to the measured 3 ps pulse width of these lasers, which implies that the saturable absorber can be modelled as a slow saturable absorber.

The data shows that the ratio of the maximum to minimum transmission varies with the bias level. For biases of -1 V, -1.5 V, and -2 V, the maximum to minimum transmission ratios are 4.44, 15, and 25, respectively.

For the slow saturable absorber, equation A.61 tells us that the transmission before the pulse (the minimum level) is $\exp(-L_A)$ and that the transmission after the pulse (the maximum level) is $\exp[-L_A(1-w_0/w_A)]$. We set ratio of these two values equal to the experimentally measured values with a pump pulse energy of $w_0 = 1$ pJ and

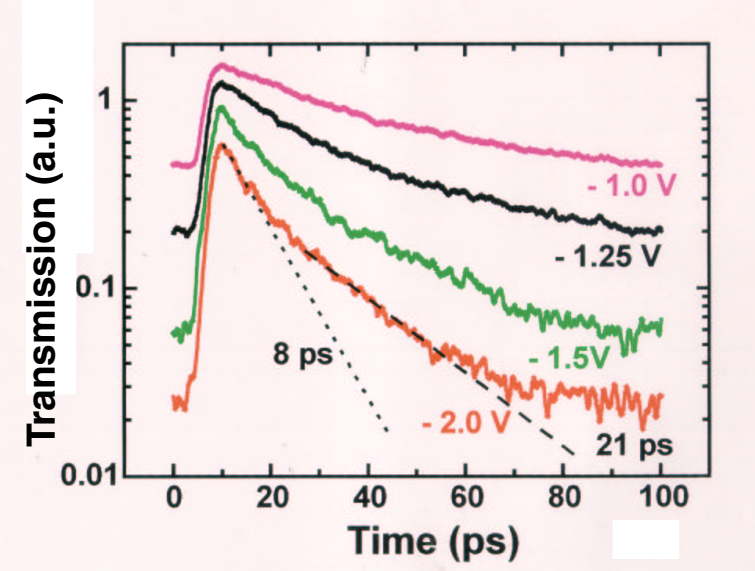

Figure A-8: Reverse bias dependence of saturable absorbers. Courtesy of H. Yokoyama from NEC.

get

$$\exp\left(L_A \frac{w_0}{w_A}\right) = 4.44, 15, \text{ or } 25 \tag{A.73}$$

to find that $\boxed{L_A/w_A = 1.49, 2.71, \text{ or } 3.22 \text{ pJ}}$, respectively. Note that L_A is a unitless quantity.

For the fast saturable absorber, equation A.61 tells us that the transmission before the pulse (the minimum level) is $\exp(-L_A)$ and that the transmission after the pulse (the maximum level) is $\exp[-L_A + 2\gamma|a(0)|^2]$. We set ratio of these two values equal to the experimentally measured values with a peak pump pulse power of $|a_0|^2 = w_0/(3 \text{ ps}) = 1/3$ J/s and get

$$\exp\left(2\gamma|a(0)|^2\right) = 4.44, 15, \text{ or } 25 \tag{A.74}$$

to find that $\boxed{\gamma = 2.24, 4.06, \text{ or } 4.83 \text{ W}^{-1}}$, respectively.

A.7 Propagation through the GVD Section

According to Agrawal's book [78, p.64,eq.3.2.4], the output electric-field after propagation through a dispersive medium is related to the input electric-field by

$$\hat{a}_{out}(\Omega) = \hat{a}_{in}(\Omega) \exp\left(j\frac{\beta_2 z}{2}\Omega^2\right), \tag{A.75}$$

where z is the propagation distance, $\beta_2 = \partial^2 k/\partial\Omega^2$ is the group velocity dispersion, and the substitution $-i \rightarrow j$ was used since we define the inverse Fourier transform as

$$a(t) = \int_{-\infty}^{\infty} \hat{a}(\Omega) \exp(j\Omega t)\frac{d\Omega}{2\pi} \tag{A.76}$$

and Agrawal defines his inverse Fourier transform as [78, p.32, eq.2.2.2]

$$E(t) = \int_{-\infty}^{\infty} \hat{E}(\Omega) \exp(-i\Omega t)\frac{d\Omega}{2\pi}. \tag{A.77}$$

Equation A.75 is further simplified to

$$\hat{a}_{out}(\Omega) = \hat{a}_{in}(\Omega) \exp\left(-jD\Omega^2\right), \tag{A.78}$$

after making the substitution

$$D \equiv -\frac{\beta_2 z}{2} \tag{A.79}$$

which is not the usual definition of D since it has units of ps^2 instead of ps/nm/km. This definition is kept to keep consistent notation with Haus's modelocked laser noise paper [10].

We take the inverse Fourier transform of equation A.78 to find

$$a_{out}(t) = \exp\left(jD\frac{\partial^2}{\partial t^2}a_{in}(t)\right) \tag{A.80}$$

where $-\Omega^2 \rightarrow \partial^2/\partial t^2$ and the following relation was used

$$\mathcal{F}^{-1}\left\{\exp\left[P(\Omega)\right]F(\Omega)\right\} = \exp\left[P\left(-j\frac{\partial}{\partial t}\right)\right] f(t) \tag{A.81}$$

where $P(\Omega)$ is a polynomial and $F(\Omega) \rightarrow f(t)$ are Fourier transform pairs. This relation can be proved by expanding the exponential into a Taylor series.

From equation A.80 and A.2, it is apparent that

$$\hat{O}_{GVD} = jD\frac{\partial^2}{\partial t^2}. \tag{A.82}$$

For 1 km of Corning SMF-28 singlemode fiber, $\beta_2 z = -20$ ps^2 (anomalous at 1.5 μm) and $D = -\frac{-20\text{ps}^2}{2} = 10$ ps^2. Notice that the sign of D is such that $D > 0$ is anomalous and $D < 0$ is normal.

The GVD of bulk and multiple quantum well InGaAsP devices at 1.5 μm have been characterized by cross-correlating the output pulse train produced by a single pulse incident on an uncoated laser diode [79]. The GVD for bulk and MQW devices is approximately -2 fs/nm/(500 μm) = -4000 ps/nm/km and -2.5 fs/nm/(500 μm) = -5000 ps/nm/km for TE and TM polarizations, respectively.[2] The corresponding values for D for a 500 μm long chip are 0.001274697 ps^2 and 0.001593372 ps^2, respectively.[3] This dispersion is equivalent in magnitude to approximately 12 cm of SMF-28 fiber.

A.8 Propagation through the Kerr Section

From Agrawal's book [78, p.90,eq.4.1.3,4.1.4; p.61,eq.3.1.3], the output electric-field after propagation through a Kerr medium is related to the input electric-field by

$$\begin{aligned} a_{out}(t) &= \exp\left(-j\frac{|a_{in}(t)|^2}{P_0}\frac{z_{eff}}{L_{NL}}\right) a_{in}(t) \\ &= \exp\left(-j\gamma_{agrawal} z_{eff}|a_{in}(t)|^2\right) a_{in}(t) \\ &= \exp\left(-j\delta|a_{in}(t)|^2\right) a_{in}(t) \end{aligned} \tag{A.83}$$

[2] $D_{agrawal} = -\frac{2\pi c}{\lambda^2}\beta_2$. For $\lambda = 1.55\mu$m, $D_{agrawal}[ps/nm/km] = 0.7845\beta_2[ps^2/km]$

[3] The devices have normal dispersion.

where P_0 is the peak power, $z_{eff} = [1-\exp(-\alpha z)]/\alpha$ is the effective length accounting for the loss α, $L_N L = (\gamma_{agrawal} P_0)^{-1}$ is the nonlinear length, $\gamma_{agrawal} = n_2\omega_0/cA_{eff}$ is a nonlinear constant defined in Agrawal's book [78, p.42,eq.2.3.28] which is typically equal to 20 $\mathrm{W}^{-1}\mathrm{km}^{-1}$ in singlemode fiber, and

$$\delta = \gamma_{agrawal} z_{eff} \tag{A.84}$$

is a nonlinear constant proportional to the Kerr effect. Typical values for δ are 0.01954 for MLLDs[4] and 434 W^{-1} for EDFLs[5].

[4] $z = 0.001$ km, $\alpha = 0.046\ km^{-1}$ (0.2 dB/km), $z_{eff} \approx 0.977$, $\gamma_{agrawal} = 20\ \mathrm{W}^{-1}\mathrm{km}^{-1}$

[5] $z > 200$ km, $\alpha = 0.046\ km^{-1}$ (0.2 dB/km), $z_{eff} \approx 21.7$ km, $\gamma_{agrawal} = 20\ \mathrm{W}^{-1}\mathrm{km}^{-1}$

Appendix B

Theory of the Noise in Modelocked Lasers

There are several theories of noise in actively modelocked lasers [80, 81, 82, 83], but few have been as rigorously tested as the currently presented theory. The actively modelocked laser theory is based on the theoretical work by Haus[73, 84] and the soliton modelocked laser theory is based on the work of Grein[51], Moores[11], and Haus[10]. The new contributions to the theory in this thesis are (1) the addition of rf oscillator phase noise to the theory, (2) investigate the effect of gain relaxation oscillations in the theory, (3) compare soliton noise theory with actively modemodelock laser theory, (4) show that the noise of semiconductor lasers is not so much worse than that of fiber lasers, and (5) point out several salient features of the noise theory such as the dependence of timing jitter on pulse width.

Our approach for describing the noise in semiconductor modelocked lasers is as follows:

1. Find *master equation* that describes the evolution of pulses in laser cavity. The master equation is derived by a lumped-element model of the cavity in chapter A.

2. Simplify the equation for the specific problem at hand.

3. Find solution or *ansatz* to master equation in absence of noise.

4. Perturb ansatz and derive *equations of motion* for the different noise fluctuations: amplitude, timing, frequency, phase, and carrier density.

5. Find power spectral density and correlations of the different noise fluctuations.

Modelocked laser diodes generally have negligible dispersion and hence are modelled well by the actively modelocked laser noise theory in section B.2. Soliton lasers, such as some Erbium-doped fiber lasers, have nonlinear noise dynamics and hence require special treatment. Their noise is described in section B.3. Both noise theories give the same trends for timing jitter as a function of modulation depth, modulation frequency, cavity loss, and pulse width. The absolute numbers, however, differ by a factor of about 10.

B.1 The Physical Picture

This section will explain the physical processes of noise in a laser and explain the effects of the saturable absorber, modulator, optical filter, loss and gain dynamics on the laser noise.

Noise can be due to vibrations of the end mirror, RF synthesizer noise, variations in the pump current due to RF pickups, 60 Hz tones, and 1/f noise, and due to the spontaneous emission in the laser. Spontaneous emission is referred to as the quantum-noise of the laser. The spontaneous emission noise can dominate the noise of the laser if the modelocked laser is not designed correctly. To obtain the lowest noise possible for a given pulse width and repetition rate involves choosing the correct filter bandwidth, modulation depth, modulation frequency, cavity loss, RF synthesizer noise, and saturable absorption modulation depth. Until the development of high-Q sapphire crystal oscillators, it was found that the noise with frequency content greater than 10 Hz was dominated by the RF synthesizer. With these high-Q oscillators, it is possible to operate these lasers so that they are quantum-limited. This section will discuss spontaneous emission noise.

All lasers contain a photon amplifier, which can typically be an EDFA or SOA.

An amplifier with gain G converts N input photons into GN output photons. The amplifier is a source of noise. The noise of the amplifier is proportional to its gain and has been found to be equivalent to injecting n_{sp} (typically 1 to 3) noise photons per mode at the input of the amplifier. The inversion factor depends on the material gain [1, p.140]. The output noise power of the amplifier is equal to $P_{ASE} = h\nu B n_{sp}(G-1)$, where B is half the bandwidth of the most bandwidth limiting element in a system. For example, the bandwidth could be limited by an optical filter, the gain spectrum of the amplifier, or the detection bandwidth of a photodiode, depending on what quantity is being measured.

Connecting the input and output terminals of an amplifier creates a CW laser. There is some loss that is due to connector splice loss, material loss, or other loss in the feedback loop. The initial gain of the amplifier is much larger than the losses in the loop, which mean that the photon number would increase infinitely unless the gain saturated. In the steady-state, the gain saturates to the value G_{th} and is constant. The noise power from the amplifier is now equal to $P_{ASE,SS} = h\nu B n_{sp}(G_{th} - 1)$. The steady-state power reaches some value that is proportional to the losses in the cavity, see Fig. 2-3. The figure shows that increasing the cavity loss decreases the steady-state power, but the noise power generated from the amplifier is the same. Therefore, the noise of the laser increases with increasing cavity loss. The noise of a CW laser refers to either amplitude or phase noise.

In a modelocked laser, a modulator and/or a saturable absorber is added to the cavity to create laser pulses. In this case, the noise analysis becomes more complicated since the gain of the amplifier becomes a function of time. After a pulse passes through an amplifier, the gain is pulled down and then undergoes a slower recovery to a steady-state value until the pulse again returns to the amplifier. There are four fluctuations in a modelocked laser that are important: amplitude, phase, time, frequency. The spontaneous emission noise contributes to all four fluctuations. These four fluctuations can be reduced with elements put into the cavity. For example, the frequency fluctuations can be reduced with an optical bandpass filter and the timing fluctuations can be reduced with an amplitude modulator and saturable absorber.

Short pulses are usually noisier than long pulses. To obtain short pulses, the optical filter bandwidth must be increased. The pulse width and optical filter bandwidth in an actively modelocked lasers are related according to $\tau \propto 1/\sqrt{\Omega_f}$ [85]. The spontaneous emission noise scales as $B = \Omega_f/4\pi$. Therefore, if the pulse is made twice as short, the optical filtering must be made four times larger, and hence the ASE noise increases by a factor of four. For actively modelocked lasers, we will discover that the rms jitter is proportional to $1/\tau^2$.

The spontaneous emission noise overlaps with the pulse. Using overlap integrals of the pulse with the noise, the contribution of the ASE to amplitude, timing, phase, or frequency noise can be found. For example, the ASE that adds to the front of the pulse and subtracts from the back of the pulse would contribute to timing jitter. ASE that adds amplitude throughout the pulse width contributes to amplitude noise.

When the gain varies, so does the spontaneous emission. The gain is initially very large at the front of the pulse and smaller at the end of the pulse. Correspondingly, the ASE is greater at the leading edge of the pulse, as shown schematically in Fig. B-1. The asymmetry of the ASE causes the front of the pulse to see larger perturbations than the back of the pulse. The saturable absorber behaves in the opposite direction, so as to reduce this asymmetry. The saturable absorber reduces the noise ahead of the pulse, but once the pulse saturates the saturable absorber, the noise energy directly following the pulse is not attenuated. In our modelocked semiconductor lasers, when the saturable absorber bias and injection current is at a good operating point, the the pdf of the timing jitter was measured to be Gaussian and symmetric, indicating that the effect of the saturable absorber and gain saturation balance each other.

The physical difference between Erbium-doped fiber lasers and semiconductor lasers is the upper-state lifetime. In Erbium, the upper-state lifetime is typically $\tau_N =$ 10 ms [86, p.223] and in semiconductor lasers, the upper-state lifetime is typically $\tau_N = 1$ ns at threshold. There are seven orders of magnitude difference between the carrier-lifetimes of the two gain media. Assuming that the gain is constant in EDFLs is a good approximation at a 10 GHz repetition rate. The gain does not respond fast enough a 10 GHz train of pulse, but in semiconductor lasers, the gain changes

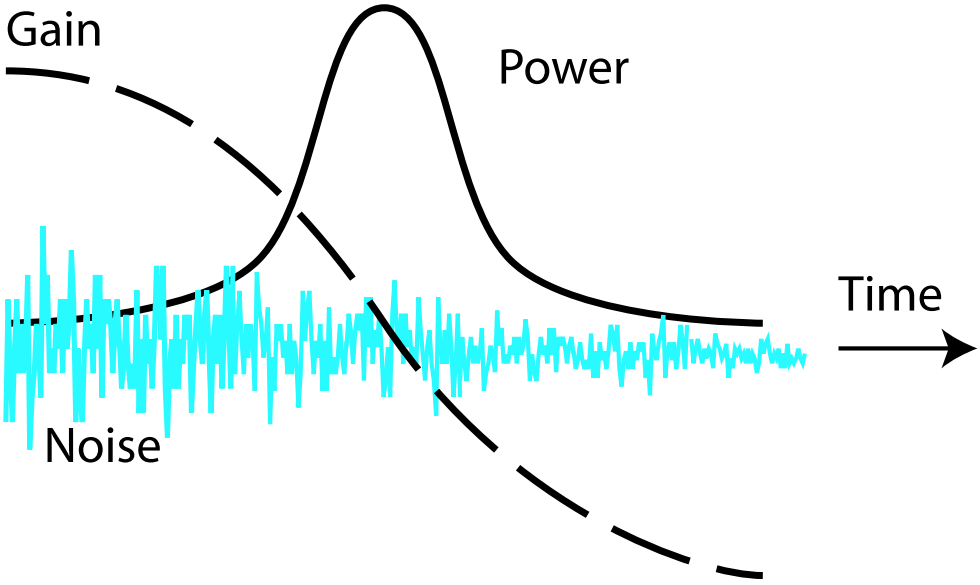

Figure B-1: ASE shown as a function of gain.

drastically after a single pulse passage. A later section will discuss the impact of the carrier dynamics in semiconductor lasers. Although the master equation does not initially include gain saturation, the resulting equations for the psd of the timing jitter fit very well to the experimentally measured results.

B.2 Noise of Actively Modelocked Lasers

In this subsection, we will analyze the noise of actively modelocked lasers with no Kerr nonlinearity, no saturable absorption, and no population density coupling to the equations of motion of the noise. We will see that the pulses that circulate inside the laser cavity are Gaussian and that the noise can be represented as a sum of Hermite Gaussians of different order.

B.2.1 The Master Equation

The master equation is given by equation A.25

$$T_R \frac{\partial a(t,T)}{\partial T} = \left\{ -l + g + \frac{1}{\Omega_f^2}\frac{\partial^2}{\partial t^2} + jD\frac{\partial^2}{\partial t^2} - \frac{M_{AM} + jM_{PM}}{4}(\omega_M t)^2 \right\} a(t,T) + T_R S(t,T). \quad \text{(B.1)}$$

where the Kerr nonlinearity and saturable absorption are ignored, and the gain filtering is much weaker than the optical bandpass filtering. By use of the abbreviations

$$\frac{1}{\tau_{lg}} \equiv \frac{l-g}{T_R} \quad \text{(B.2)}$$

$$F \equiv \left(\frac{1}{\Omega_f^2} + jD\right)\frac{1}{T_R} \quad \text{(B.3)}$$

$$A \equiv \frac{M_{AM} + jM_{PM}}{4}\frac{\omega_M^2}{T_R} \quad \text{(B.4)}$$

equation B.1 becomes

$$\frac{\partial a(t,T)}{\partial T} = \left\{ -\frac{1}{\tau_{lg}} + F\frac{\partial^2}{\partial t^2} - At^2 \right\} a(t,T) + S(t,T). \quad \text{(B.5)}$$

The abbreviations F and A correspond to filtering and modulation action, respectively. The value $1/\tau_{lg}$ contains the decay and growth time constants.

B.2.2 Equations of Motion

Ansatz

We solve the master equation by substituting the ansatz

$$a(t,T) = a_{ss}(t) + \Delta a(t,T) \quad \text{(B.6)}$$

into the master equation B.5, where a_0 is the steady-state solution of the modelocked laser in the absence of noise, and Δa is a perturbation to the steady-state solution due to all internal noise sources.

Steady-State Solution

The steady-state solution can be found by setting $\partial/\partial T = 0$ and $S(t,T) = 0$ in equation B.5 to obtain

$$\left\{F\frac{\partial^2}{\partial t^2} - \frac{1}{\tau_{lg}} - At^2\right\} a_{ss}(t) = 0. \tag{B.7}$$

We note immediately that this equation has the form of the quantum mechanical simple harmonic oscillator which is solved by Hermite-Gaussian functions. The Hermite-Gaussian function of order n is defined by

$$\phi_n(x) = e^{-x^2/2} H_n(x) \tag{B.8}$$

where $H_n(x)$ is the n-th order Hermite polynomial ($H_0(x) = 1$, $H_1(x) = 2x$, and $H_2(x) = -2 + 4x^2$). This function solves the following differential equation [87, ch.13,p.769]

$$\left\{\frac{d^2}{dx^2} + (2n + 1 - x^2)\right\} \phi_n(x) = 0. \tag{B.9}$$

After multiplication by the constant γ_0 and the substitution $x = t/\tau$, equation (B.9) becomes

$$\left\{\underbrace{\gamma_0\tau^2}_{\equiv F}\frac{\partial^2}{\partial t^2} + \underbrace{\gamma_0(2n+1)}_{\gamma_n} - \underbrace{\frac{\gamma_0}{\tau^2}}_{\equiv A} t^2\right\} \phi_n\left(\frac{t}{\tau}\right) = 0 \tag{B.10}$$

$$\left(F\frac{\partial^2}{\partial t^2} - At^2\right) \phi_n\left(\frac{t}{\tau}\right) = -\gamma_n \phi_n\left(\frac{t}{\tau}\right) \tag{B.11}$$

$$\left(F\frac{\partial^2}{\partial t^2} - At^2\right) \psi_n\left(\frac{t}{\tau}\right) = -\gamma_n \psi_n\left(\frac{t}{\tau}\right) \tag{B.12}$$

where

$$\gamma_n \equiv (2n+1)\gamma_0, \tag{B.13}$$

and

$$\psi_n\left(\frac{t}{\tau}\right) \equiv \frac{1}{\sqrt{2^n n! \tau \sqrt{\pi}}} \phi_n\left(\frac{t}{\tau}\right) \tag{B.14}$$

is the orthonormalized Hermite-Gaussian function, $\int_{-\infty}^{\infty} \psi_n^2(t/\tau)dt = 1$. The underbraced terms in equation (B.10) imply that

$$\tau^4 = \frac{F}{A} = \frac{4(1 + jD\Omega_f^2)}{(M_{AM} + jM_{PM})\Omega_f^2\omega_M^2} \tag{B.15}$$

$$\gamma_0 = \frac{F}{\tau^2} = A\tau^2 \tag{B.16}$$

Equation (B.15) with $D = 0$ and $M_{PM} = 0$ is the well known formula for the pulsewidth [85, ch.27.3,p.1067]. Equation (B.12) shows that using $F\frac{\partial^2}{\partial t^2} - At^2$ on an nth order Hermite Gaussian is equivalent to multiplying the nth order Hermite Gaussian by $-\gamma_n$. This is an eigenvalue equation. Dispersion and phase modulation in the cavity lead to a complex τ according to equation (B.15). A complex τ means that the circulating pulse is chirped.

The steady-state electric-field can have any shape since any shape can be expanded as a sum of Hermite Gaussians of various orders. Experimentally, we find that the steady-state solution is well described by a simple Gaussian. Thus, we set the steady-state solution equal to the zeroth-order Hermite Gaussian

$$a_{ss}(t) = A_0\, \psi_0\left(\frac{t}{\tau}\right), \tag{B.17}$$

and is normalized so that $\int_{-\infty}^{\infty} |a_{ss}(t)|^2 dt = A_0^2$. Substitution of equation (B.17) into equation (B.7) yields the following relation

$$-\frac{1}{\tau_{lg}} = \gamma_0, \tag{B.18}$$

or

$$g_0 = T_R\gamma_0 + l, , \tag{B.19}$$

where g_0 denotes the gain without noise inside the laser and it is a function of t and T,[1] and $g = g_0 + \Delta g$ is the total gain. In other words, the gain must overcome the

[1]It is not entirely rigorous to now assume that g is time dependent. After all, earlier, we made the substitution $\frac{1}{\tau_{lg}} = \frac{l-g}{T_R} = const$, so that we could get simple solutions (Hermite-Gaussian)

losses due to the filter and amplitude modulation, γ_0, and the other losses of the cavity, l.

Equations of Motion for Perturbations

The ansatz given by equation (B.6) is substituted into equation (B.5) to obtain

$$\begin{aligned}
\frac{\partial}{\partial T}(a_{ss}(t)+\Delta a(t,T)) &= \left\{\frac{g-l}{T_R}+F\frac{\partial^2}{\partial t^2}-At^2\right\}(a_{ss}(t)+\Delta a(t,T)) \\
&\quad +S(t,T) \qquad \text{(B.20)} \\
\frac{\partial}{\partial T}(a_{ss}(t)+\Delta a(t,T)) &= \left\{\frac{(g_0+\Delta g)-l}{T_R}+F\frac{\partial^2}{\partial t^2}-At^2\right\}(a_{ss}(t)+\Delta a(t,T)) \\
&\quad +S(t,T) \qquad \text{(B.21)} \\
\frac{\partial}{\partial T}(a_{ss}(t)+\Delta a(t,T)) &= \left\{\gamma_0+\frac{\Delta g}{T_R}+F\frac{\partial^2}{\partial t^2}-At^2\right\}(a_{ss}(t)+\Delta a(t,T)) \\
&\quad +S(t,T) \qquad \text{(B.22)} \\
\frac{\partial}{\partial T}\Delta a(t,T) &= \left\{\gamma_0+\underbrace{\frac{\Delta g}{T_R}}_{\text{small}}+F\frac{\partial^2}{\partial t^2}-At^2\right\}\Delta a(t,T) \\
&\quad +\frac{\Delta g}{T_R}a_{ss}(t)+S(t,T) \qquad \text{(B.23)} \\
\frac{\partial}{\partial T}\Delta a(t,T) &= \left\{\gamma_0+F\frac{\partial^2}{\partial t^2}-At^2\right\}\Delta a(t,T) \\
&\quad +\frac{\Delta g}{T_R}A_0\psi_0(t/\tau)+S(t,T) \qquad \text{(B.24)} \\
\frac{\partial}{\partial T}\Delta a(t,T) &= \left\{\gamma_0+F\frac{\partial^2}{\partial t^2}-At^2\right\}\Delta a(t,T) \\
&\quad +\frac{\Delta g_{sgs}(T)+\Delta g_{fgs}(t,T)}{T_R}A_0\psi_0(t/\tau)+S(t,T) \qquad \text{(B.25)}
\end{aligned}$$

where the gain was written as the sum of the gain with no noise in the cavity plus the gain perturbations due to noise

$$g(t,T)=g_0(t,T)+\Delta g(t,T). \qquad \text{(B.26)}$$

to the master equation. The justification of making this approximation is that the experimental measurements show that the pulses inside the semiconductor modelocked lasers are indeed Gaussian for saturable absorber biases below -1.6 V.

The gain perturbations can further be split into a slow and fast component according to

$$\Delta g(t,T) = \Delta g_{sgs}(T) + \Delta g_{fgs}(t,T). \tag{B.27}$$

where sgs stands for slow gain saturation and fgs stands for fast gain saturation. The slow component puts a cap on the maximum achievable gain and the fast component arises from the pulse quickly depleting the carriers. The second component will be addressed in section B.2.3.

The slow gain saturation component of the gain can be written as

$$\Delta g_{sgs}(T) \equiv \Delta a(T) \left.\frac{\partial g}{\partial a}\right|_{a=a_{ss}}. \tag{B.28}$$

Generally, the differential gain at the steady state pulse power $a = a_{ss}$ is negative, so that increasing the pulse power causes a decrease in the gain seen by the pulse, i.e. the gain is saturated. The gain is most sensitive to the real part of the zeroth-order Hermite Gaussian and hence making the substitution $\Delta a \rightarrow \Delta\Re\{A_0\}$ into equation (B.28) yields

$$\Delta g_{sgs} \equiv \Re\{\Delta A_0(T)\} \left.\frac{\partial g}{\partial a}\right|_{a=a_{ss}}. \tag{B.29}$$

The differential gain with respect to a relates to the differential gain with respect to the power $P = |a|^2$ by

$$\frac{\partial g}{\partial a} = \frac{\partial g}{\partial P}\frac{\partial P}{\partial a} = 2a\frac{\partial g}{\partial P} = 2\sqrt{P}\frac{\partial g}{\partial P}. \tag{B.30}$$

The perturbation can be expanded as a sum of Hermite-Gaussians

$$\Delta a(t,T) = \sum_{m=0}^{\infty} \Delta A_m(T)\, \psi_m\left(\frac{t}{\tau}\right) \tag{B.31}$$

where $\Delta A_n(T)$ are the expansion coefficients. Here we assumed that the gain saturates at high powers, i.e. the gain g is a function of the pulse power. Saturation of the gain prevents the amplitude noise from blowing up. Equation (B.31) can be substituted

into equation (B.25), multiplied by $\psi_n^*(t/\tau)$, and then integrated over all t to obtain

$$\begin{aligned}\frac{\partial}{\partial T}\Delta A_n(T) &= \{\gamma_0 - \gamma_n\}\,\Delta A_n(T) + \frac{\Delta g_{sgs}(T)}{T_R}\,A_0\delta(n) \\ &\quad + \int_{-\infty}^{\infty}\frac{\Delta g_{fgs}(t,T)}{T_R}A_0\psi_0(t/\tau)\psi_n^*(t/\tau)dt + S_n(T) \qquad \text{(B.32)} \\ &= -2n\gamma_0\,\Delta A_n(T) + \frac{\Delta g_{sgs}(T)}{T_R}\,A_0\delta(n) \\ &\quad + \int_{-\infty}^{\infty}\frac{\Delta g_{fgs}(t,T)}{T_R}A_0\psi_0(t/\tau)\psi_n^*(t/\tau)dt + S_n(T), \qquad \text{(B.33)}\end{aligned}$$

where

$$S_n(T) = \int_{-\infty}^{\infty} S(t,T)\,\psi_n\left(\frac{t}{\tau}\right)dt. \qquad \text{(B.34)}$$

The quantity $S_n(T)$ is the projection of the noise onto the nth Hermite-Gaussian function. The effects of fast gain saturation Δg_{fgs} will be ignored until section B.2.3.

For amplitude modulation where $D = 0$ and $M_{PM} = 0$, equation (B.16) holds when $\gamma_0 > 0$, since $F > 0$, $A > 0$ and $\tau > 0$ for physically realizable values. With $\gamma_0 > 0$, equations (B.2) and (B.18) imply that $g > l$. In other words, the gain must be greater than the loss for a stable solution. In addition, $g > l$, or equivalently $\gamma_0 > 0$, is also necessary for preventing exponential growth of the noise according to equation (B.33). This ensures that the low-intensity noise is damped.

Spontaneous Emission Autocorrelation Function

The amplified spontaneous emission (ASE) noise power of an amplifier is well known to be equal to $P_{ASE} = h\nu B n_{sp}(G-1)$ [86, p.77], where B is the single-sided detection bandwidth or half the optical amplifier bandwidth, n_{sp} is the inversion factor which is typically between 1 (fully inverted) and 3, and G is the gain of the amplifier ($P_{out} = GP_{in}$). In other words, the amplifier contributes approximately one input noise photon per pass through the amplifier per unit bandwidth (or per axial mode). Therefore, the ASE noise power of the laser is

$$P_{ASE} = h\nu B n_{sp}(G-1) \qquad \text{(B.35)}$$

Description	n_{sp}	G	B	P_{ASE}
Mitsubishi EDFA	2.5 (7 dB NF)	10^4 (40 dB)	2660 GHz (20 nm)	8.5 mW
BTI Photonics EDFA (Pre-Amp)	1 (4 dB NF)	10^3 (30 dB)	2660 GHz (20 nm)	0.341 mW
Alcatel SOA	2.5 (7 dB NF)	10^3 (30 dB)	2660 GHz (20 nm)	0.852 mW
NEC MLLD	3	32 (15 dB)	3990 GHz (30 nm)	0.049 mW
NEC MLLD with 5-nm BPF	3	32 (15 dB)	665 GHz (5 nm)	0.008 mW
NEC MLLD with 0.7-nm BPF	3	32 (15 dB)	93 GHz (5 nm)	0.001 mW

Table B.1: Spontaneous emission power from a gain medium. Note that the noise figure (NF) of the EDFA relates to the inversion factor according to NF $= 2 * n_{sp}/C_1$, where C_1 is the input coupling loss (typically $C_1 = 1$ for EDFAs without isolators). The noise figure is defined differently for SOAs, NF $= n_{sp}/C_1$, where the input coupling loss is typically 3 dB. Hence, there is a 3 dB difference between the quoted NF's of EDFAs and SOAs.

where B is the half bandwidth of the laser cavity, which is typically given by the optical bandpass filter inside the cavity. For example, if our cavity uses a 5-nm BPF, then $B = 2.5$ nm $= 333$ GHz. If the optical bandpass filter is removed, then the half bandwidth is the Erbium gain spectrum $B = 20$ nm $= 2660$ GHz. Table B.1 shows the ASE power from a gain medium with various bandwidths and gain at 1.55 μm wavelength.

The autocorrelation function of the ASE noise is given by

$$\langle S(t,T)S^*(t',T')\rangle \equiv \lim_{\Delta T\to\infty}\int_0^{\Delta T} S(t,T)S^*(t',T')dt = P_{ASE}\delta(t-t')\delta(T-T'). \quad \text{(B.36)}$$

The units check since S has units of $\sqrt{\text{Power}}/\text{time}$, P_{ASE} has units of power, and $\delta(t-t')$ and $\delta(T-T')$ each have units of $1/\text{time}$.[2] In other words, equation (B.36) is stating that the ASE noise is completely uncorrelated in time, zero mean, and the variance is given by equation (B.35): $\lim_{\Delta T\to\infty}\int_0^{\Delta T}|S(t,T)|^2dt = P_{ASE}$. Substituting

[2]The delta function has units of its argument since $1 = \int_{-\infty}^{\infty}\delta(t-t')dt$.

equation (B.35) into equation (B.36) yields

$$\langle S(t,T)S^*(t',T')\rangle = h\nu n_{sp}B(G-1)\delta(t-t')\delta(T-T'). \tag{B.37}$$

In Haus and Mecozzi's paper [10], the gain term $G-1$ is approximated with $2g$, since $G-1 = \exp(2g)-1 \approx (1+2g)-1 = 2g$. In addition, they let $B = 1/T_R$, the inverse of the round-trip time. For the equations of motion, we will be interested in finding the projection of the ASE noise onto the nth order Hermite-Gaussian basis function according to equation (B.34). The autocorrelation function of $S_n(T)$ is

$$\begin{aligned}
\langle S_n(T)S_n^*(T')\rangle &\equiv \frac{1}{\Delta T}\int_{-\Delta T/2}^{\Delta T/2} S_n(T)S_n^*(T')dT && \text{(B.38)}\\
&= \frac{1}{\Delta T}\int_{-\Delta T/2}^{\Delta T/2}\left(\int_{-\infty}^{\infty} S(t,T)\,\psi_n\left(\frac{t}{\tau}\right)dt\right)\times && \text{(B.39)}\\
&\quad \left(\int_{-\infty}^{\infty} S^*(\lambda,T')\,\psi_n^*\left(\frac{\lambda}{\tau}\right)d\lambda\right)dT && \text{(B.40)}\\
&= \int_{-\infty}^{\infty}\int_{-\infty}^{\infty}\psi_n\left(\frac{t}{\tau}\right)\psi_n^*\left(\frac{\lambda}{\tau}\right)\times && \text{(B.41)}\\
&\quad \left(\frac{1}{\Delta T}\int_{-\Delta T/2}^{\Delta T/2} S(t,T)S^*(\lambda,T')dT\right)dtd\lambda && \text{(B.42)}\\
&= \int_{-\infty}^{\infty}\int_{-\infty}^{\infty}\psi_n\left(\frac{t}{\tau}\right)\psi_n^*\left(\frac{\lambda}{\tau}\right)\langle S(t,T)S^*(\lambda,T')\rangle dtd\lambda && \text{(B.43)}\\
&= \int_{-\infty}^{\infty}\int_{-\infty}^{\infty}\psi_n\left(\frac{t}{\tau}\right)\psi_n^*\left(\frac{\lambda}{\tau}\right)\times && \text{(B.44)}\\
&\quad P_{ASE}\delta(t-\lambda)\delta(T-T')dtd\lambda && \text{(B.45)}\\
&= \int_{-\infty}^{\infty}\left|\psi_n\left(\frac{t}{\tau}\right)\right|^2 dt \times P_{ASE}\delta(T-T') && \text{(B.46)}\\
&= P_{ASE}\delta(T-T'), && \text{(B.47)}
\end{aligned}$$

where we used the fact that the magnitude squared value of the Hermite-Gaussian function is orthonormal in the integration. It is interesting to note that the ASE noise projects equally into each Hermite-Gaussian order.

Next, we wish to obtain equations of motion for the amplitude, phase, timing, and frequency noise by expressing these fluctuations as the real and imaginary parts of ΔA_n.

Amplitude or "Energy" Fluctuations

The amplitude fluctuations are given by $\Re\{\Delta A_0\}$. Hermite Gaussians with order $\neq 0$ are orthogonal to the steady state solution a_{ss}. The real part of the perturbation influences the amplitude of the pulse while the imaginary part influences its phase. The equation of motion for ΔA_0 is obtained by substituting $n = 0$ into equation (B.33) and ignoring fast gain saturation for now

$$\frac{\partial}{\partial T}\Delta A_0(T) = \frac{\Delta g_{sgs}(T)}{T_R}\, A_0 + S_0(T). \tag{B.48}$$

The amplitude fluctuations are found by taking the real part

$$\frac{\partial}{\partial T}\Re\{\Delta A_0(T)\} = \Re\{\Delta A_0(T)\}\frac{A_0}{T_R}\left.\frac{\partial g}{\partial a}\right|_{a=a_{ss}} + \Re\{S_0(T)\} \tag{B.49}$$

$$\frac{\partial}{\partial T}\Delta w(T) = A_{ww}\,\Delta w + \Re\{S_0(T)\} \tag{B.50}$$

where

$$A_{ww} \equiv \frac{A_0}{T_R}\left.\frac{\partial g}{\partial a}\right|_{a=a_{ss}} \tag{B.51}$$

is a real quantity and is defined for notational convenience and we defined the amplitude fluctuations as

$$\Delta w(T) \equiv \Re\{\Delta A_0(T)\}, \tag{B.52}$$

which has units of $\sqrt{\text{Energy}}$.[3] Next we assume that the ASE power equally split between the real and imaginary parts, so that the autocorrelation function of $\Re\{S_0(T)\} \equiv S_0^{\Re}(T)$ is

$$\langle \Re\{S_0(T)\}\Re\{S_0(T')\}\rangle = \frac{1}{2}P_{ASE}\delta(T - T'). \tag{B.53}$$

The power spectrum is equal to the Fourier transform of the autocorrelation function and equals

$$|\tilde{S}_0^{\Re}[k]|^2 = \frac{P_{ASE}}{2\Delta T}. \tag{B.54}$$

[3]This notation is a bit misleading but is kept to keep consistency with the Haus and Mecozzi paper [10]. w_0 has units of energy. a has units of $\sqrt{\text{Power}}$. So, one would think that Δw would also have units of energy, but this is not the case.

The Fourier transform of equation (B.50) yields

$$j\Omega\,\Delta\tilde{w}[k] = A_{ww}\Delta\tilde{w}[k] + \tilde{S}_0^{\Re}[k] \tag{B.55}$$

$$\Delta\tilde{w}[k] = \frac{\tilde{S}_0^{\Re}[k]}{j\Omega + A_{ww}} \tag{B.56}$$

where $\partial/\partial t \rightarrow j\Omega$ and

$$\Omega \equiv \frac{2\pi k}{\Delta T}. \tag{B.57}$$

Multiplying both sides by their conjugates yields the power spectrum of the amplitude noise

$$|\Delta\tilde{w}[k]|^2 = \frac{|\tilde{S}_0^{\Re}[k]|^2}{\Omega^2 + A_{ww}^2} \tag{B.58}$$

$$= \frac{P_{ASE}}{2\Delta T}\frac{1}{\Omega^2 + \left(\frac{A_0}{T_R}\left.\frac{\partial g}{\partial a}\right|_{a=a_{ss}}\right)^2}. \tag{B.59}$$

The quantity $|\Delta\tilde{w}[k]|^2$ has units of energy. Equations (B.54) and (B.51) were substituted into equation (B.58) to get equation (B.59). The amplitude noise is mainly determined by the level of gain saturation, or in other words, the slope of the gain versus optical power. The greater the saturation, the lower the amplitude noise. The gain saturation is related to the loss due to filtering and amplitude modulation as we will see below.

We assume a shape for the saturation of the gain. The functional form of the gain with respect to power is shown in Fig. B-2 and is given by

$$g = \frac{g_{max}}{1 + \frac{P}{P_{sat}}}. \tag{B.60}$$

The differential gain is

$$\frac{\partial g}{\partial P} = -\frac{g_{max}/P_{sat}}{\left(1 + \frac{P}{P_{sat}}\right)^2}. \tag{B.61}$$

and is negative for all bias points. Using equation (B.28), the differential gain with

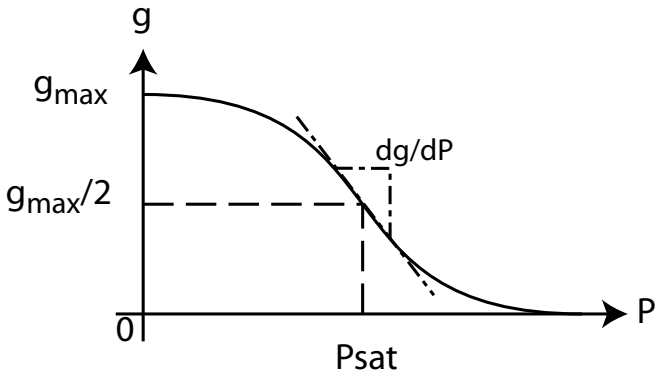

Figure B-2: Laser gain as a function of optical power.

respect to a is

$$\frac{\partial g}{\partial a} = -2a\frac{g_{max}/P_{sat}}{\left(1+\frac{|a|^2}{P_{sat}}\right)^2}. \tag{B.62}$$

Next, we assume that the steady-state power is equal to P_{sat} so that evaluation of the differential gain at $a = a_{ss} = \sqrt{P_{sat}} = A_0$ yields

$$\left.\frac{\partial g}{\partial a}\right|_{a=a_{ss}=\sqrt{P_{sat}}=A_0} = -\frac{g_{ss}}{A_0} = -\frac{T_R\,\Re\{\gamma_0\}+l}{A_0}, \tag{B.63}$$

where $g_{max}/2 = g_0$ and $g_0 = T_R\Re\{\gamma_0\} + l$ by equation (B.19). Substituting equation (B.63) into equation (B.59) results in a simplified form for the power spectrum of the amplitude noise

$$|\Delta\tilde{w}[k]|^2 = \frac{P_{ASE}}{2\Delta T}\frac{1}{\Omega^2+\left(\frac{T_R\Re\{\gamma_0\}+l}{T_R}\right)^2}. \tag{B.64}$$

This functional form shows that the energy fluctuations are now bounded by the restoring force of gain saturation.

Carrier Phase Fluctuations

The phase noise is related to $\Im\{\Delta A_0\}$ since

$$a_{ss} + j\Im\{\Delta A_0\}\psi_0 \;\; = \;\; (A_0 + j\Im\{\Delta A_0\})\psi_0 \tag{B.65}$$

$$\approx \quad A_0 \exp\left[j \tan^{-1}\left(\frac{\Im\{\Delta A_0\}}{A_0}\right)\right]\psi_0. \tag{B.66}$$

Therefore,

$$\Delta\phi \equiv \tan^{-1}\left(\frac{\Im\{\Delta A_0\}}{A_0}\right) \tag{B.67}$$

$$\approx \frac{\Im\{\Delta A_0\}}{A_0}. \tag{B.68}$$

The equation of motion for the carrier phase is found by substituting $n = 0$ into equation (B.33) and taking the imaginary part

$$\frac{\partial}{\partial T}\Im\{\Delta A_0(T)\} = \Im\{S_0(T)\} \tag{B.69}$$

$$\frac{\partial}{\partial T}\Delta\phi(T) = \frac{\Im\{S_0(T)\}}{A_0} \tag{B.70}$$

$$\frac{\partial}{\partial T}\Delta\phi(T) = \frac{S_0^{\Im}(T)}{A_0} \tag{B.71}$$

where $S_0^{\Im}(T) \equiv \Im\{S_0(T)\}$. The power spectrum of the ASE noise is equal to

$$\langle|\tilde{S}_0^{\Im}[k]|^2\rangle = \frac{P_{ASE}}{2\Delta T}. \tag{B.72}$$

since half the noise power is in the imaginary part and half in the real part (also see equation (B.54)). The Fourier transform of equation (B.71) is equal to

$$j\Omega\,\Delta\tilde{\phi}[k] = \frac{\tilde{S}_0^{\Im}[k]}{A_0}. \tag{B.73}$$

The power spectrum of the phase noise is obtained by multiplying equation B.73 by its complex conjugate to obtain

$$|\Delta\tilde{\phi}[k]|^2 = \frac{|\tilde{S}_0^{\Im}[k]|^2}{A_0^2\Omega^2} \tag{B.74}$$

$$= \boxed{\frac{P_{ASE}}{2\Delta T\, A_0^2\Omega^2}}. \tag{B.75}$$

The quantity $|\Delta\tilde{\phi}(\Omega)|^2$ is unitless. The power spectrum has a $1/\Omega^2$ dependence which implies that the phase undergoes a random walk. In other words, the phase is not restored and wanders everywhere. Increasing the pulse energy A_0^2 decreases the speed at which the phase wanders.

Timing or "Position" Fluctuations

Microwave engineers often refer to timing fluctuations as phase noise. We will not adopt this language when referring to timing jitter since it may be confused with the noise of the optical carrier.

The center of the pulse circulating in the laser cavity has the average position

$$\begin{aligned}
\Delta t(T) &= \frac{\int_{-T_R/2}^{T_R/2} t|a(t,T)|^2\,dt}{\int_{-T_R/2}^{T_R/2} |a(t,T)|^2\,dt} && \text{(B.76)}\\
&\approx \frac{\int_{-\infty}^{\infty} t|a(t,T)|^2\,dt}{\int_{-\infty}^{\infty} |a(t,T)|^2\,dt} && \text{(B.77)}\\
&= \frac{\int_{-\infty}^{\infty} t|a_{ss}(t)+\Delta a(t,T)|^2\,dt}{\int_{-\infty}^{\infty} |a_{ss}(t)+\Delta a(t,T)|^2\,dt} && \text{(B.78)}\\
&\approx \frac{\int_{-\infty}^{\infty} t(|a_{ss}(t)|^2+2a_{ss}(t)\Re\{\Delta a(t,T)\})\,dt}{\int_{-\infty}^{\infty} |a_{ss}(t)|^2\,dt} && \text{(B.79)}\\
&= \frac{\int_{-\infty}^{\infty} 2tA_0\psi_0(t/\tau)\Re\{\Delta a(t,T)\}\,dt}{A_0^2} && \text{(B.80)}\\
&= \frac{\int_{-\infty}^{\infty} \sqrt{2}A_0\tau\psi_1(t/\tau)\Re\{\Delta a(t,T)\}\,dt}{A_0^2} && \text{(B.81)}\\
&= \frac{\sqrt{2}}{A_0}\tau\int_{-\infty}^{\infty} \psi_1(t/\tau)\Re\{\Delta a(t,T)\}\,dt && \text{(B.82)}\\
&= \frac{\sqrt{2}}{A_0}\tau\int_{-\infty}^{\infty} \psi_1(t/\tau)\Re\{\sum_{m=0}^{\infty}\Delta A_m(T)\,\psi_m\left(\frac{t}{\tau}\right)\}\,dt && \text{(B.83)}\\
&= \frac{\sqrt{2}}{A_0}\tau\Re\{\Delta A_1(T)\} && \text{(B.84)}\\
&= \frac{\sqrt{2}}{A_0}\tau\Delta A_1^{\Re}(T) && \text{(B.85)}
\end{aligned}$$

where $\psi_1(t/\tau) = \sqrt{2}(t/\tau)\psi_0(t/\tau)$, $|a_{ss}(t)|^2 = A_0^2\psi_0(t/\tau)$, $\int|a_{ss}(t)|^2dt = A_0^2$, and $\Delta A_1^{\Re}(T) \equiv \Re\{\Delta A_1(T)\}$. The timing jitter is given by the real part of ΔA_1. The

equation of motion for ΔA_1 can be obtained from equation (B.33) by setting $n = 1$

$$\frac{\partial}{\partial T}\Delta A_1(T) = -2\gamma_0\, \Delta A_1(T) + S_1(T). \tag{B.86}$$

Taking the real part of equation (B.86) yields

$$\frac{\partial}{\partial T}\Delta A_1^{\Re}(T) = -2\gamma_0^{\Re}\, \Delta A_1^{\Re}(T) + 2\gamma_0^{\Im}\, \Delta A_1^{\Im}(T) + S_1^{\Re}(T), \tag{B.87}$$

where $\Re$ denotes the real part and $\Im$ denotes the imaginary part. We multiply equation (B.87) by $\frac{\sqrt{2}}{A_0}\tau$ and make use of equation (B.85) to obtain

$$\frac{\partial}{\partial T}\Delta t(T) = -2\gamma_0^{\Re}\, \Delta t(T) + 2\frac{\sqrt{2}}{A_0}\tau\gamma_0^{\Im}\, \Delta A_1^{\Im}(T) + \frac{\sqrt{2}}{A_0}\tau S_1^{\Re}(T), \tag{B.88}$$

Using equation (B.95) in equation B.88 yields

$$\frac{\partial}{\partial T}\Delta t(T) = -2\gamma_0^{\Re}\, \Delta t(T) + 2\tau^2\gamma_0^{\Im}\, \Delta p(T) + \frac{\sqrt{2}}{A_0}\tau S_1^{\Re}(T). \tag{B.89}$$

This equation indicates that timing and frequency fluctuations are coupled through $\gamma_0^{\Im}$, which is related to dispersion and phase modulation, see equation (B.105). We will continue the analysis of this equation and derive the power spectrum of the timing jitter in the next subsubsection since we also need an equation of motion for the frequency fluctuations.

Carrier Frequency or "Momentum" Fluctuations

The angular frequency fluctuations are caused by the imaginary part of ΔA_1 ($\Delta A_1^{\Im} \equiv \Im\{\Delta A_1\}$) since

$$a_{ss}(t) + j\Delta A_1^{\Im}\psi_1(t/\tau) \tag{B.90}$$

$$= A_0\psi_0(t/\tau) + j\Delta A_1^{\Im}\sqrt{2}(t/\tau)\psi_0(t/\tau) \tag{B.91}$$

$$= \left(A_0 + j\Delta A_1^{\Im}\sqrt{2}(t/\tau)\right)\psi_0(t/\tau) \tag{B.92}$$

$$\approx A_0 \exp\left[j \tan^{-1}\left(\frac{\Delta A_1^{\Im}\sqrt{2}(t/\tau)}{A_0}\right)\right]\psi_0(t/\tau) \quad \text{(B.93)}$$

$$\approx A_0 \exp\left[j\left(\frac{\sqrt{2}}{A_0}\frac{1}{\tau}\Delta A_1^{\Im}\right)t\right]\psi_0(t/\tau) \quad \text{(B.94)}$$

From equation (B.94), we can see that the change in the angular frequency is given by

$$\Delta p(T) \equiv \frac{\sqrt{2}}{A_0}\frac{1}{\tau}\Delta A_1^{\Im}(T) \quad \text{(B.95)}$$

Note that Δp has the same sign as $\Delta A_1^{\Im}$ due to our choice of representing the carrier frequency, Ω_c, in the steady-state electric-field solution as $a(t) = A_0\psi_0 t\exp(j\Omega_c t)$.

Taking the imaginary part of equation (B.86) yields the equation of motion for the frequency fluctuations

$$\frac{\partial}{\partial T}\Delta A_1^{\Im}(T) = -2\gamma_0^{\Re}\,\Delta A_1^{\Im}(T) - 2\gamma_0^{\Im}\,\Delta A_1^{\Re}(T) + S_1^{\Im}(T), \quad \text{(B.96)}$$

Multiplying equation (B.96) by $\frac{\sqrt{2}}{A_0}\frac{1}{\tau}$ and using equation (B.95) and (B.85), we get

$$\frac{\partial}{\partial T}\Delta p(T) = -2\gamma_0^{\Re}\,\Delta p(T) - 2\gamma_0^{\Im}\frac{1}{\tau^2}\,\Delta t(T) + \frac{\sqrt{2}}{A_0}\frac{1}{\tau}S_1^{\Im}(T), \quad \text{(B.97)}$$

Equations (B.89) and (B.96) are the two coupled equations of motion for the timing and frequency noise. Taking the Fourier transform of these equations yields

$$j\Omega\,\Delta\tilde{t}[k] = -2\gamma_0^{\Re}\,\Delta\tilde{t}[k] + 2\gamma_0^{\Im}\tau^2\,\Delta\tilde{p}[k] + \frac{\sqrt{2}}{A_0}\tau\tilde{S}_1^{\Re}[k] \quad \text{(B.98)}$$

$$j\Omega\,\Delta\tilde{p}[k] = -2\gamma_0^{\Im}\frac{1}{\tau^2}\,\Delta\tilde{t}[k] - 2\gamma_0^{\Re}\,\Delta\tilde{p}[k] + \frac{\sqrt{2}}{A_0}\frac{1}{\tau}\tilde{S}_1^{\Im}[k]. \quad \text{(B.99)}$$

The solution to these two equations are

$$\Delta\tilde{t}[k] = \tau\frac{\sqrt{2}}{A_0}\frac{(j\Omega + 2\gamma_0^{\Re})\tilde{S}_1^{\Re}[k] + 2\gamma_0^{\Im}\tilde{S}_1^{\Im}[k]}{j4\gamma_0^{\Re}\Omega - \Omega^2 + (2\gamma_0^{\Re})^2 + (2\gamma_0^{\Im})^2} \quad \text{(B.100)}$$

$$\Delta\tilde{p}[k] = \frac{1}{\tau}\frac{\sqrt{2}}{A_0}\frac{-2\gamma_0^{\Im}\tilde{S}_1^{\Re}[k] + (j\Omega + 2\gamma_0^{\Re})\tilde{S}_1^{\Im}[k]}{j4\gamma_0^{\Re}\Omega - \Omega^2 + (2\gamma_0^{\Re})^2 + (2\gamma_0^{\Im})^2}. \quad \text{(B.101)}$$

The power spectra are

$$|\Delta\tilde{t}[k]|^2 = \frac{\tau^2 P_{ASE}}{A_0^2\,\Delta T}\frac{\Omega^2+(2\gamma_0^{\Re})^2+(2\gamma_0^{\Im})^2}{(4\gamma_0^{\Re})^2\Omega^2+\left[-\Omega^2+(2\gamma_0^{\Re})^2+(2\gamma_0^{\Im})^2\right]^2} \tag{B.102}$$

$$|\Delta\tilde{p}[k]|^2 = \frac{P_{ASE}}{\tau^2 A_0^2\,\Delta T}\frac{\Omega^2+(2\gamma_0^{\Re})^2+(2\gamma_0^{\Im})^2}{(4\gamma_0^{\Re})^2\Omega^2+\left[-\Omega^2+(2\gamma_0^{\Re})^2+(2\gamma_0^{\Im})^2\right]^2}. \tag{B.103}$$

where $|\tilde{S}_1^{\Re}[k]|^2 = |\tilde{S}_1^{\Im}[k]|^2 = P_{ASE}/(2\Delta T)$. It is interesting to note that the timing jitter and the frequency noise have the same functional form. This should not be surprising since the ASE noise projects evenly into the timing and frequency noise components. The real and imaginary parts of γ_0 can be expressed in terms of the laser parameters as

$$\begin{aligned}\gamma_0^{\Re} &= \Re\left\{\frac{F}{\tau^2}\right\} = \frac{1}{\Omega_f^2\tau^2 T_R} \\ &= \Re\left\{A\tau^2\right\} = \frac{M_{AM}\omega_M^2\tau^2}{4T_R}\end{aligned} \tag{B.104}$$

and

$$\begin{aligned}\gamma_0^{\Im} &= \Im\left\{\frac{F}{\tau^2}\right\} = \frac{D}{\tau^2 T_R} \\ &= \Im\left\{A\tau^2\right\} = \frac{M_{PM}\omega_M^2\tau^2}{4T_R},\end{aligned} \tag{B.105}$$

where γ_0 has units of 1/time.

Equations (B.102) and (B.103) are the most important results of this section. Let's see if we can get a better physical understanding of these equations. In the next few subsections, we will see what happens when the amplitude or phase modulator is turned off, and examine the shape of the power spectral densities of the timing and frequency noise.

Turn off amplitude modulator or remove optical BPF If the amplitude modulator is turned off so that $M_{AM} \to 0$ or if the optical filter is removed so that $\Omega_f \to \infty$, then $\gamma_0^{\Re} \to 0$ according to equation B.104. Equations (B.102) and (B.103)

simplify to

$$|\Delta\tilde{t}[k]|^2 = \frac{\tau^2 P_{ASE}}{A_0^2\,\Delta T}\frac{\Omega^2+(2\gamma_0^{\Im})^2}{\left[-\Omega^2+(2\gamma_0^{\Im})^2\right]^2} \tag{B.106}$$

$$|\Delta\tilde{p}[k]|^2 = \frac{P_{ASE}}{\tau^2 A_0^2\,\Delta T}\frac{\Omega^2+(2\gamma_0^{\Im})^2}{\left[-\Omega^2+(2\gamma_0^{\Im})^2\right]^2}. \tag{B.107}$$

These equations show that the noise blows up at $\Omega = 2\gamma_0^{\Im}$ since there is no amplitude modulation to restore the pulses to their time slots or optical filtering to restore the spectrum to its center frequency. Equations (B.98) and (B.99) show that the restoration force to the timing and frequency is given by the real part of γ_0 Decreasing the amplitude modulation is equivalent to opening up the optical filtering bandwidth according to equation (B.104).

Turn off phase modulator If the phase modulator is turned off so that $M_{PM} \to 0$, then $\gamma_0^{\Im} \to 0$. Here we assume that the amplitude modulator is still on. Equations (B.102) and (B.103) simplify to

$$|\Delta\tilde{t}[k]|^2 = \frac{\tau^2 P_{ASE}}{A_0^2\,\Delta T}\frac{1}{\Omega^2+(2\gamma_0^{\Re})^2} \tag{B.108}$$

$$|\Delta\tilde{p}[k]|^2 = \frac{P_{ASE}}{\tau^2 A_0^2\,\Delta T}\frac{1}{\Omega^2+(2\gamma_0^{\Re})^2}. \tag{B.109}$$

These equations do not have a zero in the denominator and hence the timing jitter and frequency noise is finite without phase modulation. For an AM actively mode-locked laser, the power spectral density simply has a Lorentzian shape. Decreasing amount of phase modulation is equivalent to decreasing the dispersion according to equation (B.105).

Plot of PSD of Timing and Frequency Noise Equations (B.102) and (B.103) have only one of two general shapes. Equation (B.102) is rewritten in pole-zero form

$$|\Delta\tilde{t}[k]|^2 = \frac{\tau^2 P_{ASE}}{A_0^2\,\Delta T}\frac{(\Omega-\Omega_{z1})(\Omega-\Omega_{z2})}{(\Omega-\Omega_{p1})(\Omega-\Omega_{p2})(\Omega-\Omega_{p3})(\Omega-\Omega_{p4})}, \tag{B.110}$$

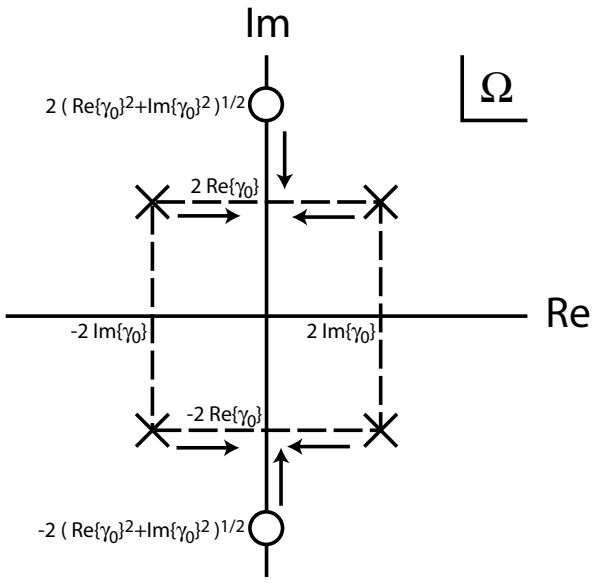

Figure B-3: Pole-zero diagram of the psd of the timing jitter.

where

$$\Omega_{p1} = 2(\gamma_0^{\Im} + j\gamma_0^{\Re}) \tag{B.111}$$

$$\Omega_{p2} = -2(\gamma_0^{\Im} - j\gamma_0^{\Re}) \tag{B.112}$$

$$\Omega_{p3} = 2(\gamma_0^{\Im} - j\gamma_0^{\Re}) \tag{B.113}$$

$$\Omega_{p4} = -2(\gamma_0^{\Im} + j\gamma_0^{\Re}) \tag{B.114}$$

$$\Omega_{z1} = 2\sqrt{\Omega_{p1}\Omega_{p2}} = 2j\sqrt{(\gamma_0^{\Im})^2 + (\gamma_0^{\Re})^2} \tag{B.115}$$

$$\Omega_{z2} = -2\sqrt{\Omega_{p1}\Omega_{p2}} = -2j\sqrt{(\gamma_0^{\Im})^2 + (\gamma_0^{\Re})^2}. \tag{B.116}$$

The pole-zero diagram of the timing jitter power spectral density is shown in Fig. B-3. Note that this is the Ω plane, not the usual s plane that electrical engineers are comfortable with. Therefore, we evaluate the function on the real axis (not the imaginary axis). The arrows show the movement of the poles and zeros as $\gamma_0^{\Im} \to 0$. When $\gamma_0^{\Im} = 0$, the pole-zero plot has two poles on the imaginary axis.

The bode plot of the timing jitter power spectral density is shown in Fig. B-4. The maximum value at $\Omega = 0$ is $|\Delta\tilde{t}[0]|^2 = \frac{\tau^2 P_{ASE}}{A_0^2\,\Delta T}\frac{1}{(2\gamma_0^{\Re})^2+(2\gamma_0^{\Im})^2}$. The denominator is

proportional to the square of the magnitude of the zero. Integrating equation (B.102) over all Ω yields the pulse-to-clock (pc) timing jitter

$$\sigma_{t,pc}^2 = \sum_{k=-\infty}^{\infty} |\Delta\tilde{t}[k]|^2 = \int_{-\infty}^{\infty} |\Delta\tilde{t}[k]|^2 \Delta T \, \frac{d\Omega}{2\pi} = \frac{\tau^2 P_{ASE}}{A_0^2 \, \Delta T} \frac{\pi}{\gamma_0^{\Re}} \frac{1}{2\pi} = \frac{\tau^2}{A_0^2 \gamma_0^{\Re}} \frac{P_{ASE}}{2}. \quad \text{(B.117)}$$

Integrating equation (B.103) over all Ω yields the pulse-to-clock (pc) frequency variance

$$\sigma_{p,pc}^2 = \frac{1}{\tau^2 A_0^2 \gamma_0^{\Re}} \frac{P_{ASE}}{2}. \quad \text{(B.118)}$$

The total timing jitter and frequency noise is determined by the real part of γ_0. The total timing jitter variance scales inversely with amplitude modulation depth. Fig. B-4 shows that the timing jitter power spectral density always rolls off at 20 dB/decade. This is not necessarily true in soliton lasers where 40 dB/decade is possible. If dispersion were introduced into the cavity, then, according to equation (B.105), $\gamma_0^{\Im}$ would be non-zero and one would need to integrate equation (B.110) to obtain the total timing jitter.

For amplitude modulation ($D = 0$ and $M_{PM} = 0$), we can use equation (B.15) and (B.104) in equation (B.117) and (B.118) to obtain

$$\sigma_{t,pc}^2 = \frac{4}{M_{AM}\omega_M^2} \times \frac{P_{ASE} T_R}{2w_0} = 2\frac{P_{ASE} T_R}{M_{AM}\omega_M^2 w_0} \quad \text{(B.119)}$$

$$\sigma_{p,pc}^2 = \Omega_f^2 \times \frac{P_{ASE} T_R}{2w_0}, \quad \text{(B.120)}$$

where $w_0 = A_0^2$ is the pulse energy. The timing variance is inversely proportional to $4M_{AM}\omega_M^2$ and the frequency variance is proportional to Ω_f^2. In addition, notice that the variances are proportional to the ASE energy divided by the pulse energy. For a harmonically modelocked laser, T_R should be replaced by T_M, since it is the amount of ASE energy per time slot that counts. Another way to look at it is to keep T_R equal to the cavity round-trip time, but note that w_0 becomes the sum of the energy of all the pulses in the cavity.

The theoretical expressions for the timing jitter are compared to the measured residual phase noise of the temperature controlled external-cavity modelocked semi-

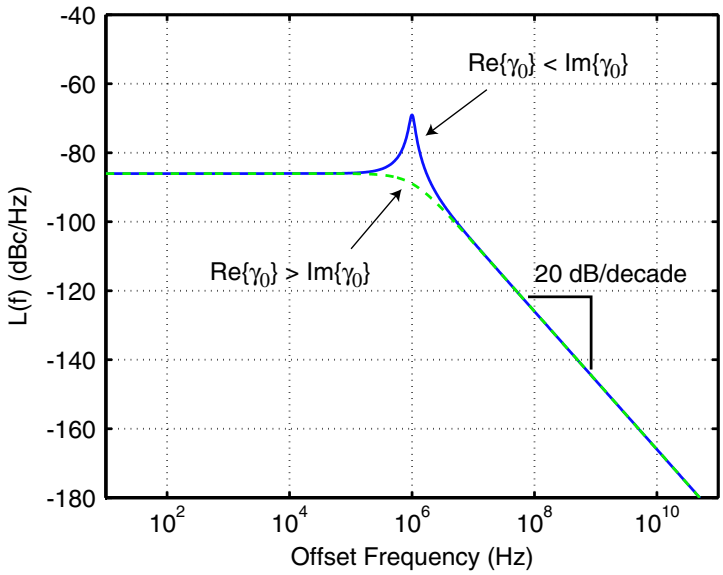

Figure B-4: Bode plot (log-log plot) of timing jitter psd. Phase modulation and dispersion causes Q-ing of the curve. Parameters for dotted line: $2\gamma_0^{\Re} = 2\pi \times 100$ kHz, and $2\gamma_0^{\Im} = 2\pi \times 1$ MHz. Parameters for solid line: $2\gamma_0^{\Re} = 2\pi \times 1$ MHz, and $2\gamma_0^{\Im} = 2\pi \times 100$ kHz. Common parameters: $P_{ASE} = 1.1897\ \mu$W, $n_{sp} = 3$, $B = 3.325 \times 10^{11}$ Hz, $\tau = 3$ ps, $\tau_p = 10^{-11}$ and $T_R = 100$ ps. $L(f)$ is defined by equation (B.121).

conductor laser at 10 GHz. The results are shown in Fig. B-5. The power spectral density of the timing jitter can be converted to the phase noise power spectral density by the following relation

$$L(f) = \left(\frac{2\pi}{T_M}\right)^2 \times \frac{\Delta T}{2\pi} \times |\Delta t[k]|^2, \tag{B.121}$$

where the first factor on the r.h.s of the equal sign converts from a timing jitter psd to a phase noise psd, and the second factor converts the discrete timing jitter psd into a continuous timing jitter psd. The single-sided phase noise spectrum for an actively modelocked laser can be found by substituting equation (B.106) into equation (B.121) to obtain

$$L(f) = \left(\frac{2\pi}{T_M}\right)^2 \frac{\tau^2 P_{ASE}}{2\pi A_0^2} \frac{1}{(2\pi f)^2 + (2\gamma_0^{\Re})^2}. \tag{B.122}$$

The values used in constructing the dashed lines in Fig. B-5 were $P_{ASE} = 0.008$ mW, $A_0^2 = 0.7$ pJ, $\tau = 3.5$ ps, $T_M = 100$ ps, $2\gamma_0^{\Re}(24 \text{ dBm}) = 2\pi \times 1.8$ MHz, and $2\gamma_0^{\Re}(15 \text{ dBm}) = 2\pi \times 450$ kHz.[4] As one can clearly see from the figure, this simple analytic theory can accurately describe the noise in the modelocked semiconductor laser. The figure shows that as the modulation depth is decreased, the noise increases. The integrated noise values from 10 Hz to 10 MHz are 951 fs (with 24 dBm drive)

[4]The fitting parameters for $\gamma_0^{\Re}$ are

$$2\gamma_0^{\Re} = 2\frac{1}{\Omega_f^2 \tau^2 T_R} = \frac{1}{(2\pi \times 333 \text{ GHz})^2 (3.5 \text{ ps})^2 (100 \text{ ps})} = 2\pi \times 29.678 \text{ MHz} \tag{B.123}$$

$$2\gamma_0^{\Re} = 2\frac{M_{AM}\omega_M^2 \tau^2}{4T_R} = 2\frac{0.0234 \times (2\pi \times 10 \text{ GHz})^2 (3.5 \text{ ps})^2}{4 \times (100 \text{ ps})} = 2\pi \times 1.8 \text{ MHz} \tag{B.124}$$

$$2\gamma_0^{\Re} = 2\frac{M_{AM}\omega_M^2 \tau^2}{4T_R} = 2\frac{0.00585 \times (2\pi \times 10 \text{ GHz})^2 (3.5 \text{ ps})^2}{4 \times (100 \text{ ps})} = 2\pi \times 450 \text{ kHz}. \tag{B.125}$$

The first estimate using the optical filter bandwidth gives an answer that is much larger than the experimental results. The next two estimates indicate that the amplitude modulator must be very weak, 0.0234 and 0.00585, for the 24 and 15 dBm cases, respectively. The modulation depth of the hybridly modelocked semiconductor lasers is small since they are primarily passively modelocked with the saturable absorber. By increasing the rf drive power to the saturable absorber results in a decreased saturable absorber effect and gives rise to satellite pulses. According to these numbers, a 9 dB (×6) change in the RF drive power causes a 6 dB (×4) change of M_{AM}. If the modulator were an electro-optic modulator, one would expect that the modulation depth should change as $M \propto V \propto \sqrt{P}$. This would imply that a 9 dB change in power should change M by 4.5 dB. Since the modulation depth changes by 6 dB, M is not simply linear with voltage. This is not surprising since it is an electro-absorption modulator that has a more complicated relation between M and V.

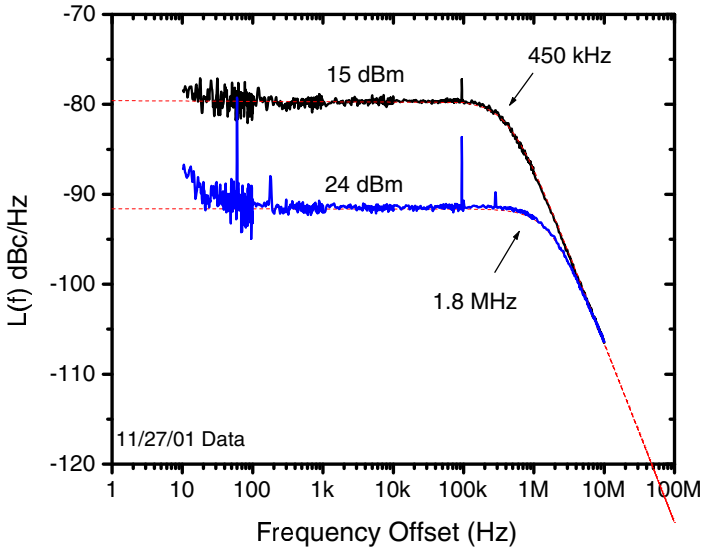

Figure B-5: Single-sideband phase noise of the temperature controlled external-cavity modelocked semiconductor laser at 10 GHz. The phase noise increases as the microwave driving power to the saturable absorber decreases from 24 dBm to 15 dBm. The dashed lines show the theoretical values.

and 1943 fs (with 15 dBm drive).

In summary, the full set of the equations of motion for actively modelocked lasers is

$$\frac{\partial}{\partial T}\Delta w(T) = A_{ww}\Delta w(T) + \Re\{S_0(T)\} \tag{B.126}$$

$$\frac{\partial}{\partial T}\Delta \phi(T) = \frac{1}{A_0}\Im\{S_0(T)\} \tag{B.127}$$

$$\frac{\partial}{\partial T}\Delta t(T) = -2\gamma_0^{\Re}\Delta t(T) + 2\tau^2\gamma_0^{\Im}\Delta p(T) + \frac{\sqrt{2}}{A_0}\tau\Re\{S_1(T)\} \tag{B.128}$$

$$\frac{\partial}{\partial T}\Delta p(T) = -2\gamma_0^{\Re}\Delta p(T) - \frac{2}{\tau^2}\gamma_0^{\Im}\Delta t(T) + \frac{\sqrt{2}}{A_0}\frac{1}{\tau}\Im\{S_1(T)\}. \tag{B.129}$$

B.2.3 Gain Dynamics

Relaxation oscillations in the amplitude of semiconductor lasers have are well known [1] and physically arise from perturbations to the laser system from ASE. The perturbation excites the laser cavity at its natural resonance determined by the product of

the carrier and photon lifetimes. The perturbation causes the photon number in the cavity to undergo a damped oscillation about the steady-state value. The relaxation oscillation frequency is typically around 1-3 GHz in semiconductor lasers [88, p.251]. The relative intensity noise (RIN = $\langle \Delta P^2 \rangle / P_0^2$) is typically -110 to -120 dB/Hz.

The importance of RIN in semiconductor lasers is hard to appreciate without comparing it to that of EDFLs.

The relaxation oscillation frequency of EDFLs is typically tens of kilohertz, whereas it is typically a gigahertz in semiconductor lasers. More importantly, the width of the RIN spectrum is tens of kilohertz for EDFLs but on the order of a gigahertz for a semiconductor laser. The RIN peak the EDFL has been measured at -50 to -60 dB/Hz [89, 90] and the RIN peak of the semiconductor laser has been measured at -110 to -125 dB/Hz [88, p.251]. The integrated value of RIN of the EDFL and semiconductor laser are approximately equal[5], and hence this indicates that the effect of gain dynamics on timing jitter should be similar in EDFLs and semiconductor lasers.

This section analyzes how the amplitude fluctuations at the relaxation oscillation frequency can enhance the timing jitter. Not only does the amplitude noise contain energy at the relaxation oscillation frequency, but so too does the timing jitter power spectral density. There are two mechanisms by which amplitude noise fluctuations couple to timing fluctuations mediated through carrier fluctuations.

- Fast gain saturation A change in the photon number causes a change in the gain. A change in the gain causes a change in the timing due to the fast saturation of the gain. Since the gain does not change much per pulse in EDFLs, this effect should be negligible in EDFLs.

- Relaxation oscillations A change in the carrier number due to any perturbation changes both the gain and the group velocity through the Kramer-Kronig relationship. The effective propagation delay through the gain medium changes on the scale of the relaxation oscillation period. This type of noise is present in

[5]For EDFL: $\sigma_{pwr}^2 = 10^{-60/10}$ 1/Hz $\times$ 10^4 Hz $= 10^{-2}$. For semiconductor lasers: $\sigma_{pwr}^2 = 10^{-110/10}$ 1/Hz $\times$ 10^9 Hz $= 10^{-2}$.

EDFLs.

The noise energy due to both these effects is centered at the relaxation oscillation frequency. In addition, injection current, saturable absorber voltage, and temperature fluctuations couple into the laser noise in a classical manner. This will be addressed in the third subsubsection.

Noise due to Fast Gain Saturation

Fast gain saturation couples amplitude fluctuations to timing jitter fluctuations. In this section we will derive the one way coupling of noise from amplitude noise to gain fluctuations to timing jitter, $\Delta w \rightarrow \Delta g \rightarrow \Delta t$. The first step in deriving the coupling constant amplitude and time fluctuations in the equations of motion is to first write the rate equations

$$\frac{\partial}{\partial T}N(T) = -\frac{N(T)}{\tau_N} - \sigma N_p(T)N(T) + \frac{I}{q} + S_N(T) \quad \text{(B.130)}$$

$$\frac{\partial}{\partial T}N_p(T) = -\frac{N_p(T)}{\tau_p} + \sigma\, N_p(T)\, N(T) + S_{N_p}(T) \quad \text{(B.131)}$$

where N is the carrier number, N_p is the photon number, τ_N is the carrier lifetime, τ_p is the photon lifetime, I is the injection current, q is the charge of a proton, σ is the gain constant or coupling constant in units of 1/time, $S_N(T)$ is the carrier noise, and $h\nu S_{N_p} = S_w(T) = \Re\{S_0(T)\}$ is the photon number noise. These equations can be linearized with the substitution $N(T) = N_0 + \Delta N(T)$ and $N_p(T) = N_{p0} + \Delta N_p(T)$ to obtain

$$\frac{\partial}{\partial T}\Delta N(T) = -\left(\frac{1}{\tau_N} + \sigma N_{p0}\right)\Delta N(T) - \sigma N_0\, \Delta N_p(T) + S_N(T) \quad \text{(B.132)}$$

$$\frac{\partial}{\partial T}\Delta N_p(T) = \sigma N_{p0}\, \Delta N(T) + S_{N_p}(T). \quad \text{(B.133)}$$

We next take the Fourier transform of these equations ($\partial/\partial T \rightarrow j2\pi k/\Delta T \equiv j\Omega$, $\Delta N(T) \rightarrow \Delta\tilde{N}[k]$, $\Delta N_p(T) \rightarrow \Delta\tilde{N}_p[k]$, $S_N(T) \rightarrow \tilde{S}_N[k]$, $S_{N_p}(T) \rightarrow \tilde{S}_{N_p}[k]$) and solve

for the carrier and amplitude fluctuations.

$$\Delta\tilde{N}[k] = \frac{j\Omega\tilde{S}_N[k] - \sigma N_0 \tilde{S}_{N_p}[k]}{\Omega_0^2 - \Omega^2 + \frac{j\Omega}{\tau_{pN}}} \tag{B.134}$$

$$\Delta\tilde{N}_p[k] = \frac{\sigma N_{p0}\tilde{S}_N[k] + \left(j\Omega + \frac{1}{\tau_{pN}}\right)\tilde{S}_{N_p}[k]}{\Omega_0^2 - \Omega^2 + \frac{j\Omega}{\tau_{pN}}} \tag{B.135}$$

where

$$\frac{1}{\tau_{pN}} = \frac{1}{\tau_N} + \sigma N_{p0} = \frac{I}{qN_0} = \sigma\tau_p\frac{I}{q} \tag{B.136}$$

is the population decay rate augmented by the induced emission rate, and

$$\Omega_0^2 = \sigma^2 N_0 N_{p0} \tag{B.137}$$

is the relaxation oscillation frequency.

The next step the derivation is to find the change of the gain after passage of a pulse.

The differential carrier number is caused by the amplitude fluctuations. Over short time scales, denoted by t, the $1/\tau_N$ term in equation (B.130) can be ignored since the carrier lifetime is much longer than the pulse duration, and the equation can be re-written as

$$\frac{\partial}{\partial t}N(t) = -\sigma N_p(t)N(t). \tag{B.138}$$

The solution to this equation is

$$N(t) = N_0 \exp\left(-\sigma\int_{-\infty}^{t} N_p(t)dt\right) \approx N_0 - N_0\sigma\int_{-\infty}^{t} N_p(t)dt. \tag{B.139}$$

where N_0 is the peak carrier number and the approximation $\exp(x) \approx 1 + x$ was used. The carrier number can be written as the sum of the steady-state noiseless carrier number plus the noise carriers $N(t) = N_{ss}(t) + \Delta N(t)$ and likewise for the the photon number, $N_p(t) = N_{p,ss}(t) + \Delta N_p(t)$. With these substitutions equation (B.139)

becomes

$$[N_{ss}(t) + \Delta N(t)] = N_0 - N_0\sigma \int_{-\infty}^{t} [N_{p,ss}(t) + \Delta N_p(t)]dt. \tag{B.140}$$

Therefore, the carrier number perturbation is related to the photon number perturbation by

$$\Delta N(t) = -N_0\sigma \int_{-\infty}^{t} \Delta N_p(t)dt. \tag{B.141}$$

The gain changes proportionally to the carrier number according to [6]

$$\Delta g_p(t) = T_R\sigma\Delta N(t) = -T_R\sigma^2 N_0 \int_{-\infty}^{t} \Delta N_p(t')dt'. \tag{B.142}$$

The instantaneous photon number is related to the pulse energy by

$$N_p(t) = \frac{T_R a_{ss}^2(t)}{h\nu} = \frac{A_0^2\,\psi_0^2(t/\tau)}{h\nu}. \tag{B.143}$$

The steady-state photon number in a time-slot is

$$N_{p0}(T) = \int_{-\infty}^{\infty} \frac{A_0^2}{h\nu}\,\psi_0^2(t/\tau)dt. = \frac{A_0^2}{h\nu} \tag{B.144}$$

The change in the photon number over one time slot is

$$\Delta N_p(t) = \Delta[\frac{T_R A_0^2\,\psi_0^2(t/\tau)}{h\nu}] = \frac{T_R\psi_0^2(t)}{h\nu}\,\Delta[A_0^2] = \frac{2T_R A_0}{h\nu}\,\Re\{\Delta A_0\}\,\psi_0^2(t/\tau). \tag{B.145}$$

The quantity "ΔA_0" was written as $\Re\{\Delta A_0\}$ since A_0 is real and we do not want to confuse this with our previous notation that assumes ΔA_0 is a complex quantity.

The expression for fast gain saturation of the amplitude gain is related to the photon number gain through

$$\Delta g_{fgs}(t,T) = \frac{\Delta g_p(t)}{2} = -\frac{T_R^2\sigma^2 N_0 A_0}{h\nu}\,\Re\{\Delta A_0(T)\}\,\int_{-\infty}^{t} \psi_0^2(t'/\tau)dt' \tag{B.146}$$

[6] The gain ($N_{p,out} = e^{g_p}N_{p,in}$ and $a_{out} = e^{g_p/2}a_{in}$) is $g_p = \sigma N(t)$. The differential pulse energy gain is $\Delta g_p = \sigma\,\Delta N(t)$.

n	C_n	n	C_n
0	0.5	11	-0.00131856
1	0.282095	12	0
2	0	13	0.00058063
3	-0.0575824	14	0
4	0	15	-0.000260437
5	0.0193137	16	0
6	0	17	0.000118435
7	-0.00745043	18	0
8	0	19	-0.000054436
9	0.00307314	20	0
10	0	21	0.0000252339

Table B.2: Tabulated values for the unitless constant $C_n \equiv \int_{-\infty}^{\infty} \left(\int_{-\infty}^{t} \psi_0^2(t'/\tau) dt' \right) \psi_0(t/\tau) \psi_n^*(t/\tau) dt$.

where equations (B.142) and (B.145) were used, and we not that $\Re\{\Delta A_0(T)\}$ is the only quantity that changes on a round-trip time scale. We can substitute equation (B.146) into equation (B.33) to obtain

$$\begin{aligned}
\frac{\partial}{\partial T}\Delta A_n(T) &= -2n\gamma_0\, \Delta A_n(T) + \frac{\Delta g_{sgs}(T)}{T_R}\, A_0 \delta(n) \\
&\quad + \int_{-\infty}^{\infty} \frac{-T_R^2 \sigma^2 N_0 A_0\, \Re\{\Delta A_0(T)\}\ \int_{-\infty}^{t} \psi_0^2(t'/\tau) dt'}{h\nu T_R} A_0 \psi_0(t/\tau) \psi_n^*(t/\tau) dt \\
&\quad + S_n(T) \\
&= -2n\gamma_0\, \Delta A_n(T) + \frac{\Delta g_{sgs}(T)}{T_R}\, A_0 \delta(n) \\
&\quad - \frac{C_n \sigma^2 N_0 A_0^2 T_R\, \Re\{\Delta A_0(T)\}}{h\nu} + S_n(T) \\
&= -2n\gamma_0\, \Delta A_n(T) + \frac{\Delta g_{sgs}(T)}{T_R}\, A_0 \delta(n) \\
&\quad - C_n \Omega_0^2 T_R\, \Re\{\Delta A_0(T)\} + S_n(T),
\end{aligned} \tag{B.147}$$

where Ω_0 is the relaxation oscillation frequency and C_n is a unitless constant whose values are tabulated as a function of n in table B.2. One can see that the C_n become vanishingly small for $n \geq 2$.

The amplitude fluctuations, $\Delta w(T) = \Re\{\Delta A_0(T)\}$, are found by taking the real

part of equation (B.147) for $n = 0$

$$\begin{aligned}\frac{\partial}{\partial T}\Delta w(T) &= \underbrace{\frac{\Delta g_{sgs}(T)}{T_R}\,A_0}_{A_{ww}\Delta w(T)} - C_0\Omega_0^2 T_R\,\Delta w(T) + S_0^{\Re}(T) \\ &= (A_{ww} - 0.5\Omega_0^2 T_R)\Delta w(T) + S_0^{\Re}(T). \end{aligned} \tag{B.148}$$

For semiconductor lasers at 10 GHz repetition rate[7], $0.5\Omega_0^2 T_R \approx 2 \times 10^9$ s^{-1}, and for EDFLs at 10 GHz[8], $0.5\Omega_0^2 T_R \approx 1$ s^{-1}. Since the gain responds much faster, the amplitude noise in semiconductor lasers is damped more quickly. For both semiconductor lasers and EDFLs, the slow gain saturation term, A_{ww}, dominates at high repetition rates. For a semiconductor lasers[9], $A_{ww} \approx 10^{10}$ s^{-1}. Therefore at high repetition rates, the damping term governing the evolution of the amplitude noise is dominated by slow gain saturation.

The timing fluctuations, $\Delta t(T) = \Re\{\Delta A_1(T)\}$, are found by taking the real part of equation (B.147) and multiplying by $\sqrt{2}\tau/A_0$ for $n = 1$

$$\begin{aligned}\frac{\partial}{\partial T}\Delta t(T) &= -2\gamma_0^{\Re}\Delta t(T) + 2\tau^2\gamma_0^{\Im}\Delta p(T) - \frac{\sqrt{2}}{A_0}\tau C_1\Omega_0^2 T_R\Delta w(T) + \frac{\sqrt{2}}{A_0}\tau S_1^{\Re}(T) \\ &= -2\gamma_0^{\Re}\Delta t(T) + 2\tau^2\gamma_0^{\Im}\Delta p(T) - 0.4\Omega_0^2\tau T_R\frac{\Delta w(T)}{A_0} \\ &\quad + \frac{\sqrt{2}}{A_0}\tau S_1^{\Re}(T) \end{aligned} \tag{B.149}$$

This equation is similar to equation (B.89) with the addition of a dependence on the amplitude fluctuations. An increase in the amplitude, $\Delta w(T) > 0$, causes the gain to compress sooner, and hence the pulse advances in time. The pulse is delayed when the amplitude noise fluctuations are negative. The amplitude noise contribution to the timing jitter is significant. If we divide equation (B.149) by T_R and compare the timing $2\gamma_0^{\Re}\frac{\Delta t}{T_R}$ and amplitude $0.4\Omega_0^2\tau\frac{\Delta w}{A_0}$ terms on the r.h.s., we note that they are approximately the same order of magnitude [10].

[7] $\Omega_0 = 2\pi \times 1$ GHz
[8] $\Omega_0 = 2\pi \times 22.5$ kHz
[9] $\gamma_0^{\Re} = 2\pi \times 225 - 900$ kHz, $l \approx 1$, $T_R = 100$ ps
[10] $2\gamma_0^{\Re} \approx 3 \times 10^6 - 10^7$ and $0.4\Omega_0^2\tau \approx 5.5 \times 10^7$

The new equations of motion are expanded to include an additional equation for the carriers

$$\frac{\partial}{\partial T}\Delta N(T) = -\left(\frac{1}{\tau_N}+\sigma N_{p0}\right)\Delta N(T) - \sigma N_0 \frac{2A_0}{h\nu}\Delta w(T) + S_N(T) \quad \text{(B.150)}$$

$$\frac{\partial}{\partial T}\Delta w(T) = \sigma\frac{A_0}{2}\Delta N(T) + \underbrace{\Re\{S_0(T)\}}_{S_w(T)} \quad \text{(B.151)}$$

$$\frac{\partial}{\partial T}\Delta \phi(T) = \underbrace{\frac{1}{A_0}\Im\{S_0(T)\}}_{S_\phi(T)} \quad \text{(B.152)}$$

$$\frac{\partial}{\partial T}\Delta t(T) = -2\gamma_0^{\Re}\Delta t(T) + 2\tau^2\gamma_0^{\Im}\Delta p(T) - 0.4\Omega_0^2\tau T_R\frac{\Delta w}{A_0} + \underbrace{\frac{\sqrt{2}}{A_0}\tau\Re\{S_1(T)\}}_{S_t(T)} \quad \text{(B.153)}$$

$$\frac{\partial}{\partial T}\Delta p(T) = -2\gamma_0^{\Re}\Delta p(T) - \frac{2}{\tau^2}\gamma_0^{\Im}\Delta t(T) + \underbrace{\frac{\sqrt{2}}{A_0}\frac{1}{\tau}\Im\{S_1(T)\}}_{S_p(T)}. \quad \text{(B.154)}$$

where $N_{p0} = A_0^2/h\nu$, $\Delta N_p(T) = \frac{2A_0}{h\nu}\Delta A_0 = \frac{2A_0}{h\nu}\Delta w(T)$, and $S_{N_p}(T) = \frac{2A_0}{h\nu}S_w(T)$. Equation (B.151) is the equation of motion for amplitude fluctuations. Instead of assuming a gain profile and deriving A_{ww}, we can directly use the carrier-photon number equations, (B.132) and (B.133), to obtain the effect of gain saturation.

The new equations of motion can be solved by taking their Fourier transform and solving for each fluctuation

$$\Delta\tilde{N}[k] = \frac{j\Omega\tilde{S}_N[k] - \sigma N_0\frac{2A_0}{h\nu}\tilde{S}_w[k]}{\Omega_0^2 - \Omega^2 + \frac{j\Omega}{\tau_{pN}}} \quad \text{(B.155)}$$

$$\Delta\tilde{w}[k] = \frac{\sigma\frac{A_0}{2}\tilde{S}_N[k] + \left(j\Omega + \frac{1}{\tau_{pN}}\right)\tilde{S}_w[k]}{\Omega_0^2 - \Omega^2 + \frac{j\Omega}{\tau_{pN}}} \quad \text{(B.156)}$$

$$\Delta\tilde{\phi}[k] = -\frac{\tilde{S}_\phi[k]}{\Omega^2} \quad \text{(B.157)}$$

$$\Delta\tilde{t}[k] = \Delta\tilde{t}_{old}[k] - \frac{0.4\Omega_0^2\tau T_R\frac{1}{A_0}(j\Omega + 2\gamma_0^{\Re})\left[\sigma\frac{A_0}{2}\tilde{S}_N[k] + \left(j\Omega + \frac{1}{\tau_{pN}}\right)\tilde{S}_w[k]\right]}{\left[j4\omega_0^{\Re}\Omega - \Omega^2 + (2\gamma_0^{\Re})^2 + (2\gamma_0^{\Im})^2\right] \times \left[\Omega_0^2 - \Omega^2 + \frac{j\Omega}{\tau_{pN}}\right]} \quad \text{(B.158)}$$

$$\Delta\tilde{p}[k] \;=\; \Delta\tilde{p}_{old}[k] + \frac{0.8\gamma_0^{\Im}\Omega_0^2\frac{T_R}{\tau A_0}\left[\sigma\frac{A_0}{2}\tilde{S}_N[k] + \left(j\Omega + \frac{1}{\tau_{pN}}\right)\tilde{S}_w[k]\right]}{\left[j4\omega_0^{\Re}\Omega - \Omega^2 + (2\gamma_0^{\Re})^2 + (2\gamma_0^{\Im})^2\right] \times \left[\Omega_0^2 - \Omega^2 + \frac{j\Omega}{\tau_{pN}}\right]} \quad \text{(B.159)}$$

where $\Omega \equiv 2\pi k/\Delta T$, and $\Delta\tilde{t}_{old}[k]$ and $\Delta\tilde{p}_{old}[k]$ are given by equations (B.100) and (B.101).[11] The power spectra are found by taking the magnitude squared value

$$|\Delta\tilde{N}[k]|^2 \;=\; \frac{\Omega^2|\tilde{S}_N[k]|^2 + \frac{4\Omega_0^4}{\sigma^2 A_0^2}|\tilde{S}_w[k]|^2}{(\Omega_0^2 - \Omega^2)^2 + \frac{\Omega^2}{\tau_{pN}^2}} \quad \text{(B.162)}$$

$$|\Delta\tilde{w}[k]|^2 \;=\; \frac{\sigma^2\frac{A_0^2}{4}|\tilde{S}_N[k]|^2 + \left(\Omega^2 + \frac{1}{\tau_{pN}^2}\right)|\tilde{S}_w[k]|^2}{(\Omega_0^2 - \Omega^2)^2 + \frac{\Omega^2}{\tau_{pN}^2}} \quad \text{(B.163)}$$

$$|\Delta\tilde{\phi}[k]|^2 \;=\; \frac{|\tilde{S}_\phi[k]|^2}{\Omega^2} \quad \text{(B.164)}$$

$$\begin{aligned} |\Delta\tilde{t}[k]|^2 \;=\; & \frac{(\Omega^2 + (2\gamma_0^{\Re})^2)|\tilde{S}_t[k]|^2 + (2\gamma_0^{\Im})^2\tau^4|\tilde{S}_p[k]|^2}{4(2\gamma_0^{\Re})^2\Omega^2 + [-\Omega^2 + (2\gamma_0^{\Re})^2 + (2\gamma_0^{\Im})^2]^2} \\ & + \frac{(\Omega^2 + (2\gamma_0^{\Re})^2)}{4(2\gamma_0^{\Re})^2\Omega^2 + [-\Omega^2 + (2\gamma_0^{\Re})^2 + (2\gamma_0^{\Im})^2]^2} \\ & \times 0.16\Omega_0^4\tau^2 T_R^2\frac{1}{A_0^2}|\Delta\tilde{w}[k]|^2 \end{aligned} \quad \text{(B.165)}$$

$$\begin{aligned} |\Delta\tilde{p}[k]|^2 \;=\; & \frac{(2\gamma_0^{\Im})^2\frac{1}{\tau^4}|\tilde{S}_t[k]|^2 + (\Omega^2 + (2\gamma_0^{\Re})^2)|\tilde{S}_p[k]|^2}{4(2\gamma_0^{\Re})^2\Omega^2 + [-\Omega^2 + (2\gamma_0^{\Re})^2 + (2\gamma_0^{\Im})^2]^2} \\ & + \frac{(2\gamma_0^{\Im})^2\frac{1}{\tau^4}}{4(2\gamma_0^{\Re})^2\Omega^2 + [-\Omega^2 + (2\gamma_0^{\Re})^2 + (2\gamma_0^{\Im})^2]^2} \\ & \times 0.16\Omega_0^4\tau^2 T_R^2\frac{1}{A_0^2}|\Delta\tilde{w}[k]|^2, \end{aligned} \quad \text{(B.166)}$$

where

$$|\tilde{S}_N[k]|^2 \;=\; \frac{2N_0}{\tau_N\,\Delta T} \quad \text{(B.167)}$$

[11] In our new notation for the frequency and timing noise, equations (B.100) and (B.101) can be re-written as

$$\Delta\tilde{t}_{old}[k] = \frac{(j\Omega + 2\gamma_0^{\Re})\tilde{S}_t[k] + 2\gamma_0^{\Im}\tau^2\tilde{S}_p[k]}{j4\gamma_0^{\Re}\Omega - \Omega^2 + (2\gamma_0^{\Re})^2 + (2\gamma_0^{\Im})^2} \quad \text{(B.160)}$$

and

$$\Delta\tilde{p}_{old}[k] = \frac{-2\gamma_0^{\Im}\frac{1}{\tau^2}\tilde{S}_t[k] + (j\Omega + 2\gamma_0^{\Re})\tilde{S}_p[k]}{j4\gamma_0^{\Re}\Omega - \Omega^2 + (2\gamma_0^{\Re})^2 + (2\gamma_0^{\Im})^2}. \quad \text{(B.161)}$$

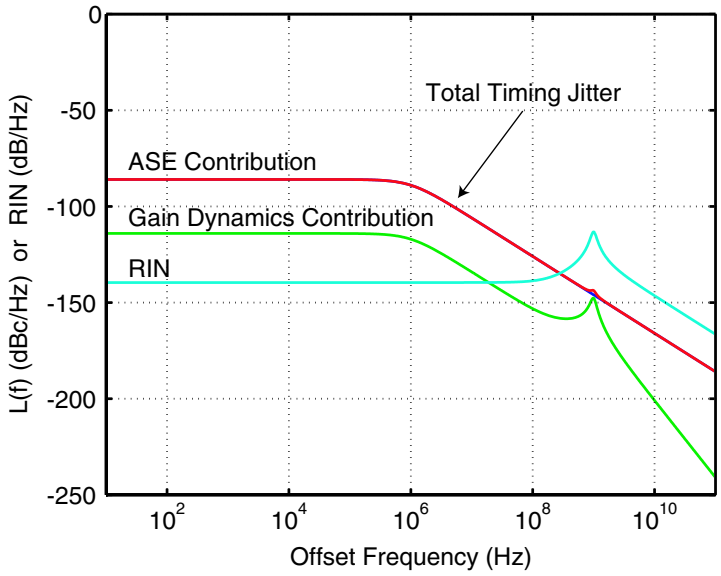

Figure B-6: Power spectral density of the timing jitter for an actively modelocked semiconductor laser. Values used: $\Omega_0 = 2\pi \times 10^9$ Hz, $2\gamma_0^{\Re} = 2\pi \times 10^6$ Hz, $\tau = 3 \times 10^{-12}$ s, $\tau_p = 10^{-11}$ s, $\tau_N = 10^{-9}$ s, $N_{p0} = 1.7 \times 10^7$ photons or intracavity power of 22 mW, $B = 3.325 \times 10^1 1$ Hz (5 nm BPF), and $n_{sp} = 3$. Computed Values: $A_0 = 2.6 \times 10^{-7}$ J$^{1/2}$, $\sigma = 23.22$ s^{-1}, $\tau_{pN} = 7.17 \times 10^{-10}$ s^{-1}, $G = 10$, $P_{ASE} = 1.1897 \times 10^{-6}$ W, and $N_0 = 4.306 \times 10^9$ carriers.

$$|\tilde{S}_w[k]|^2 = |\tilde{S}_0^{\Re}[k]|^2 = \frac{P_{ASE}}{2\,\Delta T} \tag{B.168}$$

$$|\tilde{S}_\phi[k]|^2 = \frac{|\tilde{S}_0^{\Im}[k]|^2}{A_0^2} = \frac{P_{ASE}}{2\,\Delta T\,A_0^2} \tag{B.169}$$

$$|\tilde{S}_t[k]|^2 = \frac{2\tau^2}{A_0^2}|\tilde{S}_1^{\Re}[k]|^2 = \frac{\tau^2 P_{ASE}}{\Delta T\,A_0^2} \tag{B.170}$$

$$|\tilde{S}_p[k]|^2 = \frac{2}{\tau^2 A_0^2}|\tilde{S}_1^{\Re}[k]|^2 = \frac{P_{ASE}}{\Delta T\,\tau^2\,A_0^2} \tag{B.171}$$

The diffusion constant for the shot noise of the injection can be included and derived by setting its mean equal to its variance. The gain dynamics gives rise to an additional term in the power spectral density of the timing and frequency. The second term on the r.h.s. in equations (B.165) and (B.166) is due to gain dynamics.

To determine the importance of the gain dynamics, we plot the single-sided phase noise spectrum of the timing jitter for a fundamentally modelocked semiconductor modelocked laser (Fig. B-6) and a fundamentally modelocked Erbium-doped fiber

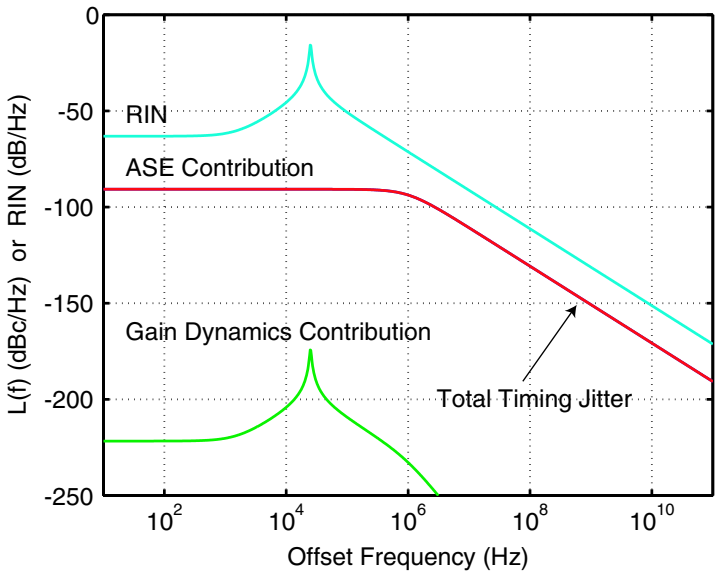

Figure B-7: Power spectral density of the timing jitter for an actively modelocked Erbium-doped fiber laser. Values used: $\Omega_0 = 2\pi \times 25$ kHz, $2\gamma_0^{\Re} = 2\pi \times 10^6$ Hz, $\tau = 3 \times 10^{-12}$ s, $\tau_p = 10^{-11}$ s, $\tau_N = 10^{-4}$ s, $N_{p0} = 1.7 \times 10^7$ photons or intracavity power of 22 mW, $B = 3.325 \times 10^1 1$ Hz (5 nm BPF), and $n_{sp} = 1$. Computed Values: $A_0 = 2.6 \times 10^{-7}$ $J^{1/2}$, $\sigma = 1.45 \times 10^{-8}$ s^{-1}, $\tau_{pN} = 10^{-6}$ s^{-1}, $G = 10$, $P_{ASE} = 3.966 \times 10^{-7}$ W, and $N_0 = 6.890 \times 10^{18}$ carriers.

laser (Fig. B-7). The gain dynamics contribution to the timing jitter in the semiconductor laser is 30 dB lower than the ASE contribution for offsets less than 1 MHz. In the fiber laser, the gain dynamics contribution is over 100 dB lower than the ASE contribution. The total timing noise is therefore mainly due to the ASE contribution. The line indicating the total timing noise and the line indicating the ASE contribution are almost indistinguishable. The gain dynamics contribution is therefore insignificant.

The theory is consistent with what has been measured in fiber lasers [91] in which the "enhanced phase noise" at the relaxation oscillation was amplitude noise bleed through in the phase noise measurement. Typically a phase sensitive detector used in a residual phase noise measurement suppresses amplitude noise by 20 dB.

Fig. B-7 shows the timing jitter power spectral density for a *fundamentally* modelocked fiber laser. Since it is difficult to obtain enough gain in a 1.5 cm section of fiber, these lasers are always harmonically modelocked. The power spectral density of the timing jitter for a modelocked fiber laser operated at the Mth harmonic is shown in Fig. B-8. The parameters are the same as for the fundamentally modelocked fiber laser, but the the single-sided phase noise spectrum looks completely different. The maximum value of $L(f)$ stays the same, but the bandwidth of the phase noise decreases by a factor of M. To derive Fig. B-8 from Fig. B-7, one needs to divide $\gamma_0^{\Re}$ by M, divide $L(f)$ by M^2, replicate the noise spectrum M times at harmonics of the fundamental cavity frequency, and finally sum the noise spectra to get the result in Fig. B-8. This follows from the theory since equation (B.104) shows that $\gamma_0^{\Re}$ is inversely proportional to the round-trip time T_R. By increasing the round-trip time by a factor of M, decreases $\gamma_0^{\Re}$ by a factor of M. This reduces the amplitude of the timing jitter power spectral density by a factor of M and the knee moves in by a factor of M. In addition, the noise is evenly distributed among the M supermodes. Therefore, the amplitude of the timing jitter power spectral density at 0 Hz offset is reduced by a total of M^2.

From a physical picture, the total noise of the laser does not decrease as the length of the cavity is increased. The noise energy does redistribute among the supermodes,

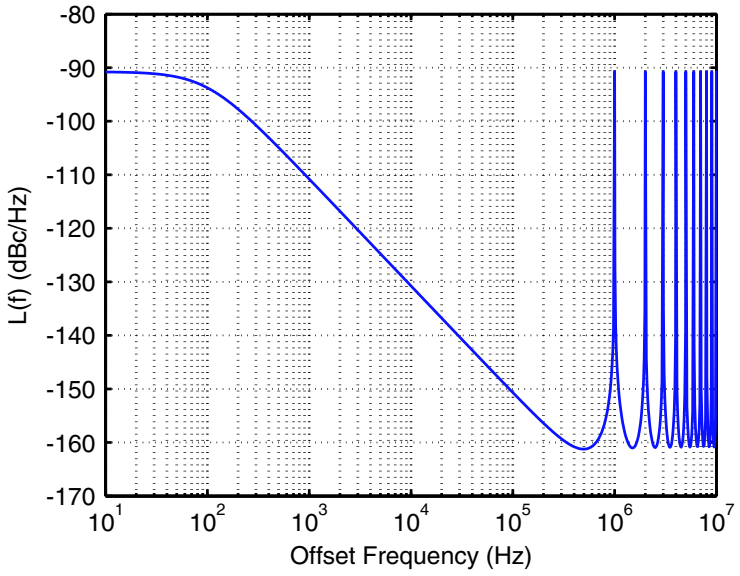

Figure B-8: Power spectral density of the timing jitter for an AM actively and harmonically modelocked Erbium-doped fiber laser.

but the total integrated value remains constant.

The mean square fluctuation of each noise component can be obtained by integrating equations (B.162), (B.163), (B.165), and (B.166). Note that the phase fluctuations given by equation (B.162) are not bounded since and the variance increases linearly. The mean square values relative to an absolute clock are [12]

$$\sigma_N^2 = \frac{|\tilde{S}_N[k]|^2\Delta T}{4\beta} + \frac{\Omega_0^4 P_{ASE}}{\beta(\alpha^2+\beta^2)\sigma^2 A_0^2} \tag{B.172}$$

$$\sigma_w^2 = \frac{\sigma^2\frac{A_0^2}{4}|\tilde{S}_N[k]|^2\Delta T + \frac{1}{2\tau_{pN}^2}P_{ASE}}{4\beta(\alpha^2+\beta^2)} + \frac{P_{ASE}}{8\beta} \tag{B.173}$$

$$\begin{aligned}\sigma_\phi^2(T) &= \langle[\phi(T+t)-\phi(t)]^2\rangle \\ &= \frac{P_{ASE}}{2A_0^2}\,T\end{aligned} \tag{B.174}$$

$$\begin{aligned}\sigma_t^2 = {} & \sigma_{t,old}^2 + 0.16\Omega_0^4\tau^2 T_R^2\frac{1}{A_0^2} \\ & \times\left[\frac{P_{ASE}}{2}I_{11} + \left(\left((2\gamma_0^{\Re})^2+\frac{1}{\tau_{pN}^2}\right)\frac{P_{ASE}}{2} + \sigma^2\frac{A_0^2}{4}|\tilde{S}_N[k]|^2\Delta T\right)I_{12}\right.\end{aligned}$$

[12] integrals needed in derivation

$$+(2\gamma_0^{\Re})^2\left(\sigma^2\frac{A_0^2}{4}|\tilde{S}_N[k]|^2\Delta T+\frac{P_{ASE}}{2\tau_{pN}^2}\right)I_{13}\Bigg] \tag{B.175}$$

$$\sigma_{t,old}^2 = \frac{\tau^2 P_{ASE}}{4bA_0^2}\left(1+\frac{(2\gamma_0^{\Re})^2+(2\gamma_0^{\Im})^2}{a^2+b^2}\right) \tag{B.176}$$

$$\begin{aligned}\sigma_p^2 &= \sigma_{p,old}^2+0.16(2\gamma_0^{\Im})^2\Omega_0^4\frac{T_R^2}{\tau^2A_0^2}\\ &\times\left[\frac{P_{ASE}}{2}I_{12}+\left(\sigma^2\frac{A_0^2}{4}|\tilde{S}_N[k]|^2\Delta T+\frac{P_{ASE}}{2\tau_{pN}^2}\right)I_{13}\right]\end{aligned} \tag{B.177}$$

$$\sigma_{p,old}^2 = \frac{P_{ASE}}{4b\tau^2A_0^2}\left(1+\frac{(2\gamma_0^{\Im})^2+(2\gamma_0^{\Re})^2}{a^2+b^2}\right) \tag{B.178}$$

where $\sigma_{t,old}^2$ and $\sigma_{p,old}^2$ are the mean square fluctuations of the timing and frequency without gain dynamics. Note that $\sigma_\phi^2(T)$ is the pulse-to-pulse noise and the other σ's are pulse-to-clock noise.

Useful integrals to find the pulse-to-pulse noise

$$\int_{-\infty}^{\infty}\frac{1-\cos(\Omega T)}{(\Omega-\Omega_{++})(\Omega-\Omega_{--})(\Omega-\Omega_{+-})(\Omega-\Omega_{-+})}\frac{d\Omega}{\pi}= \frac{1}{2\beta(\alpha^2+\beta^2)}\left[1-e^{-\beta T}\left(\cos(\alpha T)+\frac{\beta}{\alpha}\sin(\alpha T)\right)\right] \tag{B.179}$$

$$\int_{-\infty}^{\infty}\frac{\Omega^2[1-\cos(\Omega T)]}{(\Omega-\Omega_{++})(\Omega-\Omega_{--})(\Omega-\Omega_{+-})(\Omega-\Omega_{-+})}\frac{d\Omega}{\pi}= \frac{1}{2\beta}\left[1-e^{-\beta T}\left(\cos(\alpha T)-\frac{\beta}{\alpha}\sin(\alpha T)\right)\right], \tag{B.180}$$

where

$$\Omega_{++} = +\alpha+j\beta \tag{B.181}$$

$$\Omega_{--} = -\alpha-j\beta \tag{B.182}$$

$$\Omega_{+-} = +\alpha-j\beta \tag{B.183}$$

$$\Omega_{-+} = -\alpha+j\beta \tag{B.184}$$

$$\Upsilon_{++} = +a+jb \tag{B.185}$$

$$\Upsilon_{--} = -a-jb \tag{B.186}$$

$$\Upsilon_{+-} = +a-jb \tag{B.187}$$

$$\Upsilon_{-+} \;=\; -a + jb \tag{B.188}$$

and a , b, α, and β are positive real numbers and are given by

$$\alpha \;=\; \sqrt{\frac{\Omega_0\sqrt{\Omega_0^2+\frac{1}{2\tau_{pN}^2}}}{1+\frac{4\Omega_0^2-1/\tau_{pN}^2}{4\tau_{pN}^2(2\Omega_0^2+1/\tau_{pN}^2)^2}}} \tag{B.189}$$

$$\beta \;=\; \sqrt{\frac{\Omega_0\sqrt{\Omega_0^2+\frac{1}{2\tau_{pN}^2}}}{1+\frac{4\tau_{pN}^2(2\Omega_0^2+1/\tau_{pN}^2)^2}{4\Omega_0^2-1/\tau_{pN}^2}}} \tag{B.190}$$

$$a \;=\; \sqrt{\frac{\sqrt{(2\gamma_0^{\Re})^2+(2\gamma_0^{\Im})^2}\sqrt{3(2\gamma_0^{\Re})^2+(2\gamma_0^{\Im})^2}}{1+\frac{(2\gamma_0^{\Re})^2(2\gamma_0^{\Im})^2}{[(2\gamma_0^{\Im})^2-(2\gamma_0^{\Re})^2]^2}}} \tag{B.191}$$

$$b \;=\; \sqrt{\frac{\sqrt{(2\gamma_0^{\Re})^2+(2\gamma_0^{\Im})^2}\sqrt{3(2\gamma_0^{\Re})^2+(2\gamma_0^{\Im})^2}}{1+\frac{[(2\gamma_0^{\Im})^2-2\gamma_0^{\Re})^2]^2}{(2\gamma_0^{\Re})^2(2\gamma_0^{\Im})^2}}} \tag{B.192}$$

Useful integrals to find the total noise

$$\begin{aligned}
I_{11} \;&\equiv\; \int_{-\infty}^{\infty} \frac{\Omega^4}{\substack{(\Omega-\Omega_{++})(\Omega-\Omega_{--})(\Omega-\Omega_{+-})(\Omega-\Omega_{-+})\\(\Omega-\Upsilon_{++})(\Omega-\Upsilon_{--})(\Omega-\Upsilon_{+-})(\Omega-\Upsilon_{-+})}}\frac{d\Omega}{2\pi}\\
&=\; \frac{j\Omega_{++}^4}{\substack{(\Omega_{++}-\Omega_{--})(\Omega_{++}-\Omega_{+-})(\Omega_{++}-\Omega_{-+})\\(\Omega_{++}-\Upsilon_{++})(\Omega_{++}-\Upsilon_{--})(\Omega_{++}-\Upsilon_{+-})(\Omega_{++}-\Upsilon_{-+})}}\\
&\quad+\frac{j\Omega_{-+}^4}{\substack{(\Omega_{-+}-\Omega_{++})(\Omega_{-+}-\Omega_{--})(\Omega_{-+}-\Omega_{-+})\\(\Omega_{-+}-\Upsilon_{++})(\Omega_{-+}-\Upsilon_{--})(\Omega_{-+}-\Upsilon_{+-})(\Omega_{-+}-\Upsilon_{-+})}}\\
&\quad+\frac{j\Upsilon_{++}^4}{\substack{(\Upsilon_{++}-\Omega_{++})(\Upsilon_{++}-\Omega_{--})(\Upsilon_{++}-\Omega_{+-})(\Upsilon_{++}-\Omega_{-+})\\(\Upsilon_{++}-\Upsilon_{--})(\Upsilon_{++}-\Upsilon_{+-})(\Upsilon_{++}-\Upsilon_{-+})}}\\
&\quad+\frac{j\Upsilon_{-+}^4}{\substack{(\Upsilon_{++}-\Omega_{++})(\Upsilon_{-+}-\Omega_{--})(\Upsilon_{-+}-\Omega_{+-})(\Upsilon_{-+}-\Omega_{-+})\\(\Upsilon_{-+}-\Upsilon_{++})(\Upsilon_{-+}-\Upsilon_{--})(\Upsilon_{-+}-\Upsilon_{+-})}}\\
I_{12} \;&\equiv\; \int_{-\infty}^{\infty} \frac{\Omega^2}{\substack{(\Omega-\Omega_{++})(\Omega-\Omega_{--})(\Omega-\Omega_{+-})(\Omega-\Omega_{-+})\\(\Omega-\Upsilon_{++})(\Omega-\Upsilon_{--})(\Omega-\Upsilon_{+-})(\Omega-\Upsilon_{-+})}}\frac{d\Omega}{2\pi}
\end{aligned} \tag{B.193}$$

$$
\begin{aligned}
&= \frac{j\Omega_{++}^2}{(\Omega_{++}-\Omega_{--})(\Omega_{++}-\Omega_{+-})(\Omega_{++}-\Omega_{-+})} \\
&\quad (\Omega_{++}-\Upsilon_{++})(\Omega_{++}-\Upsilon_{--})(\Omega_{++}-\Upsilon_{+-})(\Omega_{++}-\Upsilon_{-+}) \\
&\quad + \frac{j\Omega_{-+}^2}{(\Omega_{-+}-\Omega_{++})(\Omega_{-+}-\Omega_{--})(\Omega_{-+}-\Omega_{-+})} \\
&\quad (\Omega_{-+}-\Upsilon_{++})(\Omega_{-+}-\Upsilon_{--})(\Omega_{-+}-\Upsilon_{+-})(\Omega_{-+}-\Upsilon_{-+}) \\
&\quad + \frac{j\Upsilon_{++}^2}{(\Upsilon_{++}-\Omega_{++})(\Upsilon_{++}-\Omega_{--})(\Upsilon_{++}-\Omega_{+-})(\Upsilon_{++}-\Omega_{-+})} \\
&\quad (\Upsilon_{++}-\Upsilon_{--})(\Upsilon_{++}-\Upsilon_{+-})(\Upsilon_{++}-\Upsilon_{-+}) \\
&\quad + \frac{j\Upsilon_{-+}^2}{(\Upsilon_{++}-\Omega_{++})(\Upsilon_{-+}-\Omega_{--})(\Upsilon_{-+}-\Omega_{+-})(\Upsilon_{-+}-\Omega_{-+})} \\
&\quad (\Upsilon_{-+}-\Upsilon_{++})(\Upsilon_{-+}-\Upsilon_{--})(\Upsilon_{-+}-\Upsilon_{+-})
\end{aligned} \tag{B.194}
$$

$$
\begin{aligned}
I_{13} &\equiv \int_{-\infty}^{\infty} \frac{1}{(\Omega-\Omega_{++})(\Omega-\Omega_{--})(\Omega-\Omega_{+-})(\Omega-\Omega_{-+})} \frac{d\Omega}{2\pi} \\
&\quad (\Omega-\Upsilon_{++})(\Omega-\Upsilon_{--})(\Omega-\Upsilon_{+-})(\Omega-\Upsilon_{-+}) \\
&= \frac{j}{(\Omega_{++}-\Omega_{--})(\Omega_{++}-\Omega_{+-})(\Omega_{++}-\Omega_{-+})} \\
&\quad (\Omega_{++}-\Upsilon_{++})(\Omega_{++}-\Upsilon_{--})(\Omega_{++}-\Upsilon_{+-})(\Omega_{++}-\Upsilon_{-+}) \\
&\quad + \frac{j}{(\Omega_{-+}-\Omega_{++})(\Omega_{-+}-\Omega_{--})(\Omega_{-+}-\Omega_{-+})} \\
&\quad (\Omega_{-+}-\Upsilon_{++})(\Omega_{-+}-\Upsilon_{--})(\Omega_{-+}-\Upsilon_{+-})(\Omega_{-+}-\Upsilon_{-+}) \\
&\quad + \frac{j}{(\Upsilon_{++}-\Omega_{++})(\Upsilon_{++}-\Omega_{--})(\Upsilon_{++}-\Omega_{+-})(\Upsilon_{++}-\Omega_{-+})} \\
&\quad (\Upsilon_{++}-\Upsilon_{--})(\Upsilon_{++}-\Upsilon_{+-})(\Upsilon_{++}-\Upsilon_{-+}) \\
&\quad + \frac{j}{(\Upsilon_{++}-\Omega_{++})(\Upsilon_{-+}-\Omega_{--})(\Upsilon_{-+}-\Omega_{+-})(\Upsilon_{-+}-\Omega_{-+})} \\
&\quad (\Upsilon_{-+}-\Upsilon_{++})(\Upsilon_{-+}-\Upsilon_{--})(\Upsilon_{-+}-\Upsilon_{+-})
\end{aligned} \tag{B.195}
$$

$$
\begin{aligned}
I_{14} &\equiv \int_{-\infty}^{\infty} \frac{\Omega^2}{(\Omega-\Omega_{++})(\Omega-\Omega_{--})(\Omega-\Omega_{+-})(\Omega-\Omega_{-+})} \frac{d\Omega}{2\pi} \\
&= \frac{j\Omega_{++}^2}{(\Omega_{++}-\Omega_{--})(\Omega_{++}-\Omega_{+-})(\Omega_{++}-\Omega_{-+})} \\
&\quad + \frac{j\Omega_{-+}^2}{(\Omega_{-+}-\Omega_{++})(\Omega_{-+}-\Omega_{--})(\Omega_{-+}-\Omega_{-+})} \\
&\quad \frac{1}{4\beta}
\end{aligned} \tag{B.196}
$$

$$
\begin{aligned}
I_{15} &\equiv \int_{-\infty}^{\infty} \frac{1}{(\Omega-\Omega_{++})(\Omega-\Omega_{--})(\Omega-\Omega_{+-})(\Omega-\Omega_{-+})} \frac{d\Omega}{2\pi} \\
&= \frac{j}{(\Omega_{++}-\Omega_{--})(\Omega_{++}-\Omega_{+-})(\Omega_{++}-\Omega_{-+})} \\
&\quad + \frac{j}{(\Omega_{-+}-\Omega_{++})(\Omega_{-+}-\Omega_{--})(\Omega_{-+}-\Omega_{-+})}
\end{aligned}
$$

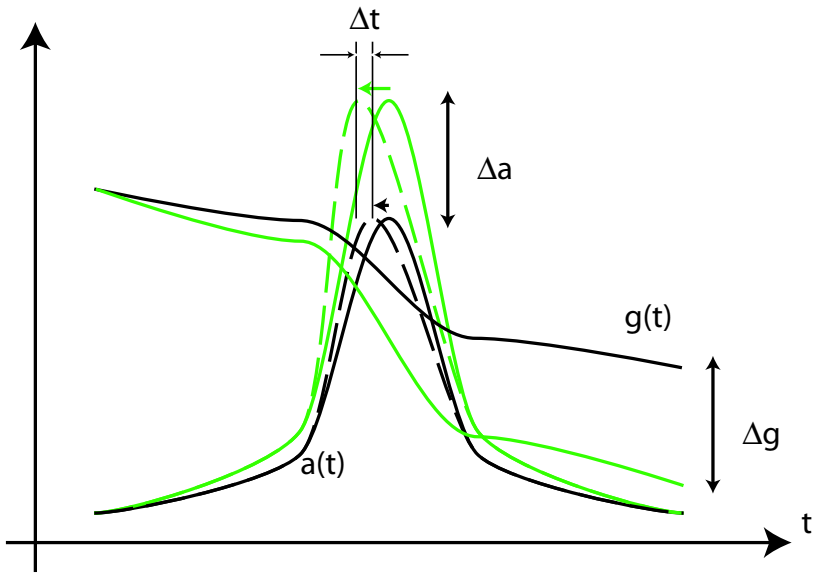

Figure B-9: Fast gain dynamics of semiconductor gain medium.

$$\frac{1}{4\beta(\alpha^2+\beta^2)} \tag{B.197}$$

B.2.4 Noise due to Wavelength Shifts

Small changes in the injection current or saturable absorber bias voltage shift the operating wavelength of the semiconductor laser due to a shift of the gain peak. This effect is largely exploited for phase-shifting interferometry. Typical phase shifts are 0.006 nm/mA in an AlGaAs laser diode [92], and 30 GHz/mA for a Sharp LTO80MD laser diode (probably at 785 nm) [93].

The dispersion in the external-cavity semiconductor laser cavity was measured at approximately 15 fs/nm. This implies that a 1 mA change in current would only cause a timing shift of 0.006 nm/mA $\times$ 15 fs/nm = 0.090 fs. Therefore, the noise due to wavelength shifts is negligible.

B.2.5 Length Fluctuations

Fluctuations of the cavity length changes the pulse by

$$\begin{aligned} a_{n+1}(t) &= a_n\left(t - \frac{\Delta L}{v_g}\right) && \text{(B.198)} \\ &= a_n(t) - \frac{\Delta L}{v_g}\frac{\partial a_n}{\partial t} && \text{(B.199)} \\ a_{n+1}(t) - a_n(t) &= -\frac{\Delta L}{v_g}\frac{\partial a_n}{\partial t} && \text{(B.200)} \\ T_R\frac{\partial a}{\partial T} &= \underbrace{-\frac{\Delta L(T)}{v_g}\frac{\partial a_{ss}(t)}{\partial t}}_{T_R S_L(t,T)} && \text{(B.201)} \end{aligned}$$

The noise contribution is therefore equal to

$$S_L(t,T) = -\frac{\Delta L(T)}{v_g T_R}\frac{d}{dt}a_s(t) = -\frac{\Delta L}{v_g T_R}\frac{d}{dt}\left(A_0\psi_0(t/\tau)\right) = -\frac{\Delta L(T)}{v_g T_R}\frac{A_0}{\sqrt{2}\tau}\psi_1(t/\tau) \tag{B.202}$$

The noise contribution due to fluctuations in the refractive index can be obtained by replacing ΔL with $L(\Delta n/n)$.

Projecting the length fluctuations into the timing noise component yields

$$S_{t,L}(T) = \Re\left\{\int_{-\infty}^{\infty} S_L(t,T)\psi_1(t/\tau)dt\right\} = -\frac{\Delta L(T)}{v_g T_R}\frac{A_0}{\sqrt{2}\tau}. \tag{B.203}$$

The length fluctuations do not contribute to frequency noise.

The power spectral density of the timing noise component due to length fluctuations is found by finding the square magnitude of the Fourier series

$$|\tilde{S}_{t,L}[k]|^2 = \frac{A_0^2}{2\tau^2}\left(\frac{1}{v_g T_R}\right)^2 |\Delta\tilde{L}[k]|^2. \tag{B.204}$$

Taking the limit $\Delta T \to \infty$, we convert this to a continuous function according to

$$|\tilde{S}_{t,L}(\Omega)|^2 = \frac{A_0^2}{2\tau^2}\left(\frac{1}{v_g T_R}\right)^2 |\Delta\tilde{L}(\Omega)|^2. \tag{B.205}$$

where $|\Delta\tilde{L}(\Omega)|^2 = \frac{\Delta T}{2\pi}|\Delta\tilde{L}[k]|^2$. Most of the power spectral energy of the length

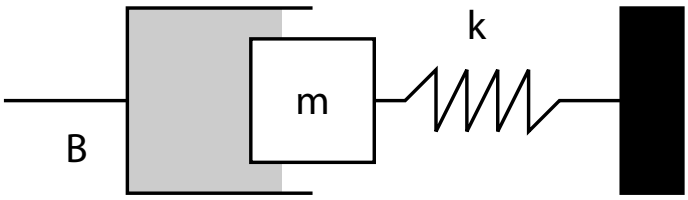

Figure B-10: The model for the fluctuations of the end-mirror in a semiconductor laser.

fluctuations is less than 10 kHz.

The length fluctuations of the end-mirror in the semiconductor laser can be modelled by a mass attached to a spring and a dashpot (see Fig. B-10). The equation describing the motion of the end-mirror is

$$m\frac{d^2}{dt^2}x(t) = -kx(t) - B\frac{d}{dt}x(t) + N(t) \tag{B.206}$$

where x is the lateral displacement from the equilibrium position, m is the mass of the end-mirror, k is the spring constant, B is the dashpot viscosity, and N is the random noise driving force. The eigensolutions to equation (B.206) are

$$x(t) = \exp(-\alpha t \pm j\omega_0 t) \tag{B.207}$$

where $2\alpha = B/m$ and $\omega_0^2 + \alpha^2 = k/m$. Taking the Fourier transform of equation (B.206), solving for $\tilde{X}(\omega)$, and taking the square magnitude to find the power spectral density yields

$$|\tilde{X}(\omega)|^2 = \frac{|\tilde{N}(\omega)|^2}{m^2}\frac{1}{(\omega_0^2 + \alpha^2 - \omega^2)^2 + (2\alpha\omega)^2} \tag{B.208}$$

For critical damping, $\omega_0 = 0$ and $\alpha = \sqrt{k/m}$, and equation (B.208) simplifies to a Lorentzian function

$$|\tilde{X}(\omega)|^2 = \frac{|\tilde{N}(\omega)|^2}{m^2}\frac{1}{(\omega^2 + \alpha^2)^2}. \tag{B.209}$$

We will use equation (B.209) for modelling the length fluctuations.

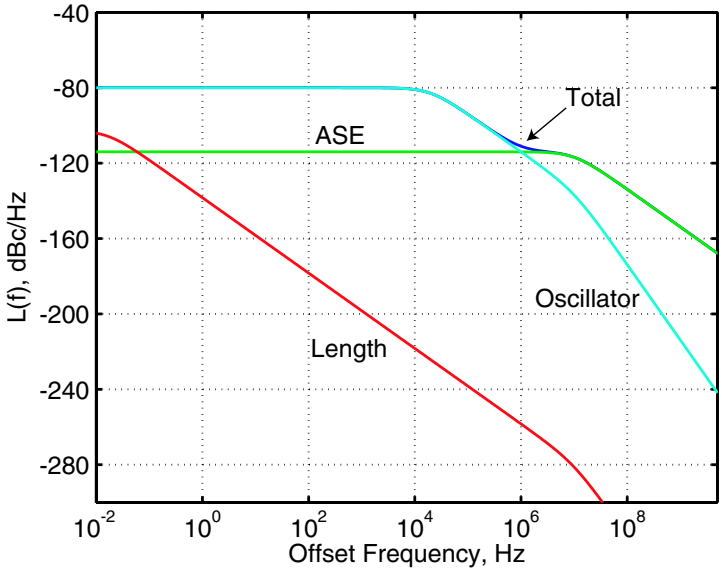

Figure B-11: The noise contribution of length fluctuations to the entire phase noise spectrum can be significant with harmonically modelocked fiber lasers due to their long cavities.

The length fluctuations in a fiber laser are a little more important and hence care in packaging the fiber is necessary. If the cavity length is 500 m long, and the temperature changes the index of refraction of fiber by $10^{-5}/^0$C, then the effective cavity length changes by 50 μm for a 0.01 ^{0}C change in temperature.[13] Exposed fiber shows large length fluctuations, as can be seen in Fig. B-12.

B.2.6 Microwave Oscillator Noise

Expanding the cosinusoidal modulation term of equation (A.24) yields

$$\cos(\omega_M t + \Delta\phi_{osc}(T)) \approx 1 - \frac{(\omega_M t)^2}{2} - \frac{2(\omega_M t)\Delta\phi_{osc}(T)}{2} + \ldots \qquad \text{(B.210)}$$

The last part is due to the phase noise of the microwave oscillator. Note that the phase noise term is only a function of T (not t) since the majority of the phase noise

[13] $\frac{\Delta x}{x} = \frac{\Delta n}{n}$. Putting a fiber laser in a box typically controls the temperature to within 0.01 ^{0}C. This corresponds to a change of 0.01 kΩ on a 10 kΩ thermistor.

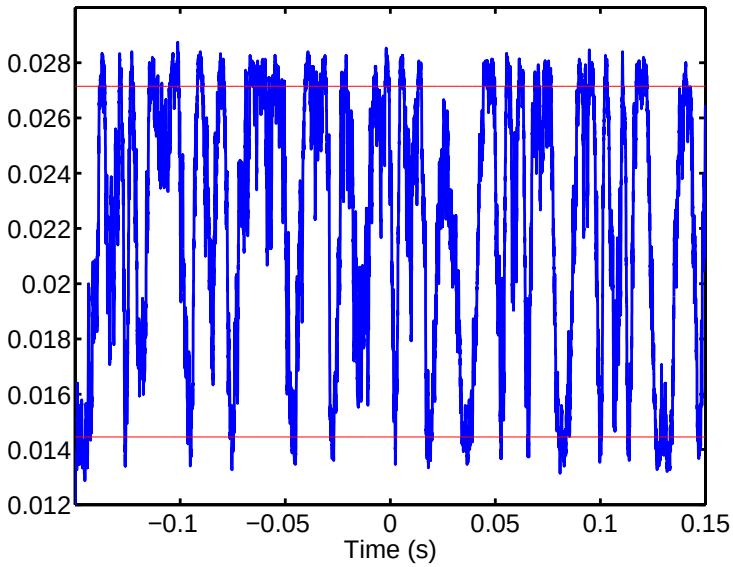

Figure B-12: Fiber length fluctuations in a 50 m length of silica-core fiber over a 300 ms time interval. This graph shows the power output of an all-fiber Mach-Zehnder interferometer in which one arm was longer by 50 m. The non-zero extinction ratio is due to imperfect splitting, power differences, and finite coherence length of the laser. The two horizontal lines show the approximate powers corresponding to constructive and destructive interference.

energy is typically under 10 MHz and hence slower than the round-trip time of the laser.

$$\begin{aligned} T_R\frac{\partial a}{\partial T} &= -\frac{M_{AM}+jM_{PM}}{4}\times 2\omega_M t\Delta\phi_{osc}(T)\times a(t,T) \\ &= -\frac{M_{AM}+jM_{PM}}{4}\times 2\omega_M t\Delta\phi_{osc}(T)\times \underbrace{a_{ss}(t)}_{A_0\psi_0(t/\tau)} \\ &= -\frac{M_{AM}+jM_{PM}}{4T_R}\psi_1(t/\tau)\ \sqrt{2}A_0\omega_M\tau\ \Delta\phi_{osc}(T) \\ &\equiv T_R S_{\Delta\phi_{osc}}(t,T) \end{aligned} \tag{B.211}$$

where we used the equality $t\psi_0(t/\tau)=\tau\psi_1(t/\tau)/\sqrt{2}$, hence

$$S_{\Delta\phi_{osc}}(t,T) = -\frac{M_{AM}+jM_{PM}}{4T_R}\psi_1(t/\tau)\ \sqrt{2}A_0\omega_M\tau\ \Delta\phi_{osc}(T). \tag{B.212}$$

Projecting the microwave oscillator noise into the timing noise component yields[14]

$$S_{t,osc}(T) = -\frac{M_{AM}}{4T_R}\sqrt{2}A_0\omega_M\tau\ \Delta\phi_{osc}(T). \tag{B.213}$$

Projecting into the frequency noise component yields

$$S_{p,osc}(T) = -\frac{M_{PM}}{4T_R}\sqrt{2}A_0\omega_M\tau\ \Delta\phi_{osc}(T). \tag{B.214}$$

The power spectral density of the timing and frequency noise is equal to the Fourier transform of their autocorrelation functions

$$|S_{t,osc}[k]|^2 = \frac{1}{8}\left(\frac{A_0 M_{AM}\omega_M\tau}{T_R}\right)^2|\Delta\tilde{\phi}_{osc}[k]|^2 \tag{B.215}$$

$$|S_{p,osc}[k]|^2 = \frac{1}{8}\left(\frac{A_0 M_{PM}\omega_M\tau}{T_R}\right)^2|\Delta\tilde{\phi}_{osc}[k]|^2. \tag{B.216}$$

[14]Remember that the timing fluctuations are parallel to the real part multiplying ψ_1 and the frequency fluctuations are parallel to the imaginary part multiplying ψ_1.

These equations can be made continuous by equation (B.343),

$$\langle |S_{t,osc}(\Omega)|^2 \rangle = \frac{1}{8}\left(\frac{A_0 M_{AM}\omega_M \tau}{T_R}\right)^2 |\Delta\tilde{\phi}_{osc}(\Omega)|^2 \tag{B.217}$$

$$\langle |S_{p,osc}(\Omega)|^2 \rangle = \frac{1}{8}\left(\frac{A_0 M_{PM}\omega_M \tau}{T_R}\right)^2 |\Delta\tilde{\phi}_{osc}(\Omega)|^2, \tag{B.218}$$

where $|\Delta\tilde{\phi}_{osc}(\Omega)|^2 = \frac{\Delta T}{2\pi}|\Delta\tilde{\phi}_{osc}[k]|^2$ is the phase noise of the oscillator. A good analytical model that fits the HP83732B synthesizer phase noise shown in Fig. F-3 is

$$|\Delta\tilde{\phi}_{osc}(\Omega)|^2 = \frac{\Omega_{0L}^2 10^{-80/10}}{\Omega^2 + \Omega_{0L}^2}, \tag{B.219}$$

where $\Omega_{0L} = 2\pi \times 20$ kHz, and the phase noise is -80 dBc/Hz for offsets less than 20 kHz.

B.2.7 Total Noise and RMS Timing Jitter

The power spectral density of the spontaneous emission noise, length fluctuations, and microwave oscillator noise drive the timing and frequency fluctuations according to equations (B.100) and (B.101). These equations can be converted from discrete to continuous in frequency using equation (B.343),

$$\Delta\tilde{t}(\Omega) = \tau\frac{\sqrt{2}}{A_0}\frac{(j\Omega + 2\gamma_0^{\Re})\tilde{S}_1^{\Re}(\Omega) + 2\gamma_0^{\Im}\tilde{S}_1^{\Im}(\Omega)}{j4\gamma_0^{\Re}\Omega - \Omega^2 + (2\gamma_0^{\Re})^2 + (2\gamma_0^{\Im})^2} \tag{B.220}$$

$$\Delta\tilde{p}(\Omega) = \frac{1}{\tau}\frac{\sqrt{2}}{A_0}\frac{-2\gamma_0^{\Im}\tilde{S}_1^{\Re}(\Omega) + (j\Omega + 2\gamma_0^{\Re})\tilde{S}_1^{\Im}(\Omega)}{j4\gamma_0^{\Re}\Omega - \Omega^2 + (2\gamma_0^{\Re})^2 + (2\gamma_0^{\Im})^2}. \tag{B.221}$$

Taking the magnitude squared of equations (B.220) and (B.220) yields

$$|\Delta\tilde{t}(\Omega)|^2 = \frac{2\tau^2}{A_0^2}\frac{\left[\Omega^2 + (2\gamma_0^{\Re})^2\right]|\tilde{S}_1^{\Re}(\Omega)|^2 + (2\gamma_0^{\Im})^2|\tilde{S}_1^{\Im}(\Omega)|^2}{(4\gamma_0^{\Re})^2\Omega^2 + \left[-\Omega^2 + (2\gamma_0^{\Re})^2 + (2\gamma_0^{\Im})^2\right]^2} \tag{B.222}$$

$$|\Delta\tilde{p}(\Omega)|^2 = \frac{2}{\tau^2 A_0^2}\frac{\left[\Omega^2 + (2\gamma_0^{\Re})^2\right]|\tilde{S}_1^{\Im}(\Omega)|^2 + (2\gamma_0^{\Im})^2|\tilde{S}_1^{\Re}(\Omega)|^2}{(4\gamma_0^{\Re})^2\Omega^2 + \left[-\Omega^2 + (2\gamma_0^{\Re})^2 + (2\gamma_0^{\Im})^2\right]^2}. \tag{B.223}$$

where $\tilde{S}_1^{\Re}(\Omega)$ and $\tilde{S}_1^{\Im}(\Omega)$ are uncorrelated. The noise terms, $\tilde{S}_1^{\Re}(\Omega)$ and $\tilde{S}_1^{\Im}(\Omega)$, are driven by spontaneous emission, length fluctuations, and microwave oscillator noise according to [15]

$$\begin{aligned}
\langle|\tilde{S}_1^{\Re}(\Omega)|^2\rangle &= \frac{P_{ASE}}{4\pi} + \langle|S_{t,L}(\Omega)|^2\rangle + \langle|S_{t,osc}(\Omega)|^2\rangle \\
&= \frac{P_{ASE}}{4\pi} + \frac{A_0^2}{2\tau^2}\left(\frac{1}{v_g T_R}\right)^2 |\Delta\tilde{L}(\Omega)|^2 \\
&\quad + \frac{1}{8}\left(\frac{A_0 M_{AM}\omega_M \tau}{T_R}\right)^2 |\Delta\tilde{\phi}_{osc}(\Omega)|^2 \qquad \text{(B.224)} \\
\langle|\tilde{S}_1^{\Im}(\Omega)|^2\rangle &= \frac{P_{ASE}}{4\pi} + \langle|S_{p,osc}(\Omega)|^2\rangle \\
&= \frac{P_{ASE}}{4\pi} + \frac{1}{8}\left(\frac{A_0 M_{PM}\omega_M \tau}{T_R}\right)^2 |\Delta\tilde{\phi}_{osc}(\Omega)|^2 \qquad \text{(B.225)}
\end{aligned}$$

Equation (B.222) with (B.224) and (B.224) yield the power spectral density of the timing jitter. It can be seen that the power spectral density of the length changes and oscillator do not add any poles to the total noise spectrum. They simply multiply the natural cavity response function. For the case of amplitude modulation only ($M_{PM} = 0$ and $\gamma_0^{\Im} = 0$), equation (B.222) becomes

$$\begin{aligned}
\langle|\Delta\tilde{t}(\Omega)|^2\rangle &= \frac{2\tau^2}{A_0^2}\frac{1}{\Omega^2 + (2\gamma_0^{\Re})^2}\left[\frac{P_{ASE}}{4\pi} + \frac{A_0^2}{2\tau^2}\left(\frac{1}{v_g T_R}\right)^2 |\Delta\tilde{L}(\Omega)|^2\right. \\
&\quad \left. + \frac{1}{8}\left(\frac{A_0 M_{AM}\omega_M \tau}{T_R}\right)^2 |\Delta\tilde{\phi}_{osc}(\Omega)|^2\right] \qquad \text{(B.226)}
\end{aligned}$$

with the help of equations (B.224) and (B.224). The single-side band phase noise is plotted in Fig. B-13 for an actively modelocked 10 GHz semiconductor laser. The SSB phase noise is related to equation (B.226) by $L(\Omega) = (2\pi/T_R)^2\langle|\Delta\tilde{t}(\Omega)|^2\rangle$. For Fig. B-13, the oscillator noise and length fluctuations were assumed to be Lorentzian $\propto 1/(\Omega^2 + \Omega_0^2)$. The length fluctuations from the end-mirror were modelled as a mass attached to a spring and dashpot, which results in a Lorentzian spectrum when

[15] The ASE noise power is $|\tilde{S}_1^{\Re}[k]|^2 = |\tilde{S}_1^{\Im}[k]|^2 = \frac{P_{ASE}}{2\,\Delta T}$. Converting this to the continuous domain yields $|\tilde{S}_1^{\Re}(\Omega)|^2 = |\tilde{S}_1^{\Im}(\Omega)|^2 = \frac{\Delta T}{2\pi}|\tilde{S}_1^{\Im}[k]|^2 = \frac{P_{ASE}}{4\pi}$. To get the variance, we integrate by $\int_{-\infty}^{\infty}|\tilde{S}_1^{\Im}(\Omega)|^2 d\Omega$.

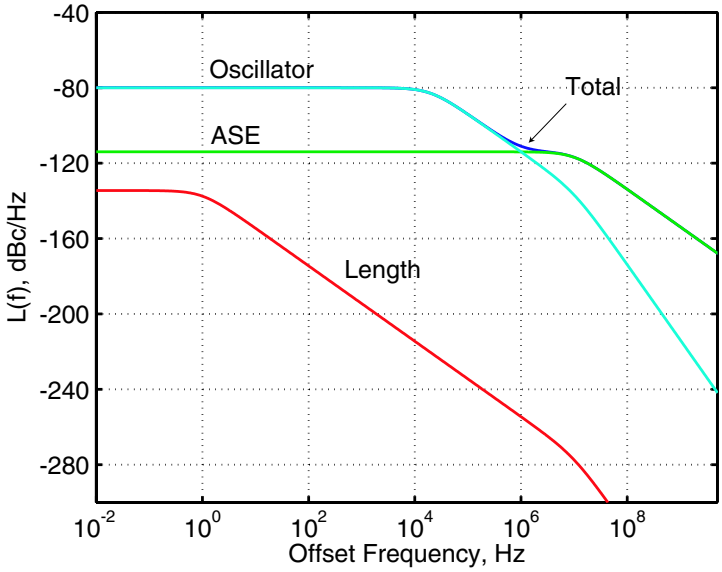

Figure B-13: SSB phase noise of actively modelocked 10 GHz semiconductor laser. Contributions from microwave oscillator (HP83732B), length fluctuations (10 μm rms length deviations with bandwidth of 1 Hz), and ASE ($\gamma_0^{\Re} = 2\pi \times 5$ MHz).

critically damped.[16] In any case, it can be seen that by overestimating the end-mirror deviations with 10 μ displacements, the cavity length fluctuations do not significantly contribute to the phase noise of the laser.

B.3 Noise of Actively Modelocked Soliton Lasers

The starting point for the noise analysis for the actively modelocked soliton laser is given by the master equation, equation (A.25), which describes the evolution of pulses in the cavity. Since the gain bandwidth in semiconductor and fiber lasers is usually much larger than the optical filter bandwidth, the gain filtering term is ignored, and the new master equation is

$$T_R \frac{\partial a(t,T)}{\partial T} = \left\{ -l + g + \frac{1}{\Omega_f^2}\frac{\partial^2}{\partial t^2} + jD\frac{\partial^2}{\partial t^2} - \frac{M_{AM} + jM_{PM}}{4}(\omega_M t)^2 \right.$$

[16] If the end-mirror was not critically damped, then there would be some oscillations at the natural frequency of the system. This would show up in the SSB phase noise as a noise enhancement around the natural oscillation frequency.

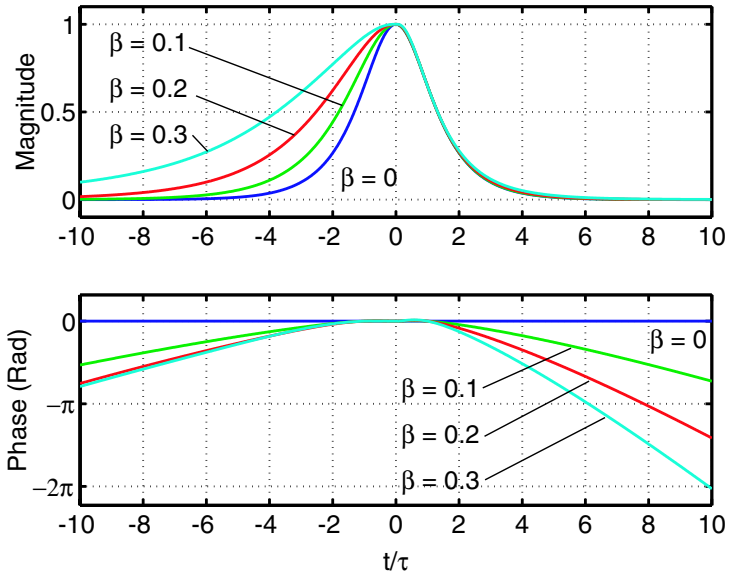

Figure B-14: Magnitude and phase of the chirped sech solution to the soliton master equation. For this plot, $\mathcal{A}_0 = 1$, $t_0 = 0$, $\psi = 0$ and $\theta = 0$.

$$
\begin{aligned}
& (\gamma - j\delta)|a(t,T)|^2\Big\}\, a(t,T) + T_R S(t,T) \\
= \quad & \left[\hat{O}_{sol} - \frac{M_{AM} + jM_{PM}}{4}(\omega_M t)^2\right] a(t,T) + T_R S(t,T). \quad \text{(B.227)}
\end{aligned}
$$

Compared to the Hermite-Gaussian noise analysis, we keep the the Kerr nonlinearity and saturable absorption terms in the master equation.

The solution to the master equation (B.227) without the modulation terms ($M_{AM} = 0$ and $M_{PM} = 0$) is a chirped hyperbolic secant

$$a(t,T) = \mathcal{A}_0 \text{sech}\left[\left(\frac{t-t_0}{\tau}\right)^{1+j\beta}\right] \exp\left[j\psi\frac{T}{T_R} + j\theta\right]. \quad \text{(B.228)}$$

Fig. B-14 shows this function plotted for different chirp parameters; β runs from 0 to 0.3. Notice that the phase is not strictly parabolic and hence the chirp is nonlinear.

If we assume that the saturable absorption ($\gamma > 0$), self-phase modulation ($\delta > 0$), filtering, and dispersion are related by

$$\frac{\gamma}{\delta} = \frac{1/\Omega_f^2}{-D} \equiv \mu \quad \text{(B.229)}$$

then, substitution of the chirped-sech solution into the master equation yields the following relations

$$\begin{aligned} \beta &= 0 && \text{(B.230)} \\ \mathcal{A}_0^2\tau^2 &= \frac{2|D|}{\delta} && \text{(B.231)} \\ \psi &= -\frac{|D|}{\tau^2} = -\frac{\delta}{2}\mathcal{A}_0^2 && \text{(B.232)} \\ g-l &= -\frac{1}{\tau^2}\frac{1}{\Omega_f^2} = -\frac{\gamma}{2}\mathcal{A}_0^2 && \text{(B.233)} \end{aligned}$$

which follow from setting the real and imaginary parts of the $\text{sech}(t/\tau)$ and $\text{sech}^3(t/\tau)$ terms equal to zero. Note that $D < 0$ is anomalous dispersion, which is the necessary sign to support solitons. Equation (B.230) implies that the resulting pulse is chirpless. Equation (B.231) is the so-called "Area Theorem" for solitons.

The chirped-sech solution given by equation (B.228) can be simplified by letting $\beta = 0$, t_0 and $\theta = 0$, so that

$$a_{ss}(t,T) = \mathcal{A}_0 \,\text{sech}\left[\frac{t}{\tau}\right] \exp\left[-j\frac{\delta}{2}\mathcal{A}_0^2\frac{T}{T_R}\right], \qquad \text{(B.234)}$$

where the subscript ss denotes the steady-state solution and

$$\tau = \frac{1}{\mathcal{A}_0}\sqrt{\frac{2|D|}{\delta}}. \qquad \text{(B.235)}$$

Note that $a_{ss}(t)$ is an eigensolution to the soliton operator:

$$T_R\frac{\partial}{\partial t}a_{ss}(t) = \hat{O}_{sol}a_{ss}(t). \qquad \text{(B.236)}$$

We can re-write the steady-state solution as

$$a_{ss}(t,T) = a_s(t)\exp\left[-j\frac{\delta}{2}\mathcal{A}_0^2\frac{T}{T_R}\right], \qquad \text{(B.237)}$$

where

$$a_s(t) = \mathcal{A}_0 \text{ sech}\left[\frac{t}{\tau}\right]. \tag{B.238}$$

The steady-state solution is normalized so that [17]

$$\int_{-\infty}^{\infty} |a_s(t)|^2 dt = 2\mathcal{A}_0^2\tau. \tag{B.239}$$

Therefore $\mathcal{A}_0^2$ has units of power, which contrasts with the Hermite-Gaussian analysis where A_0^2 has units of energy. The difference in units is due to the fact that ψ_0 is not unitless.

The next step is to find equations that describe the evolution of a perturbation to the steady-state solution. We assume that the solution can be written as the steady-state solution plus a small perturbation term according to

$$a(t,T) = a_{ss}(t,T) + \underline{\Delta a}(t,T), \tag{B.240}$$

where

$$\underline{\Delta a}(t,T) \equiv \Delta a(t,T) \times \exp\left(-j\frac{\delta}{2}\mathcal{A}_0^2\frac{T}{T_R}\right). \tag{B.241}$$

Substitution of equation (B.240) into the master equation (B.227) yields a master equation for the perturbation solution

$$\begin{aligned}
T_R\frac{\partial}{\partial T}\left[a_{ss}(t,T) + \underline{\Delta a}(t,T)\right] &= \left[\hat{O}_{sol} - \frac{M_{AM} + jM_{PM}}{4}(\omega_M t)^2\right]\left[a(t,T) + \underline{\Delta a}(t,T)\right] \\
&\quad + T_R S(t,T) \qquad \text{(B.242)} \\
T_R\frac{\partial}{\partial T}\underline{\Delta a}(t,T) &= \hat{O}_{sol}\underline{\Delta a}(t,T) - \frac{M_{AM} + jM_{PM}}{4}(\omega_M t)^2\left[a(t,T) + \underline{\Delta a}(t,T)\right] \\
&\quad + T_R S(t,T) \qquad \text{(B.243)} \\
T_R\frac{\partial}{\partial T}\Delta a(t,T) &= \hat{O}_{sol2}\Delta a(t,T) + (\gamma - j\delta)a_s^2(t)\Delta a^*(t,T) \\
&\quad - \frac{M_{AM} + jM_{PM}}{4}(\omega_M t)^2\left[a(t,T) + \Delta a(t,T)\right] \\
&\quad + T_R S(t,T)\exp\left(j\frac{\delta}{2}\mathcal{A}_0^2\frac{T}{T_R}\right), \qquad \text{(B.244)}
\end{aligned}$$

[17] $\int_{-\infty}^{\infty} \text{sech}x dx = 2$

where

$$\hat{O}_{sol2} \equiv \hat{O}_{sol} + (\gamma - j\delta)|a_s(t)|^2 \tag{B.245}$$

$$= -l + g + \frac{1}{\Omega_f^2}\frac{\partial^2}{\partial t^2} + jD\frac{\partial^2}{\partial t^2} + 2(\gamma - j\delta)|a_s(t)|^2 \tag{B.246}$$

The perturbation Δa is expanded into four orthogonal fluctuations

$$\Delta a(t,T) = f_w(t)\Delta w(T) + f_\theta(t)\Delta\theta(T) + f_p(t)\Delta p(T) + f_t(t)\Delta t(T) + \Delta a_c(t,T) \tag{B.247}$$

where the last term is the continuum contribution and is not part of the pulse. The four adjoint functions are defined as

$$f_w(t) = \frac{\partial a_0}{\partial w_0} = \frac{1}{w_0}\left[1 - \frac{t}{\tau}\tanh\left(\frac{t}{\tau}\right)\right]a_s(t) \tag{B.248}$$

$$f_\Theta(t) = \frac{\partial a_0}{\partial \Theta} = j a_s(t) \tag{B.249}$$

$$f_p(t) = \frac{\partial a_0}{\partial p} = j t a_s(t) \tag{B.250}$$

$$f_t(t) = -\frac{\partial a_0}{\partial t} = \frac{1}{\tau}\tanh\left(\frac{t}{\tau}\right)a_s(t) \tag{B.251}$$

and the corresponding orthogonal adjoint functions are

$$\underline{f}_w(t) = 2a_s(t) \tag{B.252}$$

$$\underline{f}_\Theta(t) = 2j\frac{1}{w_0}\left[1 - \frac{t}{\tau}\tanh\left(\frac{t}{\tau}\right)\right]a_s(t) \tag{B.253}$$

$$\underline{f}_p(t) = j\left(\frac{2}{w_0\tau}\tanh\left(\frac{t}{\tau}\right)\right)a_s(t) \tag{B.254}$$

$$\underline{f}_t(t) = \frac{2}{w_0} t a_s(t) \tag{B.255}$$

These functions obey the orthogonality relation

$$\Re\int_{-\infty}^{\infty} dt\, \underline{f}_i^*(t) f_j(t) = \delta_{ij} \tag{B.256}$$

The spontaneous emission noise adds energy randomly in time to either the real or

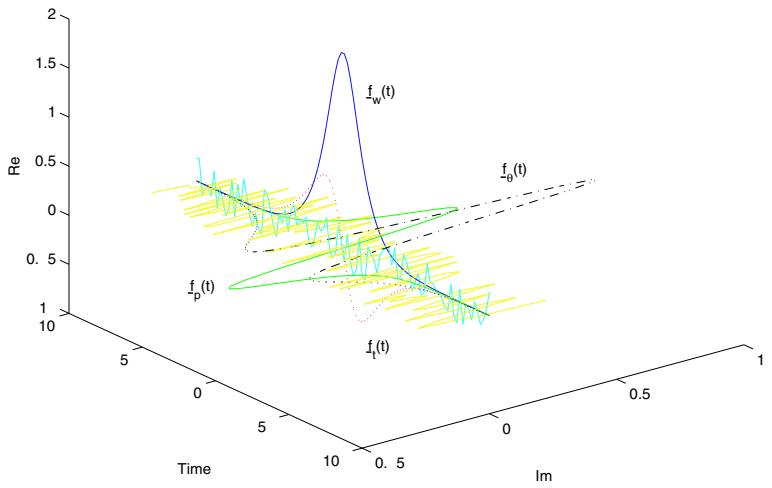

Figure B-15: Orthogonal projection functions. The real and imaginary noise is also shown.

imaginary part of the pulse. To find the ASE that causes amplitude fluctuations, the spontaneous emission in the pulse window is multiplied by a hyperbolic secant, $\underline{f}_w(t)$, which results in the component of ASE that contributes to the amplitude noise. The orthogonal adjoint functions are plotted in Fig. B-15.

B.3.1 Equations of Motion

The equations of motion are obtained by substituting equation (B.247) into equation (B.244). Both sides are multiplied by $\underline{f}_x(t)$, and integrated with respect to t, resulting in the equations of motion. These operations are rather algebraically involved, and therefore, the following approach simplifies this process.

First, we define a new operator

$$\begin{aligned}\hat{A}_t(\Delta a) \equiv & \left(-l+g+\frac{1}{\Omega_f^2}\frac{\partial^2}{\partial t^2}+jD\frac{\partial^2}{\partial t^2}+2(\gamma-j\delta)|a_s|^2\right)\Delta a+(\gamma-j\delta)|a_s|^2\Delta a^* \\ & -\frac{M_{AM}+jM_{PM}}{4}(\omega_M t)^2(a_s+\Delta a) \qquad \text{(B.257)} \\ = & \ (\mu-j)\left[-\frac{\delta}{2}\mathcal{A}_0^2+|D|\frac{\partial^2}{\partial t^2}+2\delta a_s^2+j\frac{\delta}{2}\mathcal{A}_0^2\right]\Delta a+(\mu-j)\delta a_s^2\Delta a^*\end{aligned}$$

$$-\frac{M_{AM}+jM_{PM}}{4}(\omega_M t)^2(a_s+\Delta a). \tag{B.258}$$

The equations (B.231), (B.232), and (B.233) were used to simplify equation (B.257) to (B.258). The linear perturbation equation (B.244) can be rewritten as

$$T_R\frac{\partial}{\partial T}\Delta a(T)=\hat{A}_t(\Delta a)+T_R S(t,T)\exp\left(j\frac{\delta}{2}\mathcal{A}_0^2\frac{T}{T_R}\right). \tag{B.259}$$

The phase factor multiplying the random noise source $S(t,T)$ can be absorbed into the noise source expression without loss of generality. Therefore, equation (B.259) becomes

$$T_R\frac{\partial}{\partial T}\Delta a(T)=\hat{A}_t(\Delta a)+T_R S(t,T). \tag{B.260}$$

The following identity is useful

$$\left[-\frac{\delta}{2}+|D|\frac{\partial^2}{\partial t^2}+\delta a_s^2\right]a_s=0 \tag{B.261}$$

which follows from equations (B.238), (B.231), (B.232), and (B.233).

The use of the identity (B.261) and some lengthy algebraic manipulation allows us to show that

$$\begin{aligned}
\hat{A}_t(f_t) &= -\frac{M_{AM}+jM_{PM}}{4}(\omega_M t)^2(a_s+f_t) && \text{(B.262)}\\
\hat{A}_t(f_p) &= -2|D|(1+j\mu)f_t-\frac{M_{AM}+jM_{PM}}{4}(\omega_M t)^2(a_s+f_p) && \text{(B.263)}\\
\hat{A}_t(f_\theta) &= -\frac{M_{AM}+jM_{PM}}{4}(\omega_M t)^2(a_s+f_\theta) && \text{(B.264)}\\
\hat{A}_t(f_w) &= (\mu-j)\delta\mathcal{A}_0^2\frac{a_s}{w_0}-\frac{M_{AM}+jM_{PM}}{4}(\omega_M t)^2(a_s+f_w). && \text{(B.265)}
\end{aligned}$$

The coefficients of the perturbation expansion may be picked out of the perturbation expansion according to

$$\begin{aligned}
\Delta w(T) &= \frac{1}{2}\int_{-\infty}^{\infty}dt\left[\underline{f}_w^*\Delta a(t,T)+\underline{f}_w\Delta a^*(t,T)\right] && \text{(B.266)}\\
\Delta\theta(T) &= \frac{1}{2}\int_{-\infty}^{\infty}dt\left[\underline{f}_\theta^*\Delta a(t,T)+\underline{f}_\theta\Delta a^*(t,T)\right] && \text{(B.267)}
\end{aligned}$$

$$\Delta p(T) = \frac{1}{2}\int_{-\infty}^{\infty} dt \left[\underline{f}_p^* \Delta a(t,T) + \underline{f}_p \Delta a^*(t,T)\right] \quad \text{(B.268)}$$

$$\Delta t(T) = \frac{1}{2}\int_{-\infty}^{\infty} dt \left[\underline{f}_t^* \Delta a(t,T) + \underline{f}_t \Delta a^*(t,T)\right] \quad \text{(B.269)}$$

Similarly, the projection of the noise onto timing, frequency, amplitude, and phase are found with the following equation

$$S_j(T) = \frac{1}{2}\int_{-\infty}^{\infty} dt \left[\underline{f}_j^* S(t,T) + \underline{f}_j S^*(t,T)\right] \quad \text{(B.270)}$$

where $j = w, \theta, p,$ or t.

We proceed to find the equation of motion of the timing fluctuations by operating on both sides of equation (B.269) with $T_R\partial/\partial T$ to obtain

$$\begin{aligned}
T_R\frac{\partial}{\partial T}\Delta t &= \frac{1}{2}\int_{-\infty}^{\infty} dt \left[\underline{f}_t^* \left(T_R\frac{\partial}{\partial T}\Delta a(t,T)\right) + \underline{f}_t \left(T_R\frac{\partial}{\partial T}\Delta a^*(t,T)\right)\right] \\
&= \frac{1}{2}\int_{-\infty}^{\infty} dt \left[\underline{f}_t^* \left(\hat{A}_t(\Delta a(T)) + T_R S(t,T)\right) + \underline{f}_t \left(\hat{A}_t(\Delta a(T))^* + T_R S^*(t,T)\right)\right] \\
&= \frac{1}{2}\int_{-\infty}^{\infty} dt \left[\underline{f}_t^* \hat{A}_t(\Delta a(T)) + c.c.\right] + T_R \underbrace{\frac{1}{2}\int_{-\infty}^{\infty} dt \left[\underline{f}_t^* S(t,T) + c.c.\right]}_{S_t(T)} \\
&= \frac{1}{2}\int_{-\infty}^{\infty} dt \left[\underline{f}_t^* \hat{A}_t(f_w\Delta w + f_\theta \Delta\theta + f_p\Delta p + f_t\Delta t) + c.c.\right] + T_R S_t(T) \\
&= \frac{1}{2}\int_{-\infty}^{\infty} dt \left[\underline{f}_t^* \left(\hat{A}_t(f_w\Delta w) + \hat{A}_t(f_\theta\Delta\theta) + \hat{A}_t(f_p\Delta p) + \hat{A}_t(f_t\Delta t)\right) + c.c.\right] \\
&\quad + T_R S_t(T) \\
&= \frac{1}{2}\int_{-\infty}^{\infty} dt \left[\underline{f}_t^* \left(\hat{A}_t(f_p\Delta p) + \hat{A}_t(f_t\Delta t)\right) + c.c.\right] + T_R S_t(T) \\
&= \frac{1}{2}\int_{-\infty}^{\infty} dt \left[\underline{f}_t^* \left(-2|D|(1+j\mu) f_t\Delta p - \frac{M_{AM}+jM_{PM}}{4}(\omega_m t)^2 f_p \Delta p\right.\right. \\
&\quad \left.\left. - \frac{M_{AM}+jM_{PM}}{4}(\omega_m t)^2 f_t \Delta t\right)\right] + c.c. + T_R S_t(T) \\
&= \frac{1}{2}\int_{-\infty}^{\infty} dt \left[-2|D|(1+j\mu)\Delta p - \frac{M_{AM}+jM_{PM}}{4}(\omega_m t)^2 \frac{j7\pi^4\tau^4}{120}\Delta p\right. \\
&\quad \left. - \frac{M_{AM}+jM_{PM}}{4}(\omega_m t)^2 \frac{\pi^2\tau^2}{4}\Delta t\right] + c.c. + T_R S_t(T) \\
&= -\frac{\pi^2 M_{AM}\omega_M^2\tau^2}{16}\Delta t + \left(\frac{7\pi^4 M_{PM}\omega_M^2\tau^4}{480} - 2|D|\right)\Delta p + T_R S_t(T) \qquad \text{(B.271)}
\end{aligned}$$

where equation (B.260) was used to simplify the expression from the first to second line. A few useful integrals that were used to simplify from the third to fourth lines were

$$\begin{aligned}
\int_{-\infty}^{\infty} \underline{f}_t^* t^2 f_t dt &= \frac{\pi^2\tau^2}{4} \approx 2.5\tau^2 \\
\int_{-\infty}^{\infty} \underline{f}_p^* t^2 f_p dt &= \frac{\pi^2\tau^2}{4} \\
\int_{-\infty}^{\infty} \underline{f}_t^* t^2 f_p dt &= j\frac{7\pi^4\tau^4}{120} \approx j5.7\tau^4 \\
\int_{-\infty}^{\infty} \underline{f}_p^* t^2 f_t dt &= -j\frac{12+\pi^2}{18} \approx -1.2j \\
\int_{-\infty}^{\infty} \underline{f}_p^* f_t dt &= -j\frac{2}{3\tau^2} \approx -1.2j
\end{aligned}$$

The coefficient that multiplies Δt on the right-hand-side of equation (B.271) is the pulse-position restoration force of the amplitude modulator. The coefficient that multiplies Δp on the right-hand-side of equation (B.271) is the pulse-position restoration force of the phase modulator. Notice that we need to choose the sign of the phase modulation to be $M_{PM} < 0$ to cause a restoration force with a cavity with anomalous dispersion.

The equation of motion for the frequency fluctuations can be found using the same procedure and we find that it is

$$\begin{aligned}
T_R\frac{\partial}{\partial T}\Delta p &= \frac{1}{2}\int_{-\infty}^{\infty} dt \left[\underline{f}_p^*\left(T_R\frac{\partial}{\partial T}\Delta a(t,T)\right) + \underline{f}_p\left(T_R\frac{\partial}{\partial T}\Delta a^*(t,T)\right)\right] \\
&= \frac{1}{2}\int_{-\infty}^{\infty} dt \left[\underline{f}_p^*\left(\hat{A}_t(\Delta a(T)) + T_R S(t,T)\right) + \underline{f}_p\left(\hat{A}_t(\Delta a(T))^* + T_R S^*(t,T)\right)\right] \\
&= \frac{1}{2}\int_{-\infty}^{\infty} dt \left[\underline{f}_p^*\hat{A}_t(\Delta a(T)) + c.c.\right] + T_R \underbrace{\frac{1}{2}\int_{-\infty}^{\infty} dt \left[\underline{f}_p^* S(t,T) + c.c.\right]}_{S_p(T)} \\
&= \frac{1}{2}\int_{-\infty}^{\infty} dt \left[\underline{f}_p^*\hat{A}_t(f_w\Delta w + f_\theta\Delta\theta + f_p\Delta p + f_t\Delta t) + c.c.\right] + T_R S_p(T) \\
&= \frac{1}{2}\int_{-\infty}^{\infty} dt \left[\underline{f}_p^*\left(\hat{A}_t(f_w\Delta w) + \hat{A}_t(f_\theta\Delta\theta) + \hat{A}_t(f_p\Delta p) + \hat{A}_t(f_t\Delta t)\right) + c.c.\right] \\
&\quad + T_R S_p(T) \\
&= \frac{1}{2}\int_{-\infty}^{\infty} dt \left[\underline{f}_p^*\left(\hat{A}_t(f_p\Delta p) + \hat{A}_t(f_t\Delta t)\right) + c.c.\right] + T_R S_p(T)
\end{aligned}$$

$$
\begin{aligned}
&= \frac{1}{2}\int_{-\infty}^{\infty} dt \left[\underline{f}_p^* \left(-2|D|(1+j\mu)f_t\Delta p - \frac{M_{AM}+jM_{PM}}{4}(\omega_m t)^2 f_p \Delta p \right.\right. \\
&\quad \left.\left. -\frac{M_{AM}+jM_{PM}}{4}(\omega_m t)^2 f_t \Delta t\right)\right] + c.c. + T_R S_p(T) \\
&= \frac{1}{2}\int_{-\infty}^{\infty} dt \left[-2|D|(1+j\mu)\left(-j\frac{2}{3\tau^2}\right)\Delta p - \frac{M_{AM}+jM_{PM}}{4}(\omega_m t)^2 \frac{\pi^2\tau^2}{4}\Delta p \right. \\
&\quad \left. -\frac{M_{AM}+jM_{PM}}{4}(\omega_m t)^2 \frac{-j(12+\pi^2)}{18}\Delta t\right] + c.c. + T_R S_t(T) \\
&= -\frac{\pi(12+\pi^2)M_{AM}\omega_M^2}{72}\Delta t + \left(-\frac{4}{3\Omega_f^2\tau^2} - \frac{\pi^2 M_{AM}\omega_M^2\tau^2}{16}\right)\Delta p \\
&\quad + T_R S_p(T). \qquad \text{(B.272)}
\end{aligned}
$$

The coefficient that multiplies Δt on the right-hand-side of equation (B.272) is the carrier-frequency restoration force of the phase modulator. The coefficient that multiplies Δt on the right-hand-side of equation (B.272) is the carrier-frequency restoration force of the amplitude modulator and optical bandpass filter.

In summary, the equations of motion for the timing and frequency fluctuations are

$$
\begin{aligned}
T_R\frac{\partial}{\partial T}\Delta t &= -\frac{\pi^2 M_{AM}\omega_M^2\tau^2}{16}\Delta t + \left(\frac{7\pi^4 M_{PM}\omega_M^2\tau^4}{480} - 2|D|\right)\Delta p \\
&\quad + T_R S_t(T) \qquad \text{(B.273)} \\
T_R\frac{\partial}{\partial T}\Delta p &= -\frac{\pi(12+\pi^2)M_{PM}\omega_M^2}{72}\Delta t + \left(-\frac{4}{3\Omega_f^2\tau^2} - \frac{\pi^2 M_{AM}\omega_M^2\tau^2}{16}\right)\Delta p \\
&\quad + T_R S_p(T). \qquad \text{(B.274)}
\end{aligned}
$$

The physical origin of the $\frac{7\pi^4 M_{PM}\omega_M^2\tau^4}{480}\Delta p$ term in equation (B.273) is re-timing of the pulses due to FM modelocking. In other words, a cavity with just gain and a phase modulator will re-time pulses without dispersion. A nice physical explanation is given in [85, p.1069].

The term $\frac{7\pi^4 M_{PM}\omega_M^2\tau^4}{480}$ in equation (B.273) is relatively small in comparison to the term $2|D|$ for fiber lasers, but both terms are small for semiconductor lasers. Typical values for semiconductor lasers are $M_{PM} = 4$, $\omega_M = 2\pi \times 10$ GHz, $\tau = 1$ ps, and $D = 10^-3$ ps^2. These values yield $\frac{7\pi^4 M_{PM}\omega_M^2\tau^4}{480} = 2.243 \times 10^{-26}$ s^2 and $2|D| = 2 \times 10^{-27}$ s^2. Hence, we see that this term is very small. For fiber lasers, the $\frac{7\pi^4 M_{PM}\omega_M^2\tau^4}{480}\Delta p$ term

is usually ignored since it is much smaller than the cavity dispersion.

The term $\frac{\pi^2 M_{AM}\omega_M^2\tau^2}{16}$ in equation (B.274) can be ignored since is much smaller than the term $\frac{4}{3\Omega_f^2\tau^2}$. Typical values are $M_{AM}=4$, $\omega_M = 2\pi\times 10$ GHz, $\tau = 1$ ps, and $\Omega_f = 5/2$ nm. These values yield $\frac{4}{3\Omega_f^2\tau^2} = 12.06$ and $\frac{\pi^2 M_{AM}\omega_M^2\tau^2}{16} = 2.435\times 10^{-3}$.

Using the simplifications mentioned in the previous two paragraphs and assuming that there is only amplitude modulation results in the following simplified equations of motion

$$T_R\frac{\partial}{\partial T}\Delta t = -\frac{\pi^2 M_{AM}\omega_M^2\tau^2}{16}\Delta t - 2|D|\Delta p + T_R S_t(T) \tag{B.275}$$

$$T_R\frac{\partial}{\partial T}\Delta p = -\frac{4}{3\Omega_f^2\tau^2}\Delta p + T_R S_p(T). \tag{B.276}$$

The equations of motion for the amplitude fluctuations were not included since we did not include gain saturation in our soliton noise theory analysis, which bounds the amplitude fluctuations.

The equations (B.273) and (B.274) are used to obtain an expression for the timing and frequency fluctuations. We first take the Fourier transform of these equations ($\Delta t(T)\rightarrow\Delta\tilde{t}(\Omega)$, $\Delta p(T)\rightarrow\Delta\tilde{p}(\Omega)$, $S_t(T)\rightarrow\tilde{S}_t(\Omega)$, $S_p(T)\rightarrow\tilde{S}_p(\Omega)$ and $\partial/\partial T\rightarrow j\Omega$) and solve the algebraic equations to obtain

$$\Delta\tilde{t}(\Omega) = \frac{-\frac{2|D|}{T_R}\Delta\tilde{p} + \tilde{S}_t(\Omega)}{j\Omega + \frac{\pi^2 M_{AM}\omega_M^2\tau^2}{16T_R}} \tag{B.277}$$

$$\Delta\tilde{p}(\Omega) = \frac{\tilde{S}_p(\Omega)}{j\Omega + \frac{4}{3\Omega_f^2\tau^2 T_R}}. \tag{B.278}$$

The power spectra for the mean-square pulse parameters are

$$\langle|\Delta\tilde{t}(\Omega)|^2\rangle = \frac{1}{\Omega^2+\frac{1}{\tau_{AM}^2}}\left\{\left(2|D|\frac{1}{T_R}\right)^2\frac{\langle|\tilde{S}_p(\Omega)|^2\rangle}{\Omega^2+\frac{1}{\tau_p^2}} + \langle|\tilde{S}_t(\Omega)|^2\rangle\right\} \tag{B.279}$$

$$\langle|\Delta\tilde{p}(\Omega)|^2\rangle = \frac{\langle|\tilde{S}_p(\Omega)|^2\rangle}{\Omega^2+\frac{1}{\tau_p^2}}, \tag{B.280}$$

where the time constants are defined as

$$\frac{1}{\tau_{AM}} = \frac{\pi^2 M_{AM}\omega_M^2\tau^2}{16}\frac{1}{T_R} \tag{B.281}$$

$$\frac{1}{\tau_p} = \frac{4}{3\Omega_f^2\tau^2}\frac{1}{T_R}. \tag{B.282}$$

B.3.2 Spontaneous Emission Noise

The next step is to determine the autocorrelation function of $S_t(T)$ and $S_p(T)$. Spontaneous emission is uncorrelated white noise

$$\langle S_{qn}(t,T)S_{qn}^*(t',T')\rangle = h\nu B n_{sp}(G-1)\delta(t-t')\delta(T-T') \approx n_{sp}\frac{2g}{T_R}h\nu\delta(t-t')\delta(T-T') \tag{B.283}$$

where S_{qn} is the quantum noise. The autocorrelation function of the quantum noise can be expressed in terms of its uncorrelated real and imaginary parts

$$\langle S_{qn}(t,T)S_{qn}^*(t',T')\rangle = \langle \Re\{S_{qn}(t,T)\}\Re\{S_{qn}(t',T')\}\rangle + \langle \Im\{S_{qn}(t,T)\}\Im\{S_{qn}(t',T')\}\rangle \tag{B.284}$$

There is equal noise energy in the real and imaginary parts, which implies that

$$\langle \Re\{S_{qn}(t,T)\}\Re\{S_{qn}(t',T')\}\rangle = \langle \Im\{S_{qn}(t,T)\}\Im\{S_{qn}(t',T')\}\rangle. \tag{B.285}$$

and

$$\langle S_{qn}(t,T)S_{qn}^*(t',T')\rangle = 2\langle \Re\{S_{qn}(t,T)\}\Re\{S_{qn}(t',T')\}\rangle. \tag{B.286}$$

Also note that

$$\begin{aligned}\langle S_{qn}(t,T)S_{qn}(t',T')\rangle &= \langle \Re\{S_{qn}(t,T)\}\Re\{S_{qn}(t',T')\}\rangle \\ &\quad -\langle \Im\{S_{qn}(t,T)\}\Im\{S_{qn}(t',T')\}\rangle \\ &\quad +j\langle \Re\{S_{qn}(t,T)\}\Im\{S_{qn}(t',T')\}\rangle \\ &\quad +j\langle \Im\{S_{qn}(t,T)\}\Re\{S_{qn}(t',T')\}\rangle \qquad \text{(B.287)}\\ &= 0 \qquad \text{(B.288)}\end{aligned}$$

since the real and imaginary parts are uncorrelated. The contribution of spontaneous emission noise to timing fluctuations is $S_t(T)$ and its autocorrelation function is

$$\begin{aligned}
\langle S_t(T)S_t^*(T')\rangle &= \langle\frac{1}{2}\int_{-\infty}^{\infty}dt\left[\underline{f}_t^*S(t,T)+\underline{f}_tS^*(t,T)\right] \\
&\quad +\frac{1}{2}\int_{-\infty}^{\infty}dt\left[\underline{f}_tS^*(t,T')+\underline{f}_t^*S(t,T')\right]\rangle \\
&= \langle\frac{1}{2}\int_{-\infty}^{\infty}dt\left[\underline{f}_t^*S_{qn}(t,T)+\underline{f}_tS_{qn}^*(t,T)\right] \\
&\quad +\frac{1}{2}\int_{-\infty}^{\infty}dt\left[\underline{f}_tS_{qn}^*(t,T')+\underline{f}_t^*S_{qn}(t,T')\right]\rangle \\
&= \frac{1}{4}\int_{-\infty}^{\infty}dt\left[(\underline{f}_t^*)^2\underbrace{\langle S_{qn}(t,T)S_{qn}(t,T')\rangle}_{0}+(\underline{f}_t)^2\underbrace{\langle S_{qn}^*(t,T)S_{qn}^*(t,T')\rangle}_{0}\right. \\
&\quad \left.+(\underline{f}_t^*\underline{f}_t)\underbrace{\langle S_{qn}(t,T)S_{qn}^*(t,T')\rangle}_{2\langle\Re\{S_{qn}(t,T)\}\Re\{S_{qn}(t',T')\}\rangle}+(\underline{f}_t\underline{f}_t^*)\langle S_{qn}^*(t,T)S_{qn}(t,T')\rangle\right] \\
&= \frac{1}{4}\int_{-\infty}^{\infty}dt4\langle\Re\{S_{qn}(t,T)\}\Re\{S_{qn}(t',T')\}\rangle(\underline{f}_t^*\underline{f}_t) \\
&= \frac{1}{2}h\nu Bn_{sp}(G-1)\delta(T-T') \qquad \underbrace{\int_{-\infty}^{\infty}dt\underline{f}_t^*\underline{f}_t}_{\int 2ta_s/w_0dt=\pi^2\tau^2/(3w_0)} \\
&= \frac{1}{2}\frac{\pi^2\tau^2}{3w_0}h\nu Bn_{sp}(G-1)\delta(T-T') \\
&\approx \frac{\pi^2\tau^2}{6w_0}\left(n_{sp}\frac{2g}{T_R}h\nu\right)\delta(T-T') \qquad \text{(B.289)}
\end{aligned}$$

The projection of spontaneous emission noise onto frequency fluctuations is $S_p(T)$ and its autocorrelation function can be computed in a similar fashion

$$\begin{aligned}
\langle S_p(T)S_p^*(T')\rangle &= \langle\frac{1}{2}\int_{-\infty}^{\infty}dt\left[\underline{f}_p^*S(t,T)+\underline{f}_pS^*(t,T)\right] \\
&\quad +\frac{1}{2}\int_{-\infty}^{\infty}dt\left[\underline{f}_pS^*(t,T')+\underline{f}_p^*S(t,T')\right]\rangle \\
&= \langle\frac{1}{2}\int_{-\infty}^{\infty}dt\left[\underline{f}_p^*S_{qn}(t,T)+\underline{f}_pS_{qn}^*(t,T)\right] \\
&\quad +\frac{1}{2}\int_{-\infty}^{\infty}dt\left[\underline{f}_pS_{qn}^*(t,T')+\underline{f}_p^*S_{qn}(t,T')\right]\rangle \\
&= \frac{1}{4}\int_{-\infty}^{\infty}dt\left[(\underline{f}_p^*)^2\underbrace{\langle S_{qn}(t,T)S_{qn}(t,T')\rangle}_{0}+(\underline{f}_p)^2\underbrace{\langle S_{qn}^*(t,T)S_{qn}^*(t,T')\rangle}_{0}\right.
\end{aligned}$$

$$
\begin{aligned}
&+(\underline{f}_p^*\underline{f}_p)\underbrace{\langle S_{qn}(t,T)S_{qn}^*(t,T')\rangle}_{2\langle\Re\{S_{qn}(t,T)\}\Re\{S_{qn}(t',T')\}\rangle}+(\underline{f}_p\underline{f}_p^*)\langle S_{qn}^*(t,T)S_{qn}(t,T')\rangle\Big] \\
&= \frac{1}{4}\int_{-\infty}^{\infty}dt4\langle\Re\{S_{qn}(t,T)\}\Re\{S_{qn}(t',T')\}\rangle(\underline{f}_p^*\underline{f}_p) \\
&= \frac{1}{2}h\nu Bn_{sp}(G-1)\delta(T-T')\underbrace{\int_{-\infty}^{\infty}dt\underline{f}_p^*\underline{f}_p}_{\int(\frac{2}{w_0\tau}\tanh\frac{t}{\tau})^2a_s^2dt=4/(3w_0\tau^2)} \\
&= \frac{1}{2}\frac{4}{3w_0\tau^2}h\nu Bn_{sp}(G-1)\delta(T-T') \\
&\approx \frac{2}{3w_0\tau^2}n_{sp}\left(\frac{2g}{T_R}h\nu\right)\delta(T-T') \qquad \text{(B.290)}
\end{aligned}
$$

The diffusion coefficients for timing and frequency fluctuations are

$$
\begin{aligned}
D_t &= \frac{\pi^2\tau^2}{6w_0}\left(n_{sp}\frac{2g}{T_R}h\nu\right) &\text{(B.291)}\\
D_p &= \frac{2}{3w_0\tau^2}\left(n_{sp}\frac{2g}{T_R}h\nu\right) &\text{(B.292)}
\end{aligned}
$$

The power spectral density of the timing and frequency noise is equal to the Fourier transform of their autocorrelation functions

$$
\begin{aligned}
\langle|S_{t,qn}(\Omega)|^2\rangle &= D_t &\text{(B.293)}\\
\langle|S_{p,qn}(\Omega)|^2\rangle &= D_p. &\text{(B.294)}
\end{aligned}
$$

The above expressions assume that there is only spontaneous emission noise.

B.3.3 Length Fluctuations

Fluctuations of the cavity length changes the pulse by

$$
\begin{aligned}
a_{n+1}(t) &= a_n\left(t-\frac{\Delta L}{v_g}\right) &\text{(B.295)}\\
&= a_n(t)-\frac{\Delta L}{v_g}\frac{\partial a_n}{\partial t} &\text{(B.296)}\\
a_{n+1}(t)-a_n(t) &= -\frac{\Delta L}{v_g}\frac{\partial a_n}{\partial t} &\text{(B.297)}
\end{aligned}
$$

$$T_R \frac{\partial a}{\partial T} = \underbrace{-\frac{\Delta L}{v_g}\frac{\partial a_s(t,T)}{\partial t}}_{T_R S_L(t,T)} \tag{B.298}$$

The noise contribution is therefore equal to

$$S_L(t,T) = -\frac{\Delta L}{v_g T_R}\frac{\partial}{\partial t}a_s(t,T) = \frac{\Delta L}{v_g T_R} f_t(t) \tag{B.299}$$

The noise contribution due to fluctuations in the refractive index can be obtained by replacing ΔL with $L(\Delta n/n)$.

Projecting the length fluctuations into the timing noise component yields

$$S_t(T) = -\frac{1}{v_g T_R}\Delta L(T). \tag{B.300}$$

The length fluctuations do not contribute to frequency noise.

The power spectral density of the timing noise component due to length fluctuations is

$$\langle|\tilde{S}_{t,L}(\Omega)|^2\rangle = \left(\frac{1}{v_g T_R}\right)^2 \langle|\tilde{S}_L(\Omega)|^2\rangle, \tag{B.301}$$

where $\langle|\tilde{S}_L(\Omega)|^2\rangle$ is the power spectral density of the length fluctuations. Most of the power spectral energy of the length fluctuations is less than 10 kHz.

B.3.4 Microwave Oscillator Noise

Expanding the cosinusoidal modulation term of equation (A.24) yields

$$\cos(\omega_M t + \Delta\phi(T)) \approx 1 - \frac{(\omega_M t)^2}{2} - \frac{2(\omega_M t)\Delta\phi(T)}{2} + \ldots \tag{B.302}$$

The last part is due to the phase noise of the microwave oscillator. Note that the phase noise term is only a function of T (not t) since the majority of the phase noise energy is typically under 10 MHz and hence slower than the round-trip time of the laser.

$$T_R \frac{\partial a}{\partial T} = -\frac{M_{AM} + jM_{PM}}{4} \times 2\omega_M t \Delta\phi(T) \times a(t,T) \quad \text{(B.303)}$$

$$= -\frac{M_{AM} + jM_{PM}}{4} \times \omega_M \Delta\phi(T) \times w_0 \underline{f}_t \quad \text{(B.304)}$$

$$\equiv T_R S_{\Delta\phi}(t,T) \quad \text{(B.305)}$$

where we used the definition $\underline{f}_t = 2ta_s(t)/w_0$, hence

$$S_{\Delta\phi}(t,T) = -\frac{M_{AM} + jM_{PM}}{4T_R} \omega_M \Delta\phi(T) \times w_0 \underline{f}_t(t) \quad \text{(B.306)}$$

Projecting the microwave oscillator noise into the timing noise component yields[18]

$$S_t(T) = \frac{1}{2} \int_{-\infty}^{\infty} dt \left[\underline{f}_t^* S_{\Delta\phi}(t,T) + c.c. \right] \quad \text{(B.309)}$$

$$= -\frac{M_{AM} \omega_M \pi^2 \tau^2}{12 T_R} \Delta\phi(T). \quad \text{(B.310)}$$

Projecting into the frequency noise component yields

$$S_p(T) = \frac{M_{PM} \omega_M}{2T_R} \Delta\phi(T). \quad \text{(B.311)}$$

The power spectral density of the timing and frequency noise is equal to the Fourier transform of their autocorrelation functions

$$\langle |S_{t,osc}(\Omega)|^2 \rangle = \left(\frac{M_{AM} \omega_M \pi^2 \tau^2}{12 T_R} \right)^2 \langle |S_{osc}(\Omega)|^2 \rangle \quad \text{(B.312)}$$

$$\langle |S_{p,osc}(\Omega)|^2 \rangle = \left(\frac{M_{PM} \omega_M}{2T_R} \right)^2 \langle |S_{osc}(\Omega)|^2 \rangle. \quad \text{(B.313)}$$

[18]The following integrals are useful for this section

$$\int_{-\infty}^{\infty} dt \underline{f}_p^* \underline{f}_t = -j \frac{2}{w_0} \quad \text{(B.307)}$$

and

$$\int_{-\infty}^{\infty} dt \underline{f}_t^* \underline{f}_t = \frac{\pi^2 \tau^2}{3 w_0}. \quad \text{(B.308)}$$

where

$$\langle |S_{osc}(\Omega)|^2 \rangle = \left| \int_{-\infty}^{\infty} \Delta\phi(T) \exp(-j\Omega T) dT \right|^2 \tag{B.314}$$

is the phase noise of the oscillator.

B.3.5 Total Noise and RMS Timing Jitter

The power spectral density of the spontaneous emission noise, length fluctuations, and microwave oscillator noise drive the timing and frequency fluctuations according to equations (B.279) and (B.280). The noise driving terms in those equations are

$$\begin{aligned}
\langle |\tilde{S}_t(\Omega)|^2 \rangle &= \langle |\tilde{S}_{t,qn}(\Omega)|^2 \rangle + \langle |\tilde{S}_{t,L}(\Omega)|^2 \rangle + \langle |\tilde{S}_{t,osc}(\Omega)|^2 \rangle \\
&= D_t + \left(\frac{1}{v_g T_R} \right)^2 \langle |\tilde{S}_L(\Omega)|^2 \rangle + \left(\frac{M_{AM} \omega_M \pi^2 \tau^2}{12 T_R} \right)^2 \langle |S_{osc}(\Omega)|^2 \rangle \qquad \text{(B.315)} \\
\langle |\tilde{S}_p(\Omega)|^2 \rangle &= \langle |\tilde{S}_{p,qn}(\Omega)|^2 \rangle + \langle |\tilde{S}_{p,osc}(\Omega)|^2 \rangle \\
&= D_p + \left(\frac{M_{PM} \omega_M}{2 T_R} \right)^2 \langle |S_{osc}(\Omega)|^2 \rangle . \qquad \text{(B.316)}
\end{aligned}$$

It was assumed that the quantum noise, length fluctuations, and microwave oscillator phase noise are uncorrelated. To compare our measured residual phase noise spectra to the soliton noise theory, we use equations (B.279), (B.280), and the noise driving terms above.

The next step is to evaluate the mean-squared timing jitter from the noise spectrum. The total timing mean square fluctuations are equal to [10, p.988]

$$\begin{aligned}
\sigma_{t,pp}^2 &= \langle |\Delta t(T + T_0) - \Delta t(T_0)|^2 \rangle \\
&= \frac{1}{2\pi} \int_{-\infty}^{\infty} \langle |\Delta\tilde{t}(\Omega) \left(e^{j\Omega T} - 1 \right)|^2 \rangle \\
&= \frac{2}{\pi} \int_{0}^{\infty} \langle |\Delta\tilde{t}(\Omega)|^2 \rangle \left[1 - \cos(\Omega T) \right] \qquad \text{(B.317)}
\end{aligned}$$

For the limit $T \to \infty$, the pulse-to-pulse jitter becomes

$$\sigma_{t,pp}^2 = \frac{2}{\pi} \int_{0}^{\infty} \langle |\Delta\tilde{t}(\Omega)|^2 \rangle d\Omega. \tag{B.318}$$

The pulse-to-clock variance is less by a factor of two,

$$\sigma_{t,pc}^2 = \int_{-\infty}^{\infty} \langle |\Delta\tilde{t}(\Omega)|^2 \rangle \frac{d\Omega}{2\pi} = \frac{1}{\pi} \int_0^{\infty} \langle |\Delta\tilde{t}(\Omega)|^2 \rangle d\Omega. \tag{B.319}$$

The mean-squared timing fluctuations in the frequency of interest from f_{low} to f_{high} is

$$\sigma_{t,pc}^2 = \frac{1}{\pi} \int_{f_{low}}^{f_{high}} \langle |\Delta\tilde{t}(\Omega)|^2 \rangle d\Omega. \tag{B.320}$$

Applying equation (B.319) to equation (B.279) and considering only quantum noise yields [19]

$$\sigma_{t,pc}^2 = \frac{1}{2} \left(2|D| \frac{1}{T_R} \right)^2 \frac{\tau_{AM}^2 \tau_p^2}{\tau_p + \tau_{AM}} D_p + \frac{1}{2} \tau_{AM} D_t \tag{B.323}$$

The damping due to filtering is usually stronger than that of the modulator. Symbolically this means that $\tau_{AM} \gg \tau_p$, which reduces the equation above to[20]

$$\sigma_{t,pc}^2 = \frac{1}{2} \left(2|D| \frac{1}{T_R} \right)^2 \tau_{AM} \tau_p^2 D_p + \frac{1}{2} \tau_{AM} D_t. \tag{B.324}$$

We can substitute equations (B.291) and (B.292) for D_t and D_p in equation (B.324) to obtain

$$\sigma_{t,pc}^2 = \frac{1}{2} \left(2|D| \frac{1}{T_R} \right)^2 \tau_{AM} \tau_p^2 \frac{2}{3 w_0 \tau^2} \left(n_{sp} \frac{2g}{T_R} h\nu \right) + \frac{1}{2} \tau_{AM} \frac{\pi^2 \tau^2}{6 w_0} \left(n_{sp} \frac{2g}{T_R} h\nu \right). \tag{B.325}$$

We next substitute equations (B.281) and (B.282) for τ_{AM} and τ_p in equation (B.325)

[19] Two useful integrals for evaluating this integral are

$$\int_0^{\infty} \frac{1}{\Omega^2 + a^2} d\Omega = \frac{\pi}{2a} \tag{B.321}$$

and

$$\int_0^{\infty} \frac{1}{(\Omega^2 + a^2)(\Omega^2 + b^2)} d\Omega = \frac{\pi}{2ab(a+b)} \tag{B.322}$$

[20] For example, typical laser parameters are $\omega_M = 2\pi \times 10$ GHz, $\Omega_f = 5/2$ nm, $M_{AM} = 1$, $\tau = 1$ ps, and $T_R = 100$ ps. For these values, $\tau_{AM} = 4106.78$ ps and $\tau_p = 8.29$ ps.

to obtain

$$\begin{aligned}
\sigma_{t,pc}^2 &= \frac{1}{2}\left(2|D|\frac{1}{T_R}\right)^2 \frac{16T_R}{\pi^2 M_{AM}\omega_M^2\tau^2}\left(\frac{3\Omega_f^2\tau^2 T_R}{4}\right)^2 \frac{2}{3w_0\tau^2}\left(n_{sp}\frac{2g}{T_R}h\nu\right) \\
&\quad + \frac{1}{2}\frac{16T_R}{\pi^2 M_{AM}\omega_M^2\tau^2}\frac{\pi^2\tau^2}{6w_0}\left(n_{sp}\frac{2g}{T_R}h\nu\right) \qquad \text{(B.326)} \\
&= \frac{n_{sp}2gh\nu}{M_{AM}\omega_M^2 w_0}\left(\frac{12|D|^2\Omega_f^4}{\pi^2}+\frac{4}{3}\right) \qquad \text{(B.327)} \\
&\approx 1.25(|D|^2\Omega_f^4+1)\frac{n_{sp}2gh\nu}{M_{AM}\omega_M^2 w_0} \qquad \text{(B.328)} \\
&= 1.25(|D|^2\Omega_f^4+1)\frac{P_{ASE}T_R}{M_{AM}\omega_M^2 w_0}. \qquad \text{(B.329)}
\end{aligned}$$

Remember that this is the rms timing jitter due to spontaneous emission only. For $D = 0$, it is interesting to note that soliton timing variance is about equal ($\sigma_{t,pc}^2(sol) = 0.625\sigma_{t,pc}^2(HG)$) to the corresponding Hermite-Gaussian results that are given by equation (B.119). Since the filter bandwidth in a soliton laser is proportional to $1/\tau^2$, the Gordon-Haus rms jitter is proportional to $1/\tau^4$.

B.4 Soliton Noise Theory versus Hermite-Gaussian Noise Theory

The equations of motion for the Hermite-Gaussian noise theory are given by equation (B.126)

$$\begin{aligned}
\frac{\partial}{\partial T}\Delta t(T) &= -\frac{M_{AM}\omega_M^2\tau^2}{2T_R}\Delta t(T) + \frac{2D}{T_R}\Delta p(T) \\
&\quad + \frac{\sqrt{2}}{A_0}\tau\Re\left\{\int_{-\infty}^{\infty} S(t,T)\psi_1\left(\frac{t}{\tau}\right)dt\right\} \qquad \text{(B.330)} \\
\frac{\partial}{\partial T}\Delta p(T) &= -\frac{M_{PM}\omega_M^2}{2T_R}\Delta t(T) - \frac{2}{\Omega_f^2\tau^2 T_R}\Delta p(T) \\
&\quad + \frac{\sqrt{2}}{A_0}\frac{1}{\tau}\Im\left\{\int_{-\infty}^{\infty} S(t,T)\psi_1\left(\frac{t}{\tau}\right)dt\right\}. \qquad \text{(B.331)}
\end{aligned}$$

where equations (B.104) and (B.105) were substituted for $\gamma_0^{\Re}$ and $\gamma_0^{\Im}$.

The equations of motion for the soliton noise theory are given by equations (B.275)

and (B.276)

$$\begin{aligned}
\frac{\partial}{\partial T}\Delta t &= -\frac{\pi^2 M_{AM}\omega_M^2\tau^2}{16T_R}\Delta t + \frac{2D}{T_R}\Delta p \\
&\quad + \frac{1}{2}\int_{-\infty}^{\infty} dt\left[\left(\frac{2}{w_0}ta_s(t)\right)S(t,T) + c.c.\right] \qquad \text{(B.332)} \\
\frac{\partial}{\partial T}\Delta p &= -\frac{\pi(12+\pi^2)M_{PM}\omega_M^2}{72}\Delta t - \frac{4}{3\Omega_f^2\tau^2 T_R}\Delta p \\
&\quad + \frac{1}{2}\int_{-\infty}^{\infty} dt\left[-j\left(\frac{2}{w_0\tau^2}ta_s(t)\right)S(t,T) + c.c.\right], \qquad \text{(B.333)}
\end{aligned}$$

where we substituted in values for S_t and S_p, used the first order expansion $\tanh(t/\tau) \approx t/\tau$ for the frequency noise driving term, and included the Δt term on the r.h.s. of the equation of motion for frequency fluctuations.

We first notice that the equations of motion for both theories are quite similar. The restoration forces are very close in magnitude (within a factor of 2). If the coefficients in the Hermite-Gaussian equations of motion are scaled as

$$\frac{d}{dT}\begin{pmatrix}\Delta t\\ \Delta p\end{pmatrix} = \begin{pmatrix}a_{11} & a_{12}\\ a_{21} & a_{22}\end{pmatrix}\begin{pmatrix}\Delta t\\ \Delta p\end{pmatrix} + \begin{pmatrix}S_t^{HG}\\ S_p^{HG}\end{pmatrix} \qquad \text{(B.334)}$$

then the soliton equations of motion are scaled as

$$\frac{d}{dT}\begin{pmatrix}\Delta t\\ \Delta p\end{pmatrix} = \begin{pmatrix}1.2337a_{11} & a_{12}\\ 1.9085a_{21} & 0.6666a_{22}\end{pmatrix}\begin{pmatrix}\Delta t\\ \Delta p\end{pmatrix} + \begin{pmatrix}S_t^{sol}\\ S_p^{sol}\end{pmatrix} \qquad \text{(B.335)}$$

Equation (B.117) shows that $\sigma_{t,pc}^2$ is inversely proportional to $a_{11} = -2\gamma_0^{\Re}$. Assuming that $S_t^{sol} = S_t^{HG}$ and $S_p^{sol} = S_p^{HG}$, then a soliton laser should have a slightly lower timing jitter than a purely actively-modelocked laser according to $\sigma_{t,pc}^2(sol) = \sigma_{t,pc}^2(HG)/1.2337$.

In the previous section, we computed that the soliton laser was actually slightly quieter than the Hermite-Gaussian laser, $\sigma_{t,pc}^2(sol) = 0.625\ \sigma_{t,pc}^2(HG)$. This implies that the noise driving terms of the soliton and Hermite-Gaussian case are similar in magnitude.

B.5 Fourier Transform of Continuous-Time Power Signals

This section reviews the Fourier transform of continuous-time power signals which is important for understanding the units of the variables in the noise analysis. The signals in this section, such as $\Delta w(T)$ and $a(t,T)$, fall into this category since their time integral, $\int a(t)dt$, goes to infinity. The Fourier transform pair of a continuous-time power signal is given by [94, p.228,231]

$$\tilde{V}[k] = \frac{1}{\Delta T}\int_{-\Delta T/2}^{\Delta T/2} v(t)\exp(-jk\Omega_1 t)dt \tag{B.336}$$

$$v(t) = \sum_{k=-\infty}^{\infty} \tilde{V}[k]\exp(jk\Omega_1 t), \tag{B.337}$$

where $\Omega_1 \equiv 2\pi/\Delta T$ and ΔT can be a very long time. The units of $\tilde{V}[k]$ and $v(t)$ are the same. The power of the signal is given by Parseval's theorem

$$\text{“Power”} = \frac{1}{\Delta T}\int_{-\Delta T/2}^{\Delta T/2} |v(t)|^2 dt = \sum_{k=-\infty}^{\infty} |\tilde{V}[k]|^2. \tag{B.338}$$

The autocorrelation function for continuous-time power signals is defined as

$$R_{vv}(\mathcal{T}) = \langle v(t)v^*(t-\mathcal{T})\rangle = \frac{1}{\Delta T}\int_{-\Delta T/2}^{\Delta T/2} v(t)v^*(t-\mathcal{T})dt. \tag{B.339}$$

The autocorrelation function equals the power of the signal when $\mathcal{T} = 0$. Mathematically, this can be expressed as $P = R_{vv}(0)$. The Fourier transform of the autocorrelation function is the power spectral density

$$G_{vv}[k] = \frac{1}{\Delta T}\int_{-\Delta T/2}^{\Delta T/2} R_{vv}(\mathcal{T})\exp(-jk\Omega_1\mathcal{T})d\mathcal{T}. \tag{B.340}$$

Evaluating this integral, we obtain the Wiener-Khinechine theorem

$$G_{vv}[k] = |\tilde{V}[k]|^2. \tag{B.341}$$

This theorem indicates that the power spectral density is equal to the magnitude of the Fourier transform of $v(t)$ squared.

An important property of the Fourier transform is the following relationship $\partial/\partial t \Leftrightarrow jk\Omega_1$.

Often we are interested in comparing the power spectral density to a continuous frequency domain measurement. The following relation can be used to convert from a discrete spectrum to a continuous spectrum (see Fig. B-16) and is derived by setting the integrated spectra (power) equal

$$\begin{aligned} \int_{\frac{2\pi k_0}{\Delta T}-\frac{\pi}{\Delta T}}^{\frac{2\pi k_0}{\Delta T}+\frac{\pi}{\Delta T}} |\tilde{V}(\Omega)|^2 d\Omega &= |V[k_0]|^2 \\ |\tilde{V}(\Omega_0)|^2 \frac{2\pi}{\Delta T} &= |V[k_0]|^2 \end{aligned} \tag{B.342}$$

where $\Omega_0 = 2\pi k_0/\Delta T$. Hence,

$$|\tilde{V}(\Omega_0)|^2 = \frac{\Delta T}{2\pi} \times |\tilde{V}[k_0]|^2. \tag{B.343}$$

To obtain the variance or power, we note that for $\Delta T \to \infty$

$$\begin{aligned} P &= \sum_{k=-\infty}^{\infty} |\tilde{V}[k]|^2 \\ &= \sum_{k=-\infty}^{\infty} |\tilde{V}(\Omega)|^2 \frac{2\pi}{\Delta T} \\ &\approx \int_{-\infty}^{\infty} |\tilde{V}(\Omega)|^2 d\Omega \qquad \text{(B.344)} \\ &= \int_{-\infty}^{\infty} \frac{\Delta T}{2\pi} |\tilde{V}[k = \Omega\Delta T/2\pi]|^2 d\Omega \qquad \text{(B.345)} \end{aligned}$$

To simplify the notation in the actively modelocked laser noise theory section, we used

$$\tilde{V}(\Omega) \equiv \tilde{V}[k = \Omega\Delta T/2\pi]\Delta T. \tag{B.346}$$

This is strictly not correct, since if we take the magnitude-squared value, we do not obtain the correct expression given by equation (B.343). Nor is $\tilde{V}(\Omega)$ the aperiodic

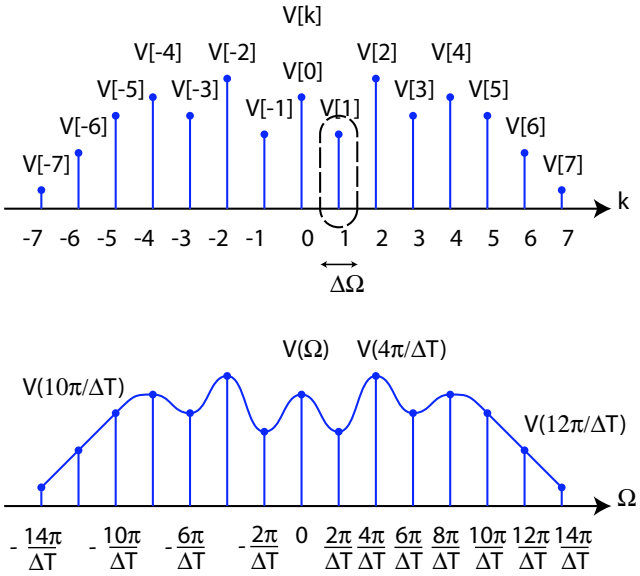

Figure B-16: Diagram showing conversion from discrete to continuous time.

Fourier transform. The only purpose of converting from a discrete frequency domain to a continuous frequency domain is to allow analytical evaluation of the rms value through integration.

For a non-stationary process such as a process where the variance increases with time, it is often useful to define a new quantity

$$Y(t;T) \equiv \Delta w(T+t) - \Delta w(t). \tag{B.347}$$

The Fourier transform of this equation, $t \Leftrightarrow k$, yields the relation

$$\tilde{Y}[k] = \Delta\tilde{w}[k]\left(e^{jk\Omega_1 T} - 1\right) \tag{B.348}$$

and the power spectral densities are related by

$$G_{YY}[k] = |\tilde{Y}[k]|^2 = 2|\Delta\tilde{w}[k]|^2\left(1 - \cos(k\Omega_1 T)\right). \tag{B.349}$$

The pulse-to-pulse amplitude mean square fluctuations are given by

$$\langle |Y(t;T)|^2 \rangle = \langle |\Delta w(T+t) - \Delta w(t)|^2 \rangle. \tag{B.350}$$

The pulse-to-pulse amplitude mean square fluctuation can be obtained by integrating the power spectral density of the amplitude noise

$$\begin{aligned}
\sigma_{pp}^2 &= \langle |\Delta w(T+t) - \Delta w(t)|^2 \rangle \\
&= R_{YY}(0) \\
&= \sum_{k=-\infty}^{\infty} G_{YY}[k] \\
&= \sum_{k=-\infty}^{\infty} |\tilde{Y}[k]|^2 \\
&\approx \int_{-\infty}^{\infty} \left(|\tilde{Y}[k = \Omega \Delta T/2\pi]|^2 \Delta T \right) \frac{d\Omega}{2\pi} \\
&= \int_{-\infty}^{\infty} \left(2|\Delta \tilde{w}[k = \Omega \Delta T/2\pi]|^2 \Delta T \right) [1 - \cos(\Omega T)] \frac{d\Omega}{2\pi}.
\end{aligned} \tag{B.351}$$

This equation was used to evaluate the pulse-to-pulse mean square fluctuations of the timing, phase, amplitude, and frequency of pulses from a modelocked laser. Note that the pulse-to-clock variance is a factor of two less than the pulse-to-pulse variance. The pulse-to-clock variance is found by taking $T \to \infty$ (this makes the cosine term drop out) and dividing by 2,

$$\sigma_{pc}^2 = \int_{-\infty}^{\infty} \underbrace{\left(\frac{\Delta T}{2\pi} |\Delta \tilde{w}[k = \Omega \Delta T/2\pi]|^2 \right)}_{\langle |\Delta \tilde{w}(\Omega)|^2 \rangle} d\Omega. \tag{B.352}$$

The underbrace shows how the continuous time domain relates to the discrete time domain.

B.6 Useful Mathematical Relations for Soliton Perturbation Theory

Hyperbolic function relations:

$$\text{sech}^2 x + \tanh^2 x = 1 \tag{B.353}$$

$$\frac{d}{dx}\text{sech}x = -\text{sech}x\tanh x \tag{B.354}$$

$$\frac{d^2}{dx^2}\text{sech}x = \text{sech}x - 2\text{sech}^3 x \tag{B.355}$$

$$\frac{d}{dx}\tanh x = -\text{sech}^2 x \tag{B.356}$$

$$\frac{d^2}{dx^2}\tanh x = -2\text{sech}^2 x\tanh x \tag{B.357}$$

Integration of orthogonal adjoint functions

$$\int_{-\infty}^{\infty} \underline{f}_p^*(-j\underline{f}_t)dt = -\frac{2}{w_0} \tag{B.358}$$

$$\int_{-\infty}^{\infty} \underline{f}_t^2 dt = -\frac{\pi^2\tau^2}{3w_0} \tag{B.359}$$

$$\int_{-\infty}^{\infty} \underline{f}_p^2 dt = -\frac{4}{3w_0\tau^2} \tag{B.360}$$

$$\int_{-\infty}^{\infty} f_t t^2 \underline{f}_t dt = \frac{\pi^2\tau^2}{4} \tag{B.361}$$

$$\int_{-\infty}^{\infty} f_p t^2 \underline{f}_p dt = -\frac{\pi^2\tau^2}{4} \tag{B.362}$$

$$\int_{-\infty}^{\infty} \underline{f}_p t^2 f_t dt = j\frac{12+\pi^2}{18} \tag{B.363}$$

$$\int_{-\infty}^{\infty} f_t A_0 \text{sech}(t/\tau)\underline{f}_t dt = \frac{A_0^2}{3} \tag{B.364}$$

B.7 Glossary of Variables and Units

Variable	Units
g, l, Δg, N, N_p, ΔN, ΔN_p	1
$a(T)$, $\Delta a(T)$	$\sqrt{\text{Power}}$
A_0, $\Delta\tilde{w}(\Omega)$, $\Delta w(T)$, $\Delta A_m(T)$	$\sqrt{\text{Energy}}$
ψ_m	$1/\sqrt{\text{Time}}$
$S(T)$, $S_L(t,T)$	$\sqrt{\text{Power}}/\text{Time}$
$\tilde{S}_0^{\Re}(\Omega)$, $S_n(T)$, $S_{t,L}(T)$	$\sqrt{\text{Power}/\text{Time}}$
P_{ASE}	Power
$\langle S(t,T)S^*(t',T')\rangle$	$\text{Power}/\text{Time}^2$
$G_{S_0S_0}[k] = \langle\lvert\tilde{S}_0^{\Re}(\Omega)\rvert^2\rangle$, $R_{S_nS_n}(T,T') = \langle S_n(T)S_n^*(T')\rangle$	Power/Time
σ, $\Delta p(T)$, $\Delta\tilde{p}(\Omega)$, A_{ww}, γ_0, $\gamma_0^{\Re}$, $\gamma_0^{\Im}$, $\Omega = 2\pi k/\Delta T$	1/Time
g	$\text{Power}^{1/4} \times \text{Time}^{-5/4}$
w_0, $\lvert St, L(\Omega)\rvert^2$	Energy
$\Delta\tilde{\phi}(\Omega)$, $\Delta\phi(T)$	Energy
t, T, τ	Time
$S_L(\Omega)$	Length $\times$ Time
$S_L[k]$	Length
$\underline{f}_w$	$\sqrt{\text{Power}}$
$\underline{f}_t$	$1/\sqrt{\text{Power}}$
$\underline{f}_\phi$	$1/(\sqrt{\text{Power}}\ \text{Time})$
$\underline{f}_p$	$1/(\sqrt{\text{Power}}\ \text{Time}^2)$
$S_t(T)$	1
$S_p(T)$	$1/\text{Time}^2$
$S_\phi(T)$	1/Time
$S_w(T)$	Power
$\mathcal{A}_0$	$\sqrt{\text{Power}}$

Appendix C

Pulse Characterization

Full pulse characterization of the phase and amplitude is necessary for the reconstruction of the timing jitter probability density function using optical cross-correlation techniques.

There are numerous schemes to characterize a pulse since there is currently no optimal technique that can satisfy all of the following requirements:

1. Yields amplitude and phase
2. Single-shot
3. Easy to implement
4. Real-time monitoring
5. Sensitive to low energy pulses
6. Applicable to a wide range of pulse widths (5 fs to 100 ps)
7. Need for trigger signal or external pulse source

Table C.1 shows the currently used methods for full-pulse characterization for different ranges of pulse widths. Notice that there is a lack of triggerless techniques for pulse widths from 1 to 30 ps. Ideally, the measurement system bandwidth should be three to five times the bit rate. At 40 Gb/s, this would imply a measurement bandwidth of

Technique	Pulse Width	Amplitude and Phase	Trig-gerless	Note
FDPM (frequency-domain phase measurement) [95, 96]	5 fs to 1 ps	✓	✓	
FROG[97]	5 fs to 1 ps	✓	✓	
TROG [98, 99]	50 fs to 30 ps	✓	✓	Difficult to use multiple fiber segments
SPIDER [100]	5 fs to 1 ps	✓	✓	
SOA [101] (section C.4)	> 1 ps	✓		Need synchronized MLL source
Amplitude Modulator [102]	100 fs to 100 ps	✓		Repetition-rate must be > 10 GHz
Optical Sampling ([103] with PPLN, [104, 101] with SOA)	> 1 ps	✓		Need synchronized MLL source
Sampling scope + optical BPF	> 100 ps	✓		

Table C.1: Pulse characterization techniques.

at least 120 GHz. Commercial systems with this much bandwidth simply don't exist today, so designers have to get by with only 40- or 50-GHz bandwidth.

C.1 Full-Pulse Characterization Using Autocorrelations and Genetic Algorithm

The amplitude and chirp of a train of optical pulses can be determined by measuring the autocorrelation of the pulses through different lengths of fiber and using a genetic algorithm [52]. The genetic algorithm easily incorporates fiber nonlinearities and the computation time is greatly reduced by expanding the electric-field solutions as a Hermite-Gaussian expansion.

C.1.1 Introduction

The recovery of a pulse's amplitude and chirp from intensity autocorrelations after different spans of fiber is a well-known method [105, 98]. The advantage of autocorrelation measurements over FROG [97] or SPIDER [106] is its enhanced sensitivity which comes from (1) the fact that the entire spectrum of the second-harmonic generated light contributes to the detected signal. By avoiding a CCD array in FROG with 128 pixels, for example, we have a factor of 128 greater signal. (2) Lock-in detection is easily implementable, which allows a signal-to-noise improvement. (3) The gain (10^6) of a single-channel photomultiplier tube is the lowest noise amplifier one can use. Therefore, the sensitivity of an autocorrelation measurement can easily be 10^5 times more sensitive than a FROG measurement. With a little additional engineering

autocorrelation measurements through different spans of fiber can be done in parallel.

One can argue that by averaging longer, the sensitivity of FROG can be improved, but if our measurement takes 5 minutes, then a corresponding measurement with the same sensitivity using FROG would take 5×10^5 minutes, assuming that averaging improves the signal, which is not always true. More likely, too much averaging on a FROG trace will just reveal scattering in the crystal or drifting of the signal source which is probably not stable over that time span.

The characterization of weak picosecond pulses is a difficult problem due to the low pulse energy and an important problem since these pulses are common in telecommunication applications [14, 17]. At the end of a transmission link, the average powers can be as low as the receiver sensitivity. Typical receiver sensitivities are -35 to -20 dBm at 10 Gbit/s, which correspond to pulse energies of only $3 \times 10^{-}3$ to 1 fJ. Amplification of these pulses is necessary to obtain a good signal-to-noise ratio in the autocorrelation trace. Amplification should proceed the lossy fiber segments to obtain a higher ratio of signal to noise photons before the autocorrelator. The enhanced signal-to-noise ratio comes at a cost of additional complexity since the Kerr nonlinearity in the fiber may need to be included in the pulse retrieval algorithm. Since nonlinear propagation is rather complicated and the evolution of a pulse cannot simply be written as a function of the known values, genetic algorithms lend themselves well to pulse-recovery since they deal directly with the solution space, while conveniently ignoring the details of the problem (i.e. don't need information about derivatives, etc.). In addition, genetic algorithms readily take advantage of parallel-computing and have already shown that there can be improved performance in recovering pulses from spectrograms [107] over that of other deterministic optimization schemes [97].

The novelty of this section is threefold: (1) We increase the sensitivity of our measurement setup by placing the amplifier before the fiber segments, (2) we demonstrate the recovery of the amplitude and phase of the amplified pulse with a genetic algorithm, and (3) we filter the search space in our retrieval algorithm by orders of magnitude by expanding the electric-field amplitude as a Hermite-Gaussian expansion and expanding the electric-field phase as a polynomial expansion.

If the propagation through the fiber is linear and the pulse only experiences first order dispersion, the phase and amplitude can be recovered by the use of a phase-retrieval algorithm [98].

The parameter range for which this can be done is rather limited, since high powers are needed to obtain good nonlinear conversion in the autocorrelator but also result in unwanted self-phase modulation in the fiber. This can either be due to the use of short pulses with high peak powers, or amplified picosecond pulses (as in the case of communication systems). There is an inherent trade-off between the amount of second harmonic generation in the autocorrelator and nonlinear Kerr effect in the fiber. Since nonlinear propagation is rather complicated and the evolution of a pulse cannot simply be written as a function of the known values, genetic algorithms lend themselves well to pulse-recovery since they deal directly with the solution space, while conveniently ignoring the details of the problem (i.e. don't need information about derivatives, etc.). In addition, genetic algorithms readily take advantage of parallel-computing and have already shown that there can be improved performance in recovering pulses from spectrograms [107] over that of other deterministic optimization schemes [97].

Here, we demonstrate the use of a genetic algorithm to recover the amplitude and phase of pulses from experimental and numerical autocorrelation data. The distinct advantage of this technique over FROG is that it can handle lower pulse powers due to the fact that the entire SHG spectral energy contributes to each data point in the autocorrelation and that the use of photomultiplier tubes and lock-in techniques (typical in most autocorrelation setups) are often more sensitive than a CCD array.

The experimental setup used to measure the amplitude and phase (or chirp) of a pulse is shown in Fig. C-1. In our experiments, a 5 GHz actively mode-locked external cavity 1.5 μm laser diode was used as the source. The pulses had a full-width at half intensity maximum (FWHM) of approximately 3 ps and were amplified to 15 dBm with an erbium-doped fiber amplifier to obtain an autocorrelation trace with a good signal-to-noise ratio. These pulses were autocorrelated after 0, 10, 20, 50, 100, 200, 400, and 500 meters of Corning LEAF fiber which has a dispersion of 4 ps/nm/km at 1540 nm and an effective area of 72 μm^2. At first glance, it may seem that only two

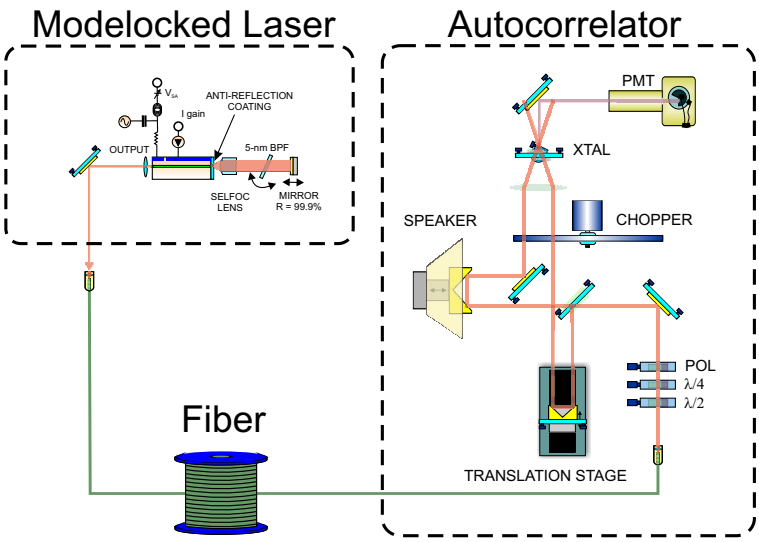

Figure C-1: The experimental setup showing a non-colinear intensity autocorrelator. The nonlinear crystal used was POM. The sum generation was detected on a photomultiplier tube (PMT). Chopping was done to increase the signal-to-noise ratio.

spans of fiber would be needed, but using more segments reduces the possibility of non-unique solutions. Assuming that the pulse is predominantly linearly chirped, we could probably get away with fewer fiber segments. For the experimental data, all eight autocorrelations corresponding to the aforementioned fiber delays were used in the fitness tests. The autocorrelation traces are shown in Fig. C-2 and wings can become apparent after 400 m of propagation due to the accumulated nonlinear phase shift due to the fiber Kerr nonlinearity. The gray lines correspond to the experimentally measured autocorrelations and the black lines correspond to the autocorrelations of the pulses recovered with the genetic algorithm. Incorporating nonlinear propagation in the pulse-recovery algorithm is important since the wings in the autocorrelation due to the Kerr nonlinearity in the fiber are incorrectly interpreted as an echo pulse when linear propagation is used. Indeed, when we run the genetic algorithm to recover the input pulse shape, an echo pulse appears, as can be seen in Fig. C-3. Using nonlinear propagation, which is easy to incorporate into the genetic algorithm code, we obtain a more accurate reconstruction of the input pulse amplitude and phase. Fig. C-4

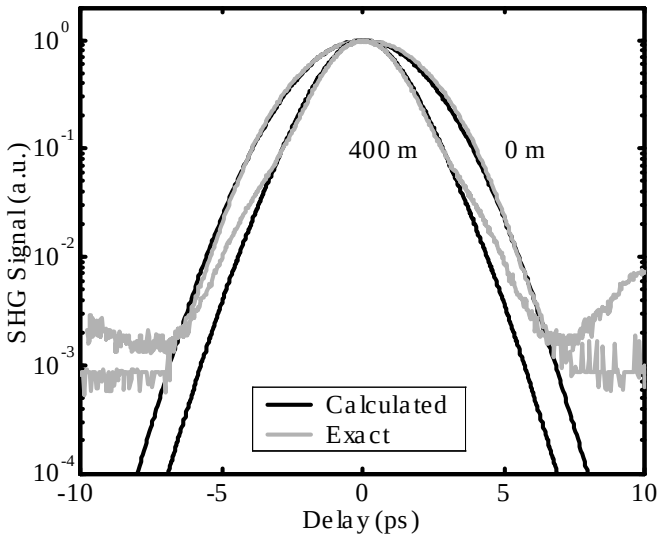

Figure C-2: Experimentally measured autocorrelation traces (exact) along with recovered autocorrelations (calculated) after propagation through 0 and 400 m of fiber. The recovered autocorrelation is the autocorrelation of the best guess for the input pulse after numerically propagating it through 0 or 400 m of fiber. The chirp of the launched signal is opposite the dispersion, which causes pulse compression after 400 m of propagation.

shows the reconstructed amplitude and phase of the input pulse using the same data, but here we also take into account the nonlinear effects of the fiber by including the Kerr nonlinearity in our pulse propagation code, and hence obtain a more accurate reconstruction of the input pulse.

Our algorithm is as follows (see Fig. C-5 for a schematic diagram of the algorithm): (1) initialize population of N_p chromosomes, (2) randomly choose pairs of chromosomes and cross their genes with probability p_c to produce $\bar{N}_p$ offspring, (3) mutate each gene of these offspring with probability p_m by adding a random value to the gene, (4) select the N_p fittest chromosomes (i.e. chromosomes that have autocorrelations with the lowest square difference from the autocorrelation data) from the N_p parents and $\bar{N}_p$ offspring and go back to step (2). Each step will be discussed in detail in the following paragraphs. There are many other ways to implement the genetic algorithm of which a few alternatives will be discussed. The main tradeoff is

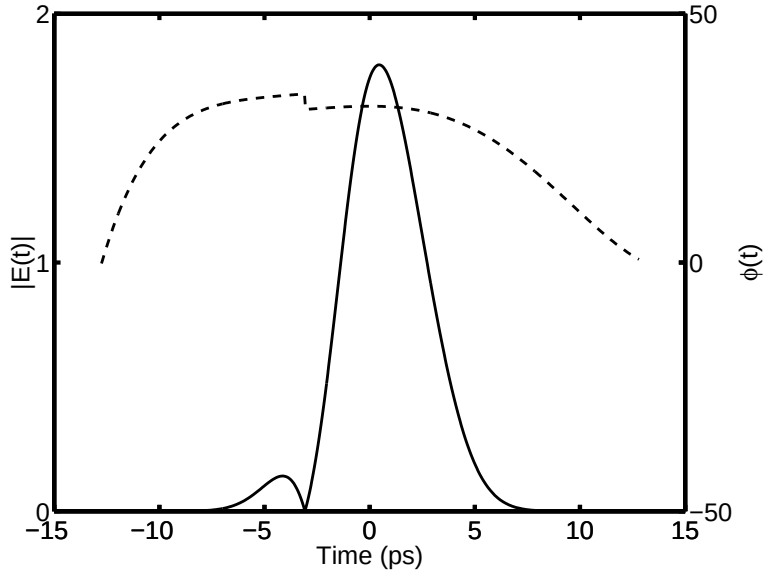

Figure C-3: Recovered electric-field of the input pulse assuming linear propagation in genetic algorithm. Solid line is the amplitude and the dotted line.

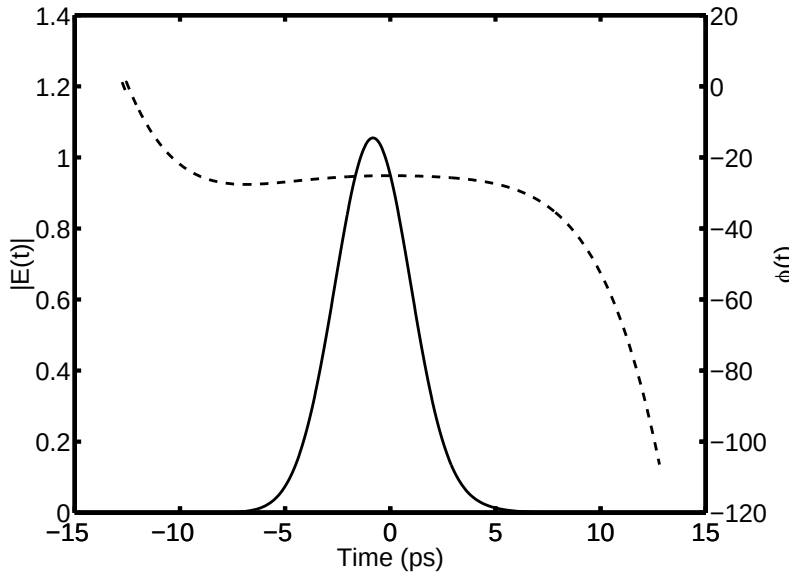

Figure C-4: Recovered electric-field of the input pulse taking into account nonlinear propagation in the genetic algorithm.

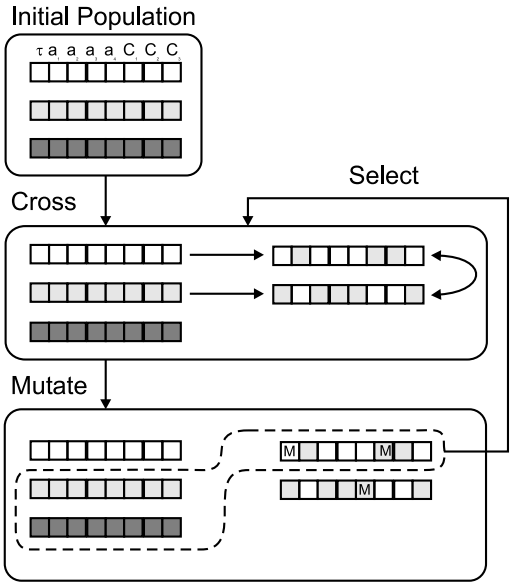

Figure C-5: Outline of genetic algorithm used in this paper. Here $N_p = 3$ and $\bar{N}_p = 2$. M denotes a mutation.

the speed of convergence due to selection pressure versus genetic diversity for a global search.

The method of encoding the electric-field into a chromosome is a key issue when using genetic algorithms. An encoding that does not suit a particular problem can greatly increase the computation time. Real-number encoding has been preferred over binary or Gray encoding since it generally performs better for function optimizations and constrained optimizations due to the existence of Hamming Cliffs, pairs of encodings have a large Hamming distance while belonging to points of minimal distance in phenotype space [108]. In our algorithm, we chose to represent the electric-field as a sum of Hermite-Gaussian functions

$$E(t) = \sqrt{P_{pk}} \exp[-i\phi(t/\tau)] \times \Sigma_{k=0}^{k=\infty} a_k H_k(t/\tau) \tag{C.1}$$

where $\phi(t) = C_1 t^2/2! + C_2 t^3/3! + C_3 t^4/4! + \ldots$ is the phase of the pulse, C_k are chirp coefficients, a_k are constants, tau is the width of the pulse, P_{pk} is the peak power, H_k

represents the kth order orthonormal Hermite-Gaussian equal to

$$H_k(t,\tau) = \frac{1}{\sqrt{\sqrt{\pi}2^k k!\tau}} P_k(t)\exp(-t^2/2) \tag{C.2}$$

where P_k is the kth order Hermite polynomial. Each chromosome is composed of the pulse width, Hermite-Gaussian coefficients, and chirp coefficients. We typically found that 13 to 20 genes were sufficient for representing the pulse shapes shown in this paper. The Hermite-Gaussian encoding obeys the following properties [108] (which are necessary for an effective genetic search): (1) nonredundancy (the mapping between encoding and solution is 1-to-1); (2) legality (any permutation of an encoding corresponds to a solution and hence guarantees that most genetic operators can easily be applied to the encoding); (3) completeness (any solution has a corresponding encoding, within the noise of the measurement); (4) Lamarckian property (one chromosome can pass its merits on to future populations through common genetic operations); and (5) strong causality (small variations on the genotype space due to mutation imply small variations in the phenotype space as to allow exploration of a neighborhood of solutions). If we had chosen to sample the real and imaginary part of the electric-field, let's say at 128 equally spaced time points, the solution space would have 256 dimensions (real and imaginary parts). This is much greater than than our Hermite-Gaussian search space of 13 to 20 dimensions. Hence, with this intelligent choice of genes, we have greatly reduced the computation time over real-number encoding of time-sampled electric-fields. For example, when we used the "sampled E-field" genes, we were not able to recover the input pulse after 100 generations since the fittest pulse looked like noise. On the other hand, when we used the Hermite-Gaussian genes, the input pulse converged to that shown in Fig. C-4 after only 20 generations.

In recovering the pulses from our experimental data, the pulse widths of the initial population were randomly chosen from 0 to 5 ps. If the initial population is chosen to have values very far away from the correct answer, and a Hermite-Gaussian expansion with many terms is chosen (hence leading to a large solution space), it is possible that the answer will converge to a local minimum rather than a global minimum. This

is the same problem as having too few sampling points in the solution space that are clustered in an unfavorable manner. The solution space can be further limited by searching values around the inverse Fourier transform of the square root of the optical spectrum, thereby alleviating this problem. To alleviate this problem further, an adaptive approach can be taken: First, the optimal chromosome with 2 genes (τ and a_0, for example) can be found. This solution can be a starting point for finding the optimal chromosome with 3 genes (τ, a_0, and a_1, for example), and this process can be continued until the fittest chromosome with n such genes is found. This is one way to narrow down the solution space in a systematic way, but does not necessarily guarantee that we reach the global optimum.

The crossover is performed by selecting two parents at random. For each gene, the child inherits the first parent's gene with probability p_c; otherwise, it receives the second parent's gene. One may also experiment with other types of crossovers, such as arithmetical, blend, boundary, and direction-based crossovers [108].

The mutation operation is performed by taking the offspring and adding a random number to randomly selected genes. With probability p_m, a random number with variance M is added to the gene. The strength of the mutation, M, is reduced for later generations to explore a smaller neighborhood around the solution at later generations. This is achieved in our case by dividing M by the generation number. There are also many other ways to implement mutation. For example, the mutation probability, p_m, can be varied either deterministically or adaptively according to a 1/5 success rule [108].

The amount of selection is an important consideration. If there is too much selection pressure, a genetic search will terminate before finding the global minimum. If there is too little selection pressure, the evolutionary progress will be slower than necessary. Many selection methods of different selection pressures have been proposed. Among them are[108]: (1) roulette wheel selection, (2) $(\mu + \lambda)$-selection, (3) tournament selection, (4) steady-state reproduction, (5) ranking and scaling, and (6) sharing. In our simulations, we tried (1), (2), and (5). We found that method (5) had a very weak selection pressure, and actually diverged for a certain set of param-

eters. Selection method (1) also had a weak selection pressure and took a long time to converge. Therefore, for the parameters that we tried, we found that method (2) allowed fast convergence due to its strong selection pressure. This method calls for taking the N_p best chromosomes from the parents and offspring ($N_p + \bar{N}_p$).

To test the algorithm, the troublesome cases of chirped double pulses with and without noise were tried numerically. The autocorrelations of the pulses after propagation through 0, 10, 20, 50, 100, 400, and 500 m of LEAF fiber were simulated. Using these autocorrelations for the fitness test, we were able to accurately reconstruct our original input pulses using our genetic algorithm. The double pulse was a sum of two hyperbolic secant pulses each with a FWHM of 1 ps and separated by 2.5 ps. The chirp was given by $C_1 = -0.5$, $C_2 = 0.1$ and $C_3 = 0.05$. It was found that the chromosomes converged to the correct answer for many different mutation strengths, crossover probabilities, and selection types. Fig. C-6 shows the recovered pulses for an initial population of 100 chromosomes after 100 generations. Each chromosome had 20 genes, $[\tau, a_0, \ldots, a_{15}, C_1, C_2, C_3]$ and was initialized to within 30% of the exact answer. The amplitude and phase matches well over the region which the pulse has significant energy. Fig. C-7 shows the fitness plotted as a function of generation, and it can be seen that the fitness of the chromosomes improves with each generation. Fig. C-8 shows that the optical spectrum of the recovered pulse matches well with the exact optical spectrum. The spectra match especially well on the blue side of the spectrum down to -50 dB. Fig. C-9 shows that the calculated and exact autocorrelations match well, even on a log scale. To test the robustness of the algorithm, Gaussian distributed noise with variance equal to 10% of the mean was added to the autocorrelation traces (see Fig. C-10). Starting with an initial population size of 10, initialized to within 100% of the exact answer, the recovered double pulse is shown in Fig. C-11. The recovered pulse is still fairly close to the original pulse shape indicating that noisy data will not necessarily prevent convergence to the correct answer.

In summary, a genetic algorithm can be used to recover the amplitude and chirp from a series of autocorrelation measurements after propagation through different spans of fiber. The strength of the genetic algorithm is the ease in which it deals with

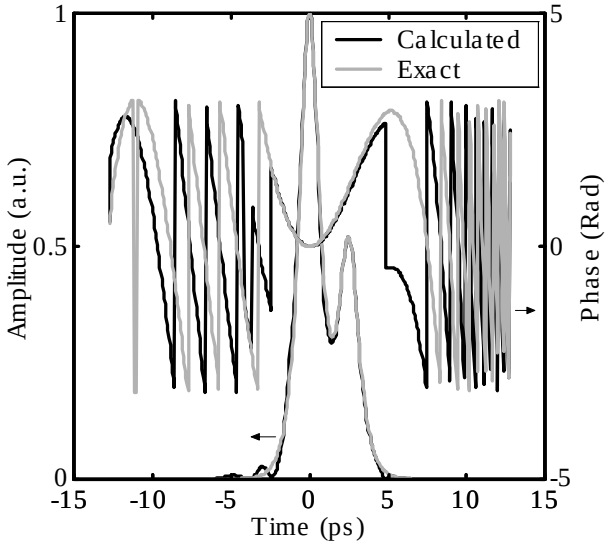

Figure C-6: Recovered electric-field of chirped double pulse. Slight ringing artifact on the leading edge of amplitude is mainly due to the finite expansion of 16 Hermite-Gaussian functions. Using more terms would reconstruct that part better.

nonlinearities in the fiber. This method is capable of recovering complicated pulse shapes, such as a chirped double pulse with noisy autocorrelations. In addition, the computation speed of the genetic algorithm was greatly enhanced by using Hermite-Gaussian coefficients and chirp coefficients for the genes, which effectively filtered the search space and reduced its dimensionality.

C.2 Frequency resolved optical gating pulse retrieval using using genetic algorithm with Hermite-Gaussian expansion

In this section, we show that second harmonic generation frequency resolved optical gating (SHG FROG) spectrograms can efficiently be inverted with a genetic algorithm. Constructing trial solutions out of a sum of Hermite-Gaussian functions allows one to represent an electric field with only a few coefficients, thereby reducing the

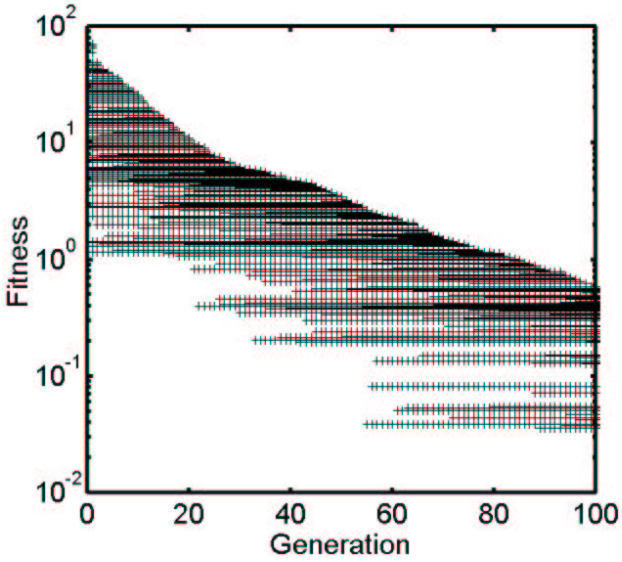

Figure C-7: Fitness plotted as a function of generation for the chirped double pulse example.

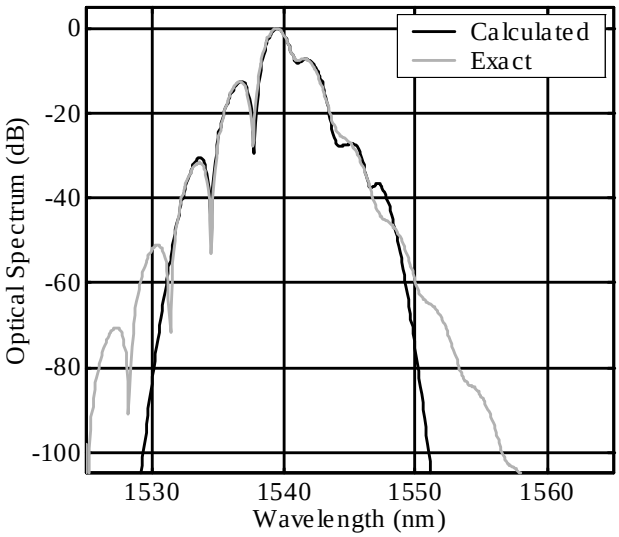

Figure C-8: A comparison of the optical spectra of the recovered pulse and the original pulse.

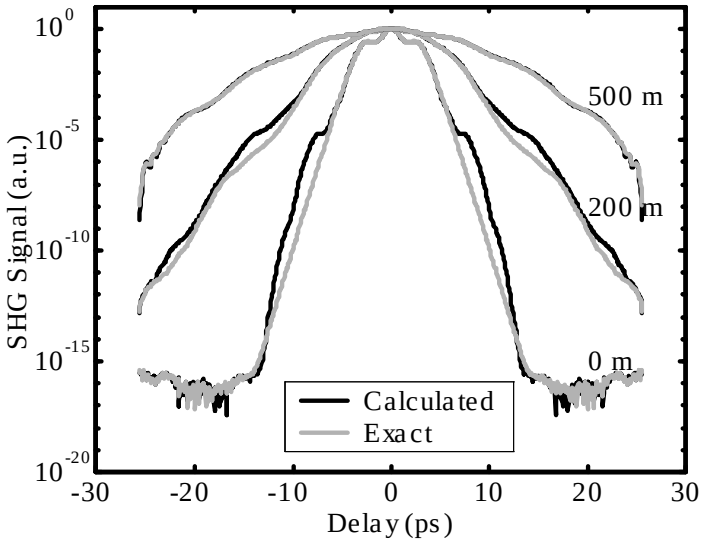

Figure C-9: The autocorrelation traces of the double pulse.

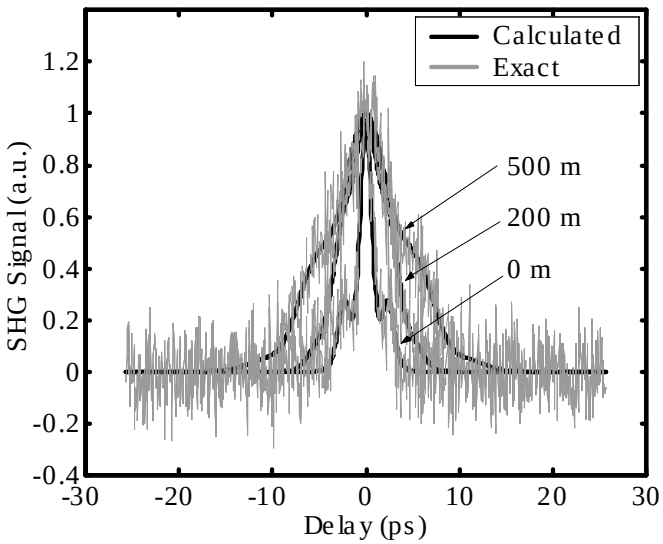

Figure C-10: Autocorrelation traces of the chirped double pulse with 10% additive noise. The autocorrelations of the recovered pulse are drawn with heavy black lines.

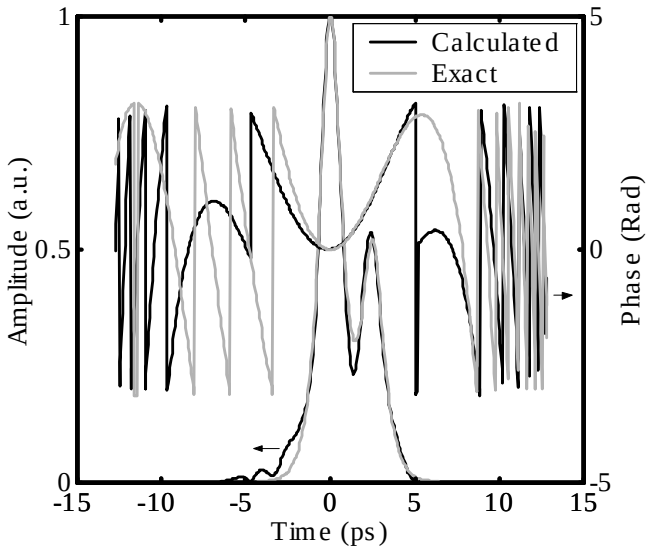

Figure C-11: Recovered electric-field of chirped double pulse with noise.

dimensionality of the solution space and leading to a significant speed-improvement for a large class of pulses.

C.2.1 Introduction

Frequency resolved optical gating (FROG) has been a popular technique for finding the amplitude and phase of optical pulses [97]. A FROG trace, or spectrogram, is obtained by measuring the spectrum of a gated signal as a function of signal-gate delay. The gate is formed by employing some sort of nonlinearity such as second harmonic generation. Much effort has focused on non-stochastic algorithms to extract the amplitude and phase of a pulse from its measured spectrogram since since phase retrieval computation can be slow and hence limits real-time performance [109, 110, 111, 112]. The use of a genetic algorithm for phase retrieval has shown that it can yield even smaller errors than its non-stochastic counterparts and that by using a multigrid approach, convergence can be fairly rapid [107].

A large class of pulses can be represented by a truncated expansion of Hermite-Gaussian functions. Some examples include pulses created by active mode-locking

[73] and dispersion-managed solitons [113]. In addition, the chirp of the pulse can often be represented by only a few chirp coefficients. For this class of pulses, a natural choice for the genes is a combination of Hermite-Gaussian coefficients plus chirp coefficients. Therefore, a complete electric-field can be described with only a few real numbers (often less than 10). This significantly reduces the dimensionality of the search space as compared to genes which represent samples of the electric field (32 to 128 samples are commonly used). A smaller search space means that the pulse recovery algorithm can be fast. We have successfully employed the Hermite-Gaussian genetic algorithm (HGGA) in the problem of recovering a pulse's amplitude and chirp from measurements of the intensity autocorrelations after different spans of fiber [55]. A benefit of this technique is that smoothing of noisy data is inherently built into our gene choice; that is, the recovery scheme is insensitive to noise spikes in the spectrogram since only smooth curves can be constructed out of a truncated Hermite-Gaussian expansion.

A fast FROG pulse recovery algorithm is important if one wants to create a real-time femtosecond oscilloscope [112]. Genetic algorithms lend themselves well to such an application, since the genetic algorithm can incorporate the previous solution in the initial population, i.e. doesn't need to start the calculation from scratch for each new oscilloscope sweep, as with generalized projections or the basic FROG algorithm. Unlike deterministic algorithms, in which progress depends on past computations, genetic algorithms directly benefit from parallel computations which can be implemented efficiently in hardware, hence allowing further speed improvements.

In cases where complete pulse characterization is not needed, the HGGA also serves well. For the problem of computing the timing jitter of a mode-locked laser, often one is only interested in the first two coefficients of the Hermite-Gaussian expansion of the pulse [114].

C.2.2 Genetic Algorithm

Our genetic algorithm begins with an initial population of N_p random chromosomes. The genes of a chromosome are real value representations of their Hermite-Gaussian

Shape	N
Gaussian	1
Sech	5
Double Sech	15
Double Gaussian	12
Asymmetric	17
3rd Order Super-Gaussian	13
9th Order Super-Gaussian	49

Figure C-12: Some examples of pulse shapes and the minimum number of Hermite-Gaussian coefficients needed to represent those shapes so that the error is less than 10^{-4}. The error is defined as the square root of the sum of the square differences between the exact and truncated expansion curves normalized to the number of sample points. These values are for the case where $\beta = 1$, number of sample points = 1000, sampling interval = 0.05 ps. The asymmetric pulse is the sum of three Gaussians of different amplitudes and delays. The double sech and Gaussian cases each consisted of two pulses with amplitudes of 1 and 0.75 offset by 2.5 their pulse width.

expansion coefficients and chirp coefficients. The electric-field is reconstructed from the genes by

$$E(t) = \exp[-i\phi(t/\tau)] \times \Sigma_{k=0}^{k=\infty} a_k A_k H_k(t/\tau) \exp(-t^2/2\tau^2) \tag{C.3}$$

where $\phi(t) = C_1 t^2/2! + C_2 t^3/3! + C_3 t^4/4! + \ldots$ is the phase of the pulse, C_k are real chirp coefficients, a_k are constants, H_k represents the kth order Hermite polynomial with normalization constant $A_k = 1/\sqrt{\sqrt{\pi} 2^n n! \tau}$, and τ is the width of the pulse. Each chromosome is composed of the pulse width, Hermite-Gaussian coefficients, and chirp coefficients. Typically, fewer than 20 genes are sufficient. The table in Fig. C-12 shows that a Hermite-Gaussian expansion may not be appropriate for some pulse shapes since sharp features require many terms to be represented accurately such as in the case of the 9th order super-Gaussian. In addition, the Hermite-Gaussian expansion is not appropriate if one is interested in determining whether the wings of the pulse are sech- or Gaussian-like.

After the population is initialized, $\bar{N}_p$ offspring are created by randomly choosing pairs of chromosomes and crossing their genes with probability p_c. Next, the individ-

ual genes of the offspring mutate with probability p_m. If a gene is mutated, a normally distributed random value with variance M is added to it. The variance M is called the mutation strength. The fitness, G, of a chromosome is computed by taking the square difference of the corresponding spectrogram from the measured spectrogram normalized by the total number of points squared:

$$G = \sqrt{\frac{1}{N^2}\sum_{i=1}^{N}\sum_{j=1}^{N}(I^{FROG}_{measured}(\omega_i,\tau_j) - I^{FROG}_{approx}(\omega_i,\tau_j))^2} \tag{C.4}$$

where the electric-field is sampled at N evenly spaced points and

$$I^{FROG}(\omega,\tau) = \left|\int E(t)E(t-\tau)\exp[-j\omega t]dt\right|^2 \tag{C.5}$$

represents the SHG FROG spectrogram, in this case. Fitter chromosomes have smaller G's. In the final step of the HGGA, the N_p fittest chromosomes from the parents and offspring are selected to undergo another generation of crossing, mutation, and selection. When quoting errors, it is important to also quote N, the number of samples in the spectrogram. For the same Hermite-Gaussian expansion, as N increases, G will decrease. Intuitively this makes sense since the non-zero signal part of the spectrogram occupies a smaller area relative to the entire spectrogram as N increases.

C.2.3 Examples

The HGGA was tested with simulated FROG spectrograms for a chirped-Gaussian pulse, a double pulse, and a asymmetric pulse. The resulting recovered pulses are shown in Fig. C-13, C-14, and C-15, and in all three cases, the pulses were recovered with errors less than 7×10^{-4}. With only a few expansion coefficients (up to 12 genes in the case of the asymmetric pulse), accurate reconstructions of the pulses are possible.

Significant speed improvements are also evident. Using the sampled E-field GA (SEFGA) [107] [115], the double pulse was recovered to an error of 6×10^{-4} in 454 gen-

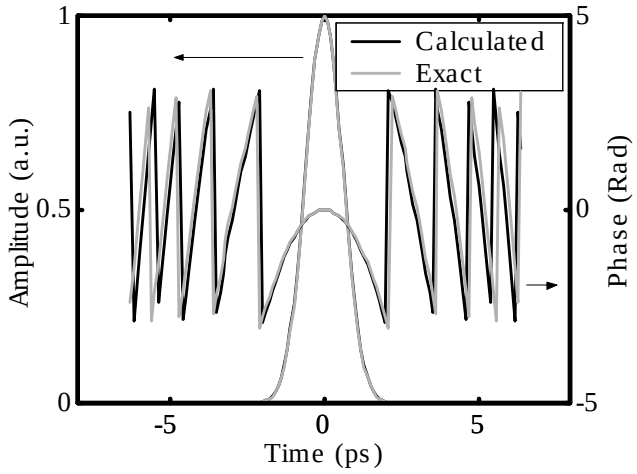

Figure C-13: Original (exact) and recovered (calculated) amplitude and phase profiles for the chirped Gaussian pulse with FWHM of 1 ps and chirp of $C_1 = 0.5$ where the electric-field is $\propto \exp(-iC_1(t/T_0)^2/2)$ where T_0 is the standard deviation of the amplitude. The simulation parameters were: $N_p = 10$, $\bar{N}_p = 4$, Generations= 50, $p_c = 0.5$, $p_m = 0.1$, $M = 0.01$, number of samples for spectrogram $N = 128$, time-interval of sampling $dt = 0.1$ ps, chromosome contained 2 genes = [width, C_1], and initial population randomized around the exact answer with standard deviation equal to 100% of the exact value. Computation time on PII-233 using non-compiled Matlab code was 32 seconds, the linear chirp of the displayed gene was $C_1 = 0.5336$, and the error was 0.00064428.

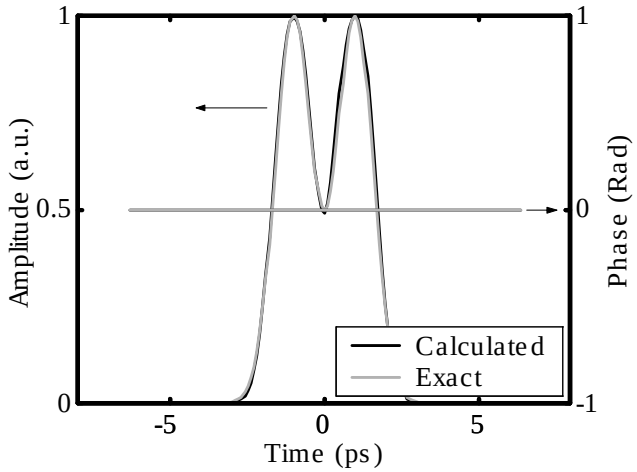

Figure C-14: Original (exact) and recovered (calculated) amplitude and phase profiles for the double pulse consisting of two Gaussians with FWHM of 1 ps and spaced apart by 2 ps. The simulation parameters are the same as for the chirped Gaussian pulse except that an expansion of 9 Hermite-Gaussian coefficients and no chirp coefficients was used. Computation time was 46 seconds and the error was 0.0006170289.

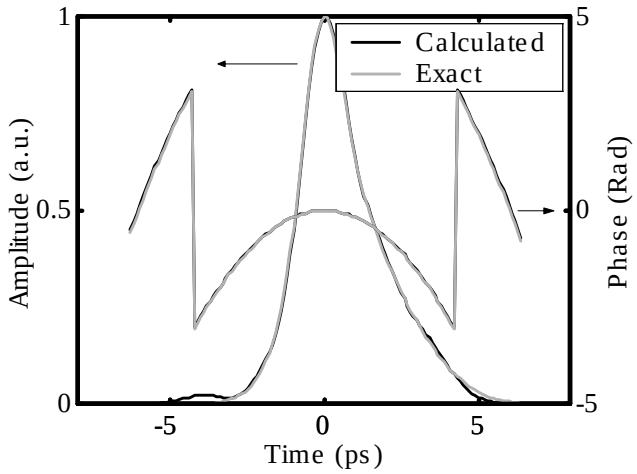

Figure C-15: Original (exact) and recovered (calculated) amplitude and phase profiles for the asymmetric pulse that was constructed by a sum of three Gaussian pulses: a 1 ps pulse plus a 2 ps pulse delayed by 0.3 ps plus a 2.5 ps pulse of half the amplitude delayed by 2.3 ps. Then a linear chirp with $C_1 = 0.5$ and FWHM of 2 ps was multiplied to the asymmetric pulse. The simulation parameters are the same as for the chirped Gaussian pulse except that an expansion of 10 Hermite-Gaussian coefficients was used, Generations=500, and $M = 0.05$. Computation time was 53 seconds and the error was 0.00041005.

erations (Simulation parameters: Population size=100, select size=10, crossover=0.5, mutation=0.5, mutation strength=0.05, iterations=20, pulse1 width=10, pulse2 width=10, pulse1 amplitude=1, pulse2 amplitude=1, pulse separation=2.5), as compared to only 50 generations using the HGGA. The SEFGA had problems recovering the chirped Gaussian pulse and achieved an error of 0.0874908 after 259 generations (Simulation parameters: Population size=100, select size=10, crossover=0.5, mutation=0.5, mutation strength=0.05, iterations=20, pulse width=10, amplitude=1, chirp=0.1). In comparison, the HGGA achieved an error of 6.4×10^{-4} after 50 generations. Nevertheless, it should be noted that it was not clear how the initial population of Nicholson's SEFGA [115] was selected and better performance might be expected if the initial population was selected closer to the desired solution.

The fitness of the chromosomes are plotted as a function of generation in Fig. C-16, C-17, and C-18 for the chirped gaussian pulse, double pulse, and asymmetric pulse, respectively. Since our algorithm uses lambda + mu selection (i.e. taking the N_p fittest chromosomes from the parents and offspring every generation)[108], after many generations, the population converges and further improvements are mainly due to mutations. This can best be seen in Fig. C-18 where the HGGA has been run for 500 generations. This implies that a combined algorithm using both random and local search components would be ideal. The random search explores the entire solution space and allows escaping from a local optimum while local searching allows for efficiently finding a local optimum. Therefore, combining the genetic algorithm with a gradient search method or other local search algorithm should lead to even better performance.

The spectra of the recovered pulses are shown in Fig. C-19, C-20, and C-21. The spectra agree down to 40 dB of the original spectrum.

C.2.4 Summary

The HGGA can further be improved by using a combined algorithm that uses a deterministic approach to more quickly converge to a local minimum. In addition, since the bulk of the computation time is spent on constructing spectrograms, incorporating a

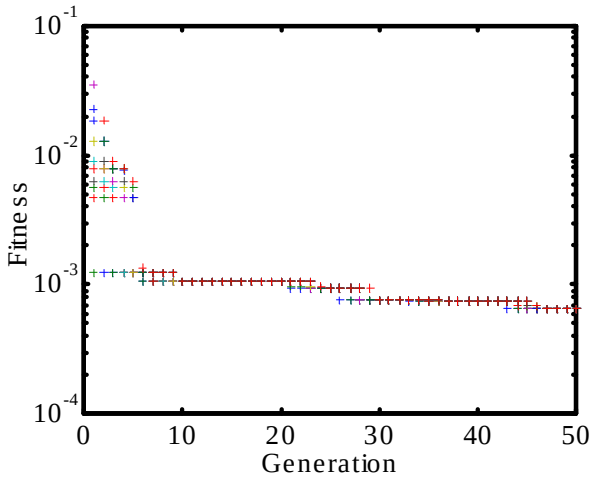

Figure C-16: Fitness versus generation for the chirped Gaussian pulse.

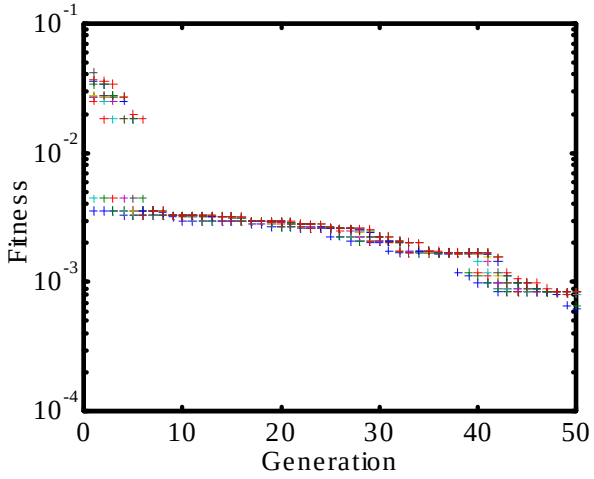

Figure C-17: Fitness versus generation for the double pulse.

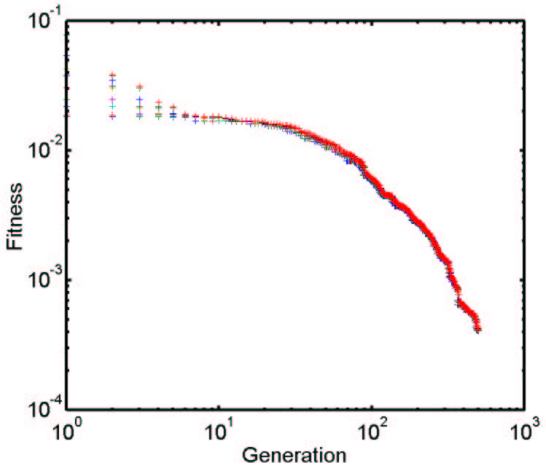

Figure C-18: Fitness versus generation for the asymmetric pulse.

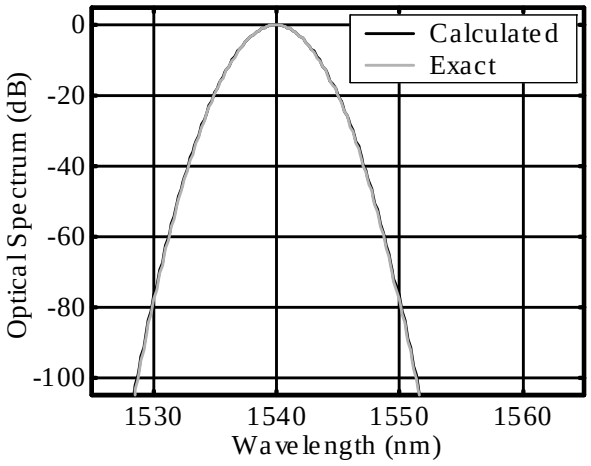

Figure C-19: Spectrum of the chirped Gaussian pulse.

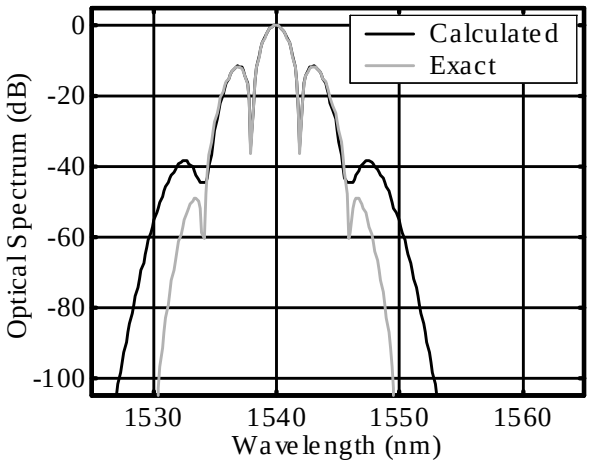

Figure C-20: Spectrum of the double pulse.

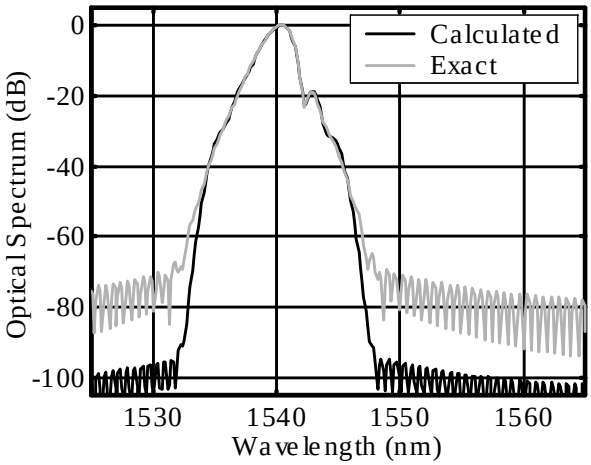

Figure C-21: Spectrum of the asymmetric pulse.s

multigrid approach in the HGGA would further reduce computation time.

We have demonstrated the use of a genetic algorithm using a Hermite-Gaussian and chirp coefficients to recover the amplitude and phase of the electric-field from a SHG FROG spectrogram. The advantages of the Hermite-Gaussian expansion is that it reduces the dimension of the search space over E-field sampling and also inherently incorporates smoothing of the measured spectrogram. The HGGA is most appropriate for pulses that can be represented with an expansion of a few Hermite Gaussian and chirp coefficients (less than about 20). Fortunately, this encompasses a broad class of pulses.

C.3 Expansion of frequency resolved optical gating spectrograms with Hermite-Gaussian functions

We show how to expand the frequency resolved optical gating spectrogram with a sum of Hermite-Gaussian functions. This provides a convenient way to filter the solution space, reduce the dimensionality of the problem, and allow an analytic error analysis.

C.3.1 Introduction

Frequency-resolved optical gating (FROG) is a popular method for completely characterizing the intensity and phase of a pulse [116]. Finding the electric-field that corresponds to the given spectrogram is a difficult problem since the solution space has $2N$ dimensions for an $N \times N$ spectrogram, where N is typically 32, 64, or 128. There are various algorithms that find an electric-field for a given spectrogram [117, 112, 107], but the solution is not guaranteed to be unique nor is it guaranteed that the solution will converge. Although there is some success in finding a close approximation to the true electric-field using these algorithms, one gains no additional insight into the errors associated with the solution (i.e. error bars on the electric-field), whether there are other solutions, the number of degenerate solutions, and what the degenerate so-

lutions are. These questions can be answered with an analytical theory relating the input and output parameters (i.e. the electric-field and spectrogram).

We show that the spectrogram can be decomposed into a set of orthogonal spectrograms, which we will call orthogonal spectrogram blocks. It is the magical properties of Hermite-Gaussian functions that allows us to expand the spectrogram in such a way. Hermite-Gaussian functions can be analytically integrated, convolved, Fourier transformed, and multiplied. The Hermite-Gaussian expansion leads to a better understanding of spectrograms, allows us to reduce the dimensionality of the problem by filtering the solution space in a reasonable manner, error bars on the electric-field can be established, and the minimum number of Hermite-Gaussian terms needed to represent an electric-field by decomposing the spectrogram can be determined.

A closed form solution for the SHG FROG spectrogram of an arbitrary order Hermite-Gaussian function is derived in section 2. Section 3 has three examples of how to find the truncated Hermite-Gaussian expansion approximation to the target electric-field using the analytic theory. Section 4 discusses how errors in the spectrogram show up in the electric-field.

C.3.2 Theory

An electric-field can be approximated with a M-th order Hermite-Gaussian expansion,

$$E(t) = \sum_{n=0}^{M-1} c_n G_n(t;\tau), \tag{C.6}$$

where $c_n = a_n + jb_n$ is a complex coefficient and the normalized Hermite-Gaussian function is given by

$$G_n(t;\tau) = A_n(\tau) H_n(t/\tau) \exp(-t^2/2\tau^2) \tag{C.7}$$

where τ is the $1/2e$ width of the pulse, H_n is the n-th order Hermite polynomial (in which the first few are tabulated in Tbl. C.2), and

$$A_n(\tau) = \frac{1}{\sqrt{\sqrt{\pi}2^n n!\tau}} \tag{C.8}$$

is the normalization constant so that

$$\int_{-\infty}^{\infty} G_m(t;\tau)G_n(t;\tau)dt = \delta(m-n). \tag{C.9}$$

n	$H_n(x)$
0	1
1	$2x$
2	$4x^2 - 2$
3	$8x^3 - 12x$
4	$16x^4 - 48x^2 + 12$
5	$32x^5 - 160x^3 + 120x$
6	$64x^6 - 480x^4 + 720x^2 - 120$
7	$128x^7 - 1344x^5 + 3360x^3 - 1680$

Table C.2: The first few Hermite polynomials.

The SHG FROG spectrogram relates to the electric-field as follows

$$I(\omega, T) = \left| \int_{-\infty}^{\infty} E(t)E(t-T)\exp(-j\omega t)dt \right|^2. \tag{C.10}$$

Using the following relations,

$$H_a(x)H_b(x) = \sum_{r=0}^{\min(a,b)} \frac{2^r a!b!}{r!(a-r)!(b-r)!} H_{a+b-2r}(x) \tag{C.11}$$

$$H_n(x)H_m(x-c) = \sum_{l=0}^{m} (-2c)^l \binom{m}{l} H_{m-l}(x)H_n(x) \tag{C.12}$$

$$\int_{-\infty}^{\infty} G_n(t;\tau)\exp(-j\omega t)dt = (-j)^n\sqrt{2\pi}G_n(\omega, 1/\tau) \tag{C.13}$$

$$\begin{aligned} B(a,b,T,\omega,\tau) &\equiv \int_{-\infty}^{\infty} G_a(t;\tau)G_b(t-T;\tau)\exp(-j\omega t)dt \\ &= A_a(\tau)A_b(\tau)\tau\exp\left[-\frac{T^2 + 2j\omega T\tau^2 + \omega^2\tau^4}{4\tau^2}\right] \end{aligned}$$

	$b=0$	$b=1$
$a=0$	1	$\frac{-T-j\tau^2\omega}{\sqrt{2}\tau}$
$a=1$	$\frac{T-j\tau^2\omega}{\sqrt{2}\tau}$	$\frac{-T^2+2\tau^2-\tau^4\omega^2}{2\tau^2}$
$a=2$	$\frac{(T-j\tau^2\omega)^2}{2\sqrt{2}\tau^2}$	$\frac{-T^3+jT^2\tau^2\omega+j\tau^4\omega(-4+\tau^2\omega^2)+T(4\tau^2-\tau^4\omega^2)}{4\tau^3}$
$a=3$	$\frac{(T-j\tau^2\omega)^3}{4\sqrt{3}\tau^3}$	$\frac{(jT+\tau^2\omega)^2(T^2-6\tau^2+\tau^4\omega^2)}{4\sqrt{6}\tau^4}$
$a=4$	$\frac{(T-j\tau^2\omega)^4}{8\sqrt{6}\tau^4}$	$-\frac{(jT+\tau^2\omega)^3(T^2-8\tau^2+\tau^4\omega^2)}{16\sqrt{3}\tau^5}$

Table C.3: Tabulation of the mini-block functions divided by a Gaussian, $B(a,b,T,\omega,\tau)\ /\exp\left[-\frac{T^2+2j\omega T\tau^2+\omega^2\tau^4}{4\tau^2}\right]$.

$$\times\sum_{l=0}^{b}\left[\left(-2\frac{T}{\tau}\right)^{l}\binom{b}{l}\right.$$
$$\left.\times\sum_{r=0}^{\min(a,b-l)}\left(\frac{2^r}{r!}\frac{a!}{(a-r)!}\frac{(b-l)!}{(b-l-r)!}\left(T/\tau-j\omega\tau\right)^{a+b-l-2r}\right)\right] \quad \text{(C.14)}$$

where B is called the mini-block function (tabulated in Table C.3), we find that the spectrogram can be written as a sum of mini-block functions

$$I(\omega,T)=\left(\sum_{m=0}^{M-1}\sum_{n=0}^{M-1}c_m c_n B(m,n,T,\omega,\tau)\right)\left(\sum_{p=0}^{M-1}\sum_{q=0}^{M-1}c_p c_q B(p,q,T,\omega,\tau)\right)^{*}. \quad \text{(C.15)}$$

The next step is to group the mini-block functions so that they are multiplied by a unique combination of the c coefficients, so that the spectrogram can be represented as a sum of spectrogram block functions according to

$$I(\omega,T)=\sum_{k=1}^{f_1(M)}\alpha_k v_k(\omega,T) \quad \text{(C.16)}$$

where v_k are the spectrogram block functions (not orthogonal yet), α_k is a coefficient that is a function of the c's,and $f_1(M)=1,6,18,\ldots$ for $M=1,2,3,\ldots$, respectively. The v_k for the specific cases of $M=1$, $M=2$, and $M=3$ are tabulated in Table C.4.

The spectrogram block functions can be orthogonalized. Each spectrogram block of size $N\times N$ can be thought of as a vector of length N^2 in which each element corresponds to one point in the spectrogram block. The orthogonal block functions

k	α_k	v_k
1	$\lvert c_0\rvert^4$	$\lvert B_{00}\rvert^2$
2	$\lvert c_1\rvert^4$	$\lvert B_{11}\rvert^2$
3	$\lvert c_0\rvert^2\lvert c_1\rvert^2$	$\lvert B_{01}\rvert^2 + \lvert B_{10}\rvert^2 + 2\Re\{B_{01}B_{10}^*\}$
4	$-2\lvert c_0\rvert^2\Im\{c_0c_1^*\}$	$\Im\{B_{00}[B_{01} + B_{10}]^*\}$
5	$2\lvert c_1\rvert^2\Im\{c_0c_1^*\}$	$\Im\{B_{11}[B_{01} + B_{10}]^*\}$
6	$2\Re\{c_0^2(c_1^*)^2\}$	$\Re\{B_{00}B_{11}^*\}$
7	$\lvert c_0\rvert^2\lvert c_2\rvert^2$	$\lvert B_{02}\rvert^2 + \lvert B_{20}\rvert^2 + 2\Re\{B_{02}B_{20}^*\}$
8	$\lvert c_2\rvert^4$	$\lvert B_{22}\rvert^2$
9	$\lvert c_1\rvert^2\lvert c_2\rvert^2$	$\lvert B_{12}\rvert^2 + \lvert B_{21}\rvert^2 + 2\Re\{B_{12}B_{21}^*\}$
10	$2\lvert c_2\rvert^2\Re\{c_0c_2^*\}$	$\Re\{B_{22}[B_{02} + B_{20}]^*\}$
11	$-2\Im\{c_0^2c_1^*c_2^*\}$	$\Im\{B_{00}[B_{12} + B_{21}]^*\}$
12	$2\lvert c_1\rvert^2\Im\{c_1^2c_2^*\}$	$\Im\{B_{11}[B_{12} + B_{21}]^*\}$
13	$2\lvert c_2\rvert^2\Im\{c_1^2c_2^*\}$	$\Im\{B_{22}[B_{12} + B_{21}]^*\}$
14	$2\Re\{c_0^2(c_2^*)^2\}$	$\Re\{B_{00}B_{22}^*\}$
15	$2\Re\{c_1^2(c_2^*)^2\}$	$\Re\{B_{11}B_{22}^*\}$
16	$-2\lvert c_0\rvert^2\Im\{c_1c_2^*\}$	$\Im\{[B_{01} + B_{10}][B_{02} + B_{20}]^*\}$
17	$2\lvert c_1\rvert^2\Re\{c_0c_2^*\}$	$\Re\{[B_{01} + B_{10}][B_{12} + B_{21}]^*\}$
18	$-2\lvert c_2\rvert^2\Im\{c_0c_1^*\}$	$\Im\{[B_{02} + B_{20}][B_{12} + B_{21}]^*\}$

Table C.4: The first 18 spectrogram block functions. The spectrogram block functions corresponding to $M = 1$, 2, and 3 are $k = 1$, $k = 1 \ldots 6$, and $k = 1 \ldots 18$, respectively.

can be found either through repeated application of the Gram-Schmidt projections or with singular value decomposition (SVD), which is found to have smaller numerical error [118, p.66]. The $M \times N^2$ matrix v, in which each row is a N^2 element vector representing v_k, can be factored into three matrices $v = u^\dagger w v^\perp$. The matrix $v^\perp$ has dimensions $S \times N^2$, where $S \leq M$. The columns of $v^\perp$ are orthogonal and denoted by $v_k^\perp$. The $S \times S$ matrix w is diagonal. The matrix $u^\dagger$ has dimensions $M \times S$. Using SVD, we can find $f_2(M) \leq f_1(M)$ orthogonal block functions denoted by

$$I(\omega, T) = \sum_{k=1}^{f_2(M)} \alpha_k^\perp v_k^\perp, \tag{C.17}$$

where the SVD will also yield information about how to construct $\alpha_k^\perp$ from a linear combination of α_k. For $M = 1, 2, 3$, $f_2(M) = 1, 6, 14$, respectively. Since the $v_k^\perp$ are orthogonal, we can find $\alpha_k^\perp$ by

$$\alpha_k^\perp = \sum_\omega \sum_T I(\omega, T) v_k^\perp(\omega, T). \tag{C.18}$$

Once the $\alpha_k^\perp$ are known, the α_k can be computed from

$$\alpha = (w^\dagger u)^{-1} \alpha^\perp. \tag{C.19}$$

The α_k are explicitly related to the c's according to Table C.4. Minimizing the square difference between the α_k and c's will yield the best guess for the pulse. Any minimization routine can be used for this lower dimensionality problem, such as the method of steepest descent. The summary of HGSHGFROG is shown in Fig. C-22.

The previous computation was carried out for SHG FROG, but could also be done for other gating functions such as PG FROG as well.

The mini-block functions obey certain properties which allow us to simplify the expression for the spectrogram block functions. We simplify the notation by defining

$$B_{mn} = B(m, n, T, \omega, \tau) \tag{C.20}$$

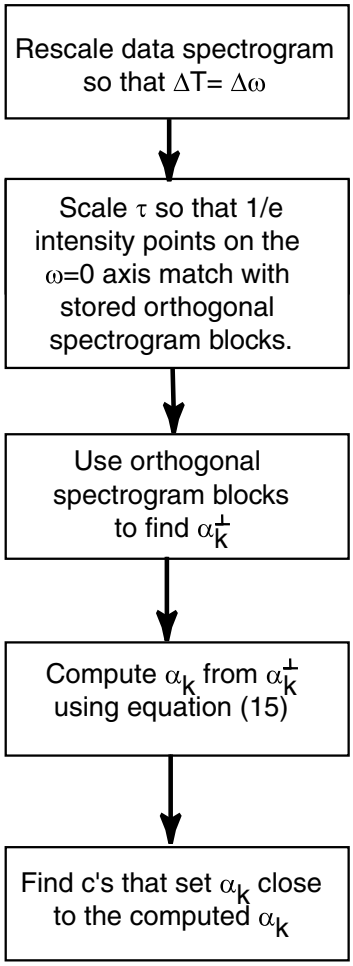

Figure C-22: Summary of operations for HGSHGFROG.

The properties of mini-block functions are:

$$\Im\{B_{mm}B_{nn}^*\} = 0 \tag{C.21}$$

for any m or n (they can be equal). A consequence of this statement is that the polynomial part of the on-diagonal mini-blocks is real. This can be seen when we set $nn = 00$. Furthermore,

$$B_{mn} = \begin{cases} -B_{nm}^* & : \quad n+m \text{ is odd} \\ B_{nm}^* & : \quad n+m \text{ is even} \end{cases}, \tag{C.22}$$

$$B_{mn} + B_{nm} = \begin{cases} 2j\Im\{B_{mn}\} & : \quad n+m \text{ is odd} \\ 2\Re\{B_{mn}\} & : \quad n+m \text{ is even} \end{cases}, \tag{C.23}$$

$$\Re\{B_{pp}(B_{mn} + B_{nm})^*\} = 0, n+m \text{ is odd} \tag{C.24}$$

$$\Im\{B_{pp}(B_{mn} + B_{nm})^*\} = 0, n+m \text{ is even}, \tag{C.25}$$

and

$$\Re\{(B_{pk} + B_{kp})(B_{mn} + B_{nm})^*\} = 0, p+k+n+m \text{ is odd} \tag{C.26}$$

$$\Im\{(B_{pk} + B_{kp})(B_{mn} + B_{nm})^*\} = 0, p+k+n+m \text{ is even}. \tag{C.27}$$

It is important to note that only one orthogonal spectrogram block for a single τ, say $\tau = 1$, needs to be computed. The $\tau = \tau_0$ orthogonal spectrogram blocks can be obtained from the $\tau = 1$ spectrogram blocks by scaling the T-axis by T/τ_0 and the ω by $\omega\tau_0$. For example, if $\tau_0 = 5$, the T-axis is stretched and the ω-axis is compressed by a factor of 5. The spectrograms in this paper have $\Delta t = \Delta\omega$ so that a transform-limited Gaussian has a circular spectrogram. For the discrete-time Fourier transform (DTFT), the frequency and time sampling intervals are related by $\Delta t \Delta\omega = 2\pi/N$, where N is the number of points in the E-field vector. If we set $\Delta t = \Delta\omega$, then $\Delta t = \Delta\omega = \sqrt{2\pi/N}$.

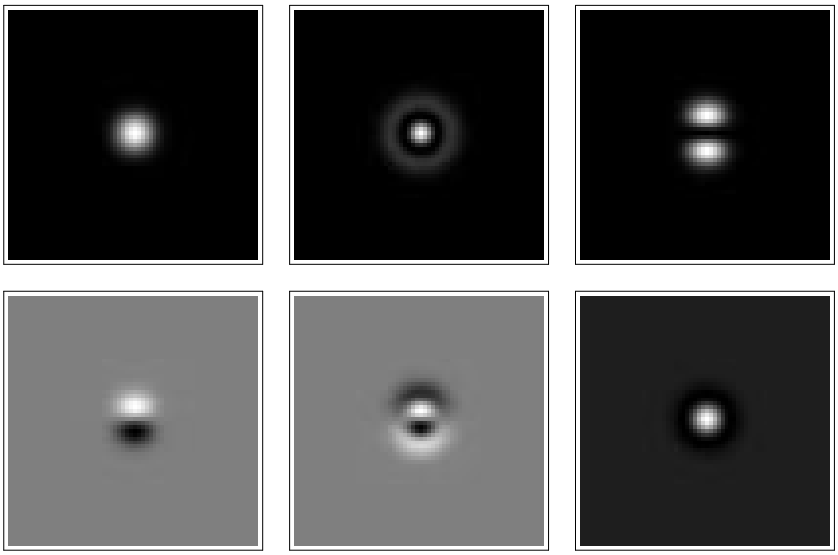

Figure C-23: Spectrogram blocks for $M = 2$ Hermite-Gaussian expansion.

C.3.3 Examples

In the following three examples, we consider recovering the electric-field from 64×64 SHG FROG spectrograms. The first example shows that when the target-electric field can be described well by a truncated Hermite-Gaussian expansion, that the recovered electric-field yields an excellent approximation. The second example shows what happens when not enough terms are considered in the Hermite-Gaussian expansion. The third example shows that rather complex pulses can be recovered with only a third-order expansion, $M = 3$.

Example 1: $M = 2$ **and** $E(t) = G(0, t, 1) + 3jG(1, t, 1)$

The original E-field is $E(t) = G(0, t, 1) + 3jG(1, t, 1)$, shown with a solid line in Fig. C-25, and its spectrogram is shown on the left-hand side of Fig. C-26. Using the procedure outlined in section 2, the target spectrogram can be projected into the orthogonal block spectrogram basis. In this case, for $M = 2$, the basis can completely characterize the target spectrogram. The sum of the scaled orthogonal block spectrograms is shown on the right hand side of Fig. C-26 and is nearly indistin-

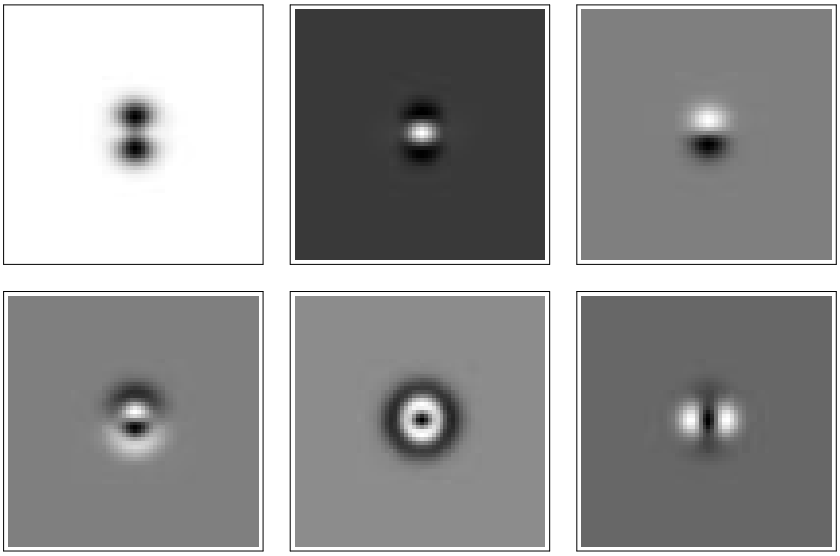

Figure C-24: Orthogonal spectrogram blocks for $M = 2$ Hermite-Gaussian expansion.

guishable from the original spectrogram on the left-hand side. Therefore, an $M = 2$ Hermite-Gaussian expansion is sufficient for describing the target spectrogram. There are errors due to numerical round-offs but these are less than 4×10^{-5}, as shown in Fig. C-27. The error is defined as the difference between the original and recovered spectrograms when the spectrograms have their peak value normalized to 1.

Recovering the the Hermite-Gaussian coefficients is the next step. The spectrogram block vector and orthogonal spectrogram block vector are related by $v = u^{\dagger} w v^{\perp}$.

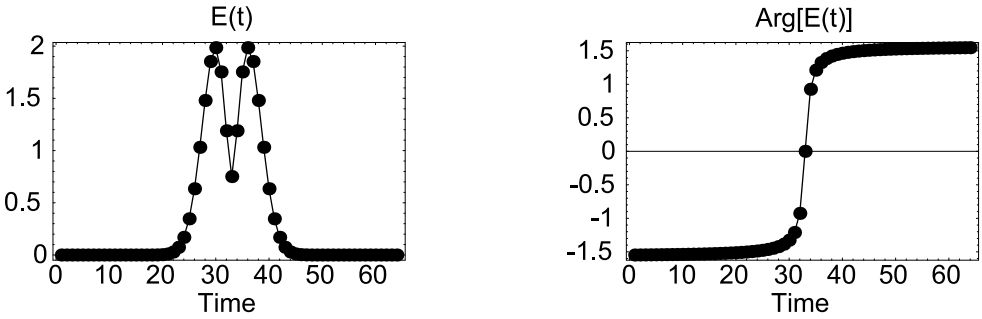

Figure C-25: Example 1: E-field $E(t) = G_0(t;1) + 3jG_1(t;1)$.

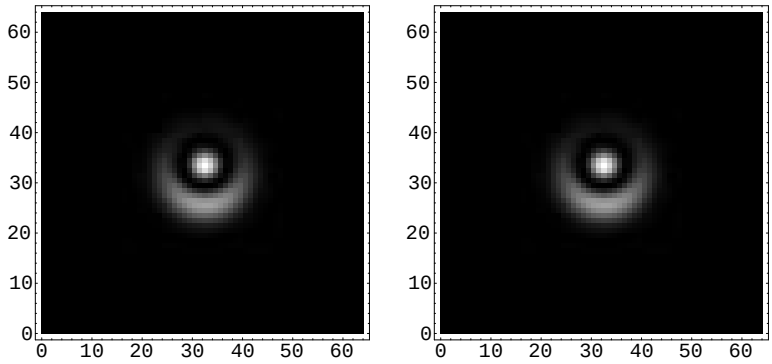

Figure C-26: Target and recovered spectrograms for example 1. Plots (a) and (b) correspond to the target spectrogram and plots (c) and (d) correspond to the recovered spectrograms.

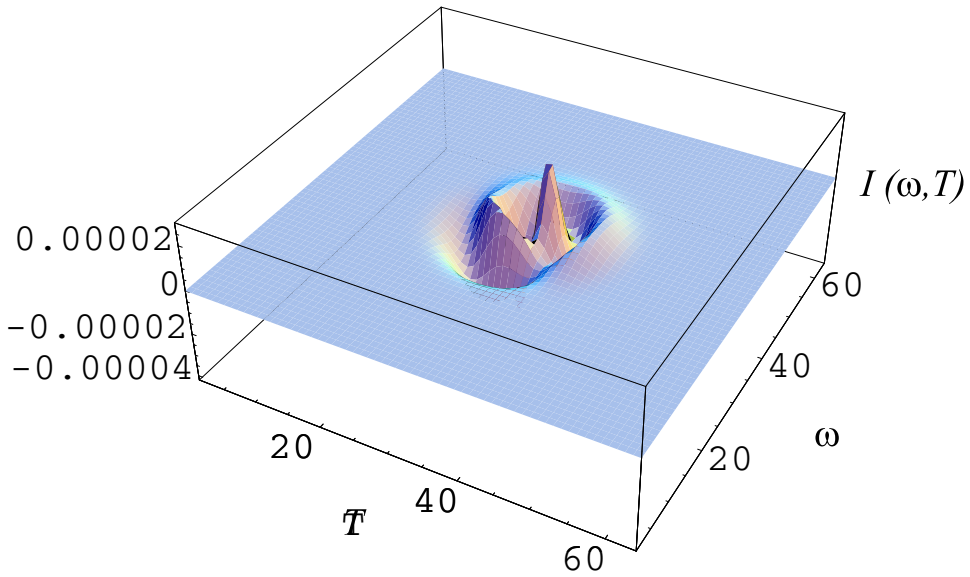

Figure C-27: Difference between target and recovered spectrograms for example 2.

The orthogonal spectrogram block coefficients, $\alpha_k^{\perp}$, are equal to the dot product of the kth row of $v^{\perp}$ and the measured spectrogram rearranged into a N^2-element vector.

The α coefficients can be found by the following relationship: $\alpha = (w^{\dagger}u)^{-1}\alpha^{\perp}$. Then we can use Table C.4 to find how $\alpha_1 \ldots \alpha_6$ relate to a_0, b_0, a_1, and b_1. By solving these equations, we find that the phase of c_0 is arbitrary, so we set $b_0 = 0$. When we do this, we find that there are two solutions which are time-reversed versions of each other. This agrees with the fact that there is an inherent time ambiguity in the SHG FROG measurement. One of the recovered solutions is shown with dots in Fig. C-25. The other recovered solution is just time reversed.

Example 2: $M = 2$ **and** $E(t) = G(0,t,1) + 0.5G(2,t,1)$

When the Hermite-Gaussian expansion has too few terms, the orthogonal block spectrograms are not able to reproduce the original spectrogram. Therefore, one can immediately determine the number of terms needed to accurately reproduce the original spectrogram. In this example, we show what happens when we try to use an $M = 2$ Hermite-Gaussian expansion to describe an electric-field that contains a higher order Hermite-Gaussian term.

In this case, the original E-field is $E(t) = G(0,t,1) + 0.5G(2,t,1)$ and is plotted with a solid line in Fig. C-30. Its spectrogram is shown on the left-hand side in Fig. C-31 and projecting this spectrogram onto the orthogonal spectrogram block basis yields plot on the right-hand side in Fig. C-31. At this point, one can easily see that a $M = 2$ expansion has no chance of accurately recovering the original electric-field since the two spectrograms can have errors as large as 0.1 for certain values of ω and T, see Fig. C-32. The correct next step is to project the original spectrogram onto $M = 3$ or higher order orthogonal spectrogram blocks. If one naively tries to recover the original electric-field anyway, the recovered pulse is shown with dots in Fig. C-31 and is seen to significantly deviate from the original pulse.

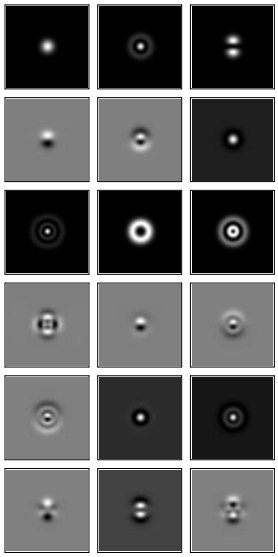

Figure C-28: Spectrogram blocks for $M = 3$ Hermite-Gaussian expansion.

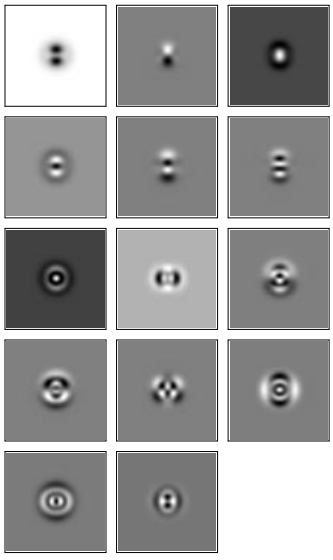

Figure C-29: Orthogonal spectrogram blocks for $M = 3$ Hermite-Gaussian expansion.

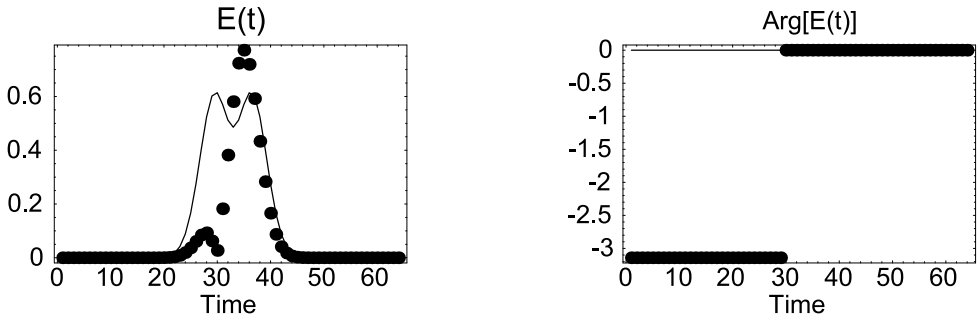

Figure C-30: Example 2: E-field $E(t) = 0.5jG_1(t;1) + G_2(t;1)$.

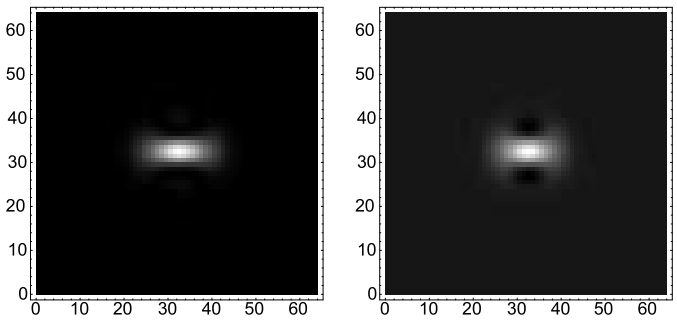

Figure C-31: Target and recovered spectrograms for example 2. Plots (a) and (b) correspond to the target spectrogram and plots (c) and (d) correspond to the recovered spectrograms.

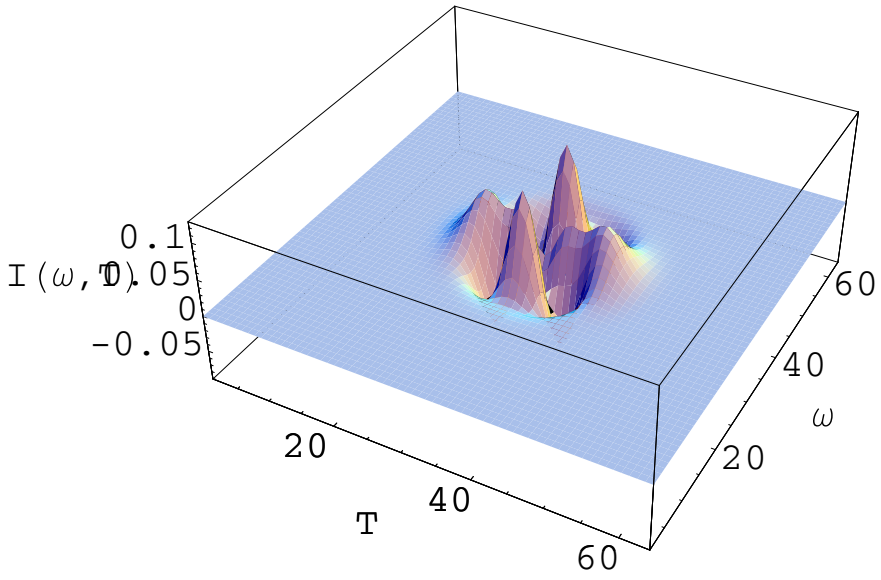

Figure C-32: Difference between target and recovered spectrograms for example 2.

Example 3: $M = 3$ **and** $E(t) = -0.1G(0,t,1) + 0.5jG(1,t,1) + G(2,t,1)$

A more complex electric-field is plotted with a solid line in Fig. C-33 and is described by $E(t) = -0.1G(0,t,1) + 0.5jG(1,t,1) + G(2,t,1)$. In this case, we consider an expansion of order $M = 3$ and we find that the recovered (dots) and original (solid line) E-field is shown in Fig. C-33 agree quite well. This is to be expected since the the original (left) and recovered (right) spectrograms in Fig. C-34 are almost the same with an error of less than 5×10^{-3}, as shown in Fig. C-35.

C.3.4 Error Bars

It is difficult to establish error bars in FROG since errors in the measured spectrogram do not have a simple relation to errors in the recovered electric-field. Several brute force computations using supercomputers have been executed to understand errors in FROG spectrograms, but little insight is gained. Our analysis may provide some more insight into error bars.

The noise in the measured spectrogram can be projected into different spectrogram blocks. The Hermite-Gaussian coefficients vary by the amount of the overlap between

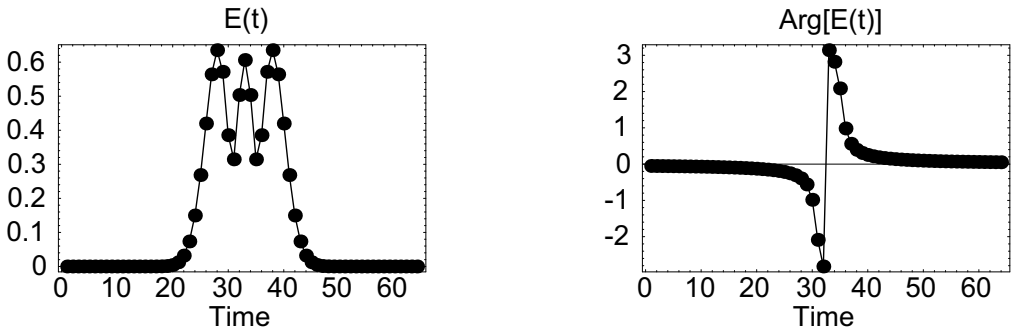

Figure C-33: Example 3: E-field $E(t) = G_0() + 0.5jG_1(t;1) + G_2(t;1)$.

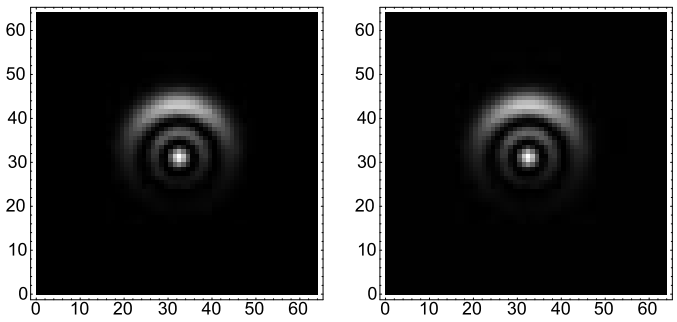

Figure C-34: Target and recovered spectrograms for example 3. Plots (a) and (b) correspond to the target spectrogram and plots (c) and (d) correspond to the recovered spectrograms.

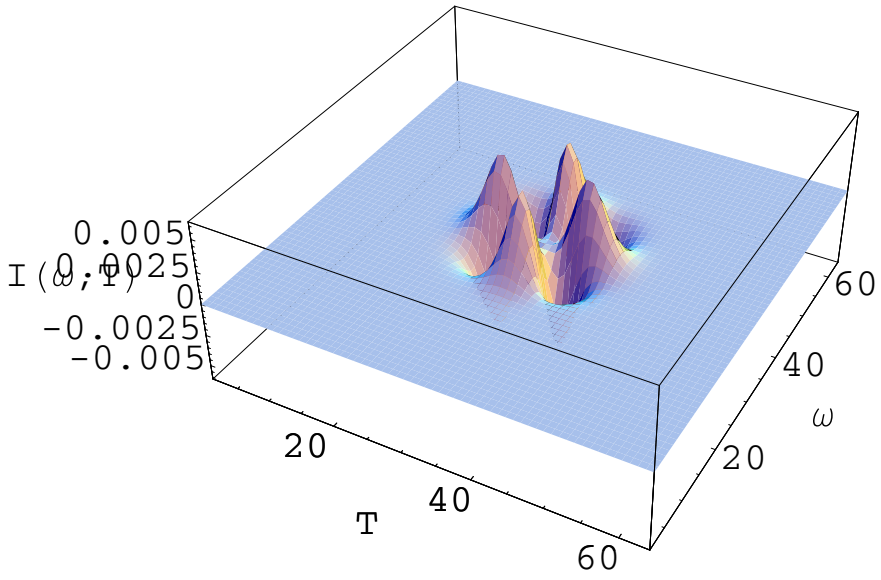

Figure C-35: Difference between target and recovered spectrograms for example 2.

the noise and the spectrogram blocks. As a first-order estimate on the Hermite-Gaussian coefficients, one can consider the overlap of $|B_{nn}|^2$ with the spectrogram noise to find the variance on $|c_n|^2$ for $n = 0, 1, 2, \ldots$.

Thermal noise in the spectrogram shows up as additive noise that is evenly weighted over the entire spectrogram. For thermal noise, all Hermite-Gaussian coefficients have the same variance since $\int_{-\infty}^{\infty}\int_{-\infty}^{\infty}|B_{nn}|^2 d\omega dT = 6.28319$ for all n.

Shot noise is a signal dependent noise source that is proportional to the signal intensity. Since the greatest values in the spectrogram generally appear in the center of the spectrogram, the variance is higher there. The variance of the Hermite-Gaussian coefficients are higher for small n since as n increases, the spectrogram block functions $|B_{nn}|^2$ spread out and overlap less with the center. Fig. C-36 shows the two spectrogram block functions, $|B_{0,0}|^2$ and $|B_{10,10}|^2$. On the other hand, although the variance increases for the lower order Hermite-Gaussian coefficients, their SNR $(\langle c\rangle^2/\sigma_c^2)$ increases since $\sigma_c^2 \propto \langle c\rangle$.

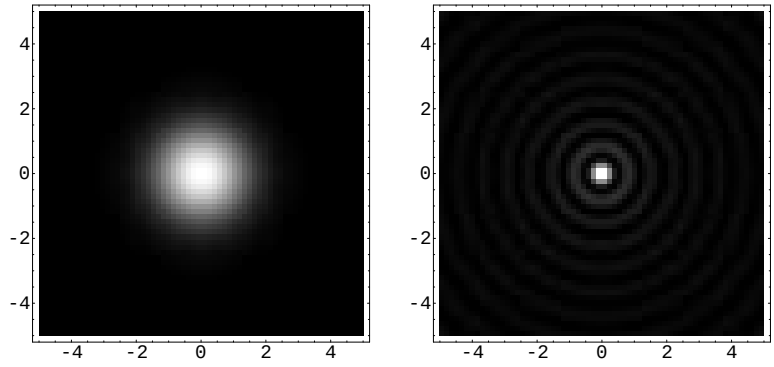

Figure C-36: The spectrogram block functions v_0 (left) and v_{10} (right). The spectrogram block function v_0 is more heavily concentrated in the center of the spectrogram than v_{10}.

C.3.5 Conclusions

We have shown how to understand FROG spectrograms in terms of an expansion of Hermite-Gaussian functions. Hermite-Gaussian functions allow us to analytically construct spectrogram block functions. Projecting the measured spectrogram into these spectrogram block functions yields a set of equations of lower dimensionality which can be minimized to yield a best fit for a given expansion number. In addition, further insight into the effects of measurement errors on the reconstructed electric-field was gained.

C.4 Sampling pulses with semiconductor optical amplifiers

This section outlines three techniques to measure the instantaneous frequency and intensity of optical pulses using semiconductor optical amplifiers (SOAs). Four-wave mixing, gain-saturation, and interferometric switching through a nonlinear optical loop mirror are three mechanisms by which sampling is done. We have experimentally measured the intensity and chirp profiles of pulses with energies as low as 10 fJ. Since the nonlinearity in the SOA is relatively slow, these measurement techniques are most

appropriate for picosecond pulses often found in telecommunication applications. The temporal resolution of these methods are limited by timing jitter, which was ≈ 0.5 ps for the mode-locked laser diodes we used in our experiments and by the width of the switching window.

C.4.1 Introduction

Pulses used in telecommunication systems typically have durations greater than half a picosecond and low power. The powers found in communication systems are dictated by the receiver sensitivity (the minimum power needed to obtain a 10^{-9} bit-error rate). Commercial high-speed Si-PIN receivers typically have sensitivities of -35 dBm at 1 Gb/s and -20 dBm at 10 Gb/s, which correspond to 0.32 fJ and 1 fJ per pulse. The most common instrument for measuring ultrashort pulses is the intensity autocorrelator, which uses a fast nonlinearity such as second harmonic generation. Unfortunately, materials with fast nonlinearities generally have low conversion efficiencies, and hence they are less useful for the direct measurement of low power pulses. In addition, an autocorrelation can only provide limited information about the chirp and intensity profile. Often, one must assume a pulse shape and fit it to the autocorrelation data. To obtain complete intensity and chirp information of a pulse, nonlinear spectrographic techniques such as frequency-resolved optical gating (FROG) can be used[97]. These methods also require relatively high powers [119].

One might consider interferometric techniques such as TADPOLE which can measure down to 42×10^{-21} J per pulse [120]. The difficulty with TADPOLE from a telecommunications point of view is that the reference pulse cannot be derived from the source and hence it is impossible to generate interference fringes. Therefore, if we want to use an interferometric technique, it must be self-referencing like SPIDER [100], but self-referencing spectral interferometry also depends on fast nonlinearities which means that high pulse powers are needed.

We refer to the three techniques we investigated as: the SLALOM (Semiconductor Laser Amplifier in a LOop Mirror) technique, the FWM technique, and the gain-saturation technique. The major advantage of these techniques is the ability to

measure very weak picosecond pulses. Experimentally, we have measured pulse energies as low as 10 fJ, but expect that the low-power limit to the SLALOM technique is closer to 0.2 fJ and even lower for the gain-saturation technique. Previously, SOAs have been used for intensity sampling [121] [103], but our techniques are different in that they also sample the instantaneous frequency, or chirp, of the pulse.

C.4.2 Description of the measurement techniques

All three measurement techniques are similar in that they all use a reference probe pulse generated by a separate laser to sample a broader signal pulse.

SLALOM Measurement Technique

A SLALOM (Semiconductor Laser Amplifier in a LOop Mirror) [122] is a nonlinear loop mirror which is imbalanced by an SOA placed asymmetrically within the loop. In Fig. C-37, a signal and probe pulse are shown to be incident to the two input ports of the SLALOM. The signal is split with a 50/50 coupler into two counter-propagating (cw and ccw) pulses which arrive at the SOA at different times. In the absence of a probe pulse and assuming that the signal pulse has low enough power so that it does not change the gain of the SOA, both cw and ccw signal pulses will see approximately the same gain, and hence phase-shift, after passage through the SOA. The cw and ccw pulses will then revisit the 50/50 coupler, but since both pulses have experienced the same round-trip phase shift, no power will be switched to the output. Now if we introduce a more powerful probe pulse and let it hit the SOA after the cw-signal pulse but before the ccw-signal pulse, then the probe pulse will saturate the SOA gain and the cw-signal pulse will experience a greater gain than the ccw-signal pulse. Therefore, there will be a phase shift between the two counter-propagating pulses and they can constructively interfere at the output port depending on several parameters (probe-signal delay and injection current, for example). Assuming a broad signal pulse (> 2 ps) and a short probe pulse (≈ 1 ps), depending on the relative signal-probe delay, part of the signal pulse will be switched to the output port of

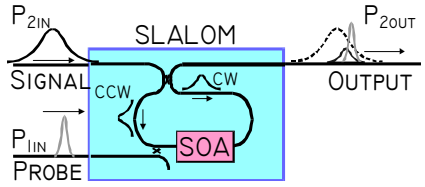

Figure C-37: Schematic of the SLALOM technique. The probe pulse opens up a switching window through which part of the signal is allowed to pass. The output is measured on the OSA and the spectrum is measured as a function of signal-probe delay, τ.

the SLALOM. The SLALOM essentially behaves as a temporal gate for the signal. The temporal location of the gate (or switching window) depends on the signal-probe delay. The shape of the switching window depends on several factors outlined in section C.4.2.

Dynamic Range Experimentally, we have used 1-ps pulses with powers of -10 to 6 dBm at 10 Gb/s (corresponding to 10 fJ to 0.4 pJ). Since the probe pulse must cause a large change in the gain of the SOA to achieve a good switching contrast (the power difference between the *on* and *off* state of the SLALOM), large probe powers are needed (typically about 10 dBm in our experiments). Fig. C-38 shows that larger switching contrast occur at high probe powers, and that we would want to use the largest possible probe power without damaging the SOA.

Fig. C-39 shows a plot illustrating switching window amplitude as a function of the input signal power. From this plot, we can determine the dynamic range of the signal powers. The largest dynamic range (the range of $P_{2\text{in}}$ values for which the switching contrast is greater than zero) for this technique is approximately -27 dBm to 17 dBm (0.2 fJ to 5 pJ/pulse), if we linearly extrapolate the data for both the left and right side of Fig. C-39. The lower limit is determined by the ASE noise floor and the upper limit is determined by the saturation of the SOA by the signal pulse (as well as the damage threshold which brings the upper limit down to about 6 dBm).

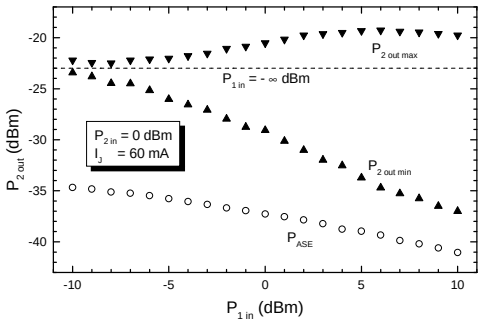

Figure C-38: The power transmitted by the switching window ($P_{2\text{out}}$) plotted as a function of the probe average power ($P_{1\text{in}}$). See Fig. C-37 for an illustration of $P_{1\text{in}}$, $P_{2\text{in}}$, and $P_{2\text{out}}$. $P_{2\text{in}}$ is average input signal power. I_j is injection current. $\triangle$ is peak of switching window. $\bigtriangledown$ is background of switching window. $\bigcirc$ is ASE. The switching contrast is given by $P_{2\text{out max}} - P_{2\text{out min}}$.

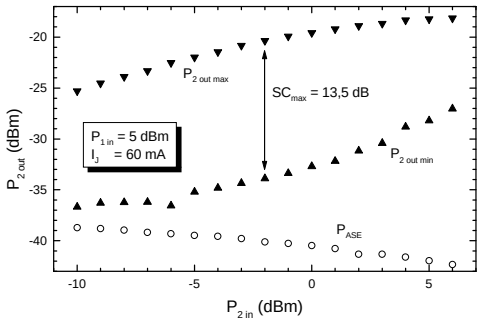

Figure C-39: The powers transmitted by the switching window plotted as a function of input signal power ($P_{2\text{in}}$). $\bigtriangledown$ is peak of switching window. $\triangle$ is background of switching window. $\bigcirc$ is ASE. SC is switching contrast.

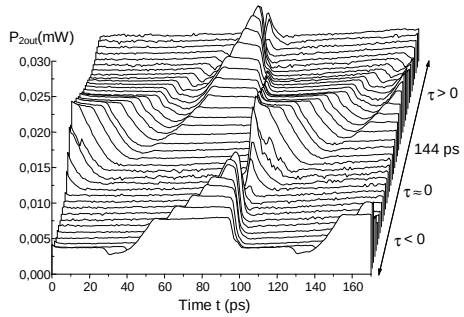

Figure C-40: Switching window dependence on the internal delay line. $\tau = 0$ is where the SOA is placed symmetrically in the fiber loop.

Switching Window Dependencies The switching window depends on many parameters [123], including the injection current, the asymmetric position of the SOA in the loop, and input optical powers. Fig. C-40 shows the switching window dependence on the placement of the SOA in the SLALOM. The variable τ is the delay between the clockwise and counterclockwise propagating signal pulses. A symmetric placing of the SOA in the loop means that the counterpropagating pulses in the fiber loop reach the SOA at the same time, or $\tau = 0$. At $\tau = 0$, both pulses see the same gain, hence same phase shift, and therefore the pulses are never switched out of the loop. The shape of the switching window can be changed from broad and flat to narrow and sharp by varying the asymmetric placing of the SOA. For optical sampling, it is important to get a sampling window with a sharp peak, rather than one with a flat peak so as to discriminate the signal pulse better. This is not the regular regime of operation used for all-optical pulse switching where a flat-top switching window is desirable.

Fig. C-41 shows the switching window for injection currents ranging from 0 to 170 mA. The optimal current for our SOA is approximately 70 mA. When the current is too low, the SOA does not provide enough gain leading to a switching window with a small contrast. When the current is too high, for example, by 160 mA, the background rises and the switching contrast worsens.

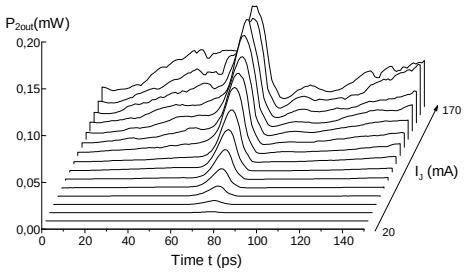

Figure C-41: Switching window dependence on the injection current.

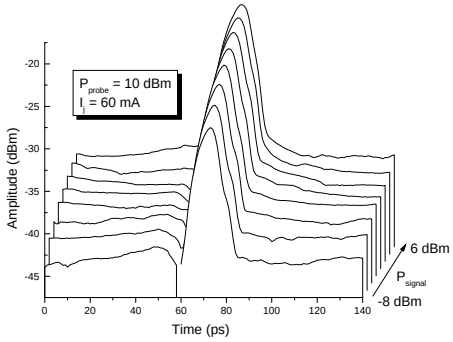

Figure C-42: Switching window dependence on signal power.

The switching window depends strongly on the asymmetric placing of the SOA and the injection current, but not as strongly on the input signal power itself. It is important to have the same switching window for each probe-signal delay. Fig. C-42 shows that even when the signal powers change by 16 dB, the shape of the switching window remains almost constant, and the switching contrast changes by only 2.6 dB. On the other hand, one must make sure that the probe pulse sufficiently saturates the SOA because the switching window shape and contrast change drastically with the input signal power, as shown in Fig. C-43, when the probe pulse is not strong enough.

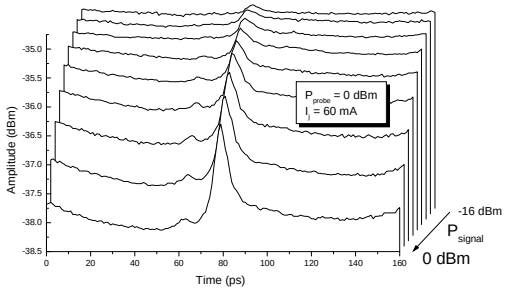

Figure C-43: Switching window dependence on signal power with a weak probe.

FWM Measurement Technique

FWM between the signal and probe in an SOA can be used to obtain the intensity and phase profile of the signal [124]. The setup for the FWM measurement technique is shown in Fig. C-44. As the probe pulse is delayed through the signal, the probe mixes with the overlapping part of the signal and generates a pulse with power proportional to the amplitude of the signal pulse at the sampled time-instant. Since the FWM component has a carrier frequency away from the signal and pulse carrier frequency ($\omega_{FWM} = 2\omega_p - \omega_s$, where ω_p=probe and ω_s=signal), the FWM spectrum can be directly observed on an OSA. As the probe is delayed through the signal, the center wavelength will shift in direct proportion to the instantaneous frequency of the signal. In addition, the instantaneous intensity is proportional to the integrated FWM spectral energy — roughly described by the peak amplitude of the FWM optical spectrum. The input and output spectrum to the SOA using the FWM technique are shown in Fig. C-45.

FWM Power Optimization To optimize the FWM component, both the signal and probe need to have the same polarization. In addition, since frequency up-conversion is more efficient than down conversion and the FWM component should

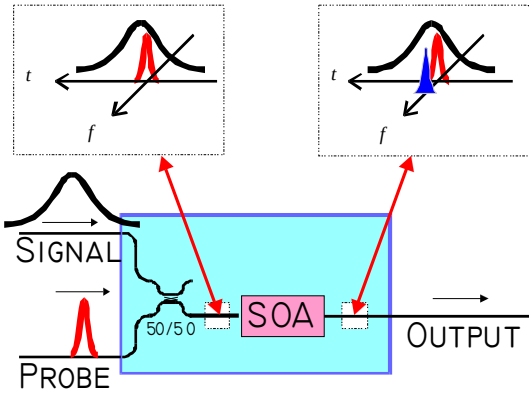

Figure C-44: The FWM measurement technique

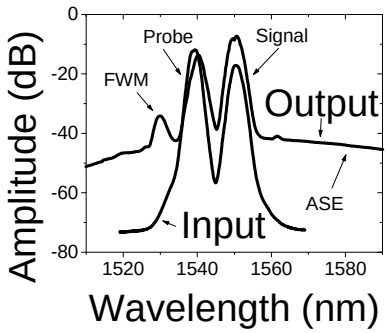

Figure C-45: The input and output spectrum from the SOA when using the FWM technique.

depend on the square of the more powerful probe pulse, the probe should have a higher carrier frequency than the signal. Therefore, the FWM power is

$$P_{FWM}(\omega) \propto P^2_{probe}(\omega) P_{signal}(\omega). \tag{C.28}$$

Using the constraint that the total power in the SOA needs to be less than some critical power, P_{cr}, dictated by the thermal damaging of the SOA, and using (C.28), the optimal probe and signal powers are $2P_{cr}/3$ and $P_{cr}/3$, respectively. Even with this simplified analysis, we experimentally found that the $2:1$ splitting of the probe and signal powers yielded approximately the largest FWM signal. The FWM conversion efficiency also depends on the injection current [125]. the dependence of the switching window on the pulsewidth of the signal and probe pulses are discussed in [125].

Dynamic Range Experimentally, we have tried signal pulse energies in the range from -10 to 6 dBm at 10 Gb/s (pulse energies as low as 10 fJ). For signal pulse energies less than -10 dBm, and high probe energies (greater than approximately 0 dBm), saturation effects of the probe become important and the gain-saturation technique (presented in section C.4.2) should be used.

Gain-Saturation Measurement Technique The gain-saturation measurement technique is analogous to the SLALOM technique. In the SLALOM technique, the SLALOM acts like a signal sampler and allows a section of the pulse through to the OSA. On the other hand, in the gain-saturation technique, the SOA acts like an intensity-notch filter in time and blocks a section of the pulse. The gain-saturation technique is illustrated in Fig. C-46. The signal and probe copropagate through an SOA. The probe pulse, which is much narrower and has higher power than the signal pulse, saturates the SOA at the time of its arrival. During the time in which the probe pulse saturates the SOA ($\approx$ 2 ps for our 1-ps pulses), the signal pulse experiences no gain. The signal pulse exiting the SOA has a temporal hole at this sampling instant. If the pulse is chirped, the temporal hole implies that there also should be a hole in the spectrum of the output signal since some of the frequencies

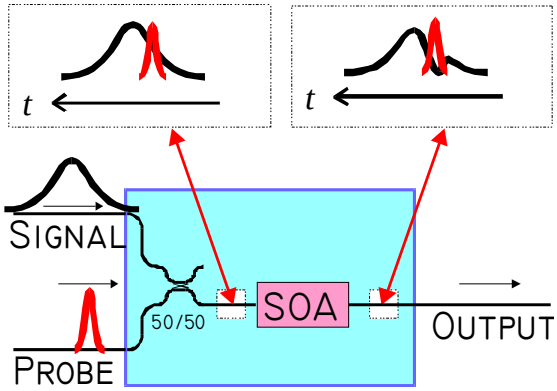

Figure C-46: Schematic of the gain-saturation technique.

that occupied the temporal hole are now removed. Fig. C-47 shows the spectrum of the signal after the SOA. Depending on the probe-signal delay, the spectral hole will occur at different locations. By tracking the wavelength and depth of the spectral hole with the OSA as a function of probe-signal delay, we can estimate both the instantaneous frequency and amplitude of the signal. Measuring the depth of the spectral hole with an OSA provides only a rough indication of the signal amplitude, since the resolution bandwidth of the OSA is at best ≈ 0.08 nm and the spectral hole is narrower. Section C.4.3 shows how to reconstruct the amplitude profile by using the instantaneous frequency profile and a measurement of the input signal spectrum. An advantage of the gain-saturation technique over the other two presented techniques is that it is polarization independent.

Dynamic Range The probe pulse should be chosen to have as high a power as possible without damaging the SOA. In our experiments, we typically used 1-ps probe pulses with an average power of 4 dBm at 10 Gb/s, and signal pulse powers from -18 to -10 dBm.

C.4.3 Theory and Simulations

This section is broken into two parts: (1) a theoretical analysis which gives the instantaneous intensity and instantaneous frequency error as a function of the signal pulse

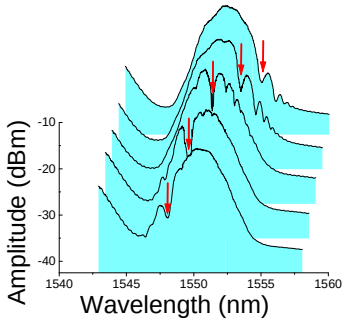

Figure C-47: Output signal spectrum from SOA when using the gain-saturation technique. The ripples in the spectrum are due to reflection from the facets of the SOA.

and window width; and (2) an overview of the algorithm used to recover the amplitude from a measurement of the instantaneous frequency and spectrum as outlined in subsection C.4.2.

Estimator Error

The SLALOM, FWM, and gain-saturation techniques involve a signal pulse which is sampled by a window. The theory in this section will clarify when these measurements can be trusted by finding an analytical expression for the instantaneous intensity and frequency error as a function of the width of the window and signal pulse.

The electrical field of the signal can be written as

$$E(t) = s(t)\exp(j\omega_0 t) \tag{C.29}$$

where ω_0 is the carrier frequency . The complex function $s(t)$ is the slowly varying amplitude and describes both amplitude and chirp. The intensity and chirp are given by

$$I(t) = |s(t)|^2 \tag{C.30}$$

and

$$\omega(t) = \Im\left\{\frac{1}{s(t)}\frac{ds(t)}{dt}\right\}, \tag{C.31}$$

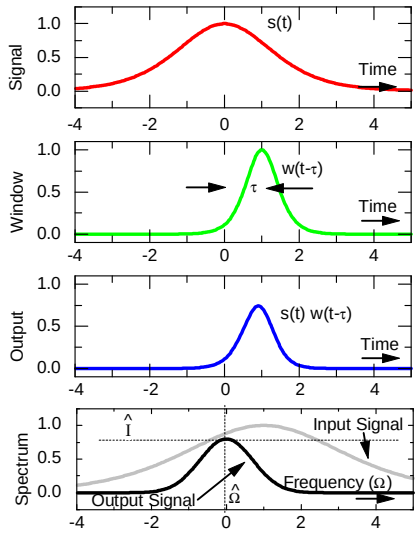

Figure C-48: A numerical example, where a pulse, $s(t)$, is sampled with a window, $w(t)$. The estimators for the intensity and frequency at time τ is given by $\hat{I}$ and $\hat{\Omega}$.

respectively. We define the instantaneous frequency as

$$\Omega(t) = \omega(t) - \omega_0. \tag{C.32}$$

The instantaneous intensity and frequency ($I(t)$ and $\Omega(t)$) at a specific time instant are estimated ($\hat{I}(t)$ and $\hat{\Omega}(t)$) by the peak value and center wavelength of the transmitted signal spectrum for each signal-probe delay. The signal and window are illustrated in the top two plots of Fig. C-48. After the signal pulse passes through the SOA, the output pulse has the form $s(t)w(t-\tau)$, which is shown by the third plot in Fig. C-48. The optical spectrum of the output pulse is shown by the last plot in Fig. C-48, and the peak value of the spectrum, $\hat{I}$, yields an estimate for $s(\tau)$ and the frequency offset from the carrier frequency, ω_0, yields an estimate, $\hat{\Omega}$, for the instantaneous frequency at time τ. The information obtained is the spectrum of the gated signal as a function of signal-probe delay — the so called spectrogram. Instead of inverting the spectrogram using a phase-retrieval algorithm, as in FROG [97], we use the estimators, $\hat{I}$ and $\hat{\Omega}$, to directly obtain the intensity and chirp profile of the

pulse without any computations. The estimators can be written explicitly as

$$\hat{I}(\tau) = \max_{\Omega} \left| \mathcal{F}\left\{ w(t-\tau)s(t) \right\} \right|^2 \tag{C.33}$$

and

$$\hat{\Omega}(\tau) = \Omega_m, \quad \text{such that} \quad G(\Omega_m) = \max_{\Omega} G(\Omega), \tag{C.34}$$

where $\mathcal{F}$ denotes the Fourier transform, τ is the delay between the center of the switching window and the center of the signal, and $G(\Omega)$ is the optical power spectrum of the windowed pulses. Here $\Omega = 0$ corresponds to the carrier frequency. These estimators are valid as long as the switching window is shorter than the signal pulse. If the switching-window width is equal or greater than the signal pulse, it is still possible to recover the original pulse, but in this case, we need to invert the spectrogram data.

Ignoring all other noise sources, the estimators $\hat{I}$ and $\hat{\omega}$ have a fundamental error associated with them. The intensity error increases as the switching window gets wider and the instantaneous frequency error increases as the width of the window becomes large compared to the chirp of the pulse. It is assumed that the window and the signal have a Gaussian shape and the signal is linearly chirped. For the SLALOM and FWM techniques, the Gaussian analysis gives a good indication about the errors of the measurement and when we can trust it, even when the pulse and window shapes are not Gaussian. The Gaussian analysis allows one to obtain analytical expressions for the instantaneous frequency and intensity errors. Mathematically, the window and signal can be written as $w(t) = \exp(-(t/\tau_w)^2/2)$ and $s(t) = \exp((1 + iC_1)(t/\tau_p)^2/2)$. One can analytically solve for the estimators by taking the Fourier-transform of $s(t)w(t-\tau)$ and finding the maximum value. Once this is done, it is found that the estimators are given by

$$\hat{\Omega}(t) = \frac{C_1 t}{\tau_p^2 + \tau_w^2} \tag{C.35}$$

and

$$\hat{I}(t) = \alpha G(\hat{\Omega}(t)) \propto \exp\left(-\frac{t^2}{\tau_p^2 + \tau_w^2} \right), \tag{C.36}$$

where $\alpha = I(0)/G(0)$ is the normalization constant so that the error is zero at the center of the pulse. Therefore the estimator errors at pulse time t, where $t = 0$ is the center of the pulse, are

$$\tilde{\Omega}(t) = \frac{\hat{\Omega} - \Omega}{\Omega} = -\frac{\tau_w^2}{\tau_w^2 + \tau_p^2} \tag{C.37}$$

where $\Omega = C_1 t/\tau_p^2$ is the true value of the instantaneous frequency and

$$\tilde{I}(t) = \frac{\hat{I} - I}{I} = \exp\left(\frac{t^2\tau_w^2}{\tau_p^2(\tau_p^2 + \tau_w^2)}\right) - 1. \tag{C.38}$$

As an example, Fig. C-49 shows a Gaussian-shaped pulse sampled by a window that is 0.28 times the width of the pulse. The dashed lines correspond to the exact shape; in this case, $\exp(-(t/\tau_p)^2)$. The circles represent the simulated values, which was done by calculating the Fourier-Transform of $w(t-\tau)s(t)$ numerically. The solid lines correspond to plotting (C.35) and (C.36). Since both the signal and window in Fig. C-49 are Gaussian, the numerical and analytical results are the same. In addition, since the window is much narrower than the signal pulse, the numerical and analytical results are almost indistinguishable from the exact result. Widening the sampling window increases the errors. For example, in Fig. C-50 a pulse is sampled by a window that is 0.85 times the width of the pulse. The chirp of the pulse is slightly underestimated and the width of the pulse is slightly overestimated. Asymmetries in the window or pulse shape lead to relatively large errors on the leading or trailing edge of the pulse (see Fig. C-51). An example where the pulse shape is Lorentzian, the window shape is a hyperbolic secant, and there is linear as well as quadratic chirp is shown in Fig. C-52. This shows that even when the window and pulse shape are not Gaussian, the Gaussian analysis for the error ((C.37) and (C.38)) yields an excellent approximation to the true error. The discontinuity in the simulated chirp profile of Fig. C-51 occurs in the tail of the pulse and is due to the vastly exaggerated asymmetric window which is made up of two Gaussians, one smaller than the other. The smaller Gaussian prematurely samples the pulse before the main Gaussian window.

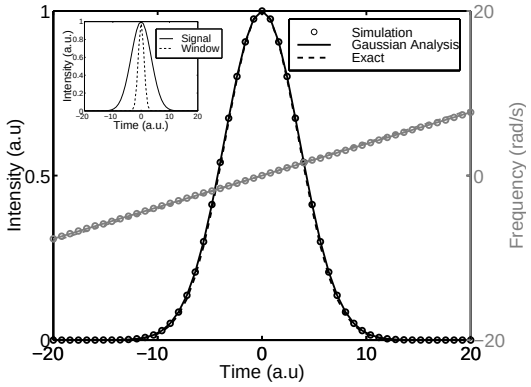

Figure C-49: The result of sampling a Gaussian linearly-chirped ($C_1 = 10$, where the chirp of the electric field is defined as $\exp[iC_1(t/\tau_p)^2/2 + iC_2(t/\tau_p)^3/3 + iC_3(t/\tau_p)^4/4 + ...]$) pulse with a Gaussian-shape window with a FWHM that is 0.28 the FWHM of the pulse. It is difficult to distinguish the difference between the original pulse (exact) and the sampled pulse (simulation).

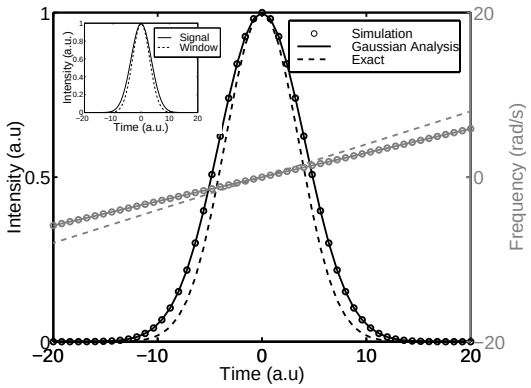

Figure C-50: The result of sampling a Gaussian linearly-chirped pulse ($C_1 = 10$) with a Gaussian-shape window with a FWHM that is 0.85 the FWHM of the pulse. Note that the black lines and circles correspond to the left axis and the gray lines and circles correspond to the right axis. The inset shows the original pulse and sampling window.

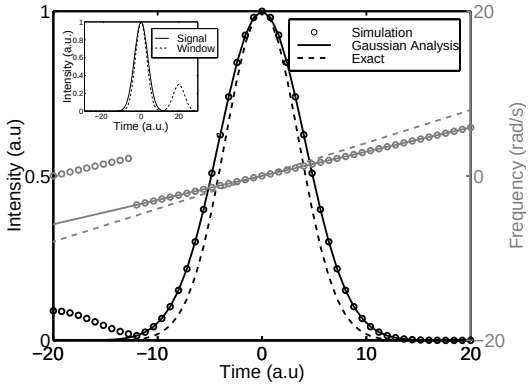

Figure C-51: The result of sampling a Gaussian linearly-chirped pulse ($C_1 = 10$) with a asymmetric window.

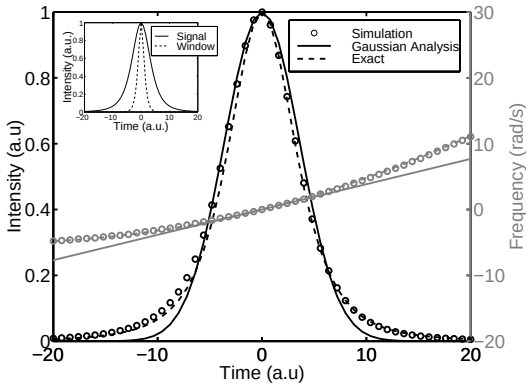

Figure C-52: The result of sampling a nonlinearly-chirped Lorentzian pulse ($C_1 = 10, C_2 = 1$) with a hyperbolic secant window.

In section C.4.4, we will use (C.37) to correct the chirp-profile of a 21-ps chirped pulse.

Amplitude Recovery Algorithm

The gain-saturation technique does not directly give a good reconstruction of the time-domain intensity profile of the signal pulse. Nevertheless, it is possible to reconstruct the intensity from the instantaneous frequency data plus a measurement of the input signal spectrum. A signal, $g(t)$, and its Fourier transform, $G(\omega)$, can be represented by its amplitude and phase:

$$\begin{aligned} g(t) &= |g(t)| \exp(i\phi(t)) \\ G(\omega) &= |G(\omega)| \exp(i\theta(t)) \end{aligned} \tag{C.39}$$

Given $\phi(t)$ and $|G(\omega)|$, then $\theta(\omega)$ and $|g(t)|$ are determined uniquely (the proof follows from re-expressing $g(t)$ and $G(\omega)$ into real and imaginary parts). The algorithm to obtain $\theta(\omega)$ and $|g(t)|$ from $\phi(t)$ and $|G(\omega)|$ is a modification of the Gerchberg-Saxton algorithm [126] which has been used to reconstruct phase from two intensity measurements. The algorithm we present here consists of transforming between the time and frequency domain and replacing either the phase with $\phi(t)$ in the time domain or the amplitude with $|G(\omega)|$ in the frequency domain. The steps of the algorithm (which are diagrammed in Fig. C-53) are:

1. Fourier transform an estimate of the time-domain signal, $g_1(t) = |g_2(t)| \exp(i\phi(t))$.

2. Replace the modulus of the resulting computed Fourier transform, $|G_1(\omega)|$, with the measured Fourier modulus, $|G(\omega)|$, to form an estimate of the Fourier transform.

3. Inverse Fourier transform the estimate of the Fourier transform, $g_2(t) = |g_2(t)| \exp(i\phi_2(t))$.

4. Replace the phase of the result of step 3, $\phi_2(t)$, with the measured time-domain phase profile, $\phi(t)$, to form a new estimate of the signal, $g_1(t)$.

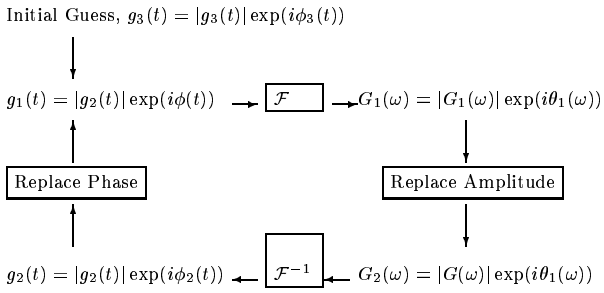

Figure C-53: Block diagram of the amplitude recovery algorithm. $\mathcal{F}$ and $\mathcal{F}^{-1}$ denote the Fourier transform and inverse Fourier transform.

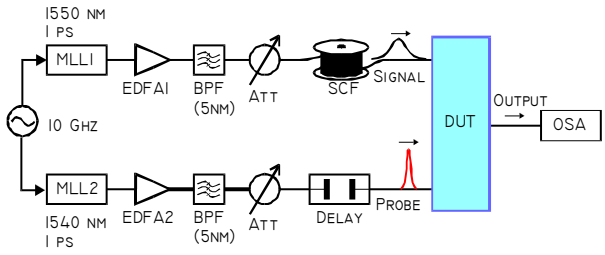

Figure C-54: Experimental setup.

The error decreases with each iteration [127]. The recovered amplitude resolution depends on the resolution of $\phi(t)$ (dictated by the fast time-scale gain recovery of the SOA) and $|G(\omega)|$ (dictated by the resolution bandwidth of the OSA).

C.4.4 Experiments

The experimental setup is shown in Fig. C-54. Two mode-locked laser diodes generate 1-ps transform-limited pulses at 10 Gb/s and are amplified by commercial erbium-doped fiber amplifiers. The pulses are then band-passed filtered (BPF) to remove the background ASE. The signal pulse is generated by passing it through silica-core fiber (SCF) which both broadens and chirps the pulse. The device-under-test (DUT) represents one of our three measurement schemes illustrated in Fig. C-37, Fig. C-44, and Fig. C-46. Finally the output is measured spectrally on an optical spectrum analyzer (OSA).

All three measurement techniques were tested by propagating the pulses through

500 m of SCF which broadened the pulses to 21 ps. Fig. C-55 shows the sampled pulses using the SLALOM technique. Fig. C-56 shows the sampled pulses using the FWM technique. Fig. C-57 shows the sampled pulses using the gain-saturation technique. The solid lines represent the intensity and chirp of a 1-ps sech pulse after 500 m propagation in a dispersive fiber with dispersion 16 ps/nm/km. The dotted lines are the experimentally measured values. The SLALOM technique faithfully reproduces the expected intensity and chirp profile of the pulses, even though we had a switching window width of 10 ps. This is due to the sharpness of the peak, which allows sufficient discrimination between adjacent intensity values. The switching window was measured independently and is shown in Fig. C-58. The chirp profile, as measured with the SLALOM technique, is slightly over/under-estimated at the leading/trailing edge of the pulse. This effect is due to the error in the estimators that we are using and can be corrected numerically, as shown in Fig. C-59. The FWM technique reproduces the chirp profile better than the SLALOM technique, mainly due to the fact that the effective switching window is narrower, and the intensity profile is quite good except for a small dent on the top trailing part of the pulse. This small dent is due to the saturation of the gain in the SOA by the leading edge of the signal pulse. Therefore it is important to keep the signal power low enough so that the leading edge of the signal pulse does not significantly saturate the gain of the SOA. The gain-saturation technique faithfully reproduces the chirp profile of the signal, but the intensity profile only gives rough information about the location of the pulse. This is to be expected since we are measuring a sharp spectral hole with an OSA which has a finite a finite bandwidth resolution. Nevertheless, we can reconstruct the intensity profile by using the amplitude recovery algorithm outlined in section C.4.3. To use this algorithm, we needed an additional measurement of the signal spectrum, which is easy to do with the OSA. The reconstructed amplitude is shown in Fig. C-60 and C-61, and is much better than the direct measurement of the intensity shown in Fig. C-57.

Aside from the inherent estimator error discussed in section C.4.3, there are other sources of error for all three measurement techniques. There is a delay-dependent loss ($\approx$ 2 dB over 170 ps delay) associated with the optical delay-line placed in

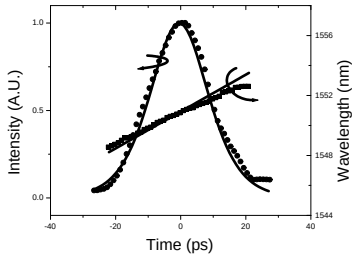

Figure C-55: SOA Techniques applied to 21-ps chirped pulses. Solid lines are exact and dots correspond to experiments. This plot was generated using the SLALOM technique with $P_{\text{Signal}} = -5$ dBm and $P_{\text{Probe}} = 12.5$ dBm.

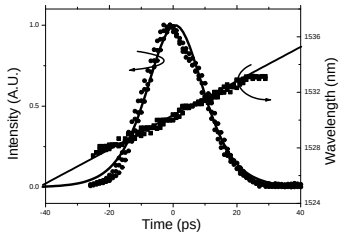

Figure C-56: The intensity and wavelength profiles using the FWM technique with $P_{\text{Signal}} = 0.23$ dBm and $P_{\text{Probe}} = 3.24$ dBm.

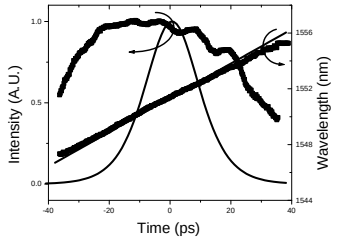

Figure C-57: This intensity and wavelength profiles using the gain-saturation technique with $P_{\text{Signal}} = -10$ dBm and $P_{\text{Probe}} = 4$ dBm.

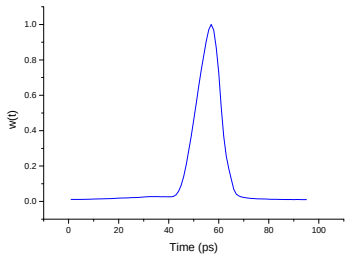

Figure C-58: SLALOM switching window.

the probe arm in Fig. C-54. Fluctuations in the probe power causes fluctuations in the estimated signal intensity. The SLALOM and FWM techniques are polarization dependent, and there are long time-scale drifts in the polarization state of the input signal and probe pulses. Finally, the timing jitter of the mode-locked lasers diodes used in these experiments is approximately 0.5 ps and effectively smears out the switching window.

C.4.5 Conclusion

SLALOM, FWM, and gain-saturation measurement techniques using SOAs have been described. These measurement techniques are ideally suited for low-energy, picosecond pulses, mainly due to the strong but weak nonlinearity provided by the SOA. The input signal power dynamic range of the SLALOM, FWM, and gain-saturation techniques were -10 to 6 dBm, -10 to 6 dBm, and -18 to -10 dBm, respectively. The temporal resolution is limited by the width of the switching window. The switching window of the SLALOM is $>$ 2 ps. The effective switching window of the FWM technique can be smaller than the in SLALOM case since it is limited by the width of the probe. (1 ps in our case). The gain-saturation switching window is determined by the fast time-scale gain recovery of the SOA and width of the probe, which was approximately 2 ps for our 1 ps probe pulses. To obtain the amplitude profile using the gain-saturation technique, one must additionally measure the spectrum of the signal. In all other cases, the amplitude and chirp profiles can be obtained directly without

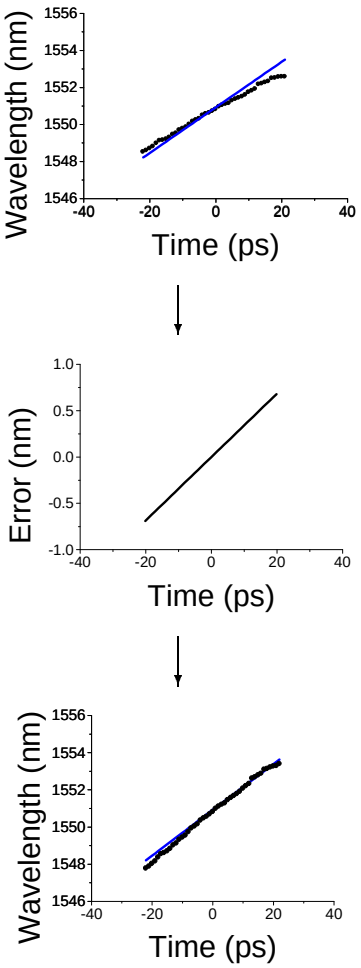

Figure C-59: Correction of the wavelength data for the SLALOM measurement technique. Top: original data. Middle: correction curve given by $\Omega - \hat{\Omega} = C_1\tau_w^2 t/[\tau_p^2(\tau_w^2 + \tau_p^2)]$. Right: corrected data. The leading and trailing chirp profiles are not equally compensated since the actual switching window is steeper on the trailing edge. The parameters used for this error correction are: $C_1 = -13.43$, $\tau_p = 10$ ps and $\tau_w = 5$ ps.

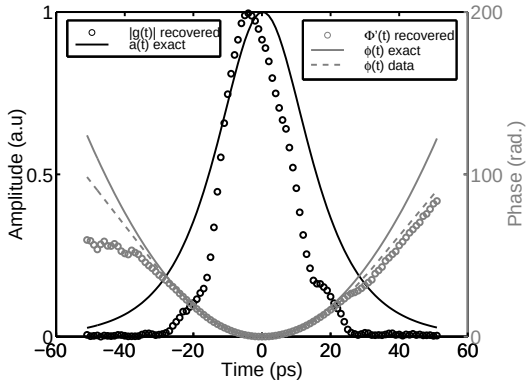

Figure C-60: Reconstructed amplitude by using the amplitude recovery algorithm. Time domain.

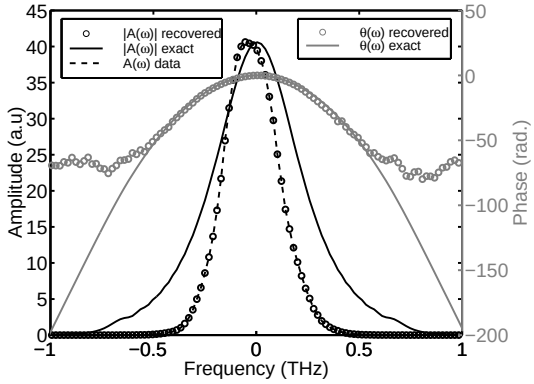

Figure C-61: Reconstructed amplitude by using the amplitude recovery algorithm. Frequency domain.

computation. The gain-saturation technique has the benefit of being polarization independent, whereas the other two techniques are polarization dependent.

Appendix D

Optimal Sampling Pulse Width

Short pulses are needed when the amplitude noise from the laser or detection circuit is large. In addition, increasing the number of quantization levels also puts stricter constraints on the allowable timing jitter. Since timing jitter increases with decreasing pulse width, the overall performance of the optical sampling system does not improve by making the pulse width arbitrarily large. Therefore there is an optimal pulse width whose minimum value is bounded by timing jitter and whose maximum value is bounded by amplitude noise.

If we assume that the signal is described by $\cos(2\pi\nu_{sig}t)$, where ν_{sig} is the frequency of the signal. The intensity of the pulse is $\frac{1}{\sqrt{\pi}\tau}\exp[-(t-t_0)^2/\tau^2]$, where the pulse energy is normalized to 1, t_0 is a time delay, and τ is the pulse width. The sampled signal is equal to

$$\int_{-\infty}^{\infty}\cos(2\pi\nu_{sig}t)\times\frac{1}{\sqrt{\pi}\tau}\exp\left[-\frac{(t-t_0)^2}{\tau^2}\right]dt = e^{-(\pi\nu_{sig}\tau)^2}\cos(2\pi\nu_{sig}t_0). \qquad \text{(D.1)}$$

Assuming that this is an N-bit quantizer, then there are 2^N levels between $\pm e^{-(\pi\nu_{sig}\tau)^2}$. The quantization spacing must be greater than the amplitude noise, say twice the rms value $2\Delta P$. Using this constraint we find that,

$$\frac{2e^{-(\pi\nu_{sig}\tau)^2}}{2^N} \quad > \quad 2\Delta P$$

$$\tau \;<\; \frac{1}{\pi\nu_{sig}}\sqrt{\ln\left(\frac{1}{2^N\Delta P}\right)}. \tag{D.2}$$

In other words, the pulse width must decrease as ΔP increases.

The error due to timing jitter is modelled by the substitution $t_0 \rightarrow t_0 - \Delta t$ in the argument of the cosine, where Δt is the rms deviation. The worst sampling error due to timing jitter occurs at the steepest part of the cosine function, which occurs when the signal equals zero. The sampled signal amplitude at $t_0 = -\pi/2$ is $e^{-(\pi\nu_{sig}\tau)^2}\cos(2\pi\nu_{sig}t_0 - \Delta t) = e^{-(\pi\nu_{sig}\tau)^2}\cos(2\pi\nu_{sig} - \pi/2 - \Delta t) = e^{-(\pi\nu_{sig}\tau)^2}\sin(2\pi\nu_{sig}\Delta t) \approx 2\pi\nu_{sig}\Delta t e^{-(\pi\nu_{sig}\tau)^2}$. To prevent an error, this value must be less than half a quantization level,

$$\begin{aligned} 2\pi\nu_{sig}\Delta t e^{-(\pi\nu_{sig}\tau)^2} &< \frac{1}{2}\frac{2e^{-(\pi\nu_{sig}\tau)^2}}{2^N} \\ \Delta t &< \frac{1}{2\pi\nu_{sig}}\frac{1}{2^N}. \end{aligned} \tag{D.3}$$

Therefore, the timing jitter must decrease as N increases. Timing jitter is related to the pulse width according to $\Delta t = K_m/\tau^m$, where K_m is a constant that depends on laser parameters (see appendix B) and $m = 2$ or 4, for non-dispersive and dispersive cavities, respectively. Using this relation, equation (D.3) can be rewritten as

$$\tau > \left(2^{N+1}\pi\nu_{sig}K_m\right)^{1/m} \tag{D.4}$$

Putting equations (D.2) and (D.4) together, we obtain the optimal sampling pulsewidth

$$\boxed{\left(2^{N+1}\pi\nu_{sig}K_m\right)^{1/m} < \tau < \frac{1}{\pi\nu_{sig}}\sqrt{\ln\left(\frac{1}{2^N\Delta P}\right)}}. \tag{D.5}$$

Next we evaluate this expression for an actively modelocked laser for $m = 2$ (no dispersion). The timing jitter for this case can be found by substituting equation (B.104) into equation (B.117)

$$(\Delta t)^2 \equiv \sigma_{t,pc}^2 = \Omega_f^2\tau^4 \times \frac{P_{ASE}T_R}{2w_0}. \tag{D.6}$$

If we ignore the relationship between Ω_f and τ, we see from this equation that $\Delta t \propto \tau^2$, or $m = 2$. In this case $K_2 = \Omega_f \sqrt{\frac{P_{ASE} T_R}{2 w_0}}$. If we assume that $\Omega_f = 2\pi \times 333$ GHz (5 nm), $P_{ASE} = 0.008$ mW, $T_R = 100$ ps, and $w_0 = 1$ pJ, then $K_2 = 2\pi \times 6.65$ GHz. For $\nu_{sig} = 5$ GHz, $N = 12.9$, and $\Delta P = 0.1/2^N$ (the standard deviation of the optical power is one-tenth the size of a quantization level), the optimal pulse width is

$$3.17 \text{ ps} < \tau < 96.6 \text{ ps}. \tag{D.7}$$

Notice that the optical pulse width can be fairly wide.

One group [24] claims that the requirement on the pulse width is given by

$$FWHM \leq \frac{2\sqrt{\ln 2}}{\pi \nu_{sig}} \sqrt{\frac{1}{2^N}} \tag{D.8}$$

which puts a very tight constraint on the pulse width: 1.2 ps for $N = 12.9$ and a 5 GHz signal. It is rather puzzling why this expression does not depend on the amplitude noise.

Appendix E

Measuring V_π of Phase Modulator

The applied voltage required to change the delay of the phase modulator by one-half an optical cycle is V_π. We measure V_π by measuring the relative heights of the modulation sidebands in the *optical* spectrum for a given microwave power.

The input electric-field to the phase modulator can be written as

$$E_{in}(t) = E_0 \cos(\omega_c t) \tag{E.1}$$

and the output electric-field is

$$E_{out}(t) = E_0 \cos\left(\omega_c t + \frac{V}{V_\pi}\pi \sin(\omega_M t)\right) \tag{E.2}$$

where ω_c is the optical carrier frequency, ω_M is the modulation frequency, and E_0 is the amplitude of the electric-field. The output electric-field can be simplified according to

$$\begin{aligned} E_{out}(t) &= E_0 \cos(\omega_c t) \cos\left(\pi \frac{V}{V_\pi} \sin(\omega_M t)\right) - E_0 \sin(\omega_c t) \sin\left(\pi \frac{V}{V_\pi} \sin(\omega_M t)\right) \\ &= E_0 \cos(\omega_c t) \left[J_0(\pi V/V_\pi) + 2\sum_{n=1}^{\infty} J_{2n}(\pi V/V_\pi) \cos(2n\omega_M t)\right] \\ &\quad -E_0 \sin(\omega_c t) \left[2\sum_{n=1}^{\infty} J_{2n-1}(\pi V/V_\pi) \sin[(2n-1)\omega_M t]\right] \end{aligned} \tag{E.3}$$

where J_n represents the nth order Bessel function of the first kind and the identities

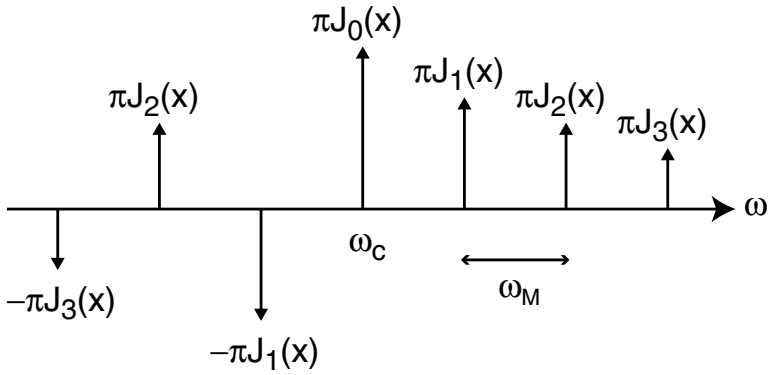

Figure E-1: Fourier transform of output electric-field.

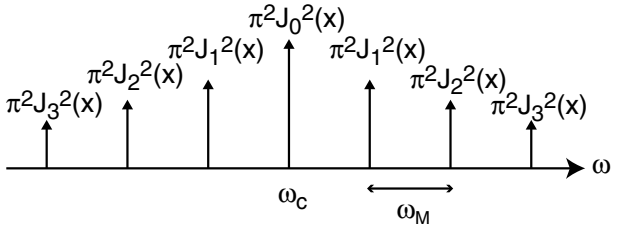

Figure E-2: Optical spectrum of output electric-field.

[87, p.632]

$$\cos(x\sin\theta) = J_0(x) + 2\sum_{n=1}^{\infty} J_{2n}(x)\cos(2n\theta) \tag{E.4}$$

$$\sin(x\sin\theta) = 2\sum_{n=1}^{\infty} J_{2n-1}(x)\sin[(2n-1)\theta] \tag{E.5}$$

were used. The Fourier transform of equation (E.3) is shown in Fig. E-1. The magnitude squared of the Fourier transform of equation (E.3) is the optical spectrum and is shown in Fig. E-2. The magnitude of each delta function is proportional to the square of the nth order Bessel function.

Next we adjust the microwave power until the first side-band has equal magnitude to the carrier. Fig. E-3 shows that $J_0^2(x) = J_1^2(x)$ when $x = 1.4349$. Therefore, we

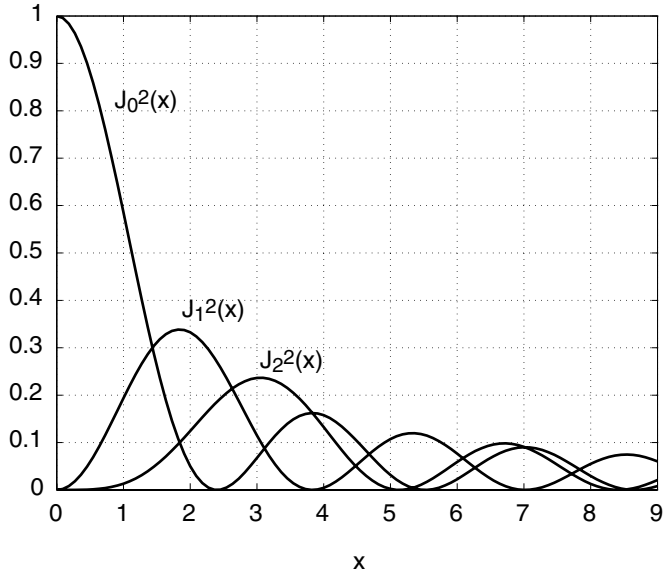

Figure E-3: Bessel functions $J_0^2(x)$, $J_1^2(x)$, and $J_2^2(x)$.

find that

$$x \equiv \pi \frac{V_p}{V_\pi} = 1.4349, \tag{E.6}$$

where V_p is the peak voltage needed to equate the magnitudes of the zeroth order and first order sidebands. Solving for V_π, we find that

$$V_\pi = \pi \frac{V_p}{1.4349}. \tag{E.7}$$

For the EO Space phase modulator, an average power of 19 dBm or a peak voltage of $V_p = 10^{(19-10)/20} = 2.8184$ V at 10 GHz was applied to the electrodes to obtain $J_0^2(x) = J_1^2(x)$. Using equation (E.7), we find that $V_\pi = 6.17$ V at 10 GHz. This performance is approximately a factor of two better than that of JDS-Uniphase modulators. In addition the insertion loss was measured at a mere 1.4 dB.

The maximum value of x is limited by the maximum applied power without burning out the internal resistor. With a 1/2 W 50 Ω internal resistor, one should not exceed 27 dBm ($V_p = 10^{(27-10)/20} = 7.079$) of applied power. This would imply a maximum modulation of $x_{max} = \pi V_{p,max}/V_\pi = \pi 7.079/6.17 = 3.6$.

Appendix F

X-Band Oscillators

Since the noise of the X-band (8-12 GHz)[1] oscillator that drives the actively mode-locked laser is critical to obtaining quantum-limited performance, this chapter presents an overview of two ultra-low phase noise oscillators: the sapphire loaded cavity oscil-

[1]Radio band designations

30-300 Hz	10-1 Mm	ELF (extremely low frequency)
300-3000 Hz	1 Mm-100 km	
3-30 kHz	100-10 km	VLF (very low frequency)
30-300 kHz	10-1 km	LF (low frequency)
300-3000 kHz	1 km-100 m	MF (medium frequency)
3-30 MHz	100-10 m	HF (high frequency)
30-300 MHz	10-1 m	VHF (very high frequency)
300-3000 MHz 1 m-10 cm	UHF (ultra high frequency)	
3-30 GHz	10-1 cm	SHF (super high frequency)
30-300 GHz	1 cm-1 mm	EHF(extremely high frequency)

The IEEE radar band designations

1-2 GHz	30-15 cm	L Band
2-4 GHz	15-7.5 cm	S Band
4-8 GHz	7.5-3.75 cm	C Band
8-12 GHz	3.75-2.50 cm	X Band
12-18 GHz	2.5-1.67 cm	Ku Band
18-27 GHz	1.67-1.11 cm	K Band
27-40 GHz	1.11 cm-7.5 mm	Ka Band
40-75 GHz		V Band
75-110 GHz		W Band
110-300 GHz		mm Band
300-3000 GHz		u mm Band

Satellite TVRO bands

1700-3000 MHz	S-Band
3700-4200 MHz	C-Band
10.9-11.75 GHz	Ku1-Band
11.75-12.5 GHz	Ku2-Band (DBS)
12.5-12.75 GHz	Ku3-Band
18.0-20.0 GHz	Ka-Band

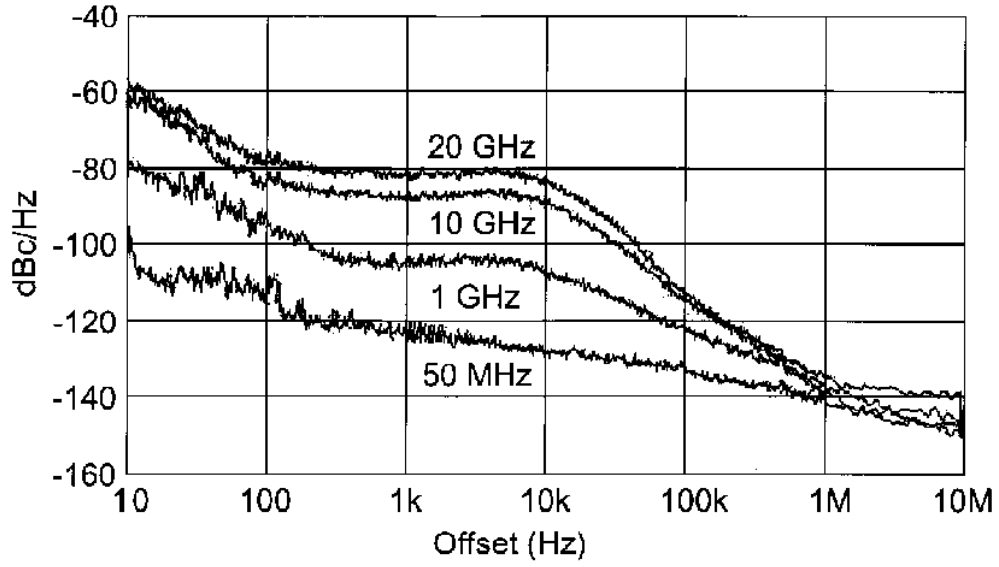

Figure F-1: Agilent 83732B phase noise [3].

lator (SCLO) and the optoelectronic oscillator (OEO). The phase noise of the Agilent 83732B synthesizer used in many of the experiments reported in this thesis is shown in Fig. F-3 and F-1.

F.1 Sapphire Loaded Cavity Oscillator

The SCLO was released in 1996 and offered the lowest phase noise signal generation at X-band frequencies (8 to 12 GHz) [5]. The SBO oscillator – nicknamed "the Shoebox" and shown in Fig. F-2 – integrates two patented technologies developed by Poseidon Scientific Instruments (www.psi.com.au) and the University of Western Austrailia: a high Q sapphire loaded "whipsering gallery mode" cavity resonator and a noise-reduction circuit. The phase noise of the Shoebox is approximately 25 dB lower than the best reported commercially-available multiplied surface acoustic wave (SAW) oscillators (see Fig. F-3).

The SBO relies on the internally reflective nature of the sapphire to trap microwave energy and realize an unloaded Q of approximately 200,000 at room temperature. The noise-reduction circuit is a real-time phase noise measuring system with good instan-

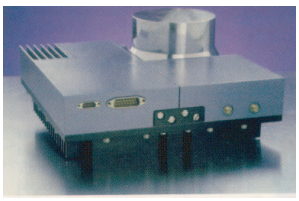

Figure F-2: The SBO-10.240-XPL oscillator.

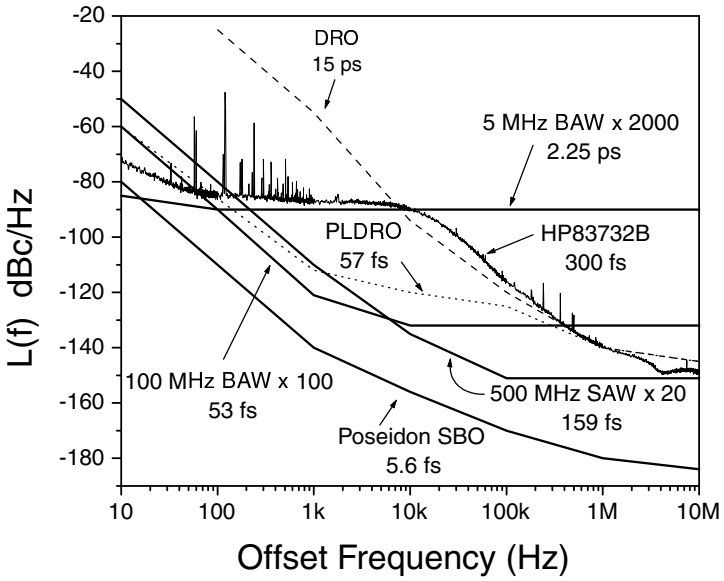

Figure F-3: Single-sideband phase noise and corresponding integrated timing jitter (10 Hz to 10 MHz) of various microwave oscillators at 9 and 10 GHz, demonstrating the superior phase noise performance of the Poseidon Shoe Box oscillator relative to that of the HP83732B synthesizer, dielectric resonant oscillator (DRO), phase-locked dielectric oscillator(PLDRO), surface acoustic wave oscillator (SAW) [4], and bulk acoustic wave oscillator (BAW) [4].

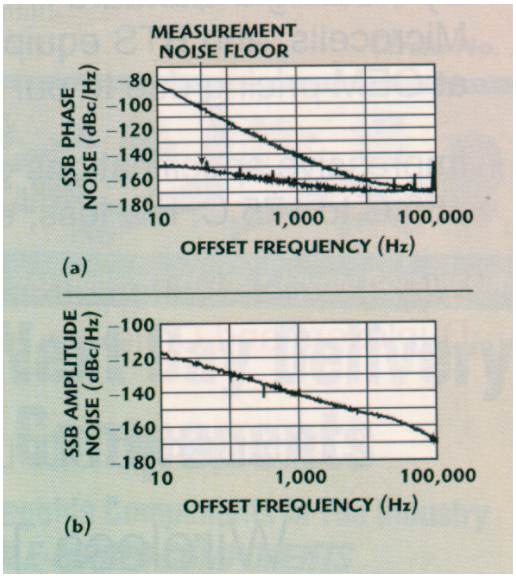

Figure F-4: The SBO-10.240-XPL oscillator's (a) phase noise and (b) amplitude noise [5].

Offset Frequency (Hz)	Phase Noise (dBc/Hz)
100	-104
1k	-138
10k	-154
100k	-160

Table F.1: Specified noise performance of SBO.

taneous band-width and noise floor. It optimizes the performance of the oscillator by reducing the phase noise contribution of active components which are otherwise fundamentally noisy.

The typical noise performance is shown in Fig. F-4, F-5, and F-6. The noise spectrum is virtually spur-free. Independent tests confirm that the single-side band phase noise approaches the thermal noise limit approximately 2 MHz from the X-band carrier. The timing jitter is 6 fs over an integrated bandwidth of 10 Hz to 10 MHz.

The SBO is a fixed frequency source with typical output powers of 13 dBm and the specified phase noise performance is shown in Table F.1.

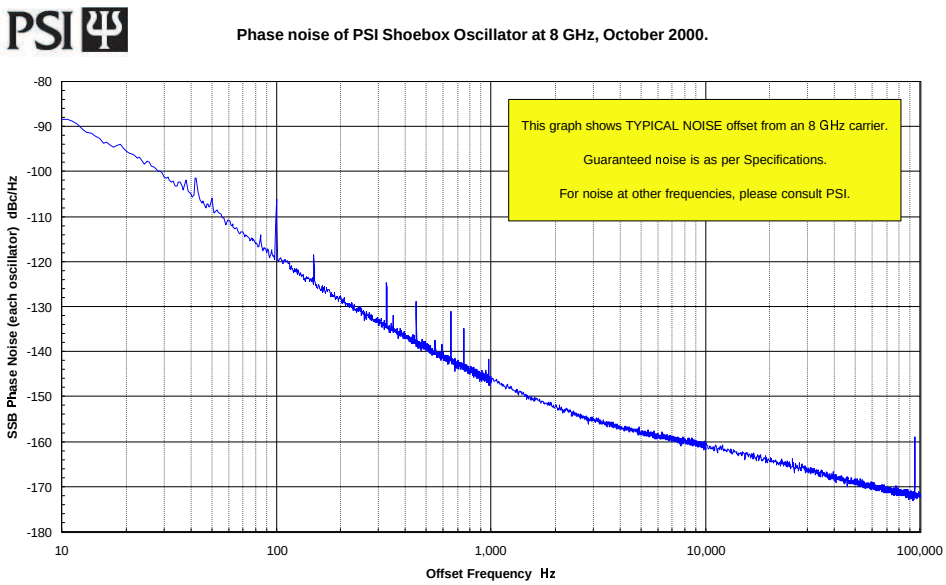

Figure F-5: Phase noise of PSI SBO at 8 GHz.

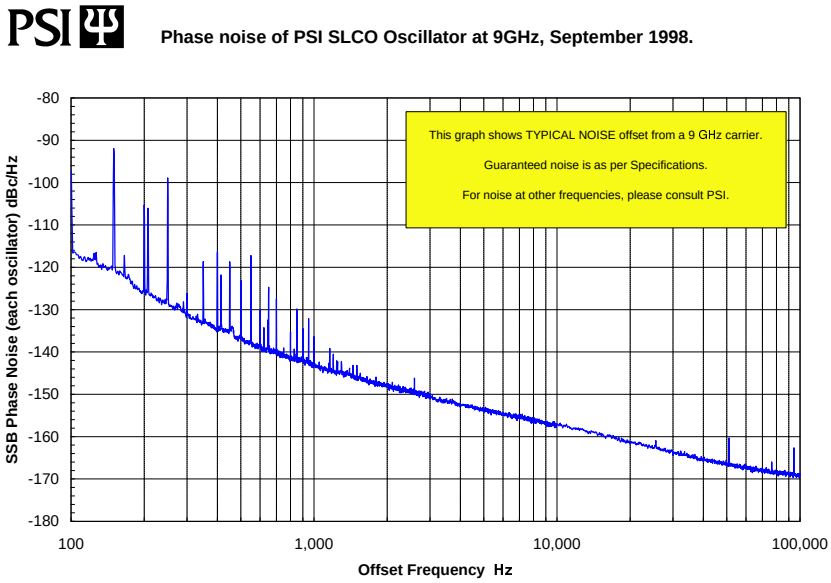

Figure F-6: Phase noise of PSI SLCO at 9 GHz.

Figure F-7: OEwaves optically generated low noise microwave clock.

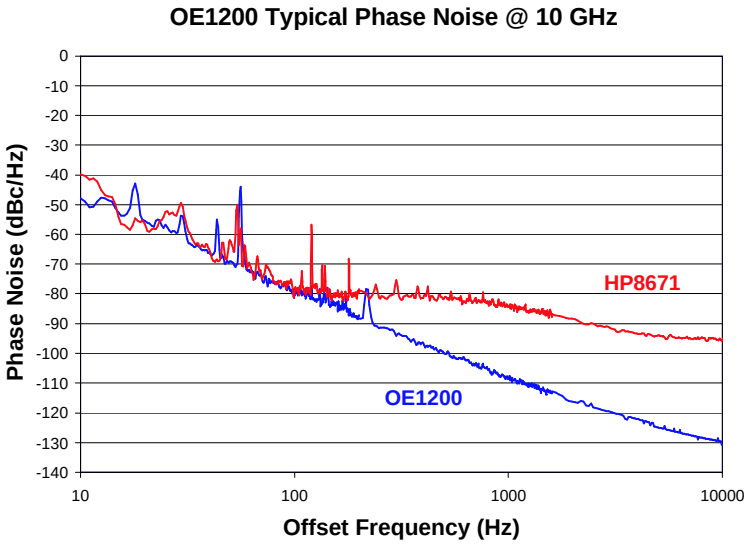

Figure F-8: OE1200 typical phase noise at 10 GHz.

F.2 Optoelectronic Oscillator

The opto-electronic oscillator shown in Fig. F-7 is a low phase noise microwave clock that is sold by OEwaves (www.oewaves.com) and was developed by Lute Maleki and Steve Yao while at the Jet Propulsion Laboratory [128, 129]. The OE1200 is a commercially available optoelectronic oscillator whose phase noise is shown in Fig. F-8. Its free running phase noise is very low (-140 dBc/Hz at 10 kHz offset), but is still lower than the SCLO.

The underlying technology is based on optical resonators, which generate higher frequencies without the need for electronic frequency multiplication. The glass microresonator is 100-500 micrometers in diameter, within which infrared light circulates

billions of times, a long pathway that results in low noise. This generates very clean microwave reference signals from 1-100 gigahertz with at least two orders of magnitude less noise than conventional quartz or dielectric oscillators.

One problem with this resonator that is not given sufficient attention are the supermode spurs that occur at multiples of the round-trip frequency in their fiber loop.

The SSB phase noise of a free-running oscillator can be modelled by five power-law noise processes that produce a particular slope on the spectral-density plot

$1/f^0$ White phase modulation (PM) – white of phase

$1/f^1$ Flicker PM – flicker of phase

$1/f^2$ White FM – white of frequency

$1/f^3$ Flicker FM – flicker of frequency

$1/f^4$ Random walk FM – random walk of frequency

The phase noise plot of the OE1200 in Fig. F-8 shows a $1/f^3$ dependence from 10 Hz to 1 kHz, and a $1/f^2$ dependence from 1 kHz to 10 kHz.

Appendix G

NEC MLLD Device Parameters

Device paramters for the MLLD structure: NEC DC-PBH +1% strained InGaAsP (10 nm) × 6 quantum wells.

Parameter	Symbol	Value	Units	Notes
Active layer width	W	1.6	μm	Typical value for DC-PBH
Active layer thickness		40	nm	Hole confined in 6.5 nm QW × 6
Active layer volume	V	6.4	μm^3	per 100 μm length
Optical confinement factor	Γ	0.05		Based on mode calculation
Waveguide refractive index	η_e	3.19		
Group velocity refractive index	η_g	3.49		$L = 725\mu$m $\rightarrow f = 59.4$ GHz
LD facet reflectivity	R	0.31		As cleaved LD
AR coating reflectivity	R_{AR}	5×10^{-4}		Measured ripples in ASE optical spectrum
Waveguide loss	α_i	13	cm^{-1}	From experimental data
Photon lifetime for 500 μm LD	τ_p	3.3	ps	$1/\{c[\alpha_i + ln(1/R)/L]/\eta_g\}$
Threshold current	I_{th}	9	mA	$L = 300\mu$m conventional LD
Threshold current density	J_{th}	1.8	kA/cm^2	$L = 300\mu$m conventional LD
Internal quantum efficiency	ξ_i or η_i	0.83		From experimental data
External differential efficiency	ξ_{id} or η_d	0.625		From experimental data
Nonradiative recombination life	γ	> 10	ns	Auger process is not included!
Auger recombination factor	C	5×10^{-29}	cm^6 s^{-1}	APL **58**, 158 (1991)
Radiative recombination factor	B	1×10^{-10}	cm^3 s^{-1}	APL **58**, 158 (1991)
Gain lifetime (1/[biomolecular+Auger recombination rates])	t_g	0.5-1.0	ns	$\approx 1/[Bn + Cn^2]$ at threshold carrier density
Carrier density at threshold	n	$5 - 6 \times 10^{18}$	cm^{-3}	Theoretical value
Threshold gain		≈ 5	dB	$G \approx 1/R$
Gain bandwidth		50-60	nm	ASE data for 1 mm LD, 50 mA
Gain for AR coated LD		15	dB	Experimental data for SOA
Linewidth enhancement factor	α	2-5		Conventional theoretical value
SA lifetime (hole lifetime)	t_{SA}	< 10	ps	-2 V reverse bias
SA absorption coefficient (unsaturated value)	α_0	230	cm^{-1}	Experimental data
SA section length	L_{SA}	30-40	μm	
Saturation energy of absorber	E_S^{SA}	0.5-1	pJ	Experimental data
Beam divergence (horizontal)	ϑ_h	20	degree	Experimental data
Beam divergence (vertical)	ϑ_v	25	degree	Experimental data
Gain, SA separation resistance	R_s	1000	Ω	Typical value
Device resistance	R_d	7	Ω	Typical value for 500 μm LD
Dispersion at 1552 nm	D	$< -16.8 \pm 1.7$	fs/nm	Four times larger than 900 μm MQW SOAs [79, p.76]

Appendix H

Related Presentations and Publications

H.1 Presentations

L. A. Jiang, M. E. Grein, B. S. Robinson, E. P. Ippen, and H. A. Haus. Experimental demonstration of a timing jitter eater. To be presented at CLEO 2002.

M. E. Grein, L. A. Jiang, H. A. Haus, E. P. Ippen, C. McNeilage, and J. Searls. Experimental observation of quantum-limited jitter in an active, harmonically modelocked fiber laser. To be presented at CLEO 2002.

M. E. Grein, L. A. Jiang, H. A. Haus, and E. P. Ippen. Timing jitter in modelocked lasers. LEOS 2001. MO1 (invited) San Diego, California. Technical Digest, p.113-114.

L. A. Jiang, M. E. Grein, J. M. Fini, E. P. Ippen and H. A. Haus. Noise of harmonically modelocked lasers. Gordon Conference on Nonlinear Optics 2001 L. A. Jiang M. E. Grein, and E. P. Ippen. Complete pulse characterization through optical correlations and genetic algorithms. CLEO 2001. CWA15. Technical Digest, p.276-277

L. A. Jiang, M. E. Grein, E. P. Ippen, and H. A. Haus. Noise of Modelocked Laser

Diodes. ISLC 2000. ThB5. Laser Dynamics. Monterey, California.

L. A. Jiang, M. E. Grein, E. P. Ippen, H. A. Haus, T. Shimizu, H. Kurita, and H. Yokoyama. Noise measurements of a 45 GHz mode-locked laser diode. CLEO 2000. CMS2. High Speed Semiconductor Lasers.

L. Jiang, E. Ippen, S. Diez, C. Schmidt, H.G. Weber. Wavelength and Intensity Sampling of Optical Signals using Semiconductor Optical Amplifiers. CLEO 1999. CThL6. Ultrashort Pulse Generation I.

H.2 Publications

L. A. Jiang, M. E. Grein, E. P. Ippen, "Region of validity for residual phase noise measurements of actively modelocked lasers." Submitted to Electronics Letters.

K. S. Abedin, J. T. Gopinath, L. A. Jiang, H. A. Haus, and E. P. Ippen. "Self-stabilized harmonic passively mode-locked stretched pulse Erbium fiber ring laser", submitted to Optics Letters.

L. A. Jiang and E. P. Ippen, "Expansion of frequency resolved optical gating spectrograms with Hermite-Gaussian functions." To be published.

L. A. Jiang, M. E. Grein, J. M. Fini, F. Rana, R. J. Ram, H. A. Haus, and E. P. Ippen, "Noise of harmonically modelocked lasers." To be published.

M. E. Grein, L. A. Jiang, H. A. Haus, and E. P. Ippen, "Quantum-limited timing jitter in actively modelocked fiber lasers." To appear in Optics Letters.

F. Rana, H. L. T. Lee, M. E. Grein, L. A. Jiang, and R. J. Ram, "Characterization of the noise and correlations in harmonically mode-locked lasers." Submitted to JOSA B

L. A. Jiang, K. S. Abedin, M. E. Grein, and E. P. Ippen. "Timing jitter reduction in modelocked semiconductor lasers with photon seeding," Applied Physics Letters **80**(10): 1707-1709 (2002).

L. A. Jiang, M. E. Grein, S. T. Wong, H. A. Haus, and E. P. Ippen, "Measuring timing jitter with optical cross-correlations." Submitted to IEEE Journal of Quantum Electronics.

L. A. Jiang, M. E. Grein, E. P. Ippen, C. McNeilage, J. Searls, and H. Yokoyama, "Quantum-limited noise performance of a mode-locked laser diode," Optics Letters **27**(1):49-51 (2002).

M. E. Grein, H. A. Haus, L. A. Jiang, and E. P. Ippen, "Action on pulse position and momentum using dispersion and phase modulation," Opt. Express **8**, 664–669 (2001).

L. A. Jiang, M. E. Grein, H. A. Haus, and E. P. Ippen, "Noise of mode-locked semiconductor lasers," IEEE J. Select. Topics Quantum Electron. **7**, 159–167 (2001).

L. A. Jiang, E. P. Ippen, U. Feiste, S. Diez, E. Hilliger, C. Schmidt, and H. G. Weber, "Sampling Pulses with Semiconductor Optical Amplifiers," IEEE J. Quantum Electron. **37**, 118–126 (2001).

M. E. Grein, L. A. Jiang, Y. Chen, H. A. Haus, and E. P. Ippen, "Timing restoration dynamics in an actively mode-locked fiber ring laser," Opt. Lett. **24**, 1687–1689 (1999).

S. Diez, C. Schmidt, D. Hoffmann, C. Bornholdt, B. Sartorius, H. G. Weber, L. A. Jiang and A. Krotkus, "Simultaneous sampling of optical pulse intensities and wavelengths by four-wave mixing in a semiconductor optical amplifier," Appl. Phys. Lett. **73**, 3821–3823 (1998).

Bibliography

[1] L. A. Coldren and S. W. Corzine, *Diode Lasers and Photonic Integrated Circuits*, John Wiley and Sons, New York, 1995.

[2] Agilent Technologies, "Calibration guide agilent technologies 8560 e-series and ec-series spectrum analyzers," Tech. Rep., Agilent Technologies, 2000.

[3] Agilent Technologies, "Agilent 83711b and 83712b synthesized cw generators agilent 83731b and 83732b synthesized signal generators data sheet," Tech. Rep., Agilent Technologies, 2000.

[4] T. E. Parker, "Characteristics and sources of phase noise in stable oscillators," in *Proc. 41st Ann. Symp. on Frequency Control*, 1987, pp. 99–110.

[5] J. Searls, "A mobile ultra-low phase noise sapphire oscillator," *Microwave Journal*, pp. 188–189, January 2002.

[6] K. Sato, A. Hirano, N. Shimizu, and I. Kotaka, "High-frequency and low-jitter optical pulse generation using semiconductor mode-locked lasers," *IEEE Transactions on Microwave Theory and Techniques*, vol. 47, no. 7, pp. 1251–1256, 1999.

[7] E. Yoshida and Nakazawa M., "Measurement of the timing jitter and pulse energy fluctuation of a PLL regeneratively mode-locked fiber laser," *IEEE Photon. Technol. Lett.*, vol. 11, no. 5, pp. 548–550, 1999.

[8] T. F. Carruthers and I. N. Duling III, "10-GHz, 1.3-ps erbium fiber laser employing soliton pulse shortening," *Opt. Lett.*, vol. 21, no. 23, pp. 1927–1929, 1996.

[9] R. Ludwig, S. Diez, A. Ehrhardt, L. Küller, W. Pieper, and H. G. Weber, ," *IEICE Trans. Electron.*, vol. E81-C, pp. 140, 1998, IEICE transactions on electronics.

[10] H. A. Haus and A. Mecozzi, "Noise of mode-locked lasers," *IEEE J. of Quantum Electron.*, vol. 29, no. 3, pp. 983–996, March 1993.

[11] John D. Moores, William S. Wong, and Hermann A. Haus, "Stability and timing maintenance in soliton transmission and storage rings," *Optics Communications*, vol. 113, pp. 153–175, 1994.

[12] M. E. Grein, L. A. Jiang, Y. Chen, H. A. Haus, and E. P. Ippen, "Timing restoration dynamics in an actively mode-locked fiber ring laser," *Opt. Lett.*, vol. 24, no. 23, pp. 1687–1689, 1999.

[13] T. R. Clark, T. F. Carruthers, P. J. Matthews, and I. N. Duling III, "Phase noise measurements of ultrastable 10 GHz harmonically modelocked fibre laser," *Electronics Letters*, vol. 35, no. 9, pp. 720–721, 1999.

[14] R. A. Barry, VWS Chan, Hall K. L., E. S. Kintzer, J. D. Moores, K. A. Rauschenbach, E. A. Swanson, L. E. Adams, C. R. Doerr, S. G. Finn, H. A. Haus, E. P. Ippen, W. S. Wong, and M Haner, "All-optical network consortium - ultrafast TDM networks," *IEEE Journal on Selected Areas in Communications*, vol. 14, no. 5, pp. 999–1013, June 1996.

[15] M. Nakazawa, E. Yoshida, T. Yamamoto, E. Yamada, and A. Sahara, "TDM single channel 640 Gbit/s experiment over 60 km using 400 fs pulse train and walk-off free, dispersion flattened nonlinear optical loop mirror," *Electron. Lett.*, vol. 34, no. 9, pp. 907–908, 1998.

[16] M. Nakazawa, T. Tamamoto, and K. R. Tamura, "1.28 Tbit/s - 70 km OTDM transmission using third- and fourth-order simultaneous dispersion compensation with a phase modulator," *Electron. Lett.*, vol. 36, no. 24, pp. 2027–2028, 2000.

[17] U. Feiste, R. Ludwig, C. Schubert, J. Berger, C. Schmidt, H. G. Weber, B. Schmauss, A. Munk, B. Buchold, D. Briggmann, F. Kueppers, and F. Rumpf, "160 Gbit/s transmission over 116 km field-installed fibre using 160 Gbit/s OTDM and 40 Gbit/s ETDM," *Electronics Letters*, vol. 37, no. 7, pp. 443–445, March 2001.

[18] P. W. Juodawlkis, J. C. Twichell, G. E. Betts, J. J. Hargreaves, R. D. Younger, J. L. Wasserman, F. J. O'Donnell, K. G. Ray, and R. C. Williamson, "Optically sampled analog-to-digital converters," *IEEE Transactions on Microwave Theory and Techniques*, vol. 49, pp. 1840, October 2001.

[19] R. P. Scott, C. Langrock, and B. H. Kolner, "High-dynamic-range laser amplitude and phase noise measurement techniques," *IEEE. J. Select. Topics Quantum Electron.*, vol. 7, no. 4, pp. 641–655, 2001.

[20] Marlon Rosendo H. Daza and Caesar A. Saloma, "Jitter dynamics of a gain-switched semiconductor laser under self-feedback and external optical injection," *IEEE Journal of Quantum Electronics*, vol. 37, no. 2, pp. 254–264, February 2001.

[21] Masahiko Jinno, "Correlated and uncorrelated timing jitte in gain-switched laser diodes," *IEEE Photonics Technology Letters*, vol. 5, no. 10, pp. 1140–1143, October 1993.

[22] M. J. Guy, S. V. Chernikov, and J. R. Taylor, "A duration-tunable, multiwavelength pulse source for OTDM and WDM communications," *IEEE Photon. Technol. Lett.*, vol. 9, no. 7, pp. 1017–1019, 1997.

[23] D. J. Derickson, A. Mar, and J. E. Bowers, "Residual and absolute timing jitter in actively mode-locked semiconductor lasers," *Electronics Letters*, vol. 26, no. 24, pp. 2026–2028, November 1990.

[24] C. M. DePriest, A. Braun, J. H. Abeles, and P. J. Delfyett Jr., "10-GHz ultralow-noise optical sampling stream from a semiconductor diode ring laser," *IEEE Photon. Technol. Lett.*, vol. 13, no. 10, pp. 1109–1111, 2001.

[25] L. A. Jiang, M. E. Grein, E. P. Ippen, C. McNeilage, J. Searls, and H. Yokoyama, "Quantum-limited noise performance of a modelocked laser diode," *Opt. Lett.*, vol. 27, no. 1, pp. 49–51, 2001.

[26] L. A. Jiang, M. E. Grein, H. A. Haus, and E. P. Ippen, "Noise of mode-locked semiconductor lasers," *IEEE J. Select. Topics Quantum Electron.*, vol. 7, no. 2, pp. 159–167, 2001.

[27] C. M. DePriest, P. J. Delfyett, J. H. Abeles, and A. Braun, "Low noise external-cavity semiconductor diode ring laser actively modelocked at 10 GHz," in *Ultrafast Electronics and Optoelectronics*, Lake Tahoe, Nevada, January 2001, OSA.

[28] C. M. DePriest, P. J. Delfyett, J. H. Abeles, and A. Braun, "Ultrahigh-stability photonic sampling streams from an actively-modelocked semiconductor diode ring laser," in *Conference on Lasers and Electro-Optics*, Baltimore, May 2001, OSA.

[29] W. Ng, R. Stephens, D. Persechini, and K. V. Reddy, "Ultra-low jitter mode-locking of er-fibre laser at 10 GHz and its application in photonic sampling for analogue-to-digital conversion," *Electron Lett.*, vol. 37, pp. 113–115, 2001.

[30] K. S. Kazi, J. T. Gopinath, L. A. Jiang, M. E. Grein, H. A. Haus, and E. P. Ippen, "Self-stabilized passive, harmonically mode-locked stretched pulse Erbium fiber ring laser," Submitted to Optics Letters, 2002.

[31] X.-L. Wang, H. Yokoyama, and T. Shimizu, "Sychronized harmonic frequency mode-locking with laser diodes through optical pulse train injection," *IEEE Photon. Technol. Lett.*, vol. 8, pp. 617, 1996.

[32] F. Rana, H. L. T. Lee, M. E. Grein, L. A. Jiang, and R. J. Ram, "Characterization of the noise and correlations in harmonically mode-locked lasers," to be published in JOSA B.

[33] L. A. Jiang, M. E. Grein, J. M. Fini, F. Rana, R. J. Ram, H. A. Haus, and E. P. Ippen, "Noise of harmonically modelocked lasers," to be published.

[34] E. R. Thoen, M. E. Grein, E. M. Koontz, E. P. Ippen, H. A. Haus, and L. A. Kolodziejski, "Stabilization of an active harmonically mode-locked fiber laser using two-photon absorption," *Optics Letters*, vol. 25, no. 13, pp. 948–950, July 2000.

[35] David A. Leep and David A. Holm, "Spectral measurement of timing jitter in gain-switched semiconductor lasers," *Appl. Phys. Lett.*, vol. 60, no. 20, pp. 2451–2453, May 1992.

[36] D. von der Linde, "Characterization of noise in continuously operating mode-locked lasers," *Appl. Phys. B*, vol. 39, pp. 201–217, 1986.

[37] Ursula Keller, Kathryn D. Li, Mark Rodwell, and David M. Bloom, "Noise characterization of femtosecond fiber raman soliton lasers," *IEEE Journal of Quantum Electronics*, vol. 25, no. 3, pp. 280–288, March 1989.

[38] K. S. Abedin, M. Hyodo, and N. Onodera, "154 GHz polarisation-maintaining dispersion-managed actively modelocked fibre ring laser," *Electron. Lett.*, vol. 36, no. 14, pp. 1185–1186, July 2000.

[39] S. H. Cho, B. E. Bouma, E. P. Ippen, and J. G. Fujimoto, "Low-repetition-rate high-peak-power kerr-lens mode-locked Ti:Al_2O_3 laser with a multiple pass cavity," *Opt. Lett.*, vol. 24, no. 6, pp. 417–419, 1999.

[40] M. E. Grein, *Stability and Noise in Modelocked Lasers*, PhD dissertation, MIT, Department of Electrical Engineering and Computer Science, 2002.

[41] P. W. Juodawlkis, J. C. Twichell, J. L. Wasserman, G. E. Betts, and R. C. Williamson, "Measurement of mode-locked laser timing jitter by use of phase-encoded optical sampling," *Opt. Lett.*, vol. 26, no. 5, pp. 289–291, March 2001.

[42] Boris Drakhlis, "Calculate oscillator jitter by using phase-noise analysis (part 1)," *Microwaves & RF*, pp. 82–90,157, January 2001.

[43] C. X. Yu, S. Namiki, and H. A. Haus, "Noise of the stretched pulse fiber laser: Part ii experiments," *IEEE J. Quantum Electron.*, vol. 33, no. 5, pp. 660–668, 1997.

[44] L. A. Jiang, M. E. Grein, and E. P. Ippen, "Region of validity for residual phase noise measurements of actively modelocked lasers," submitted to Electron. Lett.

[45] T. Yilmaz, C. M. DePriest, P. J. Delfyett Jr., J. H. Abeles, and A. Braun, "Measurement of residual phase noise in 10 GHz pulsetrain using modified Michelson optical frequency discriminator," in *Ultrafast Electronics and Optoelectronics*, Lake Tahoe, Nevada, January 2001, OSA.

[46] "Characterization of clocks and oscillators," Tech. Rep., National Institute of Standards and Technology, 1990.

[47] L. A. Jiang, M. E. Grein, S. T. Wong, H. A. Haus, and E. P. Ippen, "Measuring timing jitter with optical cross-correlations," submitted to IEEE J. of Quantum Electron.

[48] "Phase noise characterization of microwave oscillators; frequency discriminator method; product note 11729c-2," Tech. Rep., Agilent Technologies, 1985.

[49] D. E. Spence, W. E. Sleat, J. M. Evans, W. Sibbett, and J. D. Kafka, "Time synchronisation measurements between two self-modelocked ti:sapphire lasers," *Opt. Commun.*, vol. 101, pp. 286–296, 1993.

[50] M. J. W. Rodwell, D. J. Bloom, and K. J. Weingarten, "Subpicosecond laser timing stabilization," *IEEE J. of Quantum Electron.*, vol. 25, pp. 817–827, 1989.

[51] M. E. Grein, H. A. Haus, Y. Chen, and E. P. Ippen, "A theoretical study of timing jitter in an actively modelocked soliton fiber laser: comparison between amplitude and phase modulation," Tech. Rep. 89, MIT, Cambridge, MA, USA, 2000.

[52] L. A. Jiang, M. E. Grein, and E. P. Ippen, "Full-pulse characterization using autocorrelations and a genetic algorithm," in *Conference on Lasers and Electro-Optics*, Baltimore, May 2001, OSA.

[53] J. P. Gordon and H. A. Haus, "Random walk of coherently amplified solitons in optical fiber transmission," *Opt. Lett.*, vol. 11, no. 10, pp. 665–667, 1986.

[54] S. A. Crooker, F. D. Betz, J. Levy, and D. D. Awschalom, "Femtosecond synchronization of two passively mode-locked Ti:sapphire lasers," *Review of Scientific Instruments*, vol. 67, no. 6, pp. 2068–2071, June 1996.

[55] L. A. Jiang, M. E. Grein, E. P. Ippen, and H. A. Haus, "Noise of modelocked laser diodes," in *International Semiconductor Laser Conference*, Monterey, CA, USA, September 2000, OSA.

[56] L. A. Jiang, K. S. Abedin, M. E. Grein, and E. P. Ippen, "Timing jitter reduction in modelocked semiconductor lasers with photon seeding," *Appl. Phys. Lett.*, vol. 80, no. 10, pp. 1707–1709, 2002.

[57] H. Kawaguchi and K. S. Abedin, "Coherent photon seeding of actively mode locked laser diodes," *Applied Physics Letters*, vol. 62, no. 18, pp. 2164–2166, 1993.

[58] Patrick Langlois, David Gay, Nathalie McCarthy, and Michel Piché, "Noise reduction in a mode-locked semiconductor laser by coherent photon seeding," *Optics Letters*, vol. 23, no. 2, pp. 114–116, 1998.

[59] M. Schell, W. Utz, D. Huhse, J. Kässner, and D. Bimberg, "Low jitter single-mode pulse generation by a self-seeded, gain-switched fabry-perot semiconductor laser," *Appl. Phys. Lett.*, vol. 65, no. 24, pp. 3045–3047, 1994.

[60] P. Beaud, J. Q. Bi, W. Hodel, and H. P. Weber, "Experimental observation of the self-stabilization of a synchronously pumped dye laser," *Optics Communications*, vol. 80, no. 1, pp. 31–36, 1990.

[61] G. H. C. New, "Self-stabilization of synchronously mode-locked lasers," *Optics Letters*, vol. 15, no. 22, pp. 1306–1308, 1990.

[62] Blake Peterson, "Spectrum analysis, application note 150," Tech. Rep., Agilent Technologies, 1989.

[63] K. A. Williams, I. H. White, D. Burns, and W. Sibbett, "Jitter reduction through feedback for picosecond pulsed InGaAsP lasers," *IEEE Journal of Quantum Electronics*, vol. 32, no. 11, pp. 1988–1994, 1996.

[64] M. Nakazawa, E. Yamada, H. Kubota, and K. Suzuki, "10 Gbit/s soliton transmission over one million kilometres," *Electron Lett.*, vol. 27, pp. 1270–1272, 1991.

[65] M. Nakazawa, K. Suzuki, E. Yamada, H. Kubota, Y. Kimura, and M. Takaya, "Experimental demonstration of soliton data transmission over unlimited distances with soliton control in time and frequency domains," *Electron Lett.*, vol. 29, no. 9, pp. 729–730, 1993.

[66] N. J. Smith, K. J. Blow, W. J. Firth, and K. Smith, "Soliton dynamics in the presence of phase modulators," *Optics Communications*, vol. 102, no. 3-4, pp. 324–328, 1993.

[67] N. J. Smith, K. J. Dorian, K. J. Blow, and W. J. Firth, "Gordon-Haus jitter suppression using a single phase modulator," *Electron Lett.*, vol. 30, no. 12, pp. 987–988, 1994.

[68] N. J. Smith, N. J. Doran, and W. Forysiak, "Gordon-Haus jitter suppression using an intra-span phase modulator and post transmission dispersion compensator," *IEEE Photon. Technol. Lett.*, vol. 8, no. 3, pp. 455–457, 1996.

[69] J. P. King, I. Hardcastle, Harvey, and H. John, "Method and apparatus for conditioning optical solitons," US Patent, number 6,130,767, October 2000.

[70] L. A. Jiang, M. E. Grein, B. S. Robinson, H. A. Haus, and E. P. Ippen, "Experimental demonstration of a timing jitter eater," in *Conference on Lasers and Electro-Optics*, Long Beach, California, USA, May 2002, OSA.

[71] Fabrizio Forghieri, P. R. Prucnal, R. W. Tkach, and A. R. Chraplyvy, "RX versus NRZ in nonlinear WDM systems," *IEEE Photon. Technol. Lett.*, vol. 9, no. 7, pp. 1035–1037, 1997.

[72] R. I. Killey, M. Whitehead, P. N Stavrinou, G. Parry, and C. C. Cutton, "Design of InGaAsP multiple quantum-well Fabry-Perot modulators for soliton control," *IEEE J. Lightwave Technol.*, vol. 17, no. 8, pp. 1408–1414, 1999.

[73] H. A. Haus, "A theory of forced mode locking," *IEEE J. Quantum Electron.*, vol. QE-11, pp. 323–330, 1975.

[74] H. A. Haus, "Theory of mode locking with a slow saturable absorber," *IEEE J. of Quantum Electron.*, vol. QE-11, no. 9, pp. 736–746, September 1975.

[75] H. A. Haus, "Theory of mode locking with a fast saturable absorber," *Journal of Applied Physics*, vol. 46, no. 7, pp. 3049–3058, July 1975.

[76] T. Yoshida, Hoshida T., Y. Nasu, M. Kishi, and M. Tsuchiya, "Experimental investigation on carrier dynamics in sch-mqw waveguide saturable absorber of passively mode-locked monolithic laser diode," *Optical and Quantum Electronics*, vol. 33, no. 7-10, pp. 735–743, 2001.

[77] J. T. Gopinath, E. R. Thoen, E. M. Koontz, M. E. Grein, L. A. Kolodziejski, E. P. Ippen, and J. P. Donnelly, "Recovery dynamics in proton-bombarded

semiconductor saturable absorber mirrors," *Appl. Phys. Lett.*, vol. 78, no. 22, pp. 3409–3411, 2001.

[78] G. P. Agrawal, *Nonlinear fiber optics*, Academic Press, San Diego, California, second edition, 1995.

[79] K. L. Hall, *Femtosecond nonlinearities in InGaAsP diode lasers*, PhD dissertation, MIT, Department of Electrical Engineering and Computer Science, 1993.

[80] I. Kim and K. Y. Lau, "Frequency and timing stability of mode-locked semiconductor lasers – passive and active mode locking up to millimeter wave frequencies," *IEEE J. Quantum Electron.*, vol. 29, no. 4, pp. 1081–1090, 1993.

[81] Hong Lu, "Timing jitter caused by amplified spontaneous emission in mode-locked solid state lasers," *Optics Communications*, vol. 183, pp. 243–248, 2000.

[82] D. R. Hjelme and A. R. Mickelson, "Theory of timing jitter in actively mode-locked lasers," *IEEE J. of Quantum Electron.*, vol. 28, no. 6, pp. 1594–1606, 1992.

[83] B. Zhu, I. H. White, Penty. R. V., A. Wonfor, E. Lach, and H. D. Summers, "Theoretical analysis of timing jitter in monolithic multisection mode-locked DBR laser diodes," *IEEE J. Quantum Electron.*, vol. 33, no. 7, pp. 1216–1220, 1997.

[84] H. A. Haus, M. E. Grein, and L. A. Jiang, "Quantum limit on timing jitter of actively modelocked lasers," Tech. Rep. 92, MIT, Cambridge, MA, USA, 2001.

[85] A. E. Siegman, *Lasers*, University Science Books, Mill Valey, California, 1986.

[86] E. Desurvire, *Erbium-doped fiber amplifiers: Principles and Applications*, John Wiley & Sons, New York, 1994.

[87] G. B. Arfkin and H. J Weber, *Mathematical Methods for Physicists*, Academic Press, San Diego, fourth edition, 1995.

[88] G. P. Agrawal and N. K. Dutta., *Long-wavelength semiconductor lasers*, Van Nostrand Reinhold, New York, 1986.

[89] Mikael Svalgaard and Sarah L. Gilbert, "Stability of short single-mode erbium-doped fiber lasers," *Appl. Opt.*, vol. 36, no. 21, pp. 4999–5005, 1997.

[90] Steve Sanders, Namkyoo Park, Jay W. Dawson, and Kerry J. Vahala, "Reduction of the intensity noise from an erbium-doped fiber laser to the standard quantum limit by intracavity spectral filtering," *Appl. Phys. Lett.*, vol. 61, no. 16, pp. 1889–1891, 1992.

[91] Thomas R. Clark Irl N. Duling III, Robert P. Moeller, "Active filtering of the amplitude noise of a mode-locked fiber laser," in *Conference on Lasers and Electro-Optics*, San Francisco, California, USA, May 2000, OSA.

[92] Yukihiro Ishii, "Time-average holographic interferometry with a sinusoidally modulated laser diode," *Optics and Lasers in Engineering*, vol. 36, pp. 515–526, 2001.

[93] Patrcik Sandoz, Tijani Gharbi, and Gilbert Tribillon, "Phase-shifting methods for interferometers using laser-diode frequency-modulation," *Opt. Commun.*, vol. 132, pp. 227–231, 1996.

[94] Dwight F. Mix, *Random Signal Processing*, Prentice Hall, New Jersey, 1995.

[95] J. L. A. Chilla and O. E. Martinez, "Direct determination of the amplitude and phase of femtosecond light pulses," *Opt. Lett.*, vol. 16, pp. 39, 1991.

[96] S. Prein, S. Diddams, and J.-C. Diels, "Complete characterization of femtosecond pulses using an all-electronic detector," *Opt. Commun.*, vol. 123, pp. 567–573, 1996.

[97] R. Trebino and D. J. Kane, "Using phase retrieval to measure the intensity and phase of ultrashort pulses – frequency resolved optical gating," *J. Opt. Soc. Am. A*, vol. 10, pp. 1101–1111, 1993.

[98] R. G. M. P. Koumans and A. Yariv, "Time-resolved optical gating based on dispersive propagation: a new method to characterize optical pulses," *IEEE J. Quantum Electron.*, vol. 36, pp. 137–144, 2000.

[99] I. G. Cormack, W. Sibbett, and D. T. Reid, "Practical measurement of femtosecond optical pulses using time-resolved optical gating," *Optics Communications*, vol. 194, pp. 415–424, July 2001.

[100] C. Iaconis and I. A. Walmsley, "Self-referencing spectral interferometry for measuring ultrashort optical pulses," *IEEE J. of Quant. Elect.*, vol. 35, pp. 501–509, 1999.

[101] L. A. Jiang, E. P. Ippen, U. Feiste, S. Diez, E. Hilliger, C. Schmidt, and H. G. Weber, "Sampling pulses with semiconductor optical amplifiers," *IEEE Journal of Quantum Electronics*, vol. 37, no. 1, pp. 118–126, 2001.

[102] J. Debeau, B. Kowalski, and R. Boittin, "Simple method for the complete characterization of an optical pulse," *Opt. Lett.*, vol. 23, no. 22, pp. 1784–1786, 1998.

[103] H. Kawaguchi and J. Inoue, "Four-wave mixing among sub-picosecond optical pulses in a semiconductor optical amplifier and its applications," in *8th European Conference on Integrated Optics*, Royal Institute of Technology, Stockholm, Sweden, 1997.

[104] M. Shirane, Y. Hashimoto, H. Yamada, and H. Yokoyama, "A compact optical sampling measurement system using mode-locked laser-diode modules," *IEEE Photon. Technol. Lett.*, vol. 12, no. 11, pp. 1537–1539, 2000.

[105] J.-C. M. Diels, J. J. Fontaine, McMichael I. C., and Simoni F., "Control and measurements of ultrashort pulse shapes (in amplitude and phase) with femtosecond accuracy," *Appl. Opt.*, vol. 24, pp. 1270–1282, 1985.

[106] C. Iaconis and I. A. Walmsley, "Self-referencing spectral interferometry for measuring ultrashort optical pulses," *IEEE J. Quantum Electron.*, vol. 35, pp. 501–509, 1999.

[107] J. W. Nicholson, F. G. Omenetto, D. J. Funk, and A. J. Taylor, "Evolving frogs: phase retrieval from frequency-resolved optical gating measurements by use of genetic algorithms," *Opt. Lett.*, vol. 24, pp. 490–492, 1999.

[108] M. Gen and R. Cheng, *Genetic Algorithms & Engineering Optimization*, Wiley, New York, 2000.

[109] K. W. DeLong and R. Trebino, "Improved ultrashort pulse-retrieval algorithm for frequency-resolved optical gating," *J. Opt. Soc. Amer. A*, vol. 11, pp. 2429–2437, 1994, Composite algorithm.

[110] K. W. DeLong, D. N. Fittinghoff, B. Kohler R. Trebino, and K. Wilson, "Pulse retrieval in frequency-resolved optical gating based on the method of generalized projections," *Opt. Lett.*, vol. 19, pp. 2152–2154, 1994, Generalized Projections (GP) algorithm.

[111] D. J. Kane, G Rodriguez, A. J. Taylor, and Clement T. S., "Simultaneous measurement of two ultrashort laser pulses from a single spectrogram in a single shot," *J. Opt. Soc. Amer. B*, vol. 14, pp. 935–943, 1997, Principal Component Generalized Projections (PCGPA).

[112] D. J. Kane, "Real-time measurement of ultrashort laser pulses using principal component generalized projections," *IEEE J. Sel. Top. Quantum Electron.*, vol. 4, pp. 278–284, 1998, Principal Component Generalized Projections (PCGPA) w/o SVD.

[113] M. Matsumoto and H. A. Haus, "Stretched-pulse optical fiber communications," *IEEE Photonics Technology Letters*, vol. 9, no. 6, June 1997.

[114] Inho Kim and Kam Yin Lau, "Frequency and timing stability of mode-locked semiconductor lasers - passive and active mode locking up to millimeter wave

frequencies," *IEEE J. of Quantum Electron.*, vol. 29, no. 4, pp. 1081–1090, 1993.

[115] J. W. Nicholson, "The SEFGA (froggui.exe v1.01) can be downloaded from `http://www.phys.unm.edu/~jeffn/software.html`," Tech. Rep., University of New Mexico, 1998.

[116] D. J. Kane and R. Trebino, "Characterization of arbitrary femtosecond pulses using frequency-resolved optical gating," *IEEE J. Quantum Electron.*, vol. 29, pp. 571–579, 1993.

[117] R. Trebino, K. W. DeLong, D. N. Fittinghoff, J. N. Sweetser, M. A. Krumbügel, B. A. Richman, and D. J. Kane, "Measuring ultrashort laser pulses in the time-frequency domain using frequency-resolved optical gating," *Rev. Sci. Instrum.*, vol. 68, pp. 3277–3295, 1997.

[118] W. H. Press, S. A. Teukolsky, W. T. Vetterling, and B. P. Flannery, *Numerical Recipes in C: The Art of Scientific Computing*, Cambridge University Press, second edition, 1992.

[119] K. W. DeLong, D. N. Fittinghoff, and R. Trebino, "Practical issues in ultrashort-laser-pulse measurement using frequency-resolved optical gating," *IEEE Journal of Quantum Electronics*, vol. 32, pp. 1253–1264, 1996.

[120] D. N. Fittinghoff, J. L. Bowie, J. N. Sweetser, R. T. Jennings, M. A. Krumbuegel, K. W. DeLong, R. Trebino, and I. W. Walmsley, "Measurement of the intensity and phase of ultraweek, ultrashort, laser pulses," *Optics Letters*, vol. 21, pp. 884–886, 1996.

[121] K.-L. Deng, R. J. Runser, I. Glesk, and P. R. Prucnal, "Single-shot optical sampling oscilloscope for ultrafast optical waveforms," *IEEE Photon. Tech. Lett.*, vol. 10, pp. 397–399, 1998.

[122] M. Eiselt, W. Pieper, and H. G. Weber, "Slalom: semiconductor laser amplifier in a loop mirror," *Journal of Lightwave Technology*, vol. 13, pp. 2099–2112, 1995.

[123] E. Hilliger, "Interferometrische schalter mit halbleiterverstaerkern," Diplomarbeit, 1998.

[124] S. Diez, C. Schmidt, D. Hoffmann, C. Bornholdt, B. Sartorius, H. G. Weber, L. A. Jiang, and A. Krotkus, "Simultaneous sampling of optical pulse intensities and wavelengths by four-wave mixing in a semiconductor optical amplifier," *Applied Physics Letters*, vol. 73, no. 26, pp. 3821–3823, 1998.

[125] C. Schmidt, "Untersuchung zum nichtlinearen verhalten von halbleiterlaserverstaerkern mittels optischer pikosekundenpulse," Diplomarbeit, 1997.

[126] R. W. Gerchberg and W. O. Saxton, "A practical algorithm for the determination of phase from image and diffraction plane pictures," *Optik*, vol. 35, pp. 237–246, 1972.

[127] J. R. Feinup, "Phase retrieval algorithms: a comparison," *Applied Optics*, vol. 21, pp. 2758–2769, 1982.

[128] Steve X. Yao and Lute Maleki, "Optoelectronic microwave oscillator," *J. Opt. Soc. Am. B*, vol. 13, no. 8, pp. 1725–1735, 1996.

[129] Steve X. Yao and Lute Maleki, "Multiloop optoelectronic oscillator," *IEEE J. Quantum Electron.*, vol. 36, no. 1, pp. 79–84, 2000.